Investigating the Relationship Between the Gas-Phase Structures of Protein Ions and Their Charge States

Kenneth Jeffrey Laszlo

A dissertation

submitted in partial fulfillment of the

requirements for the degree of

Doctor of Philosophy

University of Washington

2017

Reading Committee:

Prof. Matthew Bush, Chair

Prof. Frantisek Tureček

Prof. Robert Synovec

Program Authorized to Offer Degree:

Chemistry

University of Washington

Abstract

Investigating the Relationship Between the Gas-Phase Structures of Protein Ions and Their Charge States

Kenneth Jeffrey Laszlo

Chair of the Supervisory Committee:
Assistant Professor Matthew Bush
Department of Chemistry

This dissertation explores the utility of cation-to-anion proton transfer reactions (CAPTR) in native mass spectrometry, and investigates the relationship between the charge state (z) and collision cross section (Ω) of gas-phase protein ions from native-like and denaturing conditions. In CAPTR, protein cations are generated via nano-electrospray ionization (nESI) and reacted with stored anions via proton transfers. The products of those reactions are then studied using ion mobility (IM), which measures the Ω of an ion-neutral pair, and mass spectrometry (MS), which measures the mass-to-charge ratio (m/z) of an ion.

Chapter 1 discusses those reactions involving native-like protein and protein complex ions. Those results indicate that CAPTR may be used to aid in z determination, and separate mixtures of ions in m/z. The following several chapters then explore the relationship between z and Ω of denatured and native-like proteins and native-like protein complexes. Charge states of

ubiquitin from denaturing conditions were *m*/*z* selected for CAPTR. The results indicate that the ions compact following each reaction, and that the Ω of the product ions depends on the product ion charge state (*C*) and is independent of the precursor charge state (*P*). Energy-dependent experiments indicate that product ions of the same *C*, but from different *P*, have different subpopulations of ions. Similar experiments were performed with cytochrome C from native-like and denaturing conditions, which showed that the lowest *C* ions from those experiments have similar Ω. Additionally, the Ω of native-like cytochrome C CAPTR product ions depend more weakly on *C* than their denatured counterparts. The Ω of CAPTR products of lysozyme from native-like, denaturing/reducing and denaturing/disulfide intact solution conditions are also similar at the lowest *C* measured. Energy-dependent experiments reveal the importance of disulfide bonds on the gas-phase structure of lysozyme ions. Ω of the CAPTR products of native-like protein and protein complexes were also studied using IM-MS, energy-dependent pre-CAPTR collisional activation, and energy-dependent post-CAPTR collisional activation experiments. Those studies reveal the stabilities of the product ions, and that their Ω weakly depends on *C* compared to protein ions from denaturing conditions. CAPTR was also performed on poly-ubiquitin ions from native-like and denaturing solution conditions. The Ω of poly-ubiquitin ions from native-like solutions were used to develop coarse-grained models to interpret the domain structure of the CAPTR products of poly-ubiquitin ions from denaturing conditions. Further, figures of merit were used to quantitate the Ω of poly-ubiquitin ions from denaturing conditions as a function of *C*. Lastly, trajectory method calculations were performed to investigate how ion-induced dipole interactions may affect Ω of native-like and denatured protein ions.

Dedication

To my family, friends, and giants with broad shoulders.

ACKNOWLEDGEMENTS

The contents of this dissertation would not have been possible without the help of friends and family. First, I would like to thank my advisor, Prof. Matthew F. Bush. Matt provided insightful advice and thoughtful criticism on an innumerable amount of manuscript drafts, oral presentations, and grant applications. Moreover, Matt provided suggestions to further my research goals, while also giving me the space to pursue experiments I found interesting. I would also like to thank the members of my dissertation committee, Prof. František Tureček, Prof. Robert Synovec, Prof. Bo Zhang, and Prof. James Bruce. Prof. Tureček also allowed me to collaborate with his graduate student, Robert Pepin, and a visiting student, Kristina Slováková. I would also like to think Prof. Xiaosong Li, who's computational chemistry class significantly aided the work in Chapter 2, and his student Patrick Lestrange who helped me run those calculations.

The members of the UW chemistry department also significantly helped with administrative duties. Ashley Zigler (previous Graduate Program Coordinator) and Kristina Holder (current Graduate Program Coordinator), who promptly answered questions regarding graduate school exams, and Diana Knight (Assistant to the Chair) who has helped me with several odds-and-ends over the years. I'd like to thank Martin Sadilek for helping me teach CHEM 428 students, and for organizing informative PacMass talks for the past several years. Finally, I'd like to thank Locklan Hickok (Stockroom manager) for going the extra mile and shooting me emails when our liquid Nitrogen dewars would arrive.

I'd also like to thank several faculty members at my Alma Mater, the Georgia Institute of Technology. George P. Burdell, Prof. Facundo Fernandez, and Prof. Chad Morris. Facundo, thank you for the opportunity to let me join your group, and for the guidance in the early years of my

research career. You instilled in me a curiosity I don't think I'll ever shake. Prof. Morris, thank you for all your encouragement. Your guidance and advisement during those years were critical to my success, and I wouldn't be graduating again without your help.

I would be remiss to forget the current and former members of the Bush group. In order of appearance: Dr. Sam Allen. Thank you for all the talks over the years, professional and otherwise. I wrote a Haiku for you:

Five Years Together

Why is nothing working? Shoot.

PDMTT

Dr. Sam Marionni, you always brought some levity to hard days. I wish I had listened to you more around when you were graduating. I may have avoided some of the mistakes I've made over the last year. Kimberly Davidson, thank you for your help with all my various questions over the years and the fun times. See you on the other side. Also, thank you for coming up with "CAPTR", it's much better than "SCAPT". Eleanor Munger, I can confidently say this dissertation would be half as long without your incredibly hard work. Thank you so much for being a pleasure to work with, and a fast learner. Rae Eaton, the end is neigh, and good luck finishing up. Let me know when the laser is working. Stephanie Heard, thank you so much for all your hard work, and good luck in graduate school. Cece Hong, you are fantastically curious, and that will carry you far in graduate school. Best of luck. Meagan Gadzuk-Shae, grind it out, and don't forget how capable you are or that you're smarter than you think. Thank you for picking up the slack in CHEM 428 this quarter, for your edits to various manuscripts, and for your future help with peer reviews. Jack Buckner, great work last summer. You showed incredible initiative,

and that will make you successful in all your endeavors. Daniele Canzani and Julia Greenwald, you'll make it out fine, just stay motivated and know when to rest when you need it.

I'd also like to thank my family. To my sister Hayley for always being supportive and visiting me in Seattle. To my grandmother, Donna Bolan, for the fun weekends at grandma's house over the last several years. I'll always be grateful that I was able to spend more time with you over the last five years that I had the previous decade. To my parents, Mary and Jeff Laszlo, thank you for all the support and guidance for the last 27 years. You gave me the worth ethic, perseverance, and support I've needed, and I am eternally indebted to the two of you. I love you all.

Lastly, and most importantly, to Ariane Erickson. You are my partner in crime, my team mate, and my best friend. You have truly been the support system I've relied on more than anyone, and without you I'm sure I would have lost my mind. Thank you for the easy evenings, the bright days, and fun times. I love you, and thank you.

Nomenclature

Da	Dalton, the unified atomic mass unit
e	elementary charge, 1.6021766208(98) x 10^{-19} C
E	Electric Field
ESI and nESI	Electrospray Ionization and nano-electrospray ionization
GDI	Glow discharge ionization
PDCH	Perfluoro-1,3-dimyethylcyclohexane
He	helium, in reference to IM buffer gas
IM	Ion Mobility
k_B	Boltzmann's constant, 1.38064852(79) x 10^{-23} J·K^{-1}
μ	reduced mass, often between ion and neutral masses
MS	Mass Spectrometry
IM	Ion Mobility
IM-MS	Ion Mobility-Mass Spectrometry
m/z	mass-to-charge ratio, the standard measurement unit in MS
Ω	ion-neutral collision cross section
ToF	time-of-flight, an MS analyzer
z	ion charge state
CAPTR	Cation-to-Anion Proton Transfer Reactions
P	CAPTR precursor ion charge state
C	CAPTR product ion charge state
PA	Projection Approximation
EHSS	Exact Hard Sphere Scattering
TM	Trajectory Method
ETD	Electron Transfer Dissociation
rf	Radio-frequency

TABLE OF CONTENTS

Chapter 1. Introduction

1.1 General Overview

Proteins are long peptide polymers that fold in on themselves to achieve a "native", biologically relevant structure, which can function in some biological task.[1] The way a protein folds on itself, or the way proteins interact with one another (*e.g.* a protein complex) is highly related to the function of the protein or protein complex.[1,2] Thus, there is a great deal of interest in understanding the folding process, and intermediate structures between a nascent polypeptide and a native protein or protein complex. Several high-resolution technologies have been designed, rigorously tested, and implemented to measure the structures of native folded proteins and protein complexes, *e.g.* X-ray diffraction of crystals (XRD)[3,4] and nuclear magnetic resonance (NMR) spectroscopy.[5] However, measurements of intermediate structures as they fold from newly expressed proteins to their native folded structures have proven to be more challenging, due to their short lifetimes and challenges associated with the many complex interactions in solution.[6] This dissertation explores the opportunities that the gas-phase affords to study protein folding in the absence of solution. As a result, this work seeks to understand the extent to which protein-intramolecular interactions affect protein folding with a specific focus on the relationship between the charge-state of a gas-phase protein ion and the ions structure. To accomplish this, ion/ion proton transfer reactions are used to reduce the charge state of protein ions from denaturing and native solutions, and ion mobility is used to monitor the structural changes following each reaction. Additionally, the analytical advantages this technology affords the native-like protein and protein complex ion community are also discussed.

1.2 Gas-Phase Structures of Protein Ions.

The advent of soft ionization techniques to generate gas-phase protein ions like matrix assisted laser desorption/ionization (MALDI)[7,8] and electrospray ionization (ESI)[9–11] lead to a plethora of gas-phase biomolecular studies. In particular, the technology to generate gas-phase ions of intact proteins directly from solution via electrospray ionization lead to many innovative methods and experiments to study the structures of those ions. Those studies, and many subsequent works have investigated the question "*How are the structures of gas-phase protein ions related to proteins in solution?"*

The most widely used analytical measurement of gas-phase ions over the last 50 years has been mass spectrometry (MS) and allied techniques, due to the technology's unrivaled speed, sensitivity, and selectivity. Mass spectrometers are analytical instruments that consist of at least three parts, *i.e.* (1) an ionization source, (2) a mass analyzer, and (3) a detector, and are used to measure the mass-to-charge ratio (m/z) of ions. However, many modern mass spectrometers include additional components that can be used to study the structure of protein ions, such as ion mobility cells,[12–18] electron mediated dissociation sources,[12,19,20] gas-phase hydrogen-deuterium exchange, [21–26] or various implementations of photo-dissociation[27–30] and spectroscopies.[31,32] Thus, MS coupled with those various experiments to probe protein structure have been at the forefront of understanding the structures of gas-phase proteins.

1.3 Time-of-Flight Mass Spectrometry.

Time-of-Flight (ToF) mass spectrometry benefits from a theoretically unlimited m/z range, and fast data acquisition. These features make ToF mass spectrometry particularly

compelling to study large macromolecules, such as protein and protein complex ions. ToF mass analyzers have three essential components: (1) an ion accelerator (2) an electric field-free flight tube, and (3) a detector. In the experiment, ions are injected into the field-free flight tube with a narrow range of kinetic energies. Figure 1.1.A shows a diagram of a linear ToF Mass analyzer. In this orientation, ions are accelerated to a narrow distribution of kinetic energies into the electric field-free flight tube with a detector positioned in the direction of ion motion. Differences in the m/z of each ion lead to different velocities in the field-free flight tube, such that low m/z ions reach the detector before high m/z ions. The ions flight time is recorded as the ions reach the detector, which is proportional to the square-root of m/z. Analysis of protein ions typically occurs on orthogonal acceleration reflectron time-of-flight mass analyzers (oa-re-ToF), which have higher resolving powers than linear ToFs. For the purposes of this dissertation, all further references to ToFs reflect the oa-re-ToF geometry, unless otherwise noted. A diagram of this geometry is shown in Figure 1.1.B

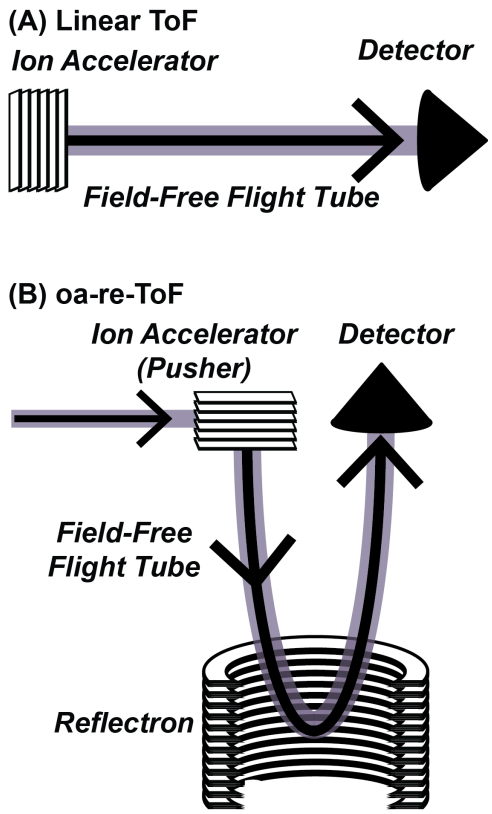

Figure 1.1. (A) Diagram of linear ToF geometry. (B) Diagram of oa-re-ToF geometry

1.3.1 *Relationship Between Time-of-Flight and m/z.*

The kinetic energy, *KE*, of an ion is related to the mass, *m*, and charge, *z*, of an ion through the following relation:

$$KE = \frac{1}{2}m(v_{ToF})^2 = ez * V \qquad \text{Equation 1.1}$$

Where *e* is the elementary charge, v_{ToF} is the velocity of the ion, and *V* is the accelerating voltage during the injection into the field-free flight tube. v_{ToF} may be determined by measuring

the time, *t*, between ion acceleration and detection and knowledge of the length of the flight path, *l*:

$$v_{ToF} = {}^{l}/_{t} \qquad \text{Equation 1.2}$$

Rearrangement of Equation 1.1 yields:

$$v_{ToF} = \sqrt{{}^{2ezV}/_{m}} \qquad \text{Equation 1.3}$$

Equation 1.2 may be inserted into Equation 1.3, and rearranged to yield the relationship between *m*/*z* and the time-of-flight:

$$t = \frac{l}{\sqrt{2eV}} * \sqrt{\frac{m}{z}} \qquad \text{Equation 1.4}$$

Thus, ions with low *m*/*z* values have shorter flight times and are detected before larger *m*/*z* ions. Notably, the relationship between *t* and *m*/*z* is not linear, but rather a square-root dependence. Therefore, there is greater data-density in the low *m*/*z* region of ToF mass spectra than compared to high.

1.4 Ion Mobility.

Ion mobility (IM) is a gas-phase electrophoretic method that separates ions based on their size and charge. IM may be used to measure the collision cross section (Ω) of the interaction between and ion and a neutral background gas, which approximates the projected surface area of an orientationally averaged ion-neutral pair. Pioneering IM experiments and theory development were conducted by Earl McDaniel at the Georgia Institute of Technology in the department of physics. His seminal textbook, "Transport Properties of Ions in Gases" was developed using experiments and theory associated with the mobility of bare metal ions in gases.[33] Remarkably, those models have proven to be well-suited for much larger systems, like proteins, when those structures are compared to XRD data, NMR data and coarse-grained models.[34–37]

Drift cell ion mobility spectrometers (also referred to as drift tube ion mobility spectrometry) are often a series of stacked ring electrodes, connected via a voltage divider network, which is filled with a neutral background gas.[38–41] Ions experience two main forces during the IM separation: (1) an electric force pulling the ion down the axis of transmission, and (2) a drag force caused by collisions with the neutral background gas. Those forces are equal and opposite in direction, which leads to a relatively constant ion velocity throughout the experiment (Figure 1.2.A). An example of the linear electric potential down the drift cell is shown in Figure 1.2.B. Ions with different size and charge are then separated in space, which is often shown as an arrival-time distribution (ATD, Figure 1.2.C). In this illustrative example, two different protein ion conformers with the same charge state are separated, such that the more compact ion exits the drift cell at a short drift time than the more extended conformer, due to fewer interactions with the neutral gas.

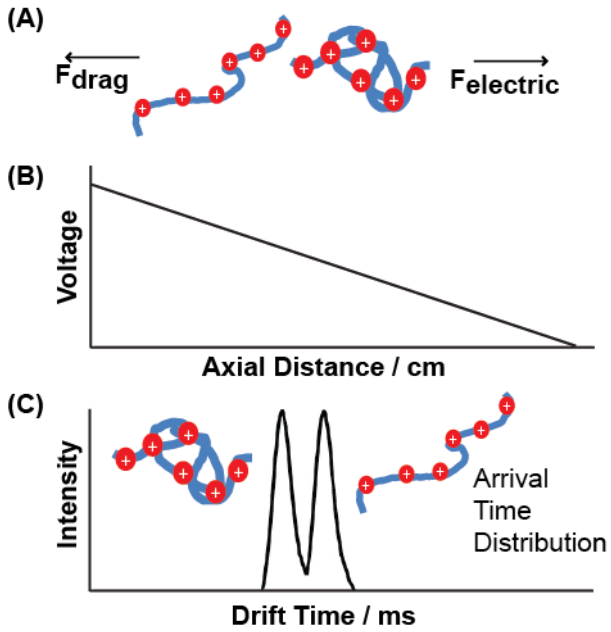

Figure 1.2. (A) Force diagram of forces acting upon protein ions in a drift cell ion mobility spectrometer. (B) Linear DC voltage as a function of the axial distance down the drift cell ion mobility spectrometer. (C) Example arrival-time distribution of a compact and extended protein conformer of the same charge state.

There are other implementations of ion mobility that have various advantages and disadvantages compared to drift cell ion mobility, which have been thoroughly reviewed elsewhere.[42] Drift cell ion mobility spectrometers operating at ~1-10 Torr can be broadly divided into two categories which differ in how ions are radially contained. One approach is to use large inner-diameter electrodes, and re-confine ions at the end of the drift cell using an ion-funnel. [43–45] In contrast, ions may be radially confined throughout the IM separation experiment via the

application of radio-frequency AC currents in opposite phases to alternating ring electrodes.[41,46] The latter approach is used in all the experiments described in this dissertation.

1.4.1 *Relationship Between Drift Time and Ω.*

The velocity, v_{IM}, of an ion in drift cell ion mobility spectrometry is related to the mobility of the ion in a gas, K, and the applied electric field, E:

$$v_{IM} = KE = K\frac{V}{L} \qquad \text{Equation 1.5}$$

Where E is equal to the applied drift voltage (V) divided by the length of the drift region (L). The experimental drift time, t_D, in IM experiments depends on the mobility-dependent drift time, t_K, and the transport time of ions from the exit of the drift cell to the detector, t_0:

$$t_D = t_K + t_0 \qquad \text{Equation 1.6}$$

t_k is related to v_{IM} and the length of the drift cell, L, by the relation:

$$t_k = \frac{L}{v_{IM}} = \frac{L^2}{K}\frac{1}{V} \qquad \text{Equation 1.7}$$

Equation 1.7 may be inserted into Equation 1.6 to yield:

$$t_D = \frac{L^2}{K}\frac{1}{V} + t_0 \qquad \text{Equation 1.8}$$

Thus, measurements of t_D over a range of V may be used to determine K by calculating the reciprocal of the slope of a plot of t_D versus $1/V$, e.g. a field-dependent method; additionally, t_0 may be determined by the y-intercept of this plot.[41,46] K may be converted to a Ω value, which is a description of the momentum transfer integral of many collisions between the ion and neutral background gas throughout the separation, via the Mason-Schamp equation:[33]

$$\Omega = \frac{3ez}{16\mathrm{N}}\left(\frac{2\pi}{\mu k_B \mathrm{T}}\right)^{1/2}\frac{1}{\mathrm{K}} \qquad \text{Equation 1.9}$$

where N is the drift-gas number density, μ is the reduced mass of the ion and drift gas, k_B is the Boltzmann constant, T is the drift-gas temperature, e is the charge of an electron, and z is the

charge state of the ion. Notably, to achieve an orientationally averaged Ω values, the experiment much be conducted under the low-field limit, which has been described in detail elsewhere.[33]

Alternatively, *K* may be determined by a t_D measurement at a single *V*, and measurement of t_0 via a field-dependent method, *e.g.* the "single-field strength" method. This approach benefits from requiring only one spectrum, therefore the *K* of low-abundant ions may be determined. t_0 is the sum of an *m*/*z* independent, t_{ind}, and *m*/*z* dependent parameter, $t_{m/z}$:

$$t_0 = t_{ind} + t_{m/z} \qquad \text{Equation 1.10}$$

where may be estimated $t_{m/z}$ by:

$$t_{m/z} = \frac{c\sqrt{m/z}}{1000} \qquad \text{Equation 1.11}$$

where *c* is an instrument specific parameter (the 'enhanced duty cycle delay coefficient' on the Waters Synapt G2)[47]. Using these relationships Equation 1.8 can be expressed as:

$$t_K = \frac{L^2}{K}\frac{1}{V} = t_D - \left(t_{ind} + \frac{c\sqrt{m/z}}{1000}\right) \qquad \text{Equation 1.12}$$

As mentioned, t_{ind} may be determined through field-dependent measurements. Equation 1.12 can be rearranged to yield:

$$\frac{1}{K} = \frac{\left[t_D - \left(t_{ind} + \frac{c\sqrt{m/z}}{1000}\right)\right] * V}{L^2} \qquad \text{Equation 1.13}$$

and thus, *K* may be determined to calculate Ω via Equation 1.13.

1.4.2 *Ion Mobility-Mass Spectrometry.*

The fast data acquisition of ToF mass analyzers (10s to 100s of μs) make it particularly compelling to couple to ion mobility spectrometers, which operate on the time scale of 10s of milliseconds. As a result, the two spectrometries may be coupled to one another as ion mobility-mass spectrometry (IM-MS). IM-MS is a two-dimensional separation, analogous to robust

methods like gas chromatography-MS (GC-MS) and liquid chromatography-MS (LC-MS), and therefore can measure the Ω and the *m*/*z* of an ion in a single experiment. There are now several examples of commercial implementations of this arrangement, such as the Waters Synapt IM-MS mass spectrometers,[48,49] and the Agilent 6560.[50,51]

1.4.3 *Comparing Ω values to structures.*

An important component in comparing IM data to other structural biology methods is the development of software models to calculate Ω values from structures measured with other methods, such as XRD, NMR, or coarse-grained models. Three main algorithms have emerged to undertake this challenge, which vary in terms of their computational costs and complexity of the physics involved: the projection approximation (PA),[52] exact hard sphere scattering (EHSS)[53,54] and the trajectory method (TM).[55] There are additional algorithms, such as the projection superposition approximation,[56] however they are not as widely used as the PA, EHSS, and TM.

The PA[52] is the most simple computational model, and acts a first approximation of the size of an ion and neutral gas-molecule. In this algorithm, an input structure is randomly rotated about the center of mass, and projected onto a 2D surface. The area of that projection is calculated using a Monte Carlo approach. This sequence is repeated until the average of the calculated areas converge. The PA model routinely underestimates experimental Ω values,[35] but serves as a computationally inexpensive approximation.

The EHSS[53,54] algorithm is more computationally expensive than the PA, however its computational cost is relatively inconsequential with modern computers. In this approach, many individual collisions between an input atomic structure and neutral gas molecules are simulated, and the momentum transfer from each collision is calculated. These calculations provide an over

estimation of experimental Ω, thus may be paired with the PA to provide a range of possible Ω values. The initial algorithm[53] was updated several years later to improve the speed of the computation.[54]

The TM[55] is most similar to the EHSS, although the TM includes a potential for long-range Lennard-Jones interaction plus a term for ion-induced dipole interactions between the ion and neutral gas.[57] Unlike that of the PA or EHSS, the input for the TM includes atomic partial charges. The TM is the most accurate of these three models and is computationally expensive. Consequentially, the TM is seldom used for large ions, such as proteins and protein complexes, although there have been several examples.[35,58]

1.5 Ionization of Proteins

Early mass spectrometers often generated gaseous ions from gaseous samples via electron ionization sources, which results in covalent fragmentation of the analyte. These experiments could be used to elucidate the molecular structure of an ion based on reproducible fragmentation patterns. However, electron ionization limited experiments to those pertaining to chemicals small enough to have high enough vapor pressures sufficient to generate the necessary number of gaseous ions. Early ionization sources, like electron ionization, were incompatible with large biomolecules because (1) they frequently resulted in covalent fragmentation, thus the entire molecule could not be studied intact by MS, and (2) they generally could not generate ions from molecules greater than several hundred Da.

The mid-to-late 1980's saw the introduction of two novel ionization sources with properties appealing to mass spectrometry of protein ions, because they could transfer much more massive molecules (kDa to MDa) into the gas phase as ions without covalent fragmentation. Those ionization sources were Matrix Assisted Laser Desorption/Ionization

(MALDI)[7,8] and electrospray ionization (ESI).[9–11] MALDI typically consists of a dry analyte in crystals of a matrix, *e.g.* nicotinic acid, urea, tris bufffer,[8] on a metal plate. The plate is then irradiated with a laser, and ions are generated as a result. Those ions are typically singly charged ($z = 1$), and thus result in very high m/z protein ions.

For structural biology studies in the gas-phase, electrospray ionization offers compelling advantages, including that it generates gas-phase ions directly from protein in solutions. Electrospray ionization consists of at three main components: (1) a capillary, (2) a DC voltage source, and (3) the sample. A diagram of the electrical circuit established between the sample, capillary, power supply and the remaining components of the mass spectrometer are shown in Figure 1.3. The liquid sample is placed inside the narrow capillary and biased by ~0.5 to 5 kV, relative to the mass spectrometer. The applied DC bias strongly depends on the surface tension of the liquid and the diameter of the capillary. This electrical bias generates a highly-charged Taylor cone[59] at the end of the capillary, which emits many charged droplets containing the analyte.[60] Through stages of solvent evaporation and coulomb fission,[61] multiply protonated gas-phase ions of the analyte of interest are produced, which may be analyzed and detected via the remaining components of the mass spectrometer. The exact mechanism behind ESI is still a hotly debated subject,[62–65] however small molecules generally follow an 'ion evaporation model',[61,66–68] large globular molecules (such as folded proteins) generally follow a 'charged residue model',[9,69,68]and long polymeric molecules (such as denatured proteins) are thought to follow the 'chain ejection model'.[68] Additionally, ESI sources with large capillaries (10s to 100s of μm) are often pneumatically assisted to help generate the flow through the capillary. In contrast, smaller diameters capillaries (1 to 3 μm), such as those pulled from borosilicate glass, generate a spontaneous electroosmotic flow following the application of the DC bias, and therefore do not

require assistance in generating flow.[70] ESI from these small capillaries, often referred to as nano-electrospray ionization (nESI), also benefit from reducing non-specific adduction of salts and non-specific oligomeric ions.[70]

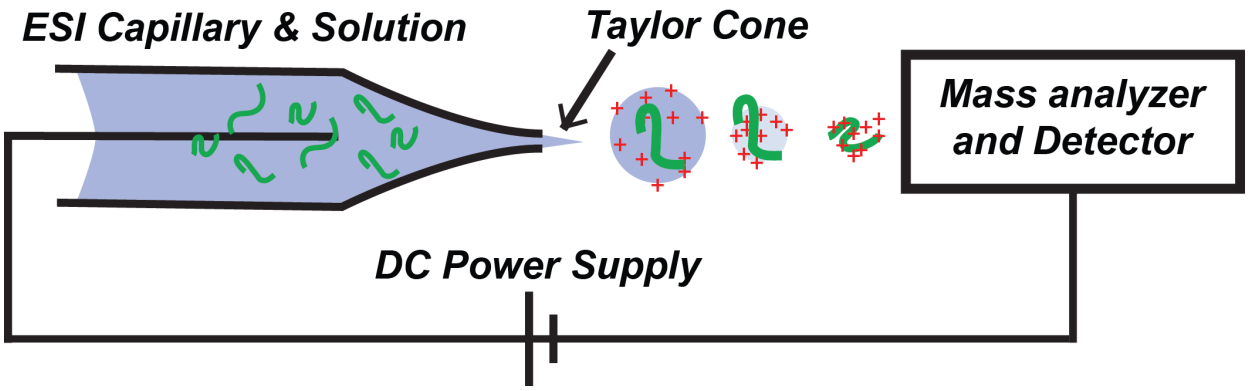

Figure 1.3. Diagram of an electrospray ionization source.

1.5.1 *Electrospray of protein ions from denaturing solutions.*

Early electrospray mass spectra of biomolecules consisted of several reports of relatively small intact proteins.[11,71–73] Albeit, 'small' intact proteins were much more massive than other ions studied at the time. John Fenn, 2002 Nobel prize in chemistry recipient for the "development of soft desorption ionisation methods for mass spectrometric analyses of biological macromolecules",[74] titled his award lecture "Electrospray Wings for Molecular Elephants".[75] In those experiments, ions were generated from denaturing solution conditions (*i.e.* low pH, organic solvents, low ionic strength), which generated wide *z* distributions with *z* high enough such that the ions had much lower *m*/*z* ratios than those generated via MALDI.

Those early studies were followed by IM-MS analysis of denatured protein ions, which revealed that denatured ions exhibited a strong correlation between the charge-state of a protein ion, and the Ω of that charge state. At the highest charge states, protein ions would approach

conformers similar to a linear structure (dihedral angles of 180˚).[39,76–78] In contrast, intermediate charge states exhibited complex Ω distributions with many unresolved structures consistent with partially folded structures, and low charge states would reach compact conformers with Ω that approach the Ω estimated from XRD and NMR data.

Further studies of denatured ions focused on the structural dynamics of the ions on time scales relevant to IM-MS experiments (10s of milliseconds), as well as much longer time scales (several minutes). In one report, Clemmer and coworkers used a home-built IM-IM-MS instrument to select portions of an arrival-time distribution and separate that selected distribution through another stage of IM to reveal if that selection isomerized on the time scales of an IM separation.[79] In fact, the selection did not isomerize, thus showing that the structures of these gas-phase ions were kinetically trapped in their conformations on the time-scale of IM-MS experiments. Further studies by Clemmer and McLafferty have revealed that ions do isomerize to lower-energy gas-phase structures on the time scale of 100s of milliseconds to minutes.[14,80]

1.5.2 *Electrospray of protein ions from native solutions.*

In contrast to proteins from denaturing conditions, MS data of globular protein ions generated from ESI of native solutions, *i.e.* pH 7, aqueous, 200 mM ammonium acetate, generates ions that are notably different than their denatured counterparts. Those differences include (1) the ions have masses reflective of their native oligomeric states, (2) their charge states are comparatively lower, and (3) the charge state distributions are comparatively narrower. These factors contribute to challenges in native MS to accurately assign charge states to m/z peaks, due to loss of isotopic resolution for these large native ions.[81,82]

Advances in IM-MS technologies have led to IM measurements of native-like protein and protein complex ions.[41,47,49] Globular native-like protein and protein complex ions from aqueous

ammonium acetate solutions exhibit much more compact Ω, are much less dependent on *z* than their denatured counterparts,[41,46,64] and have Ω consistent with XRD and NMR data.[35] In contrast, native-like ions with intrinsically disordered regions, prion proteins,[83,84] and 'supercharged' ions[85] behave more similar to denatured protein ions. These discrepancies have led to a great deal of interest in understanding how the gas-phase structures of native-like protein and protein complex ions relate to their solution-phase counter parts.

Although that question has not yet been fully answered, native mass spectrometry, and native IM-MS have made significant advances in the fields of amyloid[86,87] and serpinopathy[88] formation, virus capsid assembly,[89,90] small heat shock protein subunit dynamics,[91] and ATPase function.[92] Additionally, recent IR spectroscopic and IM experiments have shown that native-like ions retain aspects of their secondary structure and shape in the gas-phase.[32] Additional experiments have revealed that native-like ions of tobacco mosaic virus[93] and endospores of *Bacillus subtilis*[94] recollected following ESI and introduction to the vacuum system retain their biological function.

One challenge the gas-phase structural biology community faces is the interpretation of IM-MS data as a function of charge state. For instance, the dependence of Ω on *z* for denatured protein ions lead to the hypothesis that the lowest *z* native-like ions are the 'most' native-like, and thus the Ω of only low *z* native-like ions should be considered in the context of structural biology. Other conclusions considered a Ω averaged over all *z*,[95] while other groups have reported Ω for all charge states individually.[41,64] Other interpretations have called for an extrapolation of the 'zero-charge' state Ω from the experimental data.[96] These ambiguities in how to appropriately handle Ω data as a function of *z* for protein ions from various solutions makes it challenging to use Ω to draw conclusions on how the gas-phase structure of those ions

relate to the solution-phase counterparts, and ultimately their biological function. Thus, there is a great deal of effort to study the effects of charge on the structure of denatured protein ions and native-like protein and protein complex ions to bridge the gap between these two seemingly disparate data sets. One approach to study these phenomena is by modulating the charge state of these ions in the gas-phase via ion/neutral or ion/ion chemistries.

1.6 Gas-Phase Reactions of Protein Ions.

As stated previously, ESI of proteins from denaturing solutions yields ions with higher z, Ω, and a greater dependence of Ω on z than their native-like counterparts. One way to further interrogate their relationship is to develop technologies to manipulate the charge state of ions and measure how those changes effect the Ω of those ions. Several methods currently exist to manipulate the charge state of gas-phase ions, which may be broadly separated into ion/neutral reactions and ion/ion reactions.

1.6.1 *Ion/Neutral reactions.*

Early gas-phase reactions of protein ions involved leaking basic vapors into the vacuum system of the mass spectrometer.[97] These reactions generally proceeded via proton transfer reactions:

$$[M_n + xH]^{x+} + A \rightarrow [M_n + (x-1)H]^{(x-1)+} + AH^+ \qquad \text{Reaction 1}$$

Where $[M_n + xH]^{x+}$ is a multiply protonated protein ion, and A is a neutral gas with a gas-phase basicity higher than that of the cation. This approach has several distinct advantages, such as relatively easy implementation, as well as the ability to perform of kinetic bracketing experiments to measure gas-phase thermodynamic properties.[98,99] However, these reactions are limited by the relative gas-phase basicities of the reactants, and weak interactions at long

distances. Additionally, they have practical limitations with regards to the range of pressures the reactions may occur in, due to generally low volatilities of the base. These low volatities lead to several hours of hysteresis of the base based due to adsorption of the base to the walls of the vacuum system.

Several groups have reported the Ω of protein ions following ion/neutral proton transfer reactions. Reactions between a wide *z* distribution of ESI-generated cytochrome *C* ions from denaturing solutions and vapors of 1,3,4,6,7,8-hexahydro-1-methyl-2*H*-pyrimido[1,2-*a*]pyrimidine (MTBD) revealed that the lowest *z* product ions had smaller Ω than any of the reactant ions.[100] Thus, the ions had isomerized in the gas-phase to more compact conformers. One limitation to this approach is that the entire electrospray plume is simultaneously charge-reduced, therefore it is unclear how individual charge states respond to changes in their charge state. Similar experiments with denatured ubiquitin ions lead the authors to conclude that the rate of the reactions depended on the conformation of the ion, such that more compact conformers with greater coulombic repulsions would react faster than more extended ions of the same charge state.[76]

More recent experiments using various native-like protein ions showed that low-z ions generated via the intersection of an electrospray and a nebulized solution of 1,8-diazabicyclo[5.4.0]undec-7ene (DBU) external to the vacuum system yielded compact ions with compact Ω similar to the reactant ions.[101] Thus, those native-like ions did not compact on themselves as the previous denatured ions had, because they remain folded through the ESI process. In contrast, the addition of DBU directly to the electrospray solution necessitated additional activation to help desolvate the ions, which yielded larger, unfolded Ω. Similar

experiments conducted by adding tri-ethylamine to nESI solutions showed that Ω depended weakly for a large range of native-like ions.[64]

1.6.2 *Ion/Ion Reactions.*

In contrast to ion/neutral reactions, ion/ion reactions offer several advantages to manipulate the charge state of gas-phase ions. For instance, the rates of the reactions under pseudo-first order conditions are related to the product of the charge states of the reaction squared,[102] and the thermodynamics of the reactions benefit from attractive long-distance potentials.[103–105] Although conducted in different time scales, reactions of native-like pyruvate kinase via ion/neutral[101] and ion/ion reactions[106] yielded ions as low as 27+ and 15+ respectively, as an illustrative example. Additionally, the reactions can be easily modulated on and off, and thus avoid the hysteresis challenge imposed by ion/neutral reactions.

Although ion/ion reactions can yield ion adduction products and other less favorable pathways,[104,107] the majority of ion/ion reactions may be divided into two main reaction pathways: proton transfer reactions and electron transfer reactions. A thorough discussion of the partitioning between these two pathways and the dependence on the selection of the anion and Franck-Condon factors has been discussed elsewhere.[105]

The first reports of gas-phase ion/ion reactions analyzed by mass spectrometry occurred external to the vacuum system and involved the intersection of two opposite polarity electrosprays in a "Y"- tube,[108] followed by further studies implementing α emitters[109] and corona discharges.[106,110] Foundational work by McLuckey and coworkers involved sophisticated kinetic measurements[102,103] and thermodynamic considerations[103–105] of ion-ion reactions under pseudo-first order conditions,[111] where the abundance of anions was much greater than that of cations. That early work by McLuckey and co-workers focused primarily on proton transfer

reactions, although later work by Donald Hunt and several co-workers investigated electron transfer reactions,[112] in an attempt to yield peptide fragmentation patterns similar to those generated by other electron-mediated dissociation techniques.[113] The vast majority of ion/ion reactions with multiply protonated protein cations are performed on ion trap mass spectrometers, where the cations are introduced into the ion trap and *m*/*z* isolated. A mixture of molecular anions and fragments, often generated via a separate ESI or a glow discharge, are then injected into the ion trap, and allowed to interact with the stored cations for a set amount of time (typically 10s of milliseconds).

1.6.3 *Electron Transfer Reactions.*

Electron transfer reactions involving multiply protonated ions proceed through the following reaction:

$$[M + zH]^{z+} + A^{\bullet -} \rightarrow [M + zH]^{\bullet (z-1)+} + A \qquad \text{Reaction 2}$$

Note that Reaction 2 results in formation a radical cation that will often undergo the cleavage of a N and Cα peptidic bond to generate *c* and *z* ions[112], which is referred to as electron transfer dissociation (ETD). Additionally, the reactant anion is not necessarily a radical species, although it frequently is. These reactions generally complement other forms of peptide fragmentation, such as collision induced dissociation (CID)[72] or photo-dissociation methods.[114] One advantage of ETD over those methods is that ETD maintains post-translational modifications, and thus the location of post-translational modifications may be determined with residue-level accuracy.[115] However, these covalent cleavages complicate the study of intact biomolecules, as some portion of the signal is partitioned to a fragmentation pathway. Indeed, for large peptides and proteins with extensive hydrogen bonding networks, peptide cleavage may not result in dissociation. Thus, the *m*/*z* channel for the $[M + zH]^{\bullet (z-1)+}$product may be a mixture of intact, odd-electron

species,[20] as well as cleaved but non-covalently bound complexes (ETnoD), and proton transfer reactions products.[116]

1.6.4 *Proton transfer reactions.*

Ion/ion reactions also commonly proceed via proton transfer reactions. In the case involving multiply protonated cations and monoanions, the reaction proceeds via:

$$[M + zH]^{z+} + A^{-} \rightarrow [M + (z-1)H]^{(z-1)+} + AH \qquad \text{Reaction 3}$$

In contrast to electron transfer reactions, all reactants and products are, generally, even-electron species, and the products of proton transfer reactions do not undergo spontaneous peptidic cleavage. Thus, similar to ion/neutral reactions, protein ions may be studied intact following the gas-phase charge reduction reaction, while still benefiting from the favorable kinetics and thermodynamics ion/ion reactions afford.

Ion/ion proton transfer reactions have been previously used to measure the kinetics of ion/ion reactions,[102,103] aid in mass determination[117], and analyze protein mixtures.[118] Recent comparisons of ultraviolet photodissociation (UVPD) to higher energy collisional dissociation (HCD) fragmentation of low *z* proton transfer products showed that UVPD of low *z* ions resulted in better fragmentation efficiency.[28] Similar experiments comparing native-like charge states, and proton transfer product ions of the same charge revealed only subtle differences in fragmentation near the termini, indicating slight isomerization in those areas.[119] Badman and co-worked built and implemented a 3D ion trap-IM-ToF instrument to measure the Ω of several charge states of ubiquitin[120] and cytochrome *C*[121] and their charge-reduced product ions. However, these studies were limited by a narrow selection of precursor charge states.

1.7 Outline of the Present Study

The following dissertation explores the opportunities Cation to Anion Proton Transfer Reactions (CAPTR) affords as an analytical method to assign charge states in native mass spectrometry, separate ions in a mass spectrum, and investigate the relationship between a protein ion's Ω and *z*. Throughout the following experiments, quadrupole selected charge states of nESI-generated protein cations are reacted with the $[M-F]^-$ fragment of perfluoro-1,3-dimethylcyclohexane (PDCH), which is generated via glow discharge.[118] Those reactions proceed predominantly though Reaction 3, and show no propensity for electron transfer.[105,118,122] Ions are then analyzed by a combination of IM and ToF-MS using a Waters Synapt G2 HDMS. This instrument was modified to allow for ion/ion reactions in the 'Trap cell' on the instrument prior to IM-MS.[123] The standard travelling-wave IM cell[49] was physically replaced with a radio-frequency confining drift cell, which has been described elsewhere.[41,46] A diagram of the instrument and relevant pressures is shown in Figure 1.4.

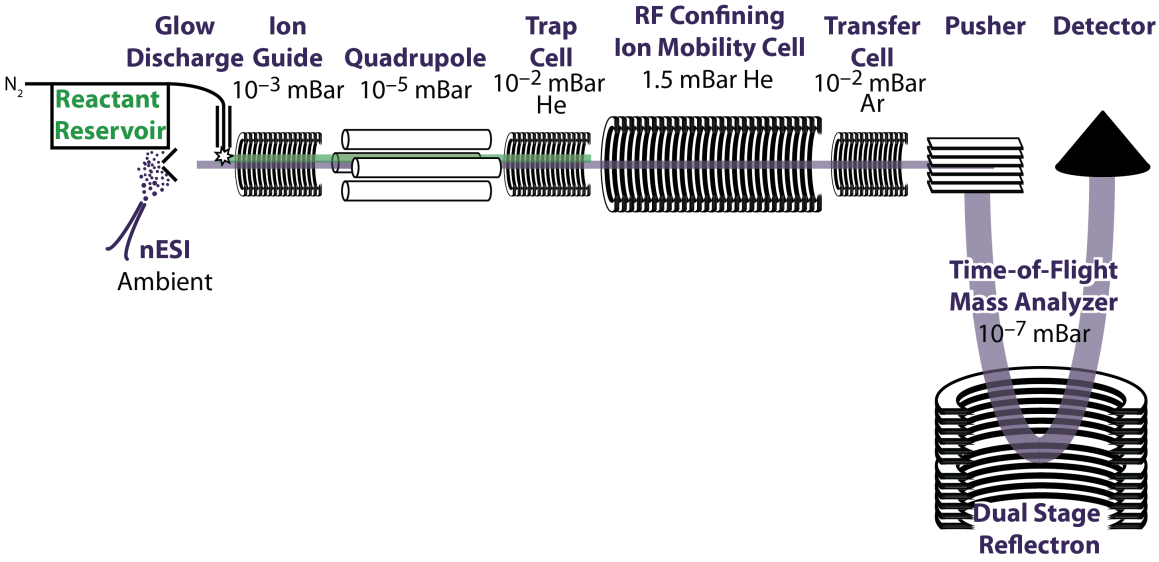

Figure 1.4. Diagram of Waters Synapt G2 used throughout this dissertation. Anions (*green*) are generated via glow discharge, quadrupole selected, and accumulated in the Trap cell. Cations (*purple*) are generated via nESI and may be quadrupole selected prior to transmission through the stored anions to initiate CAPTR. All product ions and unreacted residual precursor ions are injected into the mobility cell for IM analysis prior to ToF-MS.

Chapter 2 introduces the application of this technology to investigate the analytical utility of CAPTR to aid in charge state assignment of native-like protein and protein complex ions.[122] Additionally, proof-of-concept experiments to demonstrate how CAPTR may be used to separate ions in a mass spectrum with unresolved *m*/*z*, yet different *m* and *z*, and a framework to predict those separations in ToF-MS.

Chapter 3 reports the results of experiments in which individual charge states of a small denatured protein ion (ubiquitin, 8.6 kDa) were *m*/*z* selected, reacted via CAPTR, and analyzed

by IM-MS.[124] Those results showed that the Ω for CAPTR products of denatured ubiquitin depended on the charge state of the product ion, and weakly on the charge state of the precursor ion. Energy-dependent collisional activation of those product ions revealed that despite having similar Ω distributions, ions from different precursor charge states had folded to different structural populations. Additional energy-dependent collisional activation of the precursor ions suggested that Ω changes in the product ion may be used to identify resolved structural changes in the precursor ion. In sum, these experiments reveal that protein ions with the same sequence may fold to different structures, similar in size.

Chapter 4 discusses additional IM-MS results of the CAPTR product ions of cytochrome *C* from both native-like and denaturing conditions.[125] This chapter characterizes the design, implementation, and advantages of a temperature-controlled nano-electrospray ionization source. Additionally, a new data analysis tool that describes the width and symmetry of an apparent Ω was designed and implemented to describe the data. Results between the denatured and native-like cytochrome *C* experiments reveal that the ions compact to similar Ω at low charge states.

Chapter 5 further explores the relationship between the apparent Ω distribution of an ion and its *z*, and the effect of tertiary structure on the gas-phase folding of denatured ions.[126] To do so, lysozyme, which is a 14 kDa protein that natively contains 4 disulfide bonds, was generated from denaturing and disulfide reducing conditions, denatured and disulfide intact conditions, and native-like and disulfide intact conditions. Those experiments revealed that ions from all three solutions have similar apparent Ω distributions at low *z*, although they all had very different apparent Ω at high *z*. Additional energy-dependent collisional activation experiments revealed the importance of disulfide bonds in the gas-phase.

Chapter 6 investigates the relationship between *z* and Ω for large native-like protein and protein complex ions.[127] IM of those CAPTR Product ions shows the ions maintain their oligomeric states at low *z*, and Ω weakly depends on *z*. Energy-dependent measurements pre- and post- CAPTR further reveals insights into the stabilities of low *z* ions.

Chapter 7 probes the domain structure of the CAPTR product ions using poly-ubiquitins.[128] C-to-N linked linear ubiquitin chains were generated from native-like and denatured solutions conditions, selected for CAPTR, and those product ions were analyzed by IM-MS. Ω of the native-like ions were used to generate coarse-grained models to estimate the domain structure of low *z* denatured CAPTR products. Further, the relationship between those denatured CAPTR product ions and native-like ions was probed via energy-dependent measurements of the native-like ions.

Chapter 8 uses computational methods to investigate how ion-dipole interactions effect experimental Ω values.[129] Trajectory method calculations (using IMoS v 1.06)[130] was used to calculate the Ω_{TM} of the native, energy-minimized, α-helical, and linear structural models of ubiquitin (1UBQ) and di-ubiquitin (3AXC) and the native and energy-minimized structural models of alcohol dehydrogenase (5ENV).

1.7.1 *Investigation of ETD Mechanisms and Peptide Structure Studies in Collaboration with Prof. Frantisek Tureček.*

Over the course of my graduate work, I was fortunate enough to investigate the mechanism of ETD fragmentation, and factors contributing to peptide ion structure in a collaboration with Professor Frantisek Tureček. Although, that collaboration is not the focus of the present dissertation. Those first experiments were interested in studying properties of leucine residues modified with a photo-active diazirine ring (L*), which absorbs light between 340-360

nm, and had been previously used in protein footprinting experiments.[131–133] Using a combination of a computational conformational search,[134] ETD-MS, and deuterium labelling MS experiments, the mechanism for the loss of hydrazine from the photo-labeled peptide was elucidated.[135] That study was followed by an investigation using the same conformer search, IM-MS, and ETD-MS to reveal electronic state dependent ETD mechanisms of $(GLGGK+2H)^{+\bullet}$.[136] Another study investigated ETD mechanisms to GL*GGK, where the leucine was replaced with the modified photo-active leucine.[137] In particular, that study identified chromophores produced from the ETD products of GL*GGK, which absorbed light in the near UV region, and that N-Cα cleavages occurred from excited electronic states. Later work involving molecular dynamics simulations of AALR revealed that the facile interconversion of two low-energy conformational states, which occurred on the picosecond time scale, had a minor effect on the experimental Ω of the ion.[138] A recent study investigated the effects of peptide charge state and sequence by performing conformational searches and IM-MS experiments on the heptapeptides LKGPADR, LRGPADK, KLGPADR, and RLGPADK.[139] That study revealed the importance of the theoretical model choice in determining peptide structure and the resulting trajectory method calculated Ω in comparison to the experimental Ω.

1.8 References.

(1) Dill, K. A.; MacCallum, J. L. The Protein-Folding Problem, 50 Years On. *Science* **2012**, *338* (6110), 1042–1046.
(2) Gelman, H.; Gruebele, M. Fast Protein Folding Kinetics. *Q. Rev. Biophys.* **2014**, *47* (2), 95–142.
(3) Smyth, M. S.; Martin, J. H. J. X Ray Crystallography. *Mol. Pathol.* **2000**, *53* (1), 8–14.
(4) Shi, Y. A Glimpse of Structural Biology through X-Ray Crystallography. *Cell* **2014**, *159* (5), 995–1014.
(5) Marion, D. An Introduction to Biological NMR Spectroscopy. *Mol. Cell. Proteomics* **2013**, mcp.O113.030239.
(6) Dill, K. A.; Ozkan, S. B.; Shell, M. S.; Weikl, T. R. The Protein Folding Problem. *Annu. Rev. Biophys.* **2008**, *37* (1), 289–316.

(7) Karas, M.; Hillenkamp, F. Laser Desorption Ionization of Proteins with Molecular Masses Exceeding 10,000 Daltons. *Anal. Chem.* **1988**, *60* (20), 2299–2301.
(8) Hillenkamp, F.; Karas, M.; Beavis, R. C.; Chait, B. T. Matrix-Assisted Laser Desorption/Ionization Mass Spectrometry of Biopolymers. *Anal. Chem.* **1991**, *63* (24), 1193A–1203A.
(9) Dole, M.; Mack, L. L.; Hines, R. L.; Mobley, R. C.; Ferguson, L. D.; Alice, M. B. Molecular Beams of Macroions. *J. Chem. Phys.* **1968**, *49* (5), 2240–2249.
(10) Yamashita, M.; Fenn, J. B. Electrospray Ion Source. Another Variation on the Free-Jet Theme. *J. Phys. Chem.* **1984**, *88* (20), 4451–4459.
(11) Fenn, J. B.; Mann, M.; Meng, C. K.; Wong, S. F.; Whitehouse, C. M. Electrospray Ionization for Mass Spectrometry of Large Biomolecules. *Science* **1989**, *246* (4926), 64–71.
(12) Harvey, S. R.; Porrini, M.; Tyler, R. C.; MacPhee, C. E.; Volkman, B. F.; Barran, P. E. Electron Capture Dissociation and Drift Tube Ion Mobility-Mass Spectrometry Coupled with Site Directed Mutations Provide Insights into the Conformational Diversity of a Metamorphic Protein. *Phys. Chem. Chem. Phys.* **2015**, *17* (16), 10538–10550.
(13) Woenckhaus, J.; Mao, Y.; Jarrold, M. F. Hydration of Gas Phase Proteins: Folded +5 and Unfolded +7 Charge States of Cytochrome c. *J. Phys. Chem. B* **1997**, *101* (6), 847–851.
(14) Myung, S.; Badman, E. R.; Lee, Y. J.; Clemmer, D. E. Structural Transitions of Electrosprayed Ubiquitin Ions Stored in an Ion Trap over ~10 Ms to 30 S†. *J. Phys. Chem. A* **2002**, *106* (42), 9976–9982.
(15) Badman, E. R.; Myung, S.; Clemmer, D. E. Evidence for Unfolding and Refolding of Gas-Phase Cytochrome c Ions in a Paul Trap. *J. Am. Soc. Mass Spectrom.* **2005**, *16* (9), 1493–1497.
(16) Bohrer, B. C.; Merenbloom, S. I.; Koeniger, S. L.; Hilderbrand, A. E.; Clemmer, D. E. Biomolecule Analysis by Ion Mobility Spectrometry. *Annu. Rev. Anal. Chem.* **2008**, *1* (1), 293–327.
(17) Morrison, L. J.; Wysocki, V. H. Gas-Phase Helical Peptides Mimic Solution-Phase Behavior. *J. Am. Chem. Soc.* **2014**, *136* (40), 14173–14183.
(18) Chen, S.-H.; Chen, L.; Russell, D. H. Metal-Induced Conformational Changes of Human Metallothionein-2A: A Combined Theoretical and Experimental Study of Metal-Free and Partially Metalated Intermediates. *J. Am. Chem. Soc.* **2014**, *136* (26), 9499–9508.
(19) Breuker, K.; Oh, H.; Horn, D. M.; Cerda, B. A.; McLafferty, F. W. Detailed Unfolding and Folding of Gaseous Ubiquitin Ions Characterized by Electron Capture Dissociation. *J. Am. Chem. Soc.* **2002**, *124* (22), 6407–6420.
(20) Lermyte, F.; Williams, J. P.; Brown, J. M.; Martin, E. M.; Sobott, F. Extensive Charge Reduction and Dissociation of Intact Protein Complexes Following Electron Transfer on a Quadrupole-Ion Mobility-Time-of-Flight MS. *J. Am. Soc. Mass Spectrom.* **2015**, *26* (7), 1068–1076.
(21) Winger, B. E.; Light-Wahl, K. J.; Rockwood, A. L.; Smith, R. D. Probing Qualitative Conformation Differences of Multiply Protonated Gas-Phase Proteins via Hydrogen/Deuterium Isotopic Exchange with Water-d2. *J. Am. Chem. Soc.* **1992**, *114* (14), 5897–5898.
(22) Wood, T. D.; Chorush, R. A.; Wampler, F. M.; Little, D. P.; O'Connor, P. B.; McLafferty, F. W. Gas-Phase Folding and Unfolding of Cytochrome c Cations. *Proc. Natl. Acad. Sci. U. S. A.* **1995**, *92* (7), 2451–2454.

(23) Cassady, C. J.; Carr, S. R. Elucidation of Isomeric Structures for Ubiquitin [M+12H]12+ Ions Produced by Electrospray Ionization Mass Spectrometry. *J. Mass Spectrom.* **1996**, *31* (3), 247–254.
(24) Valentine, S. J.; Clemmer, D. E. H/D Exchange Levels of Shape-Resolved Cytochrome c Conformers in the Gas Phase. *J. Am. Chem. Soc.* **1997**, *119* (15), 3558–3566.
(25) Breuker, K.; McLafferty, F. W. Stepwise Evolution of Protein Native Structure with Electrospray into the Gas Phase, 10- 12 to 102 S. *Proc. Natl. Acad. Sci. U. S. A.* **2008**, *105* (47), 18145.
(26) Bohrer, B. C.; Atlasevich, N.; Clemmer, D. E. Transitions between Elongated Conformations of Ubiquitin [M+11H]11+ Enhance Hydrogen/Deuterium Exchange. *J. Phys. Chem. B* **2011**, *115* (15), 4509–4515.
(27) Polfer, N. C. Infrared Multiple Photon Dissociation Spectroscopy of Trapped Ions. *Chem. Soc. Rev.* **2011**, *40* (5), 2211–2221.
(28) Holden, D. D.; McGee, W. M.; Brodbelt, J. S. Integration of Ultraviolet Photodissociation with Proton Transfer Reactions and Ion Parking for Analysis of Intact Proteins. *Anal. Chem.* **2016**, *88* (1), 1008–1016.
(29) Theisen, A.; Yan, B.; Brown, J. M.; Morris, M.; Bellina, B.; Barran, P. E. Use of Ultraviolet Photodissociation Coupled with Ion Mobility Mass Spectrometry To Determine Structure and Sequence from Drift Time Selected Peptides and Proteins. *Anal. Chem.* **2016**, *88* (20), 9964–9971.
(30) Mikhailov, V. A.; Liko, I.; Mize, T. H.; Bush, M. F.; Benesch, J. L. P.; Robinson, C. V. Infrared Laser Activation of Soluble and Membrane Protein Assemblies in the Gas Phase. *Anal. Chem.* **2016**, *88* (14), 7060–7067.
(31) González Flórez, A. I.; Mucha, E.; Ahn, D.-S.; Gewinner, S.; Schöllkopf, W.; Pagel, K.; von Helden, G. Charge-Induced Unzipping of Isolated Proteins to a Defined Secondary Structure. *Angew. Chem. Int. Ed.* **2016**, *55* (10), 3295–3299.
(32) Seo, J.; Hoffmann, W.; Warnke, S.; Bowers, M. T.; Pagel, K.; von Helden, G. Retention of Native Protein Structures in the Absence of Solvent: A Coupled Ion Mobility and Spectroscopic Study. *Angew. Chem. Int. Ed Engl.* **2016**, *55* (45), 14173–14176.
(33) Mason, E. A.; McDaniel, W. *Transport Properties of Ions in Gases*; Wiley, 1988.
(34) Bernstein, S. L.; Dupuis, N. F.; Lazo, N. D.; Wyttenbach, T.; Condron, M. M.; Bitan, G.; Teplow, D. B.; Shea, J.-E.; Ruotolo, B. T.; Robinson, C. V.; et al. Amyloid-β Protein Oligomerization and the Importance of Tetramers and Dodecamers in the Aetiology of Alzheimer's Disease. *Nat. Chem.* **2009**, *1* (4), 326–331.
(35) Jurneczko, E.; Barran, P. E. How Useful Is Ion Mobility Mass Spectrometry for Structural Biology? The Relationship between Protein Crystal Structures and Their Collision Cross Sections in the Gas Phase. *Analyst* **2011**, *136*, 20–28.
(36) Benesch, J. L.; Ruotolo, B. T. Mass Spectrometry: Come of Age for Structural and Dynamical Biology. *Curr. Opin. Struct. Biol.* **2011**, *21* (5), 641–649.
(37) Wyttenbach, T.; Bleiholder, C.; Bowers, M. T. Factors Contributing to the Collision Cross Section of Polyatomic Ions in the Kilodalton to Gigadalton Range: Application to Ion Mobility Measurements. *Anal. Chem.* **2013**, *85* (4), 2191–2199.
(38) von Helden, G.; Hsu, M. T.; Temper, P. R.; Bowers, M. T. Structures of Carbon Cluster Ions from 3 to 60 Atoms: Linears to Rings to Fullerenes. *J. Chem. Phys.* **1991**, *95* (5), 3835–3837.

(39) Clemmer, D. E.; Hudgins, R. R.; Jarrold, M. F. Naked Protein Conformations: Cytochrome c in the Gas Phase. *J. Am. Chem. Soc.* **1995**, *117* (40), 10141–10142.
(40) Shelimov, K. B.; Jarrold, M. F. Conformations, Unfolding, and Refolding of Apomyoglobin in Vacuum: An Activation Barrier for Gas-Phase Protein Folding. *J. Am. Chem. Soc.* **1997**, *119* (13), 2987–2994.
(41) Bush, M. F.; Hall, Z.; Giles, K.; Hoyes, J.; Robinson, C. V.; Ruotolo, B. T. Collision Cross Sections of Proteins and Their Complexes: A Calibration Framework and Database for Gas-Phase Structural Biology. *Anal. Chem.* **2010**, *82*, 9557–9565.
(42) May, J. C.; McLean, J. A. Ion Mobility-Mass Spectrometry: Time-Dispersive Instrumentation. *Anal. Chem.* **2015**, *87* (3), 1422–1436.
(43) Kemper, P. R.; Dupuis, N. F.; Bowers, M. T. A New, Higher Resolution, Ion Mobility Mass Spectrometer. *Int. J. Mass Spectrom.* **2009**, *287* (1–3), 46–57.
(44) Tang, K.; Shvartsburg, A. A.; Lee, H.-N.; Prior, D. C.; Buschbach, M. A.; Li, F.; Tolmachev, A. V.; Anderson, G. A.; Smith, R. D. High-Sensitivity Ion Mobility Spectrometry/Mass Spectrometry Using Electrodynamic Ion Funnel Interfaces. *Anal. Chem.* **2005**, *77* (10), 3330–3339.
(45) Baker, E. S.; Clowers, B. H.; Li, F.; Tang, K.; Tolmachev, A. V.; Prior, D. C.; Belov, M. E.; Smith, R. D. Ion Mobility Spectrometry—mass Spectrometry Performance Using Electrodynamic Ion Funnels and Elevated Drift Gas Pressures. *J. Am. Soc. Mass Spectrom.* **2007**, *18* (7), 1176–1187.
(46) Allen, S. J.; Giles, K.; Gilbert, T.; Bush, M. F. Ion Mobility Mass Spectrometry of Peptide, Protein, and Protein Complex Ions Using a Radio-Frequency Confining Drift Cell. *Analyst* **2016**, *141* (3), 884–891.
(47) Ruotolo, B. T.; Benesch, J. L.; Sandercock, A. M.; Hyung, S. J.; Robinson, C. V. Ion Mobility-Mass Spectrometry Analysis of Large Protein Complexes. *Nat Protoc* **2008**, *3*, 1139–1152.
(48) Pringle, S. D.; Giles, K.; Wildgoose, J. L.; Williams, J. P.; Slade, S. E.; Thalassinos, K.; Bateman, R. H.; Bowers, M. T.; Scrivens, J. H. An Investigation of the Mobility Separation of Some Peptide and Protein Ions Using a New Hybrid Quadrupole/Travelling Wave IMS/Oa-ToF Instrument. *Int. J. Mass Spectrom.* **2007**, *261*, 1–12.
(49) Giles, K.; Williams, J. P.; Campuzano, I. Enhancements in Travelling Wave Ion Mobility Resolution. *Rapid Commun Mass Spectrom* **2011**, *25*, 1559–1566.
(50) Ibrahim, Y. M.; Prior, D. C.; Baker, E. S.; Smith, R. D.; Belov, M. E. Characterization of an Ion Mobility-Multiplexed Collision Induced Dissociation-Tandem Time-of-Flight Mass Spectrometry Approach. *Int. J. Mass Spectrom.* **2010**, *293* (1–3), 34–44.
(51) Ibrahim, Y. M.; Shvartsburg, A. A.; Smith, R. D.; Belov, M. E. Ultrasensitive Identification of Localization Variants of Modified Peptides Using Ion Mobility Spectrometry. *Anal. Chem.* **2011**, *83* (14), 5617–5623.
(52) von Helden, G.; Hsu, M. T.; Gotts, N.; Bowers, M. T. Carbon Cluster Cations with up to 84 Atoms: Structures, Formation Mechanism, and Reactivity. *J. Phys. Chem.* **1993**, *97* (31), 8182–8192.
(53) Shvartsburg, A. A.; Jarrold, M. F. An Exact Hard-Spheres Scattering Model for the Mobilities of Polyatomic Ions. *Chem. Phys. Lett.* **1996**, *261* (1–2), 86–91.
(54) Shvartsburg, A. A.; Mashkevich, S. V.; Baker, E. S.; Smith, R. D. Optimization of Algorithms for Ion Mobility Calculations. *J. Phys. Chem. A* **2007**, *111* (10), 2002–2010.

(55) Shvartsburg, A. A.; Schatz, G. C.; Jarrold, M. F. Mobilities of Carbon Cluster Ions: Critical Importance of the Molecular Attractive Potential. *J. Chem. Phys.* **1998**, *108* (6), 2416–2423.
(56) Bleiholder, C.; Wyttenbach, T.; Bowers, M. T. A Novel Projection Approximation Algorithm for the Fast and Accurate Computation of Molecular Collision Cross Sections (I). Method. *Int. J. Mass Spectrom.* **2011**, *308* (1), 1–10.
(57) Mesleh, M. F.; Hunter, J. M.; Shvartsburg, A. A.; Schatz, G. C.; Jarrold, M. F. Structural Information from Ion Mobility Measurements: Effects of the Long-Range Potential. *J. Phys. Chem.* **1996**, *100* (40), 16082–16086.
(58) Donor, M. T.; Ewing, S. A.; Zenaidee, M. A.; Donald, W. A.; Prell, J. S. Extended Protein Ions Are Formed by the Chain Ejection Model in Chemical Supercharging Electrospray Ionization. *Anal. Chem.* **2017**.
(59) Taylor, G. Disintegration of Water Drops in an Electric Field. *Proc. R. Soc. Lond. Math. Phys. Eng. Sci.* **1964**, *280* (1382), 383–397.
(60) Gomez, A.; Tang, K. Charge and Fission of Droplets in Electrostatic Sprays. *Phys. Fluids* **1994**, *6* (1), 404–414.
(61) Kebarle, P.; Peschke, M. On the Mechanisms by Which the Charged Droplets Produced by Electrospray Lead to Gas Phase Ions. *Anal. Chim. Acta* **2000**, *406* (1), 11–35.
(62) Hogan, C. J.; Carroll, J. A.; Rohrs, H. W.; Biswas, P.; Gross, M. L. Charge Carrier Field Emission Determines the Number of Charges on Native State Proteins in Electrospray Ionization. *J. Am. Chem. Soc.* **2008**, *130* (22), 6926–6927.
(63) Hogan, C. J.; Carroll, J. A.; Rohrs, H. W.; Biswas, P.; Gross, M. L. Combined Charged Residue-Field Emission Model of Macromolecular Electrospray Ionization. *Anal. Chem.* **2009**, *81* (1), 369–377.
(64) Allen, S. J.; Schwartz, A. M.; Bush, M. F. Effects of Polarity on the Structures and Charge States of Native-Like Proteins and Protein Complexes in the Gas Phase. *Anal. Chem.* **2013**, *85* (24), 12055–12061.
(65) Susa, A. C.; Xia, Z.; Tang, H. Y. H.; Tainer, J. A.; Williams, E. R. Charging of Proteins in Native Mass Spectrometry. *J. Am. Soc. Mass Spectrom.* **2017**, *28* (2), 332–340.
(66) Iribarne, J. V.; Thomson, B. A. On the Evaporation of Small Ions from Charged Droplets. *J. Chem. Phys.* **1976**, *64* (6), 2287–2294.
(67) Thomson, B. A.; Iribarne, J. V. Field Induced Ion Evaporation from Liquid Surfaces at Atmospheric Pressure. *J. Chem. Phys.* **1979**, *71* (11), 4451–4463.
(68) Konermann, L.; Ahadi, E.; Rodriguez, A. D.; Vahidi, S. Unraveling the Mechanism of Electrospray Ionization. *Anal. Chem.* **2013**, *85* (1), 2–9.
(69) Fernandez de la Mora, J. Electrospray Ionization of Large Multiply Charged Species Proceeds via Dole's Charged Residue Mechanism. *Anal. Chim. Acta* **2000**, *406* (1), 93–104.
(70) Davidson, K. L.; Oberreit, D. R.; Hogan Jr., C. J.; Bush, M. F. Nonspecific Aggregation in Native Electrokinetic Nanoelectrospray Ionization. *Submitt. Int. J. Mass Spectrom.* **2016**.
(71) Mann, M.; Meng, C. K.; Fenn, J. B. Interpreting Mass Spectra of Multiply Charged Ions. *Anal. Chem.* **1989**, *61* (15), 1702–1708.
(72) Loo, J. A.; Edmonds, C. G.; Smith, R. D. Primary Sequence Information from Intact Proteins by Electrospray Ionization Tandem Mass Spectrometry. *Science* **1990**, *248* (4952), 201–204.

(73) Van Berkel, G. J.; Glish, G. L.; McLuckey, S. A. Electrospray Ionization Combined with Ion Trap Mass Spectrometry. *Anal. Chem.* **1990**, *62* (13), 1284–1295.
(74) The Nobel Prize in Chemistry 2002 https://www.nobelprize.org/nobel_prizes/chemistry/laureates/2002/ (accessed Apr 4, 2017).
(75) Fenn, J. B. Electrospray Wings for Molecular Elephants (Nobel Lecture). *Angew. Chem. Int. Ed.* **2003**, *42* (33), 3871–3894.
(76) Valentine, S. J.; Counterman, A. E.; Clemmer, D. E. Conformer-Dependent Proton-Transfer Reactions of Ubiquitin Ions. *J. Am. Soc. Mass Spectrom.* **1997**, *8* (9), 954–961.
(77) Shelimov, K. B.; Clemmer, D. E.; Hudgins, R. R.; Jarrold, M. F. Protein Structure in Vacuo: Gas-Phase Conformations of BPTI and Cytochrome c. *J. Am. Chem. Soc.* **1997**, *119* (9), 2240–2248.
(78) Going, C. C.; Williams, E. R. Supercharging with M-Nitrobenzyl Alcohol and Propylene Carbonate: Forming Highly Charged Ions with Extended, Near-Linear Conformations. *Anal. Chem.* **2015**, *87* (7), 3973–3980.
(79) Koeniger, S. L.; Merenbloom, S. I.; Clemmer, D. E. Evidence for Many Resolvable Structures within Conformation Types of Electrosprayed Ubiquitin Ions. *J. Phys. Chem. B* **2006**, *110* (13), 7017–7021.
(80) Freitas, M. A.; Hendrickson, C. L.; Emmett, M. R.; Marshall, A. G. Gas-Phase Bovine Ubiquitin Cation Conformations Resolved by Gas-Phase Hydrogen/Deuterium Exchange Rate and extent1. *Int. J. Mass Spectrom.* **1999**, *185–187*, 565–575.
(81) Tito, M. A.; Tars, K.; Valegard, K.; Hajdu, J.; Robinson, C. V. Electrospray Time-of-Flight Mass Spectrometry of the Intact MS2 Virus Capsid. *J. Am. Chem. Soc.* **2000**, *122* (14), 3550–3551.
(82) Lössl, P.; Snijder, J.; Heck, A. J. R. Boundaries of Mass Resolution in Native Mass Spectrometry. *J. Am. Soc. Mass Spectrom.* **2014**, *25* (6), 906–917.
(83) Hilton, G. R.; Thalassinos, K.; Grabenauer, M.; Sanghera, N.; Slade, S. E.; Wyttenbach, T.; Robinson, P. J.; Pinheiro, T. J. T.; Bowers, M. T.; Scrivens, J. H. Structural Analysis of Prion Proteins by Means of Drift Cell and Traveling Wave Ion Mobility Mass Spectrometry. *J. Am. Soc. Mass Spectrom.* **2010**, *21* (5), 845–854.
(84) Beveridge, R.; Covill, S.; Pacholarz, K. J.; Kalapothakis, J. M. D.; MacPhee, C. E.; Barran, P. E. A Mass-Spectrometry-Based Framework To Define the Extent of Disorder in Proteins. *Anal. Chem.* **2014**, *86* (22), 10979–10991.
(85) Sterling, H. J.; Daly, M. P.; Feld, G. K.; Thoren, K. L.; Kintzer, A. F.; Krantz, B. A.; Williams, E. R. Effects of Supercharging Reagents on Noncovalent Complex Structure in Electrospray Ionization from Aqueous Solutions. *J. Am. Soc. Mass Spectrom.* **2010**, *21* (10), 1762–1774.
(86) Bleiholder, C.; Do, T. D.; Wu, C.; Economou, N. J.; Bernstein, S. S.; Buratto, S. K.; Shea, J.-E.; Bowers, M. T. Ion Mobility Spectrometry Reveals the Mechanism of Amyloid Formation of Aβ(25–35) and Its Modulation by Inhibitors at the Molecular Level: Epigallocatechin Gallate and Scyllo-Inositol. *J. Am. Chem. Soc.* **2013**, *135* (45), 16926–16937.
(87) Young, L. M.; Cao, P.; Raleigh, D. P.; Ashcroft, A. E.; Radford, S. E. Ion Mobility Spectrometry–Mass Spectrometry Defines the Oligomeric Intermediates in Amylin Amyloid Formation and the Mode of Action of Inhibitors. *J. Am. Chem. Soc.* **2014**, *136* (2), 660–670.

(88) Ekeowa, U. I.; Freeke, J.; Miranda, E.; Gooptu, B.; Bush, M. F.; Pérez, J.; Teckman, J.; Robinson, C. V.; Lomas, D. A. Defining the Mechanism of Polymerization in the Serpinopathies. *Proc. Natl. Acad. Sci.* **2010**, *107* (40), 17146–17151.
(89) Shepherd, D. A.; Holmes, K.; Rowlands, D. J.; Stonehouse, N. J.; Ashcroft, A. E. Using Ion Mobility Spectrometry–Mass Spectrometry to Decipher the Conformational and Assembly Characteristics of the Hepatitis B Capsid Protein. *Biophys. J.* **2013**, *105* (5), 1258–1267.
(90) Uetrecht, C.; Barbu, I. M.; Shoemaker, G. K.; van Duijn, E.; Heck, A. J. R. Interrogating Viral Capsid Assembly with Ion Mobility–mass Spectrometry. *Nat. Chem.* **2011**, *3* (2), 126–132.
(91) Baldwin, A. J.; Lioe, H.; Hilton, G. R.; Baker, L. A.; Rubinstein, J. L.; Kay, L. E.; Benesch, J. L. P. The Polydispersity of αB-Crystallin Is Rationalized by an Interconverting Polyhedral Architecture. *Structure* **2011**, *19* (12), 1855–1863.
(92) Zhou, M.; Politis, A.; Davies, R. B.; Liko, I.; Wu, K.-J.; Stewart, A. G.; Stock, D.; Robinson, C. V. Ion Mobility–mass Spectrometry of a Rotary ATPase Reveals ATP-Induced Reduction in Conformational Flexibility. *Nat. Chem.* **2014**, *6* (3), 208–215.
(93) Siuzdak, G.; Bothner, B.; Yeager, M.; Brugidou, C.; Fauquet, C. M.; Hoey, K.; Change, C.-M. Mass Spectrometry and Viral Analysis. *Chem. Biol.* **1996**, *3* (1), 45–48.
(94) Barney, B. L.; Pratt, S. N.; Austin, D. E. Survivability of Bare, Individual Bacillus Subtilis Spores to High-Velocity Surface Impact: Implications for Microbial Transfer through Space. *Planet. Space Sci.* **2016**, *125*, 20–26.
(95) van Duijn, E.; Barendregt, A.; Synowsky, S.; Versluis, C.; Heck, A. J. R. Chaperonin Complexes Monitored by Ion Mobility Mass Spectrometry. *J. Am. Chem. Soc.* **2009**, *131* (4), 1452–1459.
(96) Hogan, C. J.; Ruotolo, B. T.; Robinson, C. V.; Fernandez de la Mora, J. Tandem Differential Mobility Analysis-Mass Spectrometry Reveals Partial Gas-Phase Collapse of the GroEL Complex. *J. Phys. Chem. B* **2011**, *115* (13), 3614–3621.
(97) McLuckey, S. A.; Van Berkel, G. J.; Glish, G. L. Reactions of Dimethylamine with Multiply Charged Ions of Cytochrome c. *J. Am. Chem. Soc.* **1990**, *112* (14), 5668–5670.
(98) Graham Cooks, R.; Patrick, J. S.; Kotiaho, T.; McLuckey, S. A. Thermochemical Determinations by the Kinetic Method. *Mass Spectrom. Rev.* **1994**, *13* (4), 287–339.
(99) Schnier, P. D.; Gross, D. S.; Williams, E. R. Electrostatic Forces and Dielectric Polarizability of Multiply Protonated Gas-Phase Cytochrome c Ions Probed by Ion/Molecule Chemistry. *J. Am. Chem. Soc.* **1995**, *117* (25), 6747–6757.
(100) Shelimov, K. B.; Jarrold, M. F. "Denaturation" and Refolding of Cytochrome c in Vacuo. *J. Am. Chem. Soc.* **1996**, *118* (42), 10313–10314.
(101) Bornschein, R.; Hyung, S.-J.; Ruotolo, B. Ion Mobility-Mass Spectrometry Reveals Conformational Changes in Charge Reduced Multiprotein Complexes. *J. Am. Soc. Mass Spectrom.* **2011**, *22* (10), 1690–1698.
(102) McLuckey, S. A.; Stephenson, J. L.; Asano, K. G. Ion/Ion Proton-Transfer Kinetics: Implications for Analysis of Ions Derived from Electrospray of Protein Mixtures. *Anal. Chem.* **1998**, *70* (6), 1198–1202.
(103) Stephenson, J. L.; McLuckey, S. A. Ion/Ion Reactions in the Gas Phase: Proton Transfer Reactions Involving Multiply-Charged Proteins. *J. Am. Chem. Soc.* **1996**, *118* (31), 7390–7397.

(104) McLuckey, S. A.; Stephenson, J. L. Ion/Ion Chemistry of High-Mass Multiply Charged Ions. *Mass Spectrom. Rev.* **1998**, *17* (6), 369–407.
(105) Gunawardena, H. P.; He, M.; Chrisman, P. A.; Pitteri, S. J.; Hogan, J. M.; Hodges, B. D. M.; McLuckey, S. A. Electron Transfer versus Proton Transfer in Gas-Phase Ion/Ion Reactions of Polyprotonated Peptides. *J Am Chem Soc* **2005**, *127* (36), 12627–12639.
(106) Campuzano, I. G.; Schnier, P. Coupling Electrospray Corona Discharge, Charge Reduction and Ion Mobility Mass Spectrometry: From Peptides to Large Macromolecular Protein Complexes. *Int. J. Ion Mobil. Spectrom.* **2013**, *16* (1), 51–60.
(107) Stephenson, J. L.; McLuckey, S. A. Gaseous Protein Cations Are Amphoteric. *J. Am. Chem. Soc.* **1997**, *119* (7), 1688–1696.
(108) Ogorzalek Loo, R. R.; Udseth, H. R.; Smith, R. D. A New Approach for the Study of Gas-Phase Ion-Ion Reactions Using Electrospray Ionization. *J. Am. Soc. Mass Spectrom.* **1992**, *3* (7), 695–705.
(109) Scalf, M.; Westphall, M. S.; Krause, J.; Kaufman, S. L.; Smith, L. M. Controlling Charge States of Large Ions. *Science* **1999**, *283* (5399), 194–197.
(110) Ebeling, D. D.; Westphall, M. S.; Scalf, M.; Smith, L. M. Corona Discharge in Charge Reduction Electrospray Mass Spectrometry. *Anal. Chem.* **2000**, *72* (21), 5158–5161.
(111) Stephenson Jr, J. L.; Van Berkel, G. J.; McLuckey, S. A. Ion-Ion Proton Transfer Reactions of Bio-Ions Involving Noncovalent Interactions: Holomyoglobin. *J. Am. Soc. Mass Spectrom.* **1997**, *8* (6), 637–644.
(112) Coon, J. J.; Ueberheide, B.; Syka, J. E. P.; Dryhurst, D. D.; Ausio, J.; Shabanowitz, J.; Hunt, D. F. Protein Identification Using Sequential Ion/Ion Reactions and Tandem Mass Spectrometry. *Proc. Natl. Acad. Sci. U. S. A.* **2005**, *102* (27), 9463–9468.
(113) Zhurov, K. O.; Fornelli, L.; Wodrich, M. D.; Laskay, Ü. A.; Tsybin, Y. O. Principles of Electron Capture and Transfer Dissociation Mass Spectrometry Applied to Peptide and Protein Structure Analysis. *Chem. Soc. Rev.* **2013**, *42* (12), 5014–5030.
(114) Eyler, J. R. Infrared Multiple Photon Dissociation Spectroscopy of Ions in Penning Traps. *Mass Spectrom. Rev.* **2009**, *28* (3), 448–467.
(115) Mikesh, L. M.; Ueberheide, B.; Chi, A.; Coon, J. J.; Syka, J. E. P.; Shabanowitz, J.; Hunt, D. F. The Utility of ETD Mass Spectrometry in Proteomic Analysis. *Biochim. Biophys. Acta BBA - Proteins Proteomics* **2006**, *1764* (12), 1811–1822.
(116) Jhingree, J. R.; Beveridge, R.; Dickinson, E. R.; Williams, J. P.; Brown, J. M.; Bellina, B.; Barran, P. E. Electron Transfer with No Dissociation Ion Mobility–mass Spectrometry (ETnoD IM–MS). The Effect of Charge Reduction on Protein Conformation. *Int. J. Mass Spectrom.* **2017**, DOI: 10.1016/j.ijms.2016.08.006.
(117) Stephenson, J. L.; McLuckey, S. A. Charge Manipulation for Improved Mass Determination of High-Mass Species and Mixture Components by Electrospray Mass Spectrometry. *J. Mass Spectrom.* **1998**, *33* (7), 664–672.
(118) Stephenson, J. L.; McLuckey, S. A. Ion/Ion Proton Transfer Reactions for Protein Mixture Analysis. *Anal. Chem.* **1996**, *68* (22), 4026–4032.
(119) Holden, D. D.; Brodbelt, J. S. Ultraviolet Photodissociation of Native Proteins Following Proton Transfer Reactions in the Gas Phase. *Anal. Chem.* **2016**, *88* (24), 12354–12362.
(120) Zhao, Q.; Soyk, M. W.; Schieffer, G. M.; Fuhrer, K.; Gonin, M. M.; Houk, R. S.; Badman, E. R. An Ion Trap-Ion Mobility-Time of Flight Mass Spectrometer with Three Ion Sources for Ion/Ion Reactions. *J. Am. Soc. Mass Spectrom.* **2009**, *20* (8), 1549–1561.

(121) Zhao, Q.; Schieffer, G. M.; Soyk, M. W.; Anderson, T. J.; Houk, R. S.; Badman, E. R. Effects of Ion/Ion Proton Transfer Reactions on Conformation of Gas-Phase Cytochrome c Ions. *J. Am. Soc. Mass Spectrom.* **2010**, *21* (7), 1208–1217.
(122) Laszlo, K. J.; Bush, M. F. Analysis of Native-Like Proteins and Protein Complexes Using Cation to Anion Proton Transfer Reactions (CAPTR). *J. Am. Soc. Mass Spectrom.* **2015**, *26*, 2152–2161.
(123) Williams, J. P.; Brown, J. M.; Campuzano, I.; Sadler, P. J. Identifying Drug Metallation Sites on Peptides Using Electron Transfer Dissociation (ETD), Collision Induced Dissociation (CID) and Ion Mobility-Mass Spectrometry (IM-MS). *Chem. Commun.* **2010**, *46* (30), 5458–5460.
(124) Laszlo, K. J.; Munger, E. B.; Bush, M. F. Folding of Protein Ions in the Gas Phase after Cation-to-Anion Proton-Transfer Reactions. *J. Am. Chem. Soc.* **2016**, *138*, 9581–9588.
(125) Laszlo, K. J.; Buckner, J. H.; Munger, E. B.; Bush, M. F. Native-Like and Denatured Cytochrome c Ions Yield Cation-to-Anion Proton Transfer Reaction Products with Similar Collision Cross-Sections. *J. Am. Soc. Mass Spectrom.* **2017**, 1–10.
(126) Laszlo, K. J.; Munger, E. B.; Bush, M. F. Effects of Solution Structure on the Folding of Lysozyme Ions in the Gas Phase. *J. Phys. Chem. B* **2017**, *121* (13), 2759–2766.
(127) Laszlo, K. J.; Bush, M. F. Effects of Charge State on the Structures of Native-Like Protein Ions: Results From Cation to Anion Proton Transfer Reactions (CAPTR). *Submitt. Anal. Chem.*
(128) Laszlo, K. J.; Gadzuk-Shea, M. M.; Heard, S.; Buckner, J. H.; Bush, M. F. On The Relationship Between Native-like and Gas-Phase-Folded Poly-Ubiquitin Ions. **2017**, In Preparation.
(129) Laszlo, K. J.; Bush, M. F. Effect of Charge State, Partial Charge Distribution, and Structure on Momentum Transfer Collision Cross Sections of Protein Ions. *Prep.*
(130) IMoSPedia | Larriba's Research Lab.
(131) Hashimoto, M.; Hatanaka, Y. Recent Progress in Diazirine-Based Photoaffinity Labeling. *Eur. J. Org. Chem.* **2008**, *2008* (15), 2513–2523.
(132) Das, J. Aliphatic Diazirines as Photoaffinity Probes for Proteins: Recent Developments. *Chem. Rev.* **2011**, *111* (8), 4405–4417.
(133) Dubinsky, L.; Krom, B. P.; Meijler, M. M. Diazirine Based Photoaffinity Labeling. *Bioorg. Med. Chem.* **2012**, *20* (2), 554–570.
(134) Moss, C. L.; Chung, T. W.; Wyer, J. A.; Nielsen, S. B.; Hvelplund, P.; Tureček, F. Dipole-Guided Electron Capture Causes Abnormal Dissociations of Phosphorylated Pentapeptides. *J. Am. Soc. Mass Spectrom.* **2011**, *22* (4), 731–751.
(135) Marek, A.; Pepin, R.; Peng, B.; Laszlo, K. J.; Bush, M. F.; Tureček, F. Electron Transfer Dissociation of Photolabeled Peptides. Backbone Cleavages Compete with Diazirine Ring Rearrangements. *J. Am. Soc. Mass Spectrom.* **2013**, *24* (11), 1641–1653.
(136) Pepin, R.; Laszlo, K. J.; Peng, B.; Marek, A.; Bush, M. F.; Tureček, F. Comprehensive Analysis of Gly-Leu-Gly-Gly-Lys Peptide Dication Structures and Cation-Radical Dissociations Following Electron Transfer: From Electron Attachment to Backbone Cleavage, Ion–Molecule Complexes, and Fragment Separation. *J. Phys. Chem. A* **2014**, *118* (1), 308–324.
(137) Marek, A.; Shaffer, C. J.; Pepin, R.; Slováková, K.; Laszlo, K. J.; Bush, M. F.; Tureček, F. Electron Transfer Reduction of the Diazirine Ring in Gas-Phase Peptide Ions. On the Peculiar Loss of [NH4O] from Photoleucine. *J. Am. Soc. Mass Spectrom.* **2014**, 1–17.

(138) Pepin, R.; Petrone, A.; Laszlo, K. J.; Bush, M. F.; Li, X.; Tureček, F. Does Thermal Breathing Affect Collision Cross Sections of Gas-Phase Peptide Ions? An Ab Initio Molecular Dynamics Study. *J. Phys. Chem. Lett.* **2016**, 2765–2771.
(139) Pepin, R.; Laszlo, K. J.; Marek, A.; Peng, B.; Bush, M. F.; Lavanant, H.; Afonso, C.; Tureček, F. Toward a Rational Design of Highly Folded Peptide Cation Conformations. 3D Gas-Phase Ion Structures and Ion Mobility Characterization. *J. Am. Soc. Mass Spectrom.* **2016**, 1–14.

Chapter 2. Analysis of Native-Like Proteins and Protein Complexes Using Cation to Anion Proton Transfer Reactions (CAPTR)

This chapter is reproduced with permission from Laszlo, K. J.; Bush, M. F. "Analysis of Native-Like Proteins and Protein Complexes Using Cation to Anion Proton Transfer Reactions (CAPTR)" *Journal of The American Society for Mass Spectrometry* **2015**.

2.1 Abstract

Mass spectra of native-like protein complexes often exhibit narrow charge state distributions, broad peaks, and contributions from multiple, coexisting species. These factors can make it challenging to interpret those spectra, particularly for mixtures with significant heterogeneity. Here we demonstrate the use of ion/ion proton transfer reactions to reduce the charge states of *m*/*z*-selected, native-like ions of proteins and protein complexes, a technique that we refer to as Cation to Anion Proton Transfer Reactions (CAPTR). We then demonstrate that CAPTR can increase the accuracy of charge state assignments and the resolution of interfering species in native mass spectrometry. The CAPTR product ion spectra for pyruvate kinase exhibit ~30 peaks and enable unambiguous determination of the charge state of each peak, whereas the corresponding precursor spectra exhibit ~6 peaks and the assigned charge states have an uncertainty of ±3%. 15+ bovine serum albumin and 21+ yeast enolase dimer both appear near *m*/*z* 4450 and are completely unresolved. After a single CAPTR event, the resulting product ions are baseline resolved. The separation of the product ions increases dramatically after each subsequent CAPTR event; 12 events resulted in a 3000-fold improvement in separation relative

to the precursor ions. Finally, we introduce a framework for interpreting and predicting the figures of merit for CAPTR experiments. More generally, these results suggest that CAPTR strongly complements other mass spectrometry tools for analyzing proteins and protein complexes, particularly those in mixtures.

2.2 Introduction

Most electrospray ionization mass spectrometry experiments of proteins use denaturing solutions containing acidified mixtures of aqueous and organic solvents, which disrupt the structures of proteins and yield a wide distribution of highly charged molecular ions. Alternatively, proteins can be electrosprayed from a "native" aqueous solution that contains a volatile electrolyte, *e.g.*, ammonium acetate or ammonium bicarbonate, and has a physiologically relevant pH and ionic strength. The ions formed in such native mass spectrometry experiments have been shown to retain the stoichiometry of proteins, ligands, and metal ions of the corresponding noncovalent complexes in solution,[1–4] and are often referred to as native-like ions. Results from native mass spectrometry experiments are now used in a wide range of structural biology applications, including investigations of the formation of amyloids,[5,6] bacterial secretion,[7,8] protein oligomerization,[9] small heat shock protein structure,[10,11] and viral capsid assembly.[12–14]

Native mass spectra of proteins and protein complexes exhibit relatively narrow charge state distributions that appear at high m/z values compared to those for ions generated from denaturing solutions, which make charge-state assignments more challenging.[12] This is exacerbated for heterogeneous samples, which yield congested mass spectra.[10] Several computational approaches have been implemented to aid in the interpretation of protein mass

spectra,[11,15–20] including methods that use parameterized functions to simulate a spectrum and whose parameters are optimized to minimize the deviation with the experimental spectrum[11,17,19,20] and those that translate the *m*/*z* axis to an *m* axis.[15,16,18] Tandem mass spectrometry is used extensively to elucidate the identities of precursor ions in native mass spectrometry, although the pathways and efficiencies of dissociation can depend strongly on the timescale of energy deposition,[21] charge state,[22] and subtle aspects of the dissociation process.[23] Furthermore, there are numerous examples of noncovalent complexes of proteins that could not be dissociated via subunit loss using collision-induce dissociation.[22,24–26]

Another experimental approach for interpreting electrospray ionization mass spectra is to form additional charge states of the analyte, thus enabling complementary measurements of *m*/*z*. For example, additional charge states can be observed when supercharging or charge-reducing agents are added to electrospray solutions.[27–31] Alternatively, gas-phase proton transfer reactions offer a facile means to modulate the charge states of multiply charged ions. One option is to react a multiply charged precursor cation with a neutral molecule, A, which has a higher gas-phase basicity (ion/neutral proton transfer reactions)[32,33]:

$$[M_n + xH]^{x+} + A \rightarrow [M_n + (x-1)H]^{(x-1)+} + AH^+ \qquad \text{Reaction 1}$$

The rates of these reactions are limited by the weak interaction of the reactants at long distances and the relative basicities of the reactants. Furthermore, molecules that have high gas-phase basicities typically also have low volatilities, which (1) limits the range of pressures that can be used and (2) causes those molecules to persist after experiments due to adsorption on the walls of vacuum systems.

A second option is to react a multiply charged precursor cation with an anion (ion/ion proton transfer reactions) [34–39]:

$$[M_n + xH]^{x+} + A^- \rightarrow [M_n + (x-1)H]^{(x-1)+} + AH \qquad \text{Reaction 2}$$

The rates of these reactions benefit from long-range Coulombic interactions between the reactants and that the reaction remains exothermic even after a series of reactions.[40,41] Positioning an α emitter[37] or a corona discharge[38,39] immediately after the analyte ionization source can enable extensive charge reduction of all analyte ions. Performing ion/ion proton transfer reactions inside mass spectrometers offers additional advantages because ions can be manipulated prior to charge reduction,[42] *e.g.*, ion activation, chemistry, or *m*/*z* selection. In the context of native mass spectrometry, performing ion/ion proton transfer reactions in vacuum decouples the ionization and charge manipulation processes so as to not compromise solution chemistry, noncovalent interactions, or the ionization process. Pathways other than proton transfer may also be accessible in ion/ion reactions,[36,43] *e.g.*, electron transfer and anion adduction.

Here, we demonstrate the use of ion/ion proton transfer reactions of quadrupole selected, native-like ions, which we refer to as Cation to Anion Proton Transfer Reactions (CAPTR). We then use CAPTR to (1) assign accurately the charge states of native-like precursor ions and (2) separate two native-like precursor ions that are not initially resolved in *m*/*z*. These results indicate that CAPTR will increase the accuracy of a broad range of native mass spectrometry experiments.

2.3 Methods

Experiments were performed using a Waters Synapt G2 HDMS mass spectrometer modified with a glow-discharge ionization (GDI) source[44] (Figure 2.1A). Native-like cations were generated using nanoelectrospray ionization from borosilicate capillaries with inner diameters of 0.78 mm that were pulled to ~1–3 μm on one end using a Sutter Instruments Model

P-97 micropipette puller (Novato, CA). Electrical contact with the solution was achieved by inserting a platinum wire into the wide end of the capillary. Electrospray solutions contained ~10 μM protein or protein complex in 200 mM aqueous ammonium acetate pH = 7. Yeast enolase, alcohol dehydrogenase, and pyruvate kinase were also buffer exchanged into the same buffer using Micro Bio-Spin 6 columns (Bio-Rad, Hercules, CA). Insulin was electrosprayed from 49.5/49.5/1 methanol/water/acetic acid. The atmospheric pressure interface was held at 120 °C.

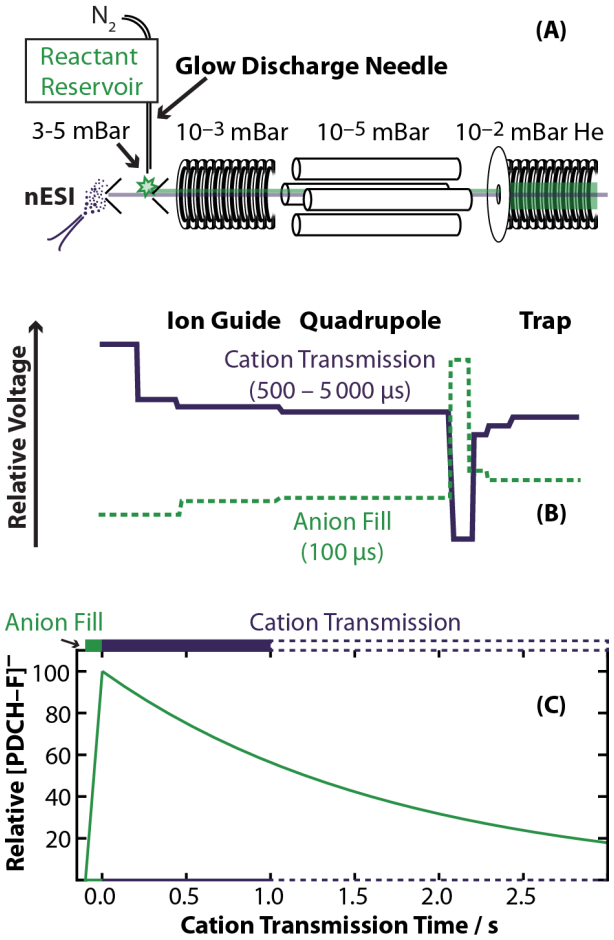

Figure 2.1. (A) Waters Synapt G2 HDMS modified with glow discharge ionization. (B) Relative potentials applied to selected ion optics during cation transmission (solid purple line) and anion fill (dashed green line). (C)

Hypothetical abundance of $[PDCH–F]^-$ in the trap cell over the course of a single experimental cycle.

For CAPTR experiments, nitrogen gas seeded with perfluoro-1,3-dimethylcyclohexane (PDCH) vapor was passed through a sharpened stainless steel discharge needle that is positioned after the atmospheric pressure sampling cone (pressure ~4 mbar). Anions were generated for 100 ms, which will be referred to as the anion fill time, by applying a 0.2–1.3 kV potential to the discharge needle that induces a discharge current of 10–100 μA. $[PDCH–F]^-$ was selected using a quadrupole mass filter and accumulated in a stacked ring ion trap cell, which contained ~0.01 mbar of He gas. Cations were then transmitted for ~2000 ms, which will be referred to as the cation transmission time, through the trap cell containing the accumulated anions. The charge-reduced products and any residual precursor cations continue through the trap cell, radio-frequency confining drift cell,[31] stacked ring transfer cell, and time-of-flight mass analyzer. To increase the detection efficiency of high *m*/*z* ions, the magnitude of the detector voltage was increased 300–475 V above that used for peptide analysis. The relative potentials of the ion optics that are modulated between the anion fill and cation transmission times are shown in Figure 2.1B. During the cation transmission time, the amplitude of the traveling waves in the trap cell was held at 0 V to maximize cation and anion spatial overlap. Representative time scales and hypothetical relative abundance of $[PDCH–F]^-$ over the course of the experiment are shown in Figure 2.1C.

2.4 Results and Discussion

2.4.1 *Cation to Anion Proton Transfer Reactions (CAPTR).*

CAPTR experiments were implemented using a dual polarity electrospray/glow-discharge ionization source that was positioned prior to a quadrupole mass filter, stacked-ring ion trap, ion mobility cell, stacked-ring collision cell, and time-of-flight mass analyzer (Waters Synapt G2 HDMS). Compared to previous instruments that have been used for ion/ion proton transfer reactions, this geometry is most similar to that reported by Badman and coworkers who used multiple independent ion sources positioned prior to a 3D ion trap, ion mobility drift tube, quadrupole collision cell, and time-of-flight mass analyzer.[45] The experimental scheme for CAPTR experiments, including the instrument, the relative potentials of selected ion optics, and the sequence are shown in Figure 2.1.

Figure 2.2A shows a typical native mass spectrum of avidin, a 64 kDa homotetramer, which exhibits peaks for the 15+ to 18+ charge states. CAPTR experiments were performed on the quadrupole selected 17+ charge state of avidin with an anion fill time of 100 ms and a cation transmission time of 500 ms. Note that the cation transmission time of 500 ms is the time that the cation beam is transmitted through the trap cell containing the anion; the interaction time between the cations and anions in these experiments is shorter and has not yet been characterized. The resulting CAPTR spectrum is shown in Figure 2.2B and exhibits peaks for 2+ through 7+ CAPTR product ions, which are the result of a series of consecutive proton transfer reactions (Reaction 2) from the multiply charged protein cation to $[PDCH–F]^{-}$. The relative intensities based on ion counting are shown in Electronic Supplementary Information Figure S1F; almost 50% of the CAPTR products observed were for the 4+ product ion.

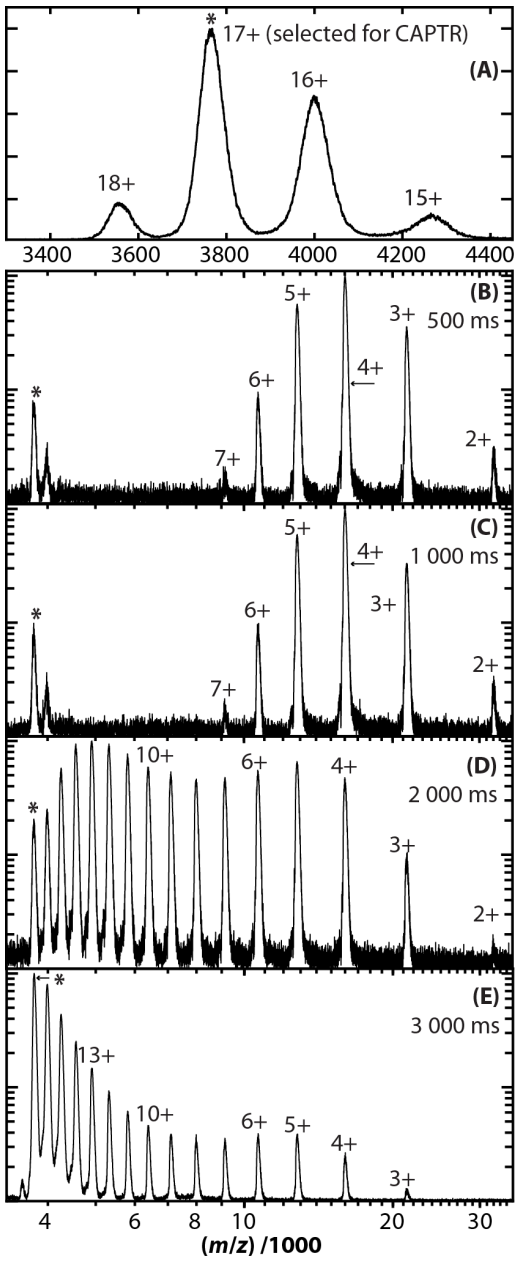

Figure 2.2. (A) Native mass spectrum of the avidin tetramer (64 kDa) plotted using linear axes. CAPTR spectra of 17+ avidin measured using an anion fill time of 100 ms and cation fill times of (B) 500, (C) 1000, (D) 2000, and (E) 3000 ms. Spectra B–E are plotted using logarithmic axes to aid in visualization. The 17+ precursor ion is labeled with an "*". Average *z* for panels A–E are 16.3, 4.4, 4.5,

9.6, and 14.7 respectively. The relative intensities based on ion counting are shown in Figure S1.

Interestingly, the intensity of the peak for the unreacted 17+ precursor ion (1.7% of total ion counts, Figure S1F) is significantly greater than that for the 16+ charge state (0.5% of total ions counts). The relative intensity of these two peaks is comparable to that observed after isolation in some native mass spectrometry experiments without CAPTR, an effect that has been attributed to other, comparatively minor charge loss mechanisms.[46] Furthermore, the intensities for any 8+ through 15+ charge state product ions are exceedingly weak. These results suggest that a small fraction (~2%) of the precursor ions do not fully interact with the trapped anions. The origin of this effect is under investigation.

2.4.2 *Kinetics and Pathways of CAPTR.*

To investigate how the experimental sequence affects CAPTR, the cation transmission time was modulated from 500–3000 ms (Figure 2.2B–E, relative intensities are plotted in Figure S1F–I). Note that although the cation transmission time is modulated, the residence time (and thus the reaction time) of a single ion in the trap cell is expected to be constant. The spectra recorded for CAPTR of 17+ avidin with cation transmission times of 500–1000 ms (Figure 2.2B–C) are indistinguishable. In contrast, the spectrum recorded with a cation transmission time of 2000 ms (Figure 2.2D) is significantly different and exhibits peaks for the 2+ through 16+ CAPTR products. This trend continues when the cation transmission time is further increased to 3000 ms (Figure 2.2E); the products observed under those conditions, on average, are the result of even fewer CAPTR events.

The similarity between the spectra measured using shorter (≤1000 ms) cation transmission times suggests that there is a large excess of anions and the abundance of anions in the trap cell does not change significantly during the first second of cation transmission, *i.e.*, the reactions occur with pseudo-first-order kinetics. Pseudo-first-order kinetics have been reported for many ion/ion chemistry reactions performed in quadrupolar ion traps[47] and transmission mode experiments performed using a modified triple quadrupole[48] during the analysis of comparatively small biomolecules. Under pseudo-first-order kinetics, rates for these reactions have been shown to increase with the square of the charge state (z^2).[47]

The appearance of additional product ions that have undergone fewer CAPTR events with longer cation transmission times suggests that the abundance of $[PDCH–F]^-$ in the trap cell decreases over the course of the longer experimental cycles (Figure 2.1C and D). Anions are refilled more frequently in most ion trap experiments in order to maintain pseudo-first-order reaction conditions,[36] although subtle deviations from the pseudo-first-order kinetic model have been attributed to the depletion of anions in some cases.[49]. The range of kinetic rates in these CAPTR experiments therefore enable the formation of an extremely broad range of charge-reduced product ions in a single experiment.

To evaluate whether the number of CAPTR events may be limited by the thermodynamics of Reaction 2, the gas-phase basicities of $[PDCH–F]^-$ were calculated at the B3LYP/6-31++G(d,p) level of theory. Detailed methods and results for these calculations are included in the Electronic Supplementary Material. The smallest gas-phase basicity calculated using this approach was 1310 kJ/mol. By comparison, the gas-phase basicity of a lysine residue in a neutral peptide is far lower (1008–1018 kJ/mol) and will decrease with increasing charge state [33,50]. The gas-phase basicity of isolated arginine is ~60 kJ/mol greater than that of isolated

lysine [51], therefore 1080 kJ/mol should represent a reasonable upper limit to the gas-phase basicity of arginine in a peptide or protein. Thus, the transfer of a proton from the reactant protein cation to $[PDCH–F]^-$ should be >200 kJ/mol exothermic for each CAPTR event. The rates of these reactions are therefore limited by the cross section for the formation of a long-range interaction complex between the reactants[36,43,52] and the density of the anions, rather than their thermodynamics.

Despite the high exothermicity of these reactions, no significant fragmentation was observed from CAPTR, consistent with results for smaller analytes.[49] These results suggest that the energy released during each CAPTR event is dissipated through other pathways and/or the energy may not partition statistically into both products. Furthermore, it is clear that protein complexes maintain native-like oligomeric stoichiometries. Preliminary ion mobility results suggest that the collision cross sections of CAPTR product ions are generally similar to those of the native-like precursor ions. More detailed studies of the effects of CAPTR on protein ion structure are underway.

It is possible that reaction pathways other than proton transfer may be accessed in ion/ion reactions,[36,43] including electron transfer and anion adduction. Electron transfer dissociation (ETD) typically results in fragmentation along the peptide backbone between the nitrogen and α-carbon generating c^+ and $z^{+\bullet}$ ions, although cleavage of disulfide bonds has also been reported.[53] In some cases dissociation may not follow bond cleavage due to noncovalent interactions tethering the fragment to the remainder of the ion (ETnoD). Following electron transfer to native-like protein complex cations in previous studies, additional activation has been shown to release noncovalently bound c^+ and $z^{+\bullet}$ fragments.[54–56] The possible contributions from each of these pathways are assessed below.

To demonstrate that protein complex cations react with $[PDCH–F]^-$ via proton transfer rather than electron transfer, denatured insulin and native-like alcohol dehydrogenase ions were activated in the collision cell on the instrument following CAPTR (Figures S2 and S3 respectively). Discussions of these results may be found in the Electronic Supplementary Material. Briefly, collision induced dissociation (CID) of the CAPTR products of insulin yielded the same product ions as CID of the precursor ions. No fragments in either experiment could be attributed to cleavage of a disulfide bond (Figure S2). CID using up to a 150 V injection voltage of the precursor (Figure S3D) and CAPTR products (Figure S3E) of tetramers of alcohol dehydrogenase resulted in the ejection of a highly charged monomer. No evidence for the loss of peptide fragments from the tetramer was observed. In contrast, CID using a 15 V injection voltage of the ETnoD products of tetramers of alcohol dehydrogenase has been reported previously to result in the appearance of c^+ and $z^{+\bullet}$ fragments.[56] These results all indicate that reacting protein ions with $[PDCH–F]^-$ results in proton transfer, rather than electron transfer, consistent with previous results for smaller biomolecular ions.[52]

Anion adduction was monitored through the mass distribution of the CAPTR products of avidin (Figure S4). The weighted average mass of the CAPTR products of avidin increase slightly with decreasing charge. For example, the weighted average mass of 3+ avidin is 199 Da greater than that for the 17+ precursor ion, which is less than the mass of $[PDCH–F]^-$ (381 Da). This shift is significantly larger than the errors expected for calibration. These spectra were externally calibrated using $Cs(CsI)_n^+$ clusters that appeared from 3,000–19,000 m/z, which resulted in residual errors spanning ±7 ppm. Although 3+ avidin (21,500 m/z) appears slightly above this range, this analysis suggests that the calibration error would be on the order of 0.5 Da. Therefore, the observed increase in average mass suggests that the 3+ product ions include

unresolved populations that have adducted zero, one, or possibly two anions. Therefore, CAPTR is a much more dominate channel than anion adduction.

2.4.3 *Assigning Charge States in Native Mass Spectrometry*

Native mass spectrometry inherently involves high mass, multiply charged ions that have high *m*/*z* values. In native mass spectrometry, charge states are often assigned by analyzing the spacing between adjacent peaks that have different charge states. However, as charge increases, the *m*/*z* difference between charge states decreases, which makes charge-state assignments ambiguous [12]. This problem is exacerbated by wide peaks and narrow charge-state distributions, which are common to native mass spectrometry experiments. For example, Figures 2.3A–C show a native mass spectrum of the homotetramer pyruvate kinase (black trace) that is assigned using spectra simulated for three models. Spectra that were simulated assuming that the charge state of the base peak is 31+, 32+, or 33+ (A, B, and C, respectively) all agree reasonably well with the experimental spectrum. A description of these simulations is included with the ESM. Visually, the simulated spectrum for which the base peak was assigned as 31+ agrees best with the experimental spectrum. Note that uncertainty in the assignments of charge states corresponds to ambiguity in the mass of the protein complex, *e.g.* assigning the base peak 31+ results in a mass of 223.1 kDa, whereas assigning the base peak 32+ results in a mass of 230.1 kDa (Δm = 30,000 ppm or 3%).

To mitigate this limitation in native mass spectrometry, the additional peaks generated by CAPTR were used to aid in the assignment of the base peak in the original native mass spectrum of pyruvate kinase. The CAPTR spectrum exhibits peaks for both the precursor ion and a long distribution of charge-reduced product ions. Using the masses determined from the charge state assignments in Figures 2.3A–C, CAPTR spectra were simulated and plotted with the

experimental CAPTR spectrum (Figures 2.3D–F). When the charge state of the precursor ion is assigned as the 31+ or 33+, the simulated CAPTR spectra disagree with the experimental CAPTR spectrum, even though spectra simulated using those assignments for the original native mass spectrum agree reasonably well. When the charge state of the precursor ion is assigned as 32+, the simulated CAPTR spectrum agrees well with the experimental CAPTR spectrum (Figure 2.3E). The additional charge states generated by CAPTR radically reduce the ambiguity of charge-state assignments. This reduces the uncertainty in the mass determination to the accuracy of the mass analyzer (better than 10 ppm with appropriate calibration) and the underlying heterogeneity in the mass of the protein ion, *e.g.*, covalent modification of the proteins as well as nonspecific adduction of molecules and ions.

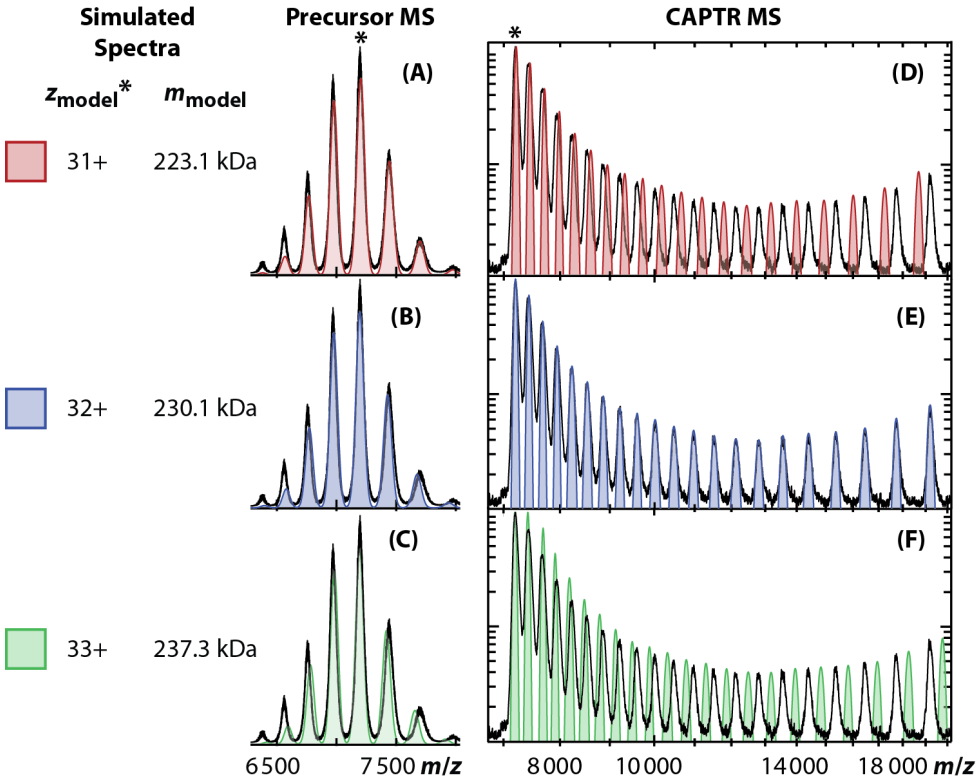

Figure 2.3. A–C each show a simulated spectrum that was used to model the experimental native mass spectrum of pyruvate kinase (black). Assigning the base peak at *m*/*z* 7200 a charge of 31+ (A, red), 32+ (B, blue), or 33+ (C, green) results in optimized masses of 223.1, 230.3, and 237.3 kDa, respectively. D–F each show a simulated spectrum that was used to model the experimental CAPTR spectrum for the *m*/*z* 7200 peak of pyruvate kinase. These spectra were simulated using the *m* determined for the corresponding model of the native mass spectrum. Intensities were set manually to resemble the intensities in the experimental spectrum.

2.4.4 *Resolution of Components in Congested Mass Spectra.*

In native mass spectrometry, it is common to observe the presence of multiple coexisting protein complexes that have different stoichiometries and masses. This causes spectral congestion, which makes it challenging to interpret the spectra, particularly for polydisperse species that adopt many coexisting stoichiometries.[10] Although experimental methods using collision-induced dissociation have been developed to deconvolute these congested spectra,[10] this approach implicitly assumes that the product ion distributions have complete fidelity with the original distributions in solution. However, the efficiency of the low-energy thermal dissociation of protein complexes has been shown to depend on the analyte, often in ways that cannot be predicted *a priori.*[22,23] In contrast, CAPTR reaction rates depend primarily on the charge state of the analyte. This strategy is analogous to charge manipulation approaches pioneered by McLuckey and coworkers to analyze mixtures of comparatively small biomolecular ions in ion traps.[32,35,47,57]

To demonstrate the utility of CAPTR for separating interfering components in a mixture, bovine serum albumin (67 kDa monomer) and yeast enolase dimer (93 kDa) were analyzed. The resolution (R) between two peaks in a mass spectrum can be defined as:

$$Resolution = R = \frac{\frac{m_x}{z_x} - \frac{m_y}{z_y}}{2(\sigma_x + \sigma_y)} \qquad \text{Equation 2.1}$$

where m, z, and σ are the mass, charge, and standard deviation for components x and y of the mixture. This definition of resolution is commonly used in chromatography to quantify the separation of two peaks in a chromatogram. Figure 2.4A shows overlaid native mass spectra of serum albumin (blue) and enolase dimer (green). The peaks for 15+ serum albumin and 21+

enolase dimer both appear near m/z 4450, and are completely unresolved ($R = 0.016 << 1$) in a mixture of serum albumin and enolase dimer. However, when the precursor ions near m/z 4450 are each isolated and subjected to CAPTR, the majority of the resulting product ions appear at unique m/z values (Figures 2.4B and 2.4C, respectively). These findings were then validated by performing CAPTR on the precursor ions near m/z 4450 that were isolated from a mixture of serum albumin and enolase (Figure 2.4D). Furthermore, these components are baseline resolved ($R = 2.06$) following a single CAPTR event (Figure 2.4E).

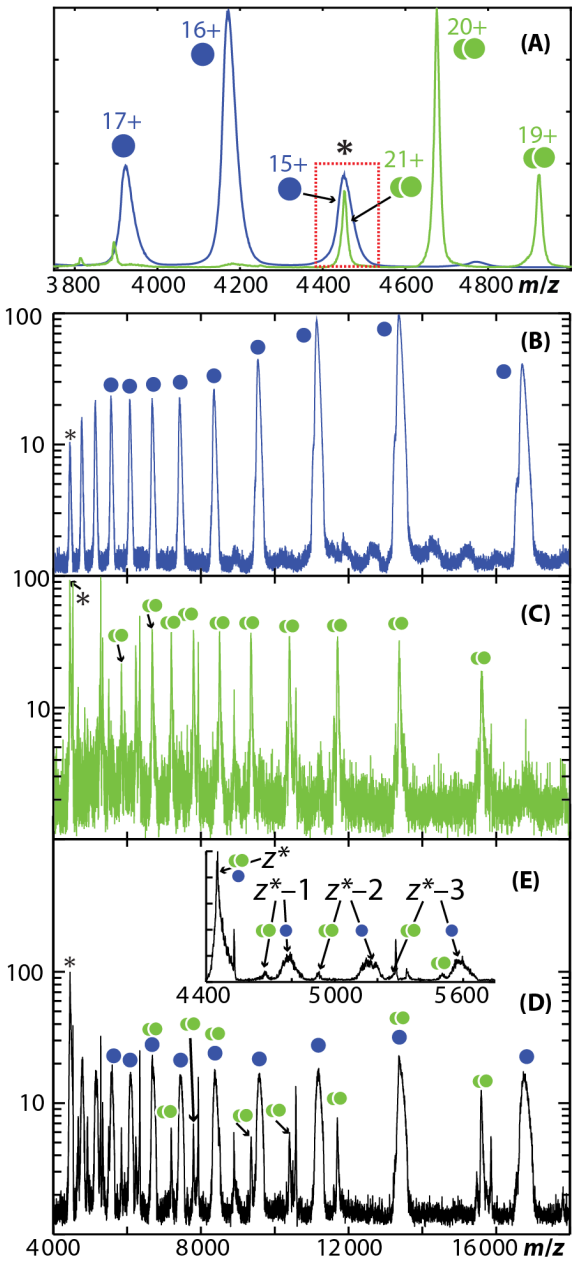

Figure 2.4. (A) Native mass spectra of bovine serum albumin (blue) and yeast enolase (green). (B) CAPTR of 15+ serum albumin. (C) CAPTR of 21+ enolase dimer. (D) CAPTR of 15+ serum albumin and 21+ enolase dimer that were quadrupole selected from a mixture of those two proteins. (E) Zoom in of D that shows the precursors and products from the first three CAPTR events. Note that

there is a contaminate originating from the enolase sample (sharp peaks, not labeled).

The resolution of CAPTR product ions were determined as a function of the number of CAPTR events from the results in Figures 2.4B and 2.4C. Briefly, the peaks in Figures 2.4B and 2.4C were each fit using a Gaussian distribution to determine the centroid and σ of each peak. These results show that the resolution increases dramatically with each subsequent CAPTR event (Figure 2.5A). After 12 CAPTR events, 3+ serum albumin and 9+ enolase dimer exhibit a resolution of 54, which is more than 3000 fold greater than that for the 15+ serum albumin and 21+ enolase dimer precursor ions. This analysis was also performed for the spectrum in Figure 2.4D. The resolution values determined in that analysis are similar to, but systematically smaller than, those determined in the previous analysis. This is attributed to the peaks in the spectrum obtained for the mixture having slightly greater widths than those measured in the spectra of the individual components, which suggests poorer ion desolvation for the former experiments. Note that values for the mixture were only determined when the centroids and widths could be determined unambiguously, *i.e.*, there were not any interferences from other CAPTR products.

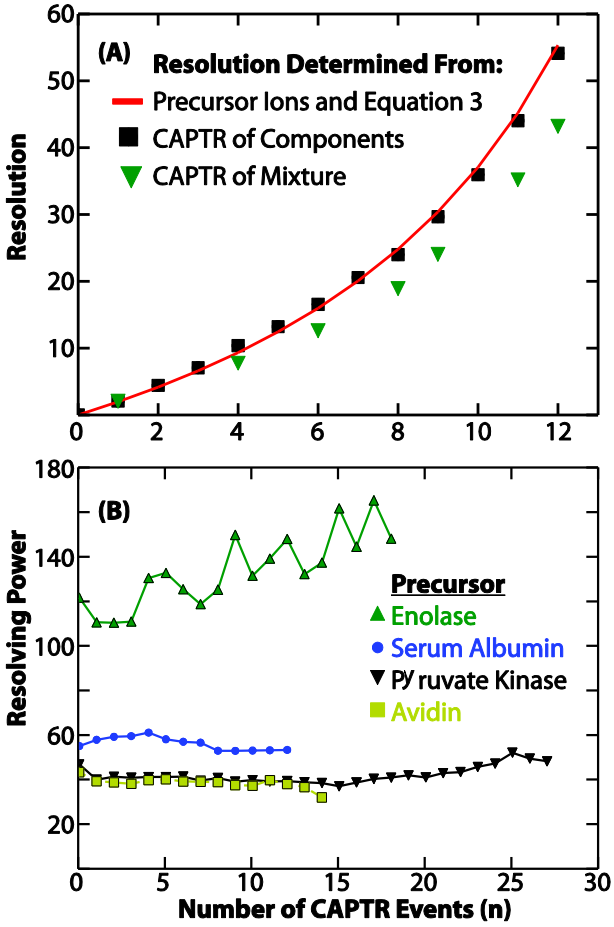

Figure 2.5. (A) Resolution of (serum albumin + (15–n)H)$^{(15-n)+}$ and (enolase dimer + (21–n)H)$^{(21-n)+}$ as a function of the number of CAPTR events determined from the individual components (from Figures 2.4B–C, black squares), from the components in a mixture (from Figure 2.4D, green triangles), and from Equation 2.3 using parameters for the individual precursor ions (from Figure 2.4A, red line). Note that values for resolution of the components in a mixture were only determined for peaks with no interferences. (B) Resolving powers of enolase (results from Figure 2.4C), serum albumin (Figure 2.4B), pyruvate kinase (Figure 2.3), and avidin (Figure 2.1E).

2.4.5 *Origin of Increasing Resolution with Each Consecutive CAPTR Event.*

The resolution of two peaks depends on the widths and centroids of their respective *m*/*z* distributions (Equation 2.1), and therefore the relationship between resolution and the number of CAPTR events can be determined from the effect that each CAPTR event has on the width and centroid of the resulting product *m*/*z* distributions. The relative increase in peak width between two different charge states may be described as a ratio,

$$\frac{\sigma_{z^*-n}}{\sigma_{z^*}} = \frac{z^*}{z^*-n} \qquad \text{Equation 2.2}$$

where n is the number of CAPTR events and z^* is the charge state of the initial precursor ion. This relationship is based on time-of-flight fundamentals[58] and is established in greater detail in the Electronic Supplementary Material. Inserting Equation 2 into Equation 1 and assuming the centroids of the peaks shift solely due to the change in charge state yields resolution as a function of the number of CAPTR events:

$$R_{CAPTR}(n) = \frac{\frac{m_x}{(z_x^*-n)} - \frac{m_y}{(z_y^*-n)}}{2\left[\sigma_x^*\left(\frac{z_x^*}{z_x^*-n}\right)+\sigma_y^*\left(\frac{z_y^*}{z_y^*-n}\right)\right]} \qquad \text{Equation 2.3}$$

Using values of σ_x and σ_y determined from the individual precursor spectra (Figure 2.4A), Equation 2.3 was plotted in Figure 2.5A. This function yields values that are very similar to those determined from the individual CAPTR spectra (Figures 2.4B and 2.4C), indicating that this function can be used to accurately predict the performance of CAPTR-based separations. Furthermore, this agreement suggests that the changes in peak widths are primarily attributable to time-of-flight effects, *i.e.*, contributions from anion adduction or desolvation are not significant.

One consequence of Equation 3 is that for precursor ions that have identical charge states, *i.e.*, $z_x^* = z_y^*$, the resolution of the CAPTR products will not depend on the number of CAPTR events. Figure S5 shows that all the CAPTR products from serum albumin and enolase dimer that have identical charge states have a resolution of ~30. In this case, resolution remains constant because the widths of the peaks change in unison with the *m*/*z* values, as predicted by Equation 2. Figure 2.5B shows the resolving power of enolase dimer (determined from the results shown in Figure 2.4B), serum albumin (Figure 2.4C), avidin (Figure 2.1E), and pyruvate kinase (Figure 2.3) as a function of the number of CAPTR events (*n*), where resolving power (R_p) is defined as:

$$Resolving\ Power = R_p = \frac{m/z}{4\sigma} \qquad \text{Equation 4}$$

Note that R_p is expressed in terms of the width at the base of the peak (4σ), rather than the full width of the peak at half of its maximum height (2.355σ), to enable facile comparison with the values determined using Equations 1 and 3. The resolving powers measured for avidin (~40), pyruvate kinase (~40), and serum albumin (~55) do not depend strongly on the number of CAPTR events, whereas the values measured for enolase dimer increase from ~120 to ~150 with increasing numbers of CAPTR events.

These results show that after each CAPTR event, the relative increase in *m*/*z* is similar to the relative increase in the width of the peak. In contrast, in most reflectron time-of-flight mass spectrometry experiments, the resolving power of ions increase with increasing charge state, which is attributed to their increased kinetic energy and reflectron penetration [59]. One explanation is that the resolving powers for CAPTR products are limited by similar initial distributions of kinetic energy [58], *e.g.*, all CAPTR product ions experience similar aerodynamic acceleration during their introduction into the time-of-flight mass analyzer. Another explanation

for these results is that the experimental distribution of *m*/*z* may be limited by the true distribution of *m*, which is consistent with incomplete desolvation during ionization and/or the adduction of molecules and ions from solution.[60]

2.5 Conclusions

These results demonstrate that CAPTR is an extremely powerful complement to the mass spectrometry toolbox for analyzing proteins and protein complexes, particularly those in mixtures. This work benefits greatly from the pioneering efforts of McLuckey and coworkers in elucidating many aspects of the thermodynamics, kinetics, and analytical utility of proton transfer reactions for smaller analytes using ion traps.[36,43] In this study, we demonstrated that the controlled charge reduction of *m*/*z*-selected native-like ions by CAPTR can increase the accuracy of charge state assignments and the resolution of interfering species in native mass spectrometry. The CAPTR product ion spectra for pyruvate kinase exhibit ~30 peaks and enable unambiguous determination of the charge state of each peak, whereas the corresponding precursor spectra exhibit ~6 peaks and the assigned charge states have an uncertainty of ±3%. 15+ serum albumin and 21+ enolase dimer both appear near *m*/*z* 4450 and have a resolution of 0.016. After isolation, each consecutive CAPTR event results in product ions whose resolution increases monotonically. After 12 CAPTR events, 3+ serum albumin and 9+ yeast enolase dimer have a resolution of 54, which is 3000 fold greater than that for the precursors.

CAPTR offers many benefits for reducing the charge states of native-like ions of proteins and protein complexes. First, the reactions are performed inside the mass spectrometer, which decouples the charge reduction and ionization processes and enables additional gas-phase manipulations, *e.g.*, *m*/*z* selection of the cation and anion reactants, ion activation, and ion chemistry, prior to charge reduction. In contrast, performing charge reduction at atmospheric

pressure results in the charge reduction of all components of the sample (potentially creating new interferences) and the increased formation of nonspecific aggregation due to a smaller fraction of droplets reaching the Rayleigh limit.[61] Second, the abundance of the $[PDCH–F]^-$ anions can be rapidly modulated or even completely cleared in seconds. These factors are very different than those for ion/neutral reactions, which typically exhibit substantial hysteresis when the pressure or identity of the neutral is varied. Third, $[PDCH–F]^-$ anions strongly favor proton transfer over electron transfer. Electron capture[54,55,62] by or electron transfer[56] to the analyte can also yield product ions with lower charge states, but can also result in the cleavage of covalent bonds. The latter can provide additional molecular insights,[54–56] but at the expense of increasing the complexity of the product ion spectra in ways that make it more challenging to assign charge states and probe the composition of mixtures. The combined attributes of CAPTR, *i.e.*, performing reactions inside a hybrid mass spectrometer using a proton acceptor with specific chemistry whose abundance can be modulated rapidly, results in a high performance analytical platform for characterizing samples containing high mass and heterogeneous analytes.

2.6 Electronic Supplementary Material.

Additional details regarding the calculations of gas-phase basicity of $[PDCH–F]^-$, simulations of native mass spectra, derivations of Equations 2 & 3, and Figures S1–S5 are available online. This material is available free of charge via the Internet, and is reprinted in Appendix A.

2.7 Acknowledgments.

Research reported in this publication was supported by the American Society for Mass Spectrometry (Research Award to M. F. B.), the National Institute of General Medical Sciences

of the National Institutes of Health under Award Number T32GM008268, and the ARCS Foundation.

2.8 References.

(1) Loo, J. A. Studying Noncovalent Protein Complexes by Electrospray Ionization Mass Spectrometry. *Mass Spectrom. Rev.* **1997**, *16* (1), 1–23.
(2) Hofstadler, S. A.; Sannes-Lowery, K. A. Applications of ESI-MS in Drug Discovery: Interrogation of Noncovalent Complexes. *Nat. Rev. Drug Discov.* **2006**, *5* (7), 585–595.
(3) Heck, A. J. R. Native Mass Spectrometry: A Bridge between Interactomics and Structural Biology. *Nat. Meth.* **2008**, *5* (11), 927–933.
(4) Hilton, G. R.; Benesch, J. L. P. Two Decades of Studying Non-Covalent Biomolecular Assemblies by Means of Electrospray Ionization Mass Spectrometry. *J. R. Soc. Interface* **2012**, *9* (70), 801–816.
(5) Smith, D. P.; Radford, S. E.; Ashcroft, A. E. Elongated Oligomers in β2-Microglobulin Amyloid Assembly Revealed by Ion Mobility Spectrometry-Mass Spectrometry. *Proc. Natl. Acad. Sci. U. S. A.* **2010**, *107* (15), 6794–6798.
(6) Bleiholder, C.; Dupuis, N. F.; Wyttenbach, T.; Bowers, M. T. Ion Mobility–mass Spectrometry Reveals a Conformational Conversion from Random Assembly to β-Sheet in Amyloid Fibril Formation. *Nat. Chem.* **2011**, *3* (2), 172–177.
(7) Walldén, K.; Williams, R.; Yan, J.; Lian, P. W.; Wang, L.; Thalassinos, K.; Orlova, E. V.; Waksman, G. Structure of the VirB4 ATPase, Alone and Bound to the Core Complex of a Type IV Secretion System. *Proc. Natl. Acad. Sci. U. S. A.* **2012**, *109* (28), 11348–11353.
(8) Lu, C.; Turley, S.; Marionni, S. T.; Park, Y.-J.; Lee, K. K.; Patrick, M.; Shah, M.; Sandkvist, M.; Bush, M. F.; Hol, W. G. J. Hexamers of the Type II Secretion ATPase GspE from Vibrio Cholerae with Increased ATPase Activity. *Structure* **2013**, *21*, 1707–1717.
(9) Ekeowa, U. I.; Freeke, J.; Miranda, E.; Gooptu, B.; Bush, M. F.; Pérez, J.; Teckman, J.; Robinson, C. V.; Lomas, D. A. Defining the Mechanism of Polymerization in the Serpinopathies. *PNAS* **2010**, *107* (40), 17146–17151.
(10) Aquilina, J. A.; Benesch, J. L. P.; Bateman, O. A.; Slingsby, C.; Robinson, C. V. Polydispersity of a Mammalian Chaperone: Mass Spectrometry Reveals the Population of Oligomers in αB-Crystallin. *Proc. Natl. Acad. Sci. U. S. A.* **2003**, *100*, 10611–10616.
(11) Stengel, F.; Baldwin, A. J.; Bush, M. F.; Hilton, G. R.; Lioe, H.; Basha, E.; Jaya, N.; Vierling, E.; Benesch, J. L. P. Dissecting Heterogeneous Molecular Chaperone Complexes Using a Mass Spectrum Deconvolution Approach. *Chemistry & Biology* **2012**, *19* (5), 599–607.
(12) Tito, M. A.; Tars, K.; Valegard, K.; Hajdu, J.; Robinson, C. V. Electrospray Time-of-Flight Mass Spectrometry of the Intact MS2 Virus Capsid. *J. Am. Chem. Soc.* **2000**, *122* (14), 3550–3551.
(13) Uetrecht, C.; Barbu, I. M.; Shoemaker, G. K.; van Duijn, E.; Heck, A. J. R. Interrogating Viral Capsid Assembly with Ion Mobility-Mass Spectrometry. *Nat Chem* **2011**, *3* (2), 126–132.

(14) Pierson, E. E.; Keifer, D. Z.; Selzer, L.; Lee, L. S.; Contino, N. C.; Wang, J. C.-Y.; Zlotnick, A.; Jarrold, M. F. Detection of Late Intermediates in Virus Capsid Assembly by Charge Detection Mass Spectrometry. *J. Am. Chem. Soc.* **2014**, *136* (9), 3536–3541.
(15) Mann, M.; Meng, C. K.; Fenn, J. B. Interpreting Mass Spectra of Multiply Charged Ions. *Anal. Chem.* **1989**, *61* (15), 1702–1708.
(16) Reinhold, B. B.; Reinhold, V. N. Electrospray Ionization Mass Spectrometry: Deconvolution by an Entropy-Based Algorithm. *J. Am. Soc. Mass Spectrom.* **1992**, *3* (3), 207–215.
(17) Ferrige, A. G.; Seddon, M. J.; Green, B. N.; Jarvis, S. A.; Skilling, J.; Staunton, J. Disentangling Electrospray Spectra with Maximum Entropy. *Rapid Commun. Mass Spectrom.* **1992**, *6* (11), 707–711.
(18) Stephenson, J. L.; McLuckey, S. A. Charge Manipulation for Improved Mass Determination of High-Mass Species and Mixture Components by Electrospray Mass Spectrometry. *J. Mass Spectrom.* **1998**, *33* (7), 664–672.
(19) Morgner, N.; Robinson, C. V. Massign: An Assignment Strategy for Maximizing Information from the Mass Spectra of Heterogeneous Protein Assemblies. *Anal. Chem.* **2012**, *84* (6), 2939–2948.
(20) Marty, M. T.; Baldwin, A. J.; Marklund, E. G.; Hochberg, G. K. A.; Benesch, J. L. P.; Robinson, C. V. Bayesian Deconvolution of Mass and Ion Mobility Spectra: From Binary Interactions to Polydisperse Ensembles. *Anal. Chem.* **2015**, *87* (8), 4370–4376.
(21) Zhou, M.; Wysocki, V. H. Surface Induced Dissociation: Dissecting Noncovalent Protein Complexes in the Gas Phase. *Acc. Chem. Res.* **2014**, *47* (4), 1010–1018.
(22) Pagel, K.; Hyung, S.-J.; Ruotolo, B. T.; Robinson, C. V. Alternate Dissociation Pathways Identified in Charge-Reduced Protein Complex Ions. *Anal. Chem.* **2010**, *82* (12), 5363–5372.
(23) Felitsyn, N.; Kitova, E. N.; Klassen, J. S. Thermal Decomposition of a Gaseous Multiprotein Complex Studied by Blackbody Infrared Radiative Dissociation. Investigating the Origin of the Asymmetric Dissociation Behavior. *Anal. Chem.* **2001**, *73* (19), 4647–4661.
(24) Uetrecht, C.; Versluis, C.; Watts, N. R.; Roos, W. H.; Wuite, G. J. L.; Wingfield, P. T.; Steven, A. C.; Heck, A. J. R. High-Resolution Mass Spectrometry of Viral Assemblies: Molecular Composition and Stability of Dimorphic Hepatitis B Virus Capsids. *PNAS* **2008**, *105* (27), 9216–9220.
(25) Ma, X.; Lai, L. B.; Lai, S. M.; Tanimoto, A.; Foster, M. P.; Wysocki, V. H.; Gopalan, V. Uncovering the Stoichiometry of Pyrococcus Furiosus RNase P, a Multi-Subunit Catalytic Ribonucleoprotein Complex, by Surface-Induced Dissociation and Ion Mobility Mass Spectrometry. *Angew. Chem. Int. Ed.* **2014**, *53* (43), 11483–11487.
(26) Ma, X.; Zhou, M.; Wysocki, V. H. Surface Induced Dissociation Yields Quaternary Substructure of Refractory Noncovalent Phosphorylase B and Glutamate Dehydrogenase Complexes. *J. Am. Soc. Mass Spectrom.* **2014**, *25* (3), 368–379.
(27) Lemaire, D.; Marie, G.; Serani, L.; Laprévote, O. Stabilization of Gas-Phase Noncovalent Macromolecular Complexes in Electrospray Mass Spectrometry Using Aqueous Triethylammonium Bicarbonate Buffer. *Anal. Chem.* **2001**, *73* (8), 1699–1706.
(28) Lomeli, S. H.; Yin, S.; Loo, R. R. O.; Loo, J. A. Increasing Charge While Preserving Noncovalent Protein Complexes for ESI-MS. *J Am Soc Mass Spectrom* **2009**, *20* (4), 593–596.

(29) Sterling, H. J.; Daly, M. P.; Feld, G. K.; Thoren, K. L.; Kintzer, A. F.; Krantz, B. A.; Williams, E. R. Effects of Supercharging Reagents on Noncovalent Complex Structure in Electrospray Ionization from Aqueous Solutions. *J Am Soc Mass Spectrom* **2010**, *21* (10), 1762–1774.
(30) Bornschein, R.; Hyung, S.-J.; Ruotolo, B. Ion Mobility-Mass Spectrometry Reveals Conformational Changes in Charge Reduced Multiprotein Complexes. *J. Am. Soc. Mass Spectrom.* **2011**, *22* (10), 1690–1698.
(31) Allen, S. J.; Schwartz, A. M.; Bush, M. F. Effects of Polarity on the Structures and Charge States of Native-Like Proteins and Protein Complexes in the Gas Phase. *Anal. Chem.* **2013**, *85* (24), 12055–12061.
(32) McLuckey, S. A.; Goeringer, D. E. Ion/Molecule Reactions for Improved Effective Mass Resolution in Electrospray Mass Spectrometry. *Anal. Chem.* **1995**, *67* (14), 2493–2497.
(33) Schnier, P. D.; Gross, D. S.; Williams, E. R. Electrostatic Forces and Dielectric Polarizability of Multiply Protonated Gas-Phase Cytochrome c Ions Probed by Ion/Molecule Chemistry. *J. Am. Chem. Soc.* **1995**, *117* (25), 6747–6757.
(34) Ogorzalek Loo, R. R.; Udseth, H. R.; Smith, R. D. A New Approach for the Study of Gas-Phase Ion-Ion Reactions Using Electrospray Ionization. *J. Am. Soc. Mass Spectrom.* **1992**, *3* (7), 695–705.
(35) Stephenson, J. L.; McLuckey, S. A. Ion/Ion Reactions in the Gas Phase: Proton Transfer Reactions Involving Multiply-Charged Proteins. *J. Am. Chem. Soc.* **1996**, *118* (31), 7390–7397.
(36) McLuckey, S. A.; Stephenson, J. L. Ion/Ion Chemistry of High-Mass Multiply Charged Ions. *Mass Spectrom. Rev.* **1998**, *17* (6), 369–407.
(37) Scalf, M.; Westphall, M. S.; Krause, J.; Kaufman, S. L.; Smith, L. M. Controlling Charge States of Large Ions. *Science* **1999**, *283* (5399), 194–197.
(38) Ebeling, D. D.; Westphall, M. S.; Scalf, M.; Smith, L. M. Corona Discharge in Charge Reduction Electrospray Mass Spectrometry. *Anal. Chem.* **2000**, *72* (21), 5158–5161.
(39) Campuzano, I. G.; Schnier, P. Coupling Electrospray Corona Discharge, Charge Reduction and Ion Mobility Mass Spectrometry: From Peptides to Large Macromolecular Protein Complexes. *Int. J. Ion Mobil. Spec.* **2013**, *16* (1), 51–60.
(40) McLuckey, S. A.; Glish, G. L.; Van Berkel, G. J. Charge Determination of Product Ions Formed from Collision-Induced Dissociation of Multiply Protonated Molecules via Ion/Molecule Reactions. *Anal. Chem.* **1991**, *63* (18), 1971–1978.
(41) Herron, W. J.; Goeringer, D. E.; McLuckey, S. A. Product Ion Charge State Determination via Ion/Ion Proton Transfer Reactions. *Anal. Chem.* **1996**, *68* (2), 257–262.
(42) Herron, W. J.; Goeringer, D. E.; McLuckey, S. A. Ion-Ion Reactions in the Gas Phase: Proton Transfer Reactions of Protonated Pyridine with Multiply Charged Oligonucleotide Anions. *J. Am. Chem. Soc.* **1995**, *6* (6), 529–532.
(43) Pitteri, S. J.; McLuckey, S. A. Recent Developments in the Ion/Ion Chemistry of High-Mass Multiply Charged Ions. *Mass Spectrom. Rev.* **2005**, *24* (6), 931–958.
(44) Williams, J. P.; Brown, J. M.; Campuzano, I.; Sadler, P. J. Identifying Drug Metallation Sites on Peptides Using Electron Transfer Dissociation (ETD), Collision Induced Dissociation (CID) and Ion Mobility-Mass Spectrometry (IM-MS). *Chem. Commun.* **2010**, *46* (30), 5458–5460.

(45) Zhao, Q.; Soyk, M. W.; Schieffer, G. M.; Fuhrer, K.; Gonin, M. M.; Houk, R. S.; Badman, E. R. An Ion Trap-Ion Mobility-Time of Flight Mass Spectrometer with Three Ion Sources for Ion/Ion Reactions. *J Am Soc Mass Spectrom* **2009**, *20* (8), 1549–1561.
(46) Sobott, F.; McCammon, M. G.; Robinson, C. V. Gas-Phase Dissociation Pathways of a Tetrameric Protein Complex. *Int. J. Mass Spectrom.* **2003**, *230* (2–3), 193–200.
(47) McLuckey, S. A.; Stephenson, J. L.; Asano, K. G. Ion/Ion Proton-Transfer Kinetics: Implications for Analysis of Ions Derived from Electrospray of Protein Mixtures. *Anal. Chem.* **1998**, *70* (6), 1198–1202.
(48) Wu, J.; Hager, J. W.; Xia, Y.; Londry, F. A.; McLuckey, S. A. Positive Ion Transmission Mode Ion/Ion Reactions in a Hybrid Linear Ion Trap. *Anal. Chem.* **2004**, *76* (17), 5006–5015.
(49) Stephenson Jr, J. L.; Van Berkel, G. J.; McLuckey, S. A. Ion-Ion Proton Transfer Reactions of Bio-Ions Involving Noncovalent Interactions: Holomyoglobin. *J. Am. Soc. Mass Spectrom.* **1997**, *8* (6), 637–644.
(50) Sterner, J. L.; Johnston, M. V.; Nicol, G. R.; Ridge, D. P. Apparent Proton Affinities of Highly Charged Peptide Ions. *J. Am. Soc. Mass Spectrom.* **1999**, *10* (6), 483–491.
(51) Bouchoux, G. Gas Phase Basicities of Polyfunctional Molecules. Part 3: Amino Acids. *Mass Spectrom. Rev.* **2012**, *31* (3), 391–435.
(52) Gunawardena, H. P.; He, M.; Chrisman, P. A.; Pitteri, S. J.; Hogan, J. M.; Hodges, B. D. M.; McLuckey, S. A. Electron Transfer versus Proton Transfer in Gas-Phase Ion/Ion Reactions of Polyprotonated Peptides. *J. Am. Chem. Soc.* **2005**, *127* (36), 12627–12639.
(53) Chrisman, P. A.; Pitteri, S. J.; Hogan, J. M.; McLuckey, S. A. SO2−· Electron Transfer Ion/Ion Reactions with Disulfide Linked Polypeptide Ions. *J. Am. Soc. Mass Spectrom.* **2005**, *16* (7), 1020–1030.
(54) Zhang, H.; Cui, W.; Wen, J.; Blankenship, R. E.; Gross, M. L. Native Electrospray and Electron-Capture Dissociation FTICR Mass Spectrometry for Top-Down Studies of Protein Assemblies. *Anal. Chem.* **2011**, *83* (14), 5598–5606.
(55) Li, H.; Wolff, J. J.; Van Orden, S. L.; Loo, J. A. Native Top-Down Electrospray Ionization-Mass Spectrometry of 158 kDa Protein Complex by High-Resolution Fourier Transform Ion Cyclotron Resonance Mass Spectrometry. *Anal. Chem.* **2014**, *86* (1), 317–320.
(56) Lermyte, F.; Williams, J. P.; Brown, J. M.; Martin, E. M.; Sobott, F. Extensive Charge Reduction and Dissociation of Intact Protein Complexes Following Electron Transfer on a Quadrupole-Ion Mobility-Time-of-Flight MS. *J. Am. Soc. Mass Spectrom.* **2015**, *26* (7), 1068–1076.
(57) Stephenson, J. L.; McLuckey, S. A. Ion/Ion Proton Transfer Reactions for Protein Mixture Analysis. *Anal. Chem.* **1996**, *68* (22), 4026–4032.
(58) Guilhaus, M. Principles and Instrumentation in Time-of-Flight Mass Spectrometry. *J. Mass Spectrom.* **1995**, *30* (11), 1519–1532.
(59) Cornish, T. J.; Cotter, R. J. High-Order Kinetic Energy Focusing in an End Cap Reflectron Time-of-Flight Mass Spectrometer. *Anal. Chem.* **1997**, *69* (22), 4615–4618.
(60) McKay, A. R.; Ruotolo, B. T.; Ilag, L. L.; Robinson, C. V. Mass Measurements of Increased Accuracy Resolve Heterogeneous Populations of Intact Ribosomes. *J. Am. Chem. Soc.* **2006**, *128* (35), 11433–11442.

(61) de la Mora, J. F.; Ude, S.; Thomson, B. A. The Potential of Differential Mobility Analysis Coupled to MS for the Study of Very Large Singly and Multiply Charged Proteins and Protein Complexes in the Gas Phase. *Biotechnol. J.* **2006**, *1* (9), 988–997.
(62) Abzalimov, R. R.; Kaltashov, I. A. Electrospray Ionization Mass Spectrometry of Highly Heterogeneous Protein Systems: Protein Ion Charge State Assignment via Incomplete Charge Reduction. *Anal. Chem.* **2010**, *82* (18), 7523–7526.

Chapter 3. Folding of Protein Ions in the Gas Phase after Cation to Anion Proton Transfer Reactions (CAPTR)

3.1 Abstract

The structure and folding of a protein in solution depends on noncovalent interactions within the protein and those with surrounding ions and molecules. Decoupling these interactions in solution is challenging, which has hindered the development of accurate physics-based models for structure prediction. Investigations of proteins in the gas phase can be used to selectively decouple factors affecting the structures of proteins. Here, we use Cation to Anion Proton Transfer Reactions (CAPTR) to reduce the charge states of denatured ubiquitin ions in the gas phase, and ion mobility to probe their structures. In CAPTR, a precursor charge state is selected (*P*) and reacted with monoanions to generate charge-reduced product ions (*C*). Following each CAPTR event, denatured ubiquitin ions (13+ to 6+) yield products that rapidly isomerize to structures that have smaller collision cross sections (Ω). The Ω of CAPTR product ions depend strongly on *C* and very weakly on *P*. Pre- and post-CAPTR activation was then used to probe the potential-energy surfaces of the precursor and product ions, respectively. Post-CAPTR activation showed that ions of different *P* fold differently and populate different regions of the potential-energy surface of that ion. Finally, pre-CAPTR activation showed that the structures of protein

ions can be indirectly investigated using ion mobility of their CAPTR product ions, even for subtle structural differences that are not apparent from ion mobility characterization of the activated precursor ions. More generally, these results show that CAPTR strongly complements existing techniques for characterizing the structures and dynamics of biological molecules in the gas phase.

3.2 Introduction

Despite progress in understanding protein folding[1,2] and protein structure prediction,[3,4] universal methods for predicting the tertiary and quaternary structures of proteins on the basis of their sequence remain elusive, partially due to limited experimental data.[1,5–7] The folding of proteins depends on covalent interactions and noncovalent interactions within the protein and with surrounding ions and molecules. Although a great deal of progress has been made,[8] how these contributions work in concert to achieve native, biologically active proteins remains difficult to predict using physics-based models.[1] Decoupling these contributions is particularly challenging in the condensed phase, where all interactions contribute simultaneously.

Mass spectrometry (MS) and associated methods have emerged as robust tools for studying proteins and noncovalent complexes in the gas phase, particularly due to their ability to selectively characterize individual components of mixtures.[9–11] Electrospray ionization of proteins from native conditions, *e.g.*, pH = 7.0 and physiological ionic strengths, enables measurements of "native-like" gas-phase ions, which can retain ligands, stoichiometries, and tertiary structures from solution.[9–11] Coupling mass spectrometry to ion/neutral proton transfer reactions,[12–15] hydrogen/deuterium exchange reactions,[14,16–20] electron-mediated dissociation techniques,[21–23] and ion mobility (IM),[23–29] enables the characterization of gas-phase structures,

which can be compared to their solution-phase counterparts.[9,29–33] For example, IM-MS measurements can be used to determine the collision cross section (Ω) of an ion with a buffer gas molecule,[34] which can be compared with Ω values calculated for atomic and coarse-grained models and structures.[35–38]

Biomolecules can adopt multiple structures that are kinetically stable in the gas phase. For example, native-like ions typically exhibit a single feature in their IM arrival-time distributions at low energies[39,40] and activation of these ions can result in the formation of multiple structures that are kinetically stable and appear at different drift times.[41–44] IM-MS of protein ions generated from denaturing solutions, *e.g.*, low pH and a large fraction of organic solvent, frequently exhibit features for multiple coexisting conformers.[27,31,45] For example, IM-MS of 3+ bradykinin from different solutions shows evidence for a total of ten conformers that are all kinetically stable on the millisecond time scale of the separation.[46] To investigate the relationship between these conformers, Clemmer and coworkers pioneered IM-IM-MS[47] and IM-IM-IM-MS[48] approaches to characterize the potential-energy surfaces of peptide ions in the gas phase. For example, six conformers of 3+ bradykinin were each mobility selected, activated, and reanalyzed using a second IM separation.[49,50] At high energies, the products of these experiments all exhibited the same three populations in approximately identical ratios.[49,50] They propose that these ions formed a quasi-equilibrium of structures in which the relative populations of those structures depended on their free energies after thermalization. These tandem IM experiments have established the ground work for quantitative thermodynamic measurements of potential-energy surfaces in the gas phase.[50]

The relationship between the structure, charge state, and original solution of protein ions remains challenging to decouple. For example, native-like ions of prion[51] and intrinsically

disordered[52] proteins as well as proteins ions from denaturing solutions[31,53,54] can exhibit a strong correlation between charge state and Ω. However, charge state[39–41,55] and polarity[40] can have a comparatively small effect on the Ω of native-like ions of large, globular proteins and protein complexes. One approach to probe the relationship between structure and charge state is to manipulate the charge states of protein ions in the gas phase. For example, in ion/neutral proton transfer reactions a multiply charged precursor cation is reacted with a neutral molecule, A, which has a higher gas-phase basicity:[13,56]

$$[M_n + zH]^{z+} + A \rightarrow [M_n + (z-1)H]^{(z-1)+} + AH^+ \qquad \text{(Reaction 1)}$$

Foundational results from ion/neutral proton transfer reactions in tandem with IM-MS have shown that charge reduction of mixtures of ions that have high-charge states and unfolded structures can yield product ions that have lower charge states and partially folded structures.[57,58]

An alternative approach to manipulate the charge states of protein ions in the gas phase is to use ion/ion proton transfer reactions, in which multiply charged protein cations react with monoanions to yield charge-reduced protein cations:

$$[M_n + zH]^{z+} + A^- \rightarrow [M_n + (z-1)H]^{(z-1)+} + AH \qquad \text{(Reaction 2)}$$

Ion/ion reactions benefit from more favorable kinetics and thermodynamics relative to ion/neutral proton transfer reactions.[59–62] Recently, we reported an approach for these reactions that we refer to as cation to anion proton transfer reactions (CAPTR).[62] CAPTR is most similar to ion/ion proton transfer reactions pioneered by McLuckey and coworkers.[60,61] However, those reactions are typically performed under pseudo first-order kinetics (effectively constant anion abundance),[60,61,63] whereas the abundance of anions in CAPTR depletes during individual experiments and as a result a wide range of product ion charge states (from different numbers of sequential proton transfer events) can be formed during a single experiment.[62] It differs from

analogous experiments using electron transfer ("electron transfer no dissociation")[22] in that charge reduction is caused by proton transfer rather than electron transfer, which can also cause bond cleavage.[64,65]

Here, CAPTR of *m*/*z*-selected precursor ions are used to monitor the stepwise changes in conformation as the charge state of a protein ion is reduced. We perform CAPTR within the vacuum system of a mass spectrometer in order to reduce an individual charge state of denatured ubiquitin, IM to characterize the structural effects of removing charge, and collisional activation to probe the structures and stabilities of CAPTR precursor and product ions. IM of CAPTR product ions show that there is a strong relationship between their charge state and Ω. Energy-dependent experiments suggest that 6+ ubiquitin can adopt at least two sets of structures that are unable to interconvert under the conditions of these experiments.

3.3 Methods

Bovine ubiquitin was purchased from Sigma Aldrich and dissolved into ultrapure (18.2 MΩ) water to a concentration of ~100 μM without additional purification. This solution was then diluted with methanol and water, which were acidified to a pH of 2 using trifluoroacetic acid. The final solution contained 10 μM ubiquitin in 70%:30% water:methanol by volume. Cations were generated using nanoelectrospray ionization from borosilicate capillaries with inner diameters of 0.78 mm that were pulled to ~1 to 3 μm on one end using a Sutter Instruments P-97 micropipette puller (Novato, CA). Electrical contact with the solution was achieved by inserting a platinum wire into the wide end of the capillary. The source was maintained at 120 °C. Note that under these conditions there is some heat transfer to the sample capillary, which is discussed with Figure S1.

Experiments were performed using a Waters Synapt G2 HDMS modified with a glow-discharge ionization source[66] and a radio-frequency confining drift cell (Figure 3.1A).[67] This instrument is equipped for ion/ion reactions in the trap cell, which contains 0.08 mBar helium and is positioned before the mobility cell and the time-of-flight mass analyzer. Voltages were selected to minimize activation and maximize transmission. Monoanions for CAPTR, the fragments of perfluoro-1,3-dimethylcyclohexane (PDCH, Sigma Aldrich) at *m*/*z* 381 ($[PDCH\text{-}F]^-$),[68] were generated via glow discharge for 100 ms, quadrupole selected, and accumulated in the trap cell.[62] The instrument was then switched into positive mode for 2 to 3 s, during which a single charge state of ubiquitin was quadrupole selected and trapped with $[PDCH\text{-}F]^-$ to initiate CAPTR. The CAPTR products and residual precursors were then pulsed into the RF-confining drift cell for 200 μs every 13.8 or 22 ms, depending on the maximum *m*/*z* measured. For selected experiments, ions were collisionally activated by increasing their kinetic energy (Figure 3.1B) prior to injection into either the trap cell (pre-CAPTR activation) or the mobility cell (post-CAPTR activation). Spontaneous charge loss following IM separation is minor relative to the other charge reduction processes in these experiments, as discussed in the Supporting Information.

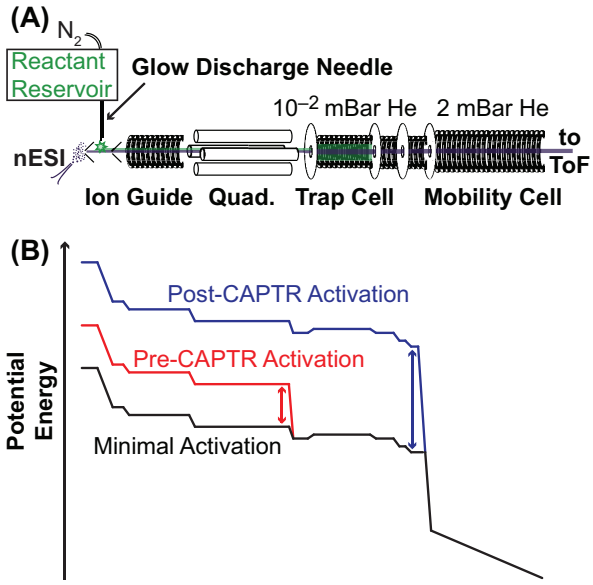

Figure 3.1. (A) Diagram of the modified Waters Synapt G2 HDMS used in these experiments. Anions (green) are generated by glow-discharge ionization[66] and accumulated in the trap cell. Cations (purple) are generated by nanoelectrospray ionization (nESI) and are trapped with anions for CAPTR. Residual precursor and CAPTR product ions are separated using IM in a radio-frequency confining drift cell[67] prior to mass analysis. (B) Representative potential-energy diagrams for cation transmission during minimal activation, pre-CAPTR activation, and post-CAPTR activation experiments. The double headed arrows indicate the DC bias adjusted relative to the minimal activation conditions.

IM arrival-time distributions were measured using a radio-frequency confining drift cell,[67] a field of 5 V·cm^{-1}, and 2.0 mBar helium. Ω values were determined from those distributions using a procedure discussed in the Supporting Information. Briefly, field-dependent measurements were used to determine the *m*/*z*-independent and *m*/*z*-dependent[69] transport times of ions from the exit of the mobility cell to the time-of-flight mass analyzer. The experimental

drift time of CAPTR ions obtained from a measurement at a single field strength were corrected for these transport times to determine their mobility (K), which was converted to Ω using the Mason-Schamp equation:[34]

$$\Omega = \frac{3ez}{16N}\left(\frac{2\pi}{\mu k_B T}\right)^{1/2}\frac{1}{K} \qquad \text{(Equation 1)}$$

where z is the charge state, e is the elementary charge, N is the number density of the drift gas, μ is the reduced mass of the ion and drift gas (helium), k_B is the Boltzmann constant, and T is the temperature of the drift gas, which was 301 K for these experiments.

3.4 Results and Discussion

Recently, we reported experiments using CAPTR to manipulate the charge states of protein complex ions.[62] Here, we couple CAPTR to reduce the charge states of protein ions generated from denaturing solutions and IM to monitor to how changes in z of protein ions affect their Ω. Figure 3.2A shows a nanoelectrospray ionization mass spectrum of ubiquitin from a denaturing solution of 70%:30% water:methanol at pH 2. 13+ to 5+ cations were observed, but the abundance of the 5+ cation was too weak for further analysis (Figure 3.2A, inset). Precursor ions were m/z selected (Figure 3.2B) and then subjected to CAPTR (Reaction 2) in the trap cell (Figure 3.2C). In this implementation, CAPTR spectra exhibit peaks for the charge-reduced product ions and a small population of unreacted precursor ions.[62] The product ions and any unreacted precursor ions were then characterized using IM-MS (Figure 3.2D). For the remainder of the discussion, precursor ions are defined as quadrupole-selected ions that have not undergone CAPTR, and will be noted as either "$P+$" or "$P \rightarrow P$". The product ions of CAPTR are noted as

"*P*→*C*", where *P* is the charge state of the precursor ion and *C* is the charge state of the product ion.

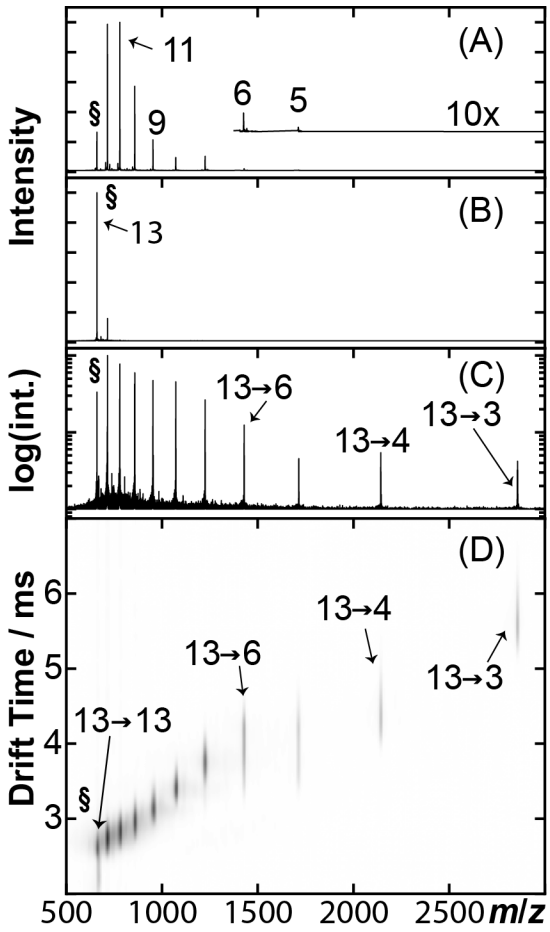

Figure 3.2. CAPTR experimental workflow. (A) Mass spectrum of ubiquitin ions generated using nanoelectrospray ionization from a denaturing solution. (B) 13+ ubiquitin (§) is *m*/*z* selected using a quadrupole mass filter. (C) Precursor ions are subjected to CAPTR; the intensity axis is plotted on a logarithmic scale to aid in visualizing the low abundance product ions. (D) CAPTR mass spectrum plotted versus the corresponding ion mobility drift times. Intensities were scaled using a nested logarithm function ($\log_{10}(\log_{10}(\text{intensity}))$) to aid in the visualization of low-intensity product ions.

3.4.1 *CAPTR of Denatured Ubiquitin.*

Figure 3.3 shows the Ω distributions for the 13→*C* ions. All of these ions, except 13→6 and 13→5, exhibit monomodal Ω distributions. The Ω distribution for the 13→6 ions exhibits three features, whereas that for the 13→5 ions exhibits two features. Figure S2 shows the Ω distributions for selected *P*→7 and *P*→6 ions, which exhibit monomodal and trimodal Ω distributions, respectively. The Ω distributions of the *P*→7 ions were fit using one Gaussian distribution and those for the *P*→6 ions were fit using three Gaussian distributions. Interestingly, all *P*→6 ions exhibit features I, II, and III, but the relative intensity of those features depend on *P*. Note that each Gaussian function used likely represents a family of conformers, rather than a single structure.[70]

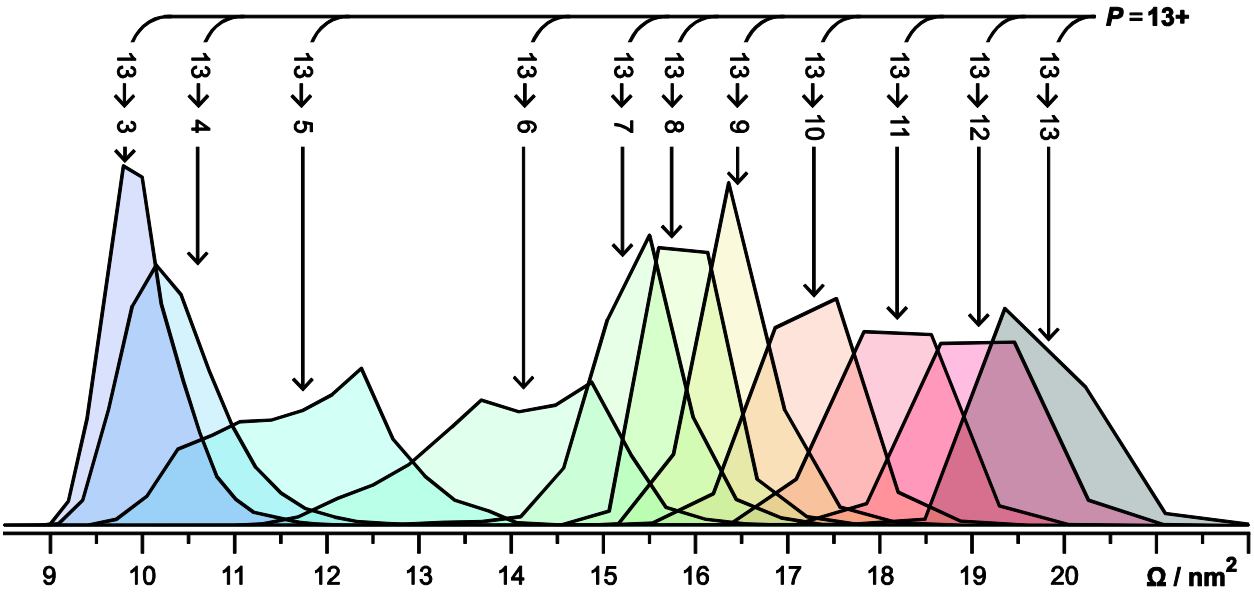

Figure 3.3. Normalized Ω distributions of all 13→*C* ions. All ions except 13→6 and 13→5 exhibit monomodal Ω distributions. 13→6 and 13→5 exhibit trimodal and bimodal Ω distributions, respectively. Ω distributions were determined using drift times measured in a radio-frequency confining drift cell[67] and the Mason-Schamp equation (Equation 1), as discussed in the Supporting Information.

Figure 3.4 shows the centroids of the Gaussians fit to the features in the Ω distributions for isolated 13+ to 6+ ubiquitin cations and the corresponding CAPTR products. For each precursor charge state selected, the resulting CAPTR products exhibit smaller Ω values. This result is consistent with the product ions isomerizing to more compact conformations after charge reduction. The Ω of each feature observed for the product ions of a given charge state (*C*) are remarkably similar. The average root-mean-square deviation (RMSD) of the Ω for each feature is 0.04 nm^2 and the greatest RMSD is 0.15 nm^2 (found for feature I of the *P*→6 cations).

These experiments show that the Ω of CAPTR product ions depend weakly on precursor charge state, regardless of whether the ion was produced via electrospray ionization or CAPTR.

The Ω values of native-like ubiquitin cations generated from buffered solutions of aqueous ammonium acetate are 9.72, 9.83, and 10.0 nm^2 for the 4+, 5+, and 6+ cations, respectively.[71] The average of those three values is 9.85 nm^2 and is also shown on Figure 3.4.[71] Features I, II, and III of the $P \rightarrow 6$ cations in these experiments range from 12.5 to 14.6 nm^2 and are significantly larger than the 6+ native-like ions. In contrast, the $P \rightarrow 3$ cations in these experiments all have Ω values near 9.9 nm^2, which are indistinguishable from the Ω of the native-like cations given the uncertainties in the mobility experiments.[39,67] Although the native-like ions and the low-*z* CAPTR product ions were formed through very different processes, these results suggest that they have similar size, and may share some structural motifs. At a minimum, these results suggest that the densities of the low-*z* CAPTR product ions converge with those of the corresponding native-like ions.

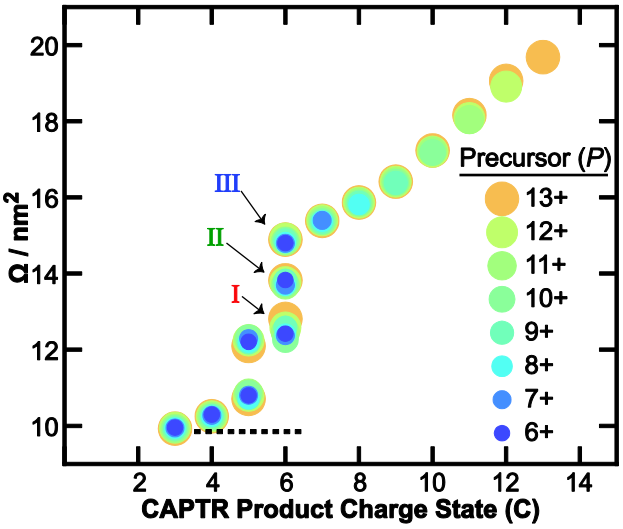

Figure 3.4. Ω of precursor (*P*) and CAPTR product ions (*P*→*C*) of ubiquitin. The lowest charge state product detected for each precursor ion was 3+. Precursor charge states are represented by differently colored circles, which were selected to facilitate visualization of the data. Average Ω of 4+ to 6+ ubiquitin from a native-like solution[71] is shown with a dotted line for comparison.

These results demonstrate that the CAPTR products of ubiquitin adopt more compact structures with decreasing *z*. This finding is consistent with results from ion/neutral proton transfer reactions in which all ions generated from electrospray were reacted simultaneously with neutrals,[57,58] *i.e.*, the charge-reduced product ions originated from precursor ions that had a range of charge states. CAPTR of *m*/*z*-selected precursor ions in this study enabled the Ω to be monitored for up to ten consecutive proton transfer reactions, *i.e.*, the products from different precursors are directly comparable to each other. Furthermore, the rates of ion/ion proton transfer reactions are expected to depend primarily on the charge state of the protein cation,[59–62] whereas those for ion/neutral proton transfer reactions also depend on the structure of the protein cation.[12,14,15] Previously, Badman and coworkers reported IM-MS analysis for ion/ion proton

transfer reactions of two adjacent charge states each of cytochrome *c*[72] and ubiquitin.[73] Similar to the results reported here, Badman and coworkers observed that the Ω for the charge-reduced products of a mixture of 7+ and 8+ ubiquitin decreased through the 3+ product ion, and the Ω of the product ions were independent of their precursor charge state.[72] In the present study, in which significantly more charge states were characterized, we can draw more general conclusions regarding the relationship between *P*, *C*, and Ω. Specifically, the results in Figure S2 show that the Ω distribution of the features observed for each *C* depend weakly on *P*, but that there are some differences in the relative intensities of those features. These results are consistent with the structure of CAPTR product ions depending strongly on *C*, or at least, that the structures formed as a function of *C* have similar Ω.

Note that each of these experiments, from ionization until time-of-flight mass analysis, take less than 44 ms. Furthermore, the widths of the arrival-time distributions are typically less than one millisecond, even though ions are formed during the entire accumulation period for the ion mobility experiment (13.8 or 22 ms). This suggests that these structural changes occur prior to IM and are therefore very fast, perhaps even sub-millisecond. For comparison, the folding time of ubiquitin in water has been estimated to be ~3 ms.[74] This suggests that structural changes for proteins in the absence of solvent can occur on time scales similar to those in solution.

3.4.2 *Post-CAPTR Activation.*

In order to probe the structures and stabilities of the CAPTR product ions in more detail, arrival-time distributions were measured as a function of the voltage used to inject the ions into the mobility cell (Figure 3.1B). The collisionally activated species will be indicated with an asterisk, *i.e.*, $P \rightarrow C^*$ indicates that the CAPTR product ions are activated following CAPTR and prior to IM separation. Figure S3 shows results for $P \rightarrow C^*$, where P = 13, 8, and 6. Interestingly,

the arrival-time distributions for the 13→13*, 13→8*, and 8→8* ions (Figures S3A to S3C, respectively) are independent of the injection voltage over the range studied. These results are consistent with those ions adopting their lowest-energy structures over all energies, those ions not overcoming the barrier to structural isomerization in these experiments, or that any new structures formed have similar Ω. Note that the range of injection voltages used in these experiments is limited by competition with covalent fragmentation of CAPTR product ions.

Figures 3.5A and 3.5B show the Ω distributions observed for the 6→6* and 8→6* ions, respectively, as a function of the injection voltage as they enter the mobility cell. Vertical dashed lines correspond to the average of the centroids of features I, II, and III for all *P*→6 ions in Figure 3.4. The 6→6* and 8→6* cations at low energies have intense populations corresponding to feature I. However, the 6→6* ions exhibit low-intensity peaks corresponding to features II and III, whereas the 8→6* ions exhibit intense peaks for features II and III. From 55 to 85 V the 6→6* ions convert predominantly to feature III. The 8→6* cations unfold to feature III similarly to the 6→6* cation, however it unfolds at ~10 V lower than the 6→6* ions and exhibits a slightly narrower feature at the highest energies. Therefore, in contrast to the Ω distributions for the 13→13*, 8→8*, and 13→8* ions, those for the *P*→6* ions depend strongly on the injection voltage.

Figure 3.6A shows a qualitative reaction coordinate that is consistent with the results for the 6→6* ions (Figure 3.5A) and has three local minima corresponding to features I to III. The energies of the three features descend from I to III, consistent with features I and II converting to III with sufficient activation. For injection voltages greater than 80 V, the Ω distributions for the 6→6* ions no longer depend on energy, which is consistent with these ions establishing a quasi-equilibrium of structures[50] at high energy. As previously discussed, the results for the 8→6* and

6→6* ions are similar, and therefore the qualitative reaction coordinate in Figure 3.6A is consistent with the results for both experiments.

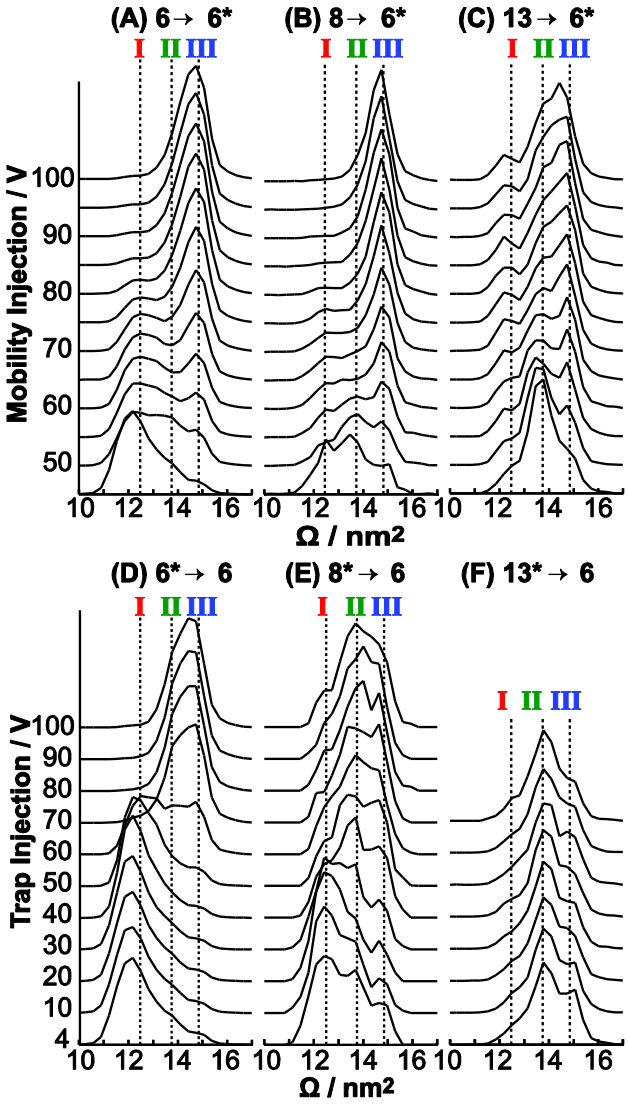

Figure 3.5. Post-CAPTR activation of (A) 6→6*, (B) 8→6*, and (C) 13→6* ubiquitin ions. Pre-CAPTR activation of (D) 6*→6, (E) 8*→6, and (F) 13*→6 ubiquitin ions. Vertical lines corresponding to the average Ω for the three features of the Ω distribution of 6+ (I to III) from Figure 3.4 are included for comparison.

The Ω distributions obtained at the lowest energies in A to C are also shown in Figure S2. These mobility experiments used a field of 6.4 $V \cdot cm^{-1}$.

At low injection energies, the 13→6* ions predominantly exhibit feature II, with less intense features centered at I and III (Figure 3.5C). With injection voltages of 45 to 70 V, feature II converts to feature III until they are roughly equal in intensity from 80 to 100 V. Interestingly, the intensity of feature I remains constant over the injection voltages studied, in contrast to that feature for the 8→6* and 6→6* ions. At high energies, the Ω distribution for the 13→6* ions (Figure 3.5C) are very different than those for the 6→6* and 8→6* ions (Figures 3.5A and 3.5B, respectively). These results are consistent with the 13→6* ions adopting different structures than the 6→6* and 8→6* ions. As a result, the qualitative reaction coordinate in Figure 3.6A alone cannot explain all the data in Figures 3.5A to 3.5C.

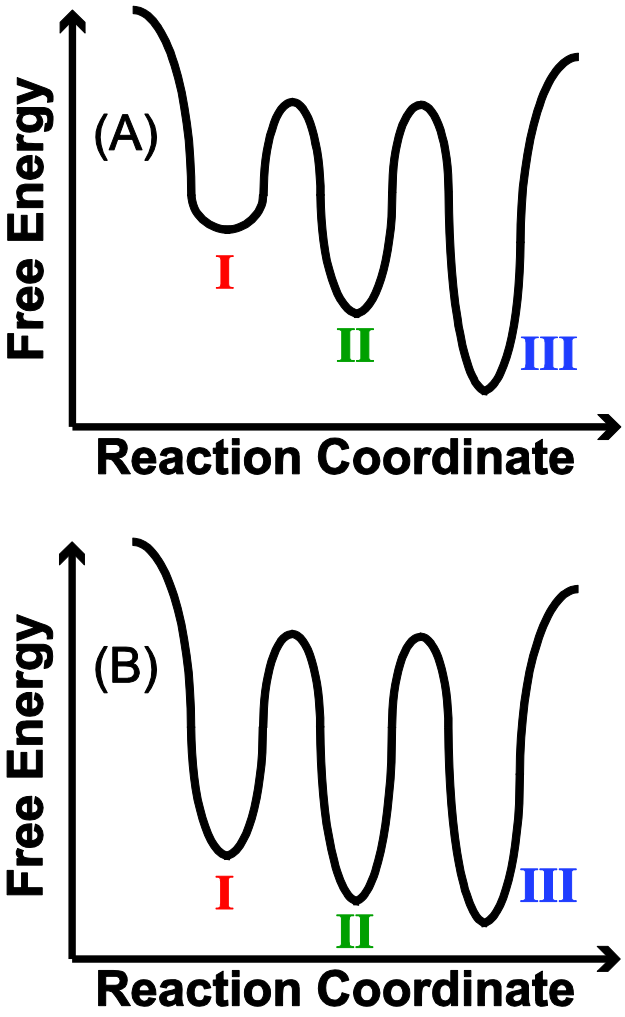

Figure 3.6. (A) Qualitative reaction coordinate of 6→6* and 8→6* ubiquitin that is consistent with the post-CAPTR activation data shown in Figures 3.5A and 3.5B. The labels for the three wells correspond to features in the Ω distributions. (B) Qualitative reaction coordinate of 13→6* ubiquitin that is consistent with the post-CAPTR activation data shown in Figure 3.5C. Again, the labels for the wells correspond to the features in the Ω distributions; the post-CAPTR activation experiments indicate that the structures populated in the wells in B are different than those in A.

A qualitative reaction coordinate that is consistent with the post-CAPTR activation of the 13→6* ions is shown in Figure 3.6B. The qualitative reaction coordinate in Figure 3.6B differs from that in Figure 3.6A in that the local minima are more similar in energy, consistent with features I to III all being populated under quasi-equilibrium conditions (Figure 3.5C). Two alternative explanations are that (1) the persistence of feature I at high energies is the result of a high barrier for isomerization from that feature to the other features or (2) the 13→6* ions have a subpopulation of ions that are consistent with the qualitative reaction coordinate in Figure 3.6A, *i.e.*, isomerize to feature III at high energies, and additional subpopulation that yield features I and II and are unable to interconvert to III even at very high energies.

The post-CAPTR activation results for the 6→6*, 8→6*, and 13→6* ions suggest that 6+ ubiquitin can adopt at least two sets of structures that are unable to interconvert under the conditions of these experiments, and that these experiments probe at least two different regions of the potential-energy surface of 6+ ubiquitin. The pair of qualitative reaction coordinates shown in Figure 3.6 are consistent with these observations. Although we do not believe that it is possible to explain all of the results for the 6→6*, 8→6*, and 13→6* ions using a single reaction coordinate with three local minima, there are other reaction coordinates that are also consistent with these results. For instance, it is possible that feature I for the 6→6* and 8→6* ions convert directly to feature III, without the formation of feature II as an intermediate.

The ions populating different regions on the potential-energy surface probed in the post-CAPTR experiments cannot interconvert and therefore have significant structural differences with barriers to isomerization that are higher than that for covalent fragmentation. One possibility is that these different regions correspond to different configurations of protonation sites. If the barriers to proton migration are sufficiently high, the protonation sites for the

precursor ions may depend on the locations favored during ionization. In contrast, the protonation sites of the CAPTR product ions will also depend on the reactivity of the protonation sites for the precursor ion. Individual CAPTR events are highly exothermic,[62] which will favor proton transfer through the most entropically favored channels. Therefore, the 6+ ions generated directly from electrospray and the 13→6 ions may have very different protonation sites, which may affect their structures and stabilities. These results all indicate that CAPTR product ions can have structural differences that depend on *P*, but that do not necessarily affect their Ω.

3.4.3 *Pre-CAPTR Activation.*

To investigate the effects of the structure of the precursor ion on those of the resulting CAPTR products, ions were activated prior to CAPTR as they were injected into the trap cell (Figure 3.1B). Ions activated prior to CAPTR are indicated with an asterisk, *i.e.*, *P**→*C*. Figure S4 shows results for *P**→*C*, where *P* = 13, 8, and 6. Our interpretation of these results will assume that pre-CAPTR activation occurs prior to charge reduction. This assumption is reasonable because the density of helium in the trap cell greatly exceeds that of the monoanions and the CAPTR cross section will decrease with increasing relative velocity of the cation and monoanion pair.[59] Note that the range of injection voltages used in these experiments is limited by competition with covalent fragmentation.

The Ω distributions for the 6*→6 ions as a function of injection voltage are shown in Figure 3.5D. With increasing injection voltage, the intensity of feature I decreases and that for feature III increases. The results for the 6*→6 ions are similar to those for the 6→6* ions, although the distribution at the highest energy for the 6*→6 ions is broader than that for the 6→6* ions, suggesting that a small population of ions that yield feature II may persist. This suggests that for a given ion, high-energy injection into either the trap or mobility cells results in

activation via a similar mechanism, despite differences in the efficiencies and activated ion lifetimes.

The Ω distributions of the 8*→6 ions (Figure 3.5E) change with increasing energy, even though the arrival-time distributions for the 8*→8 ions appear to be independent of energy (Figure S4C). The Ω distribution of the 8*→6 ions at the lowest energy studied contains features I, II and III in decreasing intensities. With activation of the 8+ precursor ion, feature I of the 8*→6 product ion becomes less abundant and features II and III become more abundant. At high energies (≥70 V), feature II is marginally more populated than feature III, which are both more intense than feature I. One explanation of these results is that the 8*→8 ions isomerize to form additional conformers with indistinguishable Ω distributions, which go on to form different structural populations of the 8*→6 ions. Thus, as the 8*→8 ions are activated and populate new conformations that yield an indistinguishable Ω distribution, those structural changes are reflected in the Ω distribution of the 8*→6 products. Therefore, CAPTR products appear to provide indirect evidence of a change in the structure of a precursor ion. Interestingly, the Ω distributions of the 8*→6 ions are indistinguishable from 70 to 100 V (Figure 3.5E). This result is consistent with the 8*→8 ions achieving a quasi-equilibrium of structures that go on to yield 8*→6 products with indistinguishable Ω distributions over this range of energies. Analogous experiments for the 13*→6 ions are consistent with the 13+ ubiquitin ions adopting a quasi-equilibrium of structures over all energies, and consequently, all 13*→6 ions have similar distributions of structures (Figure 3.5F).

Interestingly, the arrival-time distributions of the 6*→5 ion exhibit very little change over the entire voltage range (Figure S4I), even though the Ω distribution of the 6*→6 ions changes from predominantly feature I to predominantly feature III as the injection voltage is increased

from 50 to 70 V (Figure 3.5D). This suggests that CAPTR of the 6+ precursor ions associated with features I and III both result in 5+ products that have more similar structures or at least structures that have more similar Ω.

In the preceding discussion of the 6*→6, 8*→6, and 13*→6 ions, the relative intensity of features I, II, and III for the 6+ product ions depended on both *P* and energy. From these experiments alone, there is not enough information to know the extent to which the qualitative reaction coordinates in Figure 3.6 apply to the ions formed in the *P**→6 experiments, for $P > 6$. Future experiments using energy-dependent activation both before and after CAPTR (*P**→*C** experiments) may provide additional insights.

3.5 Conclusion

The experiments presented used CAPTR and IM to investigate the relationship between the Ω and charge state of a protein cation. We have shown the Ω of ubiquitin ions depend most strongly on its charge state. This conclusion is based on the observation that regardless of precursor charge state, ions of the same product ion charge state exhibit features that have similar Ω (Figure 3.4). This observation indicates that their structures may be determined predominantly by a delicate balance between intramolecular bonding and Coulombic repulsions. These results build upon those showing that ion/neutral charge reduction of mixtures of protein ions that have both high charge states and extended structures yield product ions with partially folded structures,[57,58] by tracking this process for series of precursor ions with different charge states that were each *m*/*z* selected prior to a sequential series of CAPTR events.

The results from the pre-CAPTR and post-CAPTR activation experiments provide several new insights into the effects of charge reduction and the concomitant gas-phase folding.

Despite the differences in the low-energy Ω distributions of the 6→6* and 8→6* ions, the ions isomerize to similar Ω distributions at high energies, exhibiting predominantly feature III (Figures 3.5A and 3.5B). These results are consistent with these ions forming a quasi-equilibrium of structures and the qualitative reaction coordinate in Figure 3.6A. In contrast, post-CAPTR activation of the 13→6* ions results in a different Ω distribution at high energy (Figure 3.5C), consistent with forming a different set of structures. Consequently, these data suggest that 6+ ubiquitin can adopt at least two sets of structures that are unable to interconvert under the conditions of these experiments. Therefore, these experiments probe at least two different regions of the potential-energy surface of 6+ ubiquitin.

Pre-CAPTR activation enables the exploration of the potential-energy surfaces of CAPTR precursor ions, which then is probed indirectly through Ω analysis of the corresponding CAPTR product ions. For example, the Ω distributions of 8+ ubiquitin ions do not depend on the activation energy used (Figure S4C), but the Ω distributions of 8*→6 ions do depend on the energy used to activate the 8+ precursor (Figure 3.5E). Together, these results show that subtle structural difference that are not apparent from IM of the precursor ions can be indirectly probed using IM of CAPTR product ions.

More generally, these results show that CAPTR complements existing techniques for characterizing the potential-energy surfaces of biological molecules in the gas phase. The final products ions in these experiments were characterized in terms of their *m*/*z* and ion mobility, but as illustrated several times in the present work, different structures can have similar ion mobilities. Future experiments will benefit greatly from complementary probes of structure, *e.g.*, hydrogen/deuterium exchange[16,17,14,18–20] and electron-mediated dissociation techniques.[21,23,22] Furthermore, the energy-dependent experiments reported here used collisional activation under

multicollision conditions, thus the results are qualitative. Alternative approaches in which the ions have more clearly defined internal energies and activated lifetimes may enable more quantitative analogs to the present energy-dependent experiments. Future hybrid CAPTR experiments will provide new insights into the structures and dynamics of biological molecules in the gas phase, which in turn may inform condensed-phase protein folding experiments by decoupling solvent interactions from intramolecular forces.

3.6 Supporting Information.

The Supporting Information is available free of charge on the ACS Publications website at DOI: 10.1021/jacs.6b04282. The Supporting Information is also reprinted in Appendix B.

Figures S1 to S4 and discussions of the effects of source temperature, spontaneous charge loss, and determination of collision cross sections.

3.7 Acknowledgments.

Research reported in this publication was supported by the American Society for Mass Spectrometry (Research Award to M. F. B.), the Amgen Foundation (scholarship to E. B. M.), the ARCS Foundation (fellowship to K. J. L.), Eli Lilly and Company (Young Investigator Award in Analytical Chemistry to M. F. B.), and the National Institute of General Medical Sciences of the National Institutes of Health under Award Number T32GM008268 (support to K. J. L.).

3.8 References

(1) Dill, K. A.; MacCallum, J. L. The Protein-Folding Problem, 50 Years On. *Science* **2012**, *338* (6110), 1042–1046.

(2) Gelman, H.; Gruebele, M. Fast Protein Folding Kinetics. *Q. Rev. Biophys.* **2014**, *47* (2), 95–142.

(3) Kiss, G.; Çelebi-Ölçüm, N.; Moretti, R.; Baker, D.; Houk, K. N. Computational Enzyme Design. *Angew. Chem.* **2013**, *52* (22), 5700–5725.

(4) Moretti, R.; Fleishman, S. J.; Agius, R.; Torchala, M.; Bates, P. A.; Kastritis, P. L.; Rodrigues, J. P. G. L. M.; Trellet, M.; Bonvin, A. M. J. J.; Cui, M.; et al. Community-Wide Evaluation of Methods for Predicting the Effect of Mutations on Protein–protein Interactions. *Proteins Struct. Funct. Bioinforma.* **2013**, *81* (11), 1980–1987.

(5) Shea, J.-E.; Brooks, C. L. I. From Folding Theories to Folding Proteins: A Review and Assessment of Simulation Studies of Protein Folding and Unfolding. *Annu. Rev. Phys. Chem.* **2001**, *52* (1), 499–535.

(6) Fersht, A. R. From the First Protein Structures to Our Current Knowledge of Protein Folding: Delights and Scepticisms. *Nat. Rev. Mol. Cell Biol.* **2008**, *9* (8), 650–654.

(7) Englander, S. W.; Mayne, L. The Nature of Protein Folding Pathways. *Proc. Natl. Acad. Sci. U. S. A.* **2014**, *111* (45), 15873–15880.

(8) Dill, K. A.; Ozkan, S. B.; Shell, M. S.; Weikl, T. R. The Protein Folding Problem. *Annu. Rev. Biophys.* **2008**, *37* (1), 289–316.

(9) Zhou, M.; Sandercock, A. M.; Fraser, C. S.; Ridlova, G.; Stephens, E.; Schenauer, M. R.; Yokoi-Fong, T.; Barsky, D.; Leary, J. A.; Hershey, J. W.; et al. Mass Spectrometry Reveals Modularity and a Complete Subunit Interaction Map of the Eukaryotic Translation Factor eIF3. *Proc. Natl. Acad. Sci. U. S. A.* **2008**, *105*, 18139–18144.

(10) Heck, A. J. R. Native Mass Spectrometry: A Bridge between Interactomics and Structural Biology. *Nat. Methods* **2008**, *5* (11), 927–933.

(11) Hilton, G. R.; Benesch, J. L. P. Two Decades of Studying Non-Covalent Biomolecular Assemblies by Means of Electrospray Ionization Mass Spectrometry. *J. R. Soc. Interface* **2012**, *9* (70), 801–816.

(12) Cassady, C. J.; Wronka, J.; Kruppa, G. H.; Laukien, F. H.; Hettich, R. Deprotonation Reactions of Multiply Protonated Ubiquitin Ions. *Rapid Commun. Mass Spectrom.* **1994**, *8* (5), 394–400.

(13) Schnier, P. D.; Gross, D. S.; Williams, E. R. Electrostatic Forces and Dielectric Polarizability of Multiply Protonated Gas-Phase Cytochrome c Ions Probed by Ion/Molecule Chemistry. *J. Am. Chem. Soc.* **1995**, *117* (25), 6747–6757.

(14) Cassady, C. J.; Carr, S. R. Elucidation of Isomeric Structures for Ubiquitin [M+12H]12+ Ions Produced by Electrospray Ionization Mass Spectrometry. *J. Mass Spectrom.* **1996**, *31* (3), 247–254.

(15) Valentine, S. J.; Counterman, A. E.; Clemmer, D. E. Conformer-Dependent Proton-Transfer Reactions of Ubiquitin Ions. *J. Am. Soc. Mass Spectrom.* **1997**, *8* (9), 954–961.

(16) Winger, B. E.; Light-Wahl, K. J.; Rockwood, A. L.; Smith, R. D. Probing Qualitative Conformation Differences of Multiply Protonated Gas-Phase Proteins via Hydrogen/Deuterium Isotopic Exchange with Water-d2. *J. Am. Chem. Soc.* **1992**, *114* (14), 5897–5898.

(17) Wood, T. D.; Chorush, R. A.; Wampler, F. M.; Little, D. P.; O'Connor, P. B.; McLafferty, F. W. Gas-Phase Folding and Unfolding of Cytochrome c Cations. *Proc. Natl. Acad. Sci. U. S. A.* **1995**, *92* (7), 2451–2454.
(18) Valentine, S. J.; Clemmer, D. E. H/D Exchange Levels of Shape-Resolved Cytochrome c Conformers in the Gas Phase. *J. Am. Chem. Soc.* **1997**, *119* (15), 3558–3566.
(19) Breuker, K.; McLafferty, F. W. Stepwise Evolution of Protein Native Structure with Electrospray into the Gas Phase, 10- 12 to 102 S. *Proc. Natl. Acad. Sci. U. S. A.* **2008**, *105* (47), 18145.
(20) Bohrer, B. C.; Atlasevich, N.; Clemmer, D. E. Transitions between Elongated Conformations of Ubiquitin [M+11H]11+ Enhance Hydrogen/Deuterium Exchange. *J. Phys. Chem. B* **2011**, *115* (15), 4509–4515.
(21) Breuker, K.; Oh, H.; Horn, D. M.; Cerda, B. A.; McLafferty, F. W. Detailed Unfolding and Folding of Gaseous Ubiquitin Ions Characterized by Electron Capture Dissociation. *J. Am. Chem. Soc.* **2002**, *124* (22), 6407–6420.
(22) Lermyte, F.; Williams, J. P.; Brown, J. M.; Martin, E. M.; Sobott, F. Extensive Charge Reduction and Dissociation of Intact Protein Complexes Following Electron Transfer on a Quadrupole-Ion Mobility-Time-of-Flight MS. *J. Am. Soc. Mass Spectrom.* **2015**, *26* (7), 1068–1076.
(23) Harvey, S. R.; Porrini, M.; Tyler, R. C.; MacPhee, C. E.; Volkman, B. F.; Barran, P. E. Electron Capture Dissociation and Drift Tube Ion Mobility-Mass Spectrometry Coupled with Site Directed Mutations Provide Insights into the Conformational Diversity of a Metamorphic Protein. *Phys. Chem. Chem. Phys.* **2015**, *17* (16), 10538–10550.
(24) Woenckhaus, J.; Mao, Y.; Jarrold, M. F. Hydration of Gas Phase Proteins: Folded +5 and Unfolded +7 Charge States of Cytochrome c. *J. Phys. Chem. B* **1997**, *101* (6), 847–851.
(25) Myung, S.; Badman, E. R.; Lee, Y. J.; Clemmer, D. E. Structural Transitions of Electrosprayed Ubiquitin Ions Stored in an Ion Trap over ~10 Ms to 30 S†. *J. Phys. Chem. A* **2002**, *106* (42), 9976–9982.
(26) Badman, E. R.; Myung, S.; Clemmer, D. E. Evidence for Unfolding and Refolding of Gas-Phase Cytochrome c Ions in a Paul Trap. *J. Am. Soc. Mass Spectrom.* **2005**, *16* (9), 1493–1497.
(27) Bohrer, B. C.; Merenbloom, S. I.; Koeniger, S. L.; Hilderbrand, A. E.; Clemmer, D. E. Biomolecule Analysis by Ion Mobility Spectrometry. *Annu. Rev. Anal. Chem.* **2008**, *1* (1), 293–327.
(28) Morrison, L. J.; Wysocki, V. H. Gas-Phase Helical Peptides Mimic Solution-Phase Behavior. *J. Am. Chem. Soc.* **2014**, *136* (40), 14173–14183.
(29) Chen, S.-H.; Chen, L.; Russell, D. H. Metal-Induced Conformational Changes of Human Metallothionein-2A: A Combined Theoretical and Experimental Study of Metal-Free and Partially Metalated Intermediates. *J. Am. Chem. Soc.* **2014**, *136* (26), 9499–9508.
(30) Shoemaker, G. K.; van Duijn, E.; Crawford, S. E.; Uetrecht, C.; Baclayon, M.; Roos, W. H.; Wuite, G. J. L.; Estes, M. K.; Prasad, B. V. V.; Heck, A. J. R. Norwalk Virus Assembly and Stability Monitored by Mass Spectrometry. *Mol. Cell. Proteomics* **2010**, *9* (8), 1742–1751.
(31) Wyttenbach, T.; Bowers, M. T. Structural Stability from Solution to the Gas Phase: Native Solution Structure of Ubiquitin Survives Analysis in a Solvent-Free Ion Mobility–Mass Spectrometry Environment. *J. Phys. Chem. B* **2011**, *115* (42), 12266–12275.

(32) Shi, H.; Pierson, N. A.; Valentine, S. J.; Clemmer, D. E. Conformation Types of Ubiquitin [M+8H]8+ Ions from Water:Methanol Solutions: Evidence for the N and A States in Aqueous Solution. *J. Phys. Chem. B* **2012**, *116* (10), 3344–3352.
(33) Shi, H.; Atlasevich, N.; Merenbloom, S. I.; Clemmer, D. E. Solution Dependence of the Collisional Activation of Ubiquitin [M + 7H]7+ Ions. *J. Am. Soc. Mass Spectrom.* **2014**, *25* (12), 2000–2008.
(34) Mason, E. A.; McDaniel, W. *Transport Properties of Ions in Gases*; Wiley, 1988.
(35) Bernstein, S. L.; Dupuis, N. F.; Lazo, N. D.; Wyttenbach, T.; Condron, M. M.; Bitan, G.; Teplow, D. B.; Shea, J.-E.; Ruotolo, B. T.; Robinson, C. V.; et al. Amyloid-β Protein Oligomerization and the Importance of Tetramers and Dodecamers in the Aetiology of Alzheimer's Disease. *Nat. Chem.* **2009**, *1* (4), 326–331.
(36) Jurneczko, E.; Barran, P. E. How Useful Is Ion Mobility Mass Spectrometry for Structural Biology? The Relationship between Protein Crystal Structures and Their Collision Cross Sections in the Gas Phase. *Analyst* **2011**, *136*, 20–28.
(37) Benesch, J. L.; Ruotolo, B. T. Mass Spectrometry: Come of Age for Structural and Dynamical Biology. *Curr. Opin. Struct. Biol.* **2011**, *21* (5), 641–649.
(38) Wyttenbach, T.; Bleiholder, C.; Bowers, M. T. Factors Contributing to the Collision Cross Section of Polyatomic Ions in the Kilodalton to Gigadalton Range: Application to Ion Mobility Measurements. *Anal. Chem.* **2013**, *85* (4), 2191–2199.
(39) Bush, M. F.; Hall, Z.; Giles, K.; Hoyes, J.; Robinson, C. V.; Ruotolo, B. T. Collision Cross Sections of Proteins and Their Complexes: A Calibration Framework and Database for Gas-Phase Structural Biology. *Anal. Chem.* **2010**, *82*, 9557–9565.
(40) Allen, S. J.; Schwartz, A. M.; Bush, M. F. Effects of Polarity on the Structures and Charge States of Native-Like Proteins and Protein Complexes in the Gas Phase. *Anal. Chem.* **2013**, *85* (24), 12055–12061.
(41) Hall, Z.; Politis, A.; Bush, M. F.; Smith, L. J.; Robinson, C. V. Charge-State Dependent Compaction and Dissociation of Protein Complexes: Insights from Ion Mobility and Molecular Dynamics. *J. Am. Chem. Soc.* **2012**, *134* (7), 3429–3438.
(42) Hopper, J. T. S.; Oldham, N. J. Collision Induced Unfolding of Protein Ions in the Gas Phase Studied by Ion Mobility-Mass Spectrometry: The Effect of Ligand Binding on Conformational Stability. *J. Am. Soc. Mass Spectrom.* **2009**, *20* (10), 1851–1858.
(43) Ruotolo, B. T.; Hyung, S.-J.; Robinson, P. M.; Giles, K.; Bateman, R. H.; Robinson, C. V. Ion Mobility–Mass Spectrometry Reveals Long-Lived, Unfolded Intermediates in the Dissociation of Protein Complexes. *Angew. Chem.* **2007**, *119* (42), 8147–8150.
(44) Freeke, J.; Bush, M. F.; Robinson, C. V.; Ruotolo, B. T. Gas-Phase Protein Assemblies: Unfolding Landscapes and Preserving Native-like Structures Using Noncovalent Adducts. *Chem. Phys. Lett.* **2012**, *524*, 1–9.
(45) Liu, F. C.; Kirk, S. R.; Bleiholder, C. On the Structural Denaturation of Biological Analytes in Trapped Ion Mobility Spectrometry – Mass Spectrometry. *Analyst* **2016**, *141*, 3722–3730.
(46) Pierson, N. A.; Chen, L.; Valentine, S. J.; Russell, D. H.; Clemmer, D. E. Number of Solution States of Bradykinin from Ion Mobility and Mass Spectrometry Measurements. *J. Am. Chem. Soc.* **2011**, *133* (35), 13810–13813.
(47) Koeniger, S. L.; Merenbloom, S. I.; Valentine, S. J.; Jarrold, M. F.; Udseth, H. R.; Smith, R. D.; Clemmer, D. E. An IMS−IMS Analogue of MS−MS. *Anal. Chem.* **2006**, *78* (12), 4161–4174.

(48) Merenbloom, S. I.; Koeniger, S. L.; Valentine, S. J.; Plasencia, M. D.; Clemmer, D. E. IMS−IMS and IMS−IMS−IMS/MS for Separating Peptide and Protein Fragment Ions. *Anal. Chem.* **2006**, *78* (8), 2802–2809.
(49) Pierson, N. A.; Valentine, S. J.; Clemmer, D. E. Evidence for a Quasi-Equilibrium Distribution of States for Bradykinin [M + 3H]3+ Ions in the Gas Phase. *J. Phys. Chem. B* **2010**, *114* (23), 7777–7783.
(50) Pierson, N. A.; Clemmer, D. E. An IMS–IMS Threshold Method for Semi-Quantitative Determination of Activation Barriers: Interconversion of Proline Cis ↔ Trans Forms in Triply Protonated Bradykinin. *Int. J. Mass Spectrom.* **2015**, *377*, 646–654.
(51) Hilton, G. R.; Thalassinos, K.; Grabenauer, M.; Sanghera, N.; Slade, S. E.; Wyttenbach, T.; Robinson, P. J.; Pinheiro, T. J. T.; Bowers, M. T.; Scrivens, J. H. Structural Analysis of Prion Proteins by Means of Drift Cell and Traveling Wave Ion Mobility Mass Spectrometry. *J. Am. Soc. Mass Spectrom.* **2010**, *21* (5), 845–854.
(52) Beveridge, R.; Covill, S.; Pacholarz, K. J.; Kalapothakis, J. M. D.; MacPhee, C. E.; Barran, P. E. A Mass-Spectrometry-Based Framework To Define the Extent of Disorder in Proteins. *Anal. Chem.* **2014**, *86* (22), 10979–10991.
(53) Clemmer, D. E.; Hudgins, R. R.; Jarrold, M. F. Naked Protein Conformations: Cytochrome c in the Gas Phase. *J. Am. Chem. Soc.* **1995**, *117* (40), 10141–10142.
(54) Faull, P. A.; Korkeila, K. E.; Kalapothakis, J. M.; Gray, A.; McCullough, B. J.; Barran, P. E. Gas-Phase Metalloprotein Complexes Interrogated by Ion Mobility-Mass Spectrometry. *Int. J. Mass Spectrom.* **2009**, *283* (1–3), 140–148.
(55) Hogan, C. J.; Ruotolo, B. T.; Robinson, C. V.; Fernandez de la Mora, J. Tandem Differential Mobility Analysis-Mass Spectrometry Reveals Partial Gas-Phase Collapse of the GroEL Complex. *J. Phys. Chem. B* **2011**, *115* (13), 3614–3621.
(56) McLuckey, S. A.; Goeringer, D. E. Ion/Molecule Reactions for Improved Effective Mass Resolution in Electrospray Mass Spectrometry. *Anal. Chem.* **1995**, *67* (14), 2493–2497.
(57) Shelimov, K. B.; Jarrold, M. F. "Denaturation" and Refolding of Cytochrome c in Vacuo. *J. Am. Chem. Soc.* **1996**, *118* (42), 10313–10314.
(58) Shelimov, K. B.; Jarrold, M. F. Conformations, Unfolding, and Refolding of Apomyoglobin in Vacuum: An Activation Barrier for Gas-Phase Protein Folding. *J. Am. Chem. Soc.* **1997**, *119* (13), 2987–2994.
(59) McLuckey, S. A.; Stephenson, J. L.; Asano, K. G. Ion/Ion Proton-Transfer Kinetics: Implications for Analysis of Ions Derived from Electrospray of Protein Mixtures. *Anal. Chem.* **1998**, *70* (6), 1198–1202.
(60) McLuckey, S. A.; Stephenson, J. L. Ion/Ion Chemistry of High-Mass Multiply Charged Ions. *Mass Spectrom. Rev.* **1998**, *17* (6), 369–407.
(61) Pitteri, S. J.; McLuckey, S. A. Recent Developments in the Ion/Ion Chemistry of High-Mass Multiply Charged Ions. *Mass Spectrom. Rev.* **2005**, *24* (6), 931–958.
(62) Laszlo, K. J.; Bush, M. F. Analysis of Native-Like Proteins and Protein Complexes Using Cation to Anion Proton Transfer Reactions (CAPTR). *J. Am. Soc. Mass Spectrom.* **2015**, *26*, 2152–2161.
(63) Stephenson Jr, J. L.; Van Berkel, G. J.; McLuckey, S. A. Ion-Ion Proton Transfer Reactions of Bio-Ions Involving Noncovalent Interactions: Holomyoglobin. *J. Am. Soc. Mass Spectrom.* **1997**, *8* (6), 637–644.

(64) Zhang, H.; Cui, W.; Wen, J.; Blankenship, R. E.; Gross, M. L. Native Electrospray and Electron-Capture Dissociation FTICR Mass Spectrometry for Top-Down Studies of Protein Assemblies. *Anal. Chem.* **2011**, *83* (14), 5598–5606.
(65) Lermyte, F.; Konijnenberg, A.; Williams, J. P.; Brown, J. M.; Valkenborg, D.; Sobott, F. ETD Allows for Native Surface Mapping of a 150 kDa Noncovalent Complex on a Commercial Q-TWIMS-TOF Instrument. *J. Am. Soc. Mass Spectrom.* **2014**, *25* (3), 343–350.
(66) Williams, J. P.; Brown, J. M.; Campuzano, I.; Sadler, P. J. Identifying Drug Metallation Sites on Peptides Using Electron Transfer Dissociation (ETD), Collision Induced Dissociation (CID) and Ion Mobility-Mass Spectrometry (IM-MS). *Chem. Commun.* **2010**, *46* (30), 5458–5460.
(67) Allen, S.; Giles, K.; Golbert, T.; Bush, M. Ion Mobility Mass Spectrometry of Peptide, Protein, and Protein Complex Ions Using a Radio-Frequency Confining Drift Cell. *Analyst* **2016**, *141*, 884–891.
(68) Stephenson, J. L.; McLuckey, S. A. Ion/Ion Proton Transfer Reactions for Protein Mixture Analysis. *Anal. Chem.* **1996**, *68* (22), 4026–4032.
(69) Ruotolo, B. T.; Benesch, J. L.; Sandercock, A. M.; Hyung, S. J.; Robinson, C. V. Ion Mobility-Mass Spectrometry Analysis of Large Protein Complexes. *Nat Protoc* **2008**, *3*, 1139–1152.
(70) Koeniger, S. L.; Merenbloom, S. I.; Clemmer, D. E. Evidence for Many Resolvable Structures within Conformation Types of Electrosprayed Ubiquitin Ions. *J. Phys. Chem. B* **2006**, *110* (13), 7017–7021.
(71) Salbo, R.; Bush, M. F.; Naver, H.; Campuzano, I.; Robinson, C. V.; Pettersson, I.; Jørgensen, T. J. D.; Haselmann, K. F. Traveling-Wave Ion Mobility Mass Spectrometry of Protein Complexes: Accurate Calibrated Collision Cross-Sections of Human Insulin Oligomers. *Rapid Commun. Mass Spectrom.* **2012**, *26* (10), 1181–1193.
(72) Zhao, Q.; Schieffer, G. M.; Soyk, M. W.; Anderson, T. J.; Houk, R. S.; Badman, E. R. Effects of Ion/Ion Proton Transfer Reactions on Conformation of Gas-Phase Cytochrome c Ions. *J. Am. Soc. Mass Spectrom.* **2010**, *21* (7), 1208–1217.
(73) Zhao, Q.; Soyk, M. W.; Schieffer, G. M.; Fuhrer, K.; Gonin, M. M.; Houk, R. S.; Badman, E. R. An Ion Trap-Ion Mobility-Time of Flight Mass Spectrometer with Three Ion Sources for Ion/Ion Reactions. *J. Am. Soc. Mass Spectrom.* **2009**, *20* (8), 1549–1561.
(74) Piana, S.; Lindorff-Larsen, K.; Shaw, D. E. Atomic-Level Description of Ubiquitin Folding. *Proc. Natl. Acad. Sci. U. S. A.* **2013**, *110* (15), 5915–5920.

Chapter 4. Native-like and Denatured Cytochrome *c* Ions Yield Cation-to-Anion Proton-Transfer Reaction Products with Similar Collision Cross Sections

---

This chapter is reproduced with permission from Laszlo, K. J.; Buckner J. H.; Munger, E.B.; Bush, M.F.; "Native-Like and Denatured Cytochrome c Ions Yield Cation-to-Anion Proton Transfer Reaction Products with Similar Collision Cross-Sections." *Journal of The American Society for Mass Spectrometry*, **2017**, doi:10.1007/s13361-017-1620-4.

4.1 Abstract

The relationship between structures of protein ions, their charge states, and their original structures prior to ionization remains challenging to decouple. Here, we use cation-to-anion proton-transfer reactions (CAPTR) to reduce the charge states of cytochrome *c* ions in the gas phase and ion mobility to probe their structures. Ions were formed using a new temperature-controlled, nanoelectrospray ionization source at 25 °C. Characterization of this source demonstrates that the temperature of the liquid sample is decoupled from that of the atmospheric-pressure interface, which is heated during CAPTR experiments. Ionization from denaturing conditions yields 18+ to 8+ ions, which were each isolated and reacted with monoanions to generate all CAPTR products with charge states of at least 3+. The highest, intermediate, and lowest charge-state products exhibit collision cross section distributions that are unimodal, multimodal, and unimodal, respectively. These distributions depend strongly on the charge state of the product, although those for the intermediate charge-state products also depend on that of the precursor. The distributions of the 3+ products are all similar, with averages that are less than

half that of the 18+ precursor ions. Ionization of cytochrome *c* from native-like conditions yields 7+ and 6+ ions. The 3+ CAPTR products from these precursors have slightly more compact collision cross section distributions that are indistinguishable from those for the 3+ CAPTR products from denaturing conditions. More broadly, these results indicate that the collision cross sections of ions of this single domain protein depend strongly on charge state for charge states greater than ~4.

4.2 Introduction

Ion mobility (IM), mass spectrometry (MS), and allied methods have emerged as powerful tools for characterizing the structures of biological molecules and their noncovalent complexes [1–4]. IM separates ions in a neutral gas based primarily on their charge and shape, which can be quantified by determining the collision cross section (Ω) of the ion-neutral pair [5]. For example, Ω of complexes that contain 18, 40, 60, and 80 copies of the capsid protein of norovirus are consistent with sheet-like intermediates that are capable of forming capsids, rather than assembly-incompetent aggregates [6]. These approaches can also be extended to study unfolded states, intermediates, and other forms of structural heterogeneity [7]. For example, IM spectra of $[Pro_{13} + 2H]^{2+}$ ions generated from a sample that was transferred from mostly propanol to mostly water exhibit a total of eight features with different Ω whose abundances depend on time since solvent transfer [8]. The time-dependence of the IM results is strongly correlated with that for an orthogonal analysis using capillary electrophoresis, which suggests that both experiments are sensitive to the same structural transitions in solution [9].

Despite the effort and progress in using gas-phase measurements to probe the structures of biological molecules in solution, a robust understanding of the relationship between the charge

state of the gas-phase ion, the structure of the gas-phase ion, and the original structure in solution remains elusive. Electrospray ionization of large, globular proteins and protein complexes typically yields ions that have a relatively narrow range of charge states, relative to their denatured counterparts. The Ω of those ions can depend weakly on charge state [10–13] and polarity [12], but the range of Ω values for each analyte usually exceeds the precision of those measurements. Electrospray ionization of proteins from acidic, denaturing solutions [14–16], as well as prion [17] and intrinsically disordered [18] proteins from neutral, aqueous solutions, yields ions with a broad range of charges states and whose Ω depend strongly on their charge state. An improved understanding of the phenomena underlying these observations is important for maximizing the structural information that can be drawn from IM experiments. Two of the ongoing challenges include (1) the relationship between the structure(s) in solution and the resulting charge-state distribution after ionization [12,19] and (2) the extent to which structure(s) in solution are retained or evolve in the corresponding gas-phase ions [20,21].

One strategy to probe the relationship between the structures and charge states of protein ions is to manipulate their charge states in the gas phase. For example, in ion/neutral proton-transfer reactions a multiply charged precursor cation is reacted with a neutral molecule, A, which has a higher gas-phase basicity [22,23]:

$$[M + zH]^{z+} + A \rightarrow [M + (z-1)H]^{(z-1)+} + AH^{+} \qquad \text{(Reaction 1)}$$

Foundational results combining ion/neutral proton-transfer reactions in tandem with IM-MS showed that mixtures of protein ions that have high-charge states and unfolded structures can yield product ions that have lower charge states and partially folded structures [24]. Alternatively, the charge states of multiply charged protein cations can be reduced using ion/ion proton-transfer reactions with monoanions:

$$[M + zH]^{z+} + A^- \rightarrow [M + (z-1)H]^{(z-1)+} + AH \qquad \text{(Reaction 2)}$$

Relative to ion/neutral reactions, ion/ion reactions benefit from more favorable kinetics and thermodynamics [25–27]. Ion/ion proton-transfer reactions were pioneered by McLuckey and coworkers [26,27], who perform these reactions under pseudo first-order kinetics with effectively constant anion abundance [26–28]. Recently, we reported an approach that we refer to as cation-to-anion proton-transfer reactions (CAPTR) [29], in which the abundance of anions depletes during individual experiments and as a result a wide range of product ion charge states are formed from different numbers of sequential proton-transfer events [29]. Electron transfer can also be used to reduce the charge states of protein ions (electron transfer no dissociation) [30], but electron transfer can also result in bond cleavage [31,32].

Recently, we reported the analysis of the CAPTR products of *m*/*z*-selected ions of denatured ubiquitin [33]. In those experiments, each subsequent CAPTR event resulted in the formation of a charge-reduced product ion that had a more compact Ω. The Ω of the CAPTR product ions depended on their charge state, and were independent of the charge state of the precursor ion. One particularly interesting observation from that work was that the lowest-charge-state product ion observed (3+) exhibited a Ω similar to that determined experimentally for native-like ions of ubiquitin [34,35] and determined computationally for an energy-minimized version of an NMR structure [35]. One limitation of that work was that Ω of some precursor ions depended on the temperature of the MS interface, which is heated during CAPTR experiments to prevent the buildup of byproducts of glow-discharge ionization on electrodes in the atmospheric-pressure interface. Those changes in Ω were attributed to heat transfer from the MS interface to the sample capillary [33].

Here we use IM-MS to characterize the CAPTR products of ions of cytochrome *c*, which is a single domain protein bound to a heme prosthetic group. Ions were formed using a new temperature-controlled, nanoelectrospray ionization source, which enables independent temperature control of the sample capillary and MS interface. In these experiments, the sample capillary was set to 25 °C, and ions of cytochrome *c* were generated from either denaturing or native-like conditions. These results show that the CAPTR product ions with the lowest charge state (3+) all have similar Ω distributions, regardless of the Ω distribution of the precursor ion or whether the precursors were formed from denaturing or native-like conditions.

4.3 Methods

4.3.1 *Samples and ionization.*

Cytochrome *c* from equine heart (Sigma-Aldrich, St. Louis, MO) was dissolved into either a denaturing solution of 70:30 water:methanol with 0.1% trifluoroacetic acid at pH 2 (denaturing conditions) or 200 mM aqueous ammonium acetate at pH 7 (native-like conditions). Ubiquitin (Boston Biochem, Cambridge, MA) was prepared using denaturing conditions. All cations were generated by electrokinetic nanoelectrospray ionization from borosilicate glass capillaries that were pulled to a 1 to 3 μm tip on one end using a Sutter Instruments Model P-97 micropipette puller (Novato, CA) [36].

For most experiments, the sample capillary was held at 25 ˚C using a new temperature-controlled, nanoelectrospray ionization source, which decouples the temperatures of the sample and the atmospheric-pressure interface. This source will be referred to as the "temperature-controlled source" and is shown in Figure 4.1. The sample capillary was positioned between three layers of thermally conductive and electrically insulating silicone elastomer (3M 5592 and

5591S, St. Paul, MN) that are each 1 mm thick. A platinum wire was inserted into the wide end of a capillary to apply a voltage to the solution for electrospray (Figure 4.1b). The thermally conductive elastomer layers and sample capillary were placed on top of a Peltier device (Laird Technologies 430126-503, Milpitas, CA), which moves heat between the elastomer and a ¼" by 1" by 12" bar of copper. The copper bar exchanges heat with a heat sink (Cooler Master Hyper T2, New Taipei City, Taiwan). The copper bar was then inserted into a nylon sleeve placed on top of an aluminum bracket, which was attached to a three-dimensional translational stage (Physik Instrumente, Karlsruhe, Germany). All thermal connections were made using thermal paste (TE Technologies TC-1). The temperature of the Peltier is monitored using a thermistor (TE Technologies MP-3193) placed on top of the Peltier device and next to the capillary (Figure 4.1b). Based on the thermistor temperature, the voltage supplied to the Peltier device is adjusted by a controller (TE Technologies TC-48-20 OEM). Selected experiments, as indicated, used the Waters NanoLockSpray source and the nanoelectrospray ionization glass capillary assembly (M955213AC1-S), which will be referred to as the "original source." This assembly holds the capillary near the atmospheric-pressure interface and does not have temperature control. Photographs of both sources are shown in Figure S1.

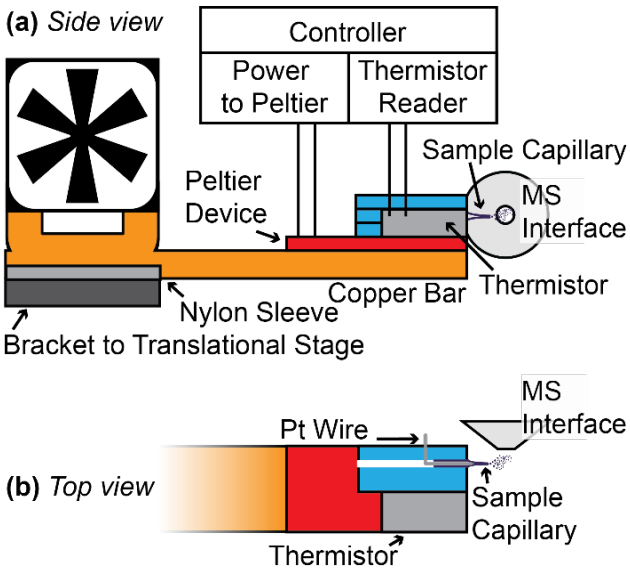

Figure 4.1. Diagram of the temperature-controlled, nanoelectrospray ionization source. (a) Side view of the source. The sample capillary is held between three layers of electrically insulating and thermally conductive elastomer placed on top of a Peltier device. Heat is moved between the sample side of the Peltier device and a copper bar, which exchanges heat with the atmosphere via a heat sink supplied with forced air by a fan. The Peltier device is controlled by a TE Technologies TC-48-20 OEM controller, based on the temperature measured using the thermistor. (b) Top-down view of the temperature-controlled source, with the top layer of thermally conductive elastomer removed to expose the sample capillary and platinum wire electrode.

4.3.2 *CAPTR and IM-MS experiments.*

All experiments were performed on a Waters Synapt G2 HDMS instrument equipped with a radio-frequency (rf) confining ion mobility drift cell [37] and ion/ion reaction capabilities [38]. CAPTR was performed as described previously [33]. Briefly, for 0.1 s the $[M\text{-}F]^-$ fragments of

perfluoro-1,3-dimethylcyclohexane (PDCH) were produced, quadrupole selected, and accumulated in the Trap Cell of the instrument. $[PDCH-F]^-$ reacts exclusively through proton transfer (Reaction 2) [29,39,40]. Following anion accumulation, the instrument was switched into positive mode for 5 to 10 s, during which time a single charge state of cytochrome *c* was quadrupole selected and transferred into the Trap Cell for CAPTR. Every 22 ms, CAPTR products and unreacted precursor ions were injected into the rf-confining drift cell [37] with a 212 V drift voltage and filled with 2.0 mbar helium. Based on the measured arrival-time distributions, the apparent Ω distributions were calculated using a method described in the Electronic Supplementary Material that is identical to that used previously for the CAPTR products of denatured ubiquitin [33].

4.3.3 *Calculated Ω.*

For the native model, Chimera [41] was used to add missing side-chain and hydrogen atoms to an x-ray crystal structure of cytochrome *c* (PDB: 1HRC [42]). The linear and α-helical models lack the heme group and were built using Chimera and the expected dihedral angles. Ω values were calculated using the projection approximation (PA) [43] and the exact hard-sphere scattering approximation (EHSS) [44] as implemented in EHSS2/k [45]. These approximations and their relationship to momentum transfer in IM have been discussed elsewhere [5,44].

4.4 Results

Previously, we reported the analysis of the CAPTR products of *m*/*z*-selected ions of ubiquitin from denaturing conditions [33]. The Ω values of the CAPTR product ions depended strongly on the charge state of the product ion. Furthermore, the Ω of the lowest charged state

product ions were similar to those for native-like ions of ubiquitin, implying that although the CAPTR product ions had folded in the gas-phase, they had a similar size to the native-like structure of ubiquitin in the gas phase. One limitation of those experiments was that Ω of the precursor ions depended on the temperature of the atmospheric-pressure interface to the mass spectrometer. In order to decouple the temperature of the interface and the liquid sample, we developed a new temperature-controlled, nanoelectrospray ionization source. Using that source, we generated ions of cytochrome *c* from both denaturing and native-like conditions, which were *m*/*z* selected prior to CAPTR and IM-MS analysis. These results provide detailed insights into how protein ions from denaturing and native-like conditions respond to changes in their charge state.

4.4.1 *Effect of the temperature of the atmospheric-pressure interface on the temperature of the sample.*

Anions for these ion/ion chemistry experiments are generated using glow-discharge ionization performed immediately after the sample cone, which is also used to transfer analyte cations from atmospheric pressure to vacuum. During these experiments, this region (the "MS interface") is resistively heated to 120 °C to minimize the buildup of byproducts of glow-discharge ionization on the interface electrodes. Previously, we reported that the Ω distributions of denatured 7+ ubiquitin using the original source depended on the temperature of the MS interface [33]. Those results are replotted in Figure 4.2a. At ambient temperature, the Ω distribution was bimodal with features centered around 13 and 15 nm^2. However, when the interface temperature was increased to 40 ˚C, the distribution shifted to a single feature centered near 15 nm^2. The latter distribution persisted as the temperature of the MS interface was increased to 120 ˚C.

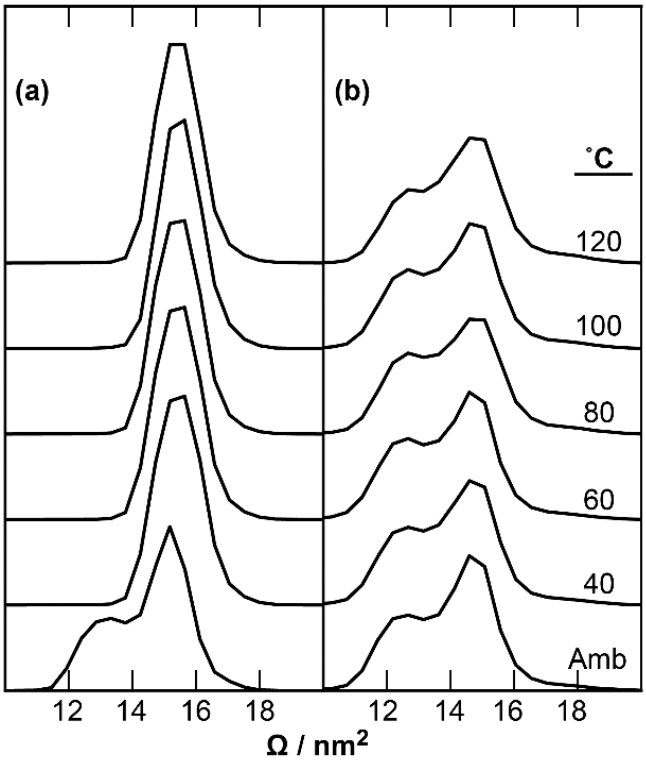

Figure 4.2. Ω distributions of 7+ ubiquitin from denaturing conditions determined as a function of the temperature of the MS interface using (a) the original source and (b) the new temperature-controlled source with the Peltier device held at 25 °C. The Ω distributions in (a) were reported previously [33]. The Ω distributions under ambient conditions in (b) are ~0.5 nm^2 more compact than those in (a), which may be due to systematic differences between the two sets of IM experiments.

In order to characterize how the temperature of the MS interface affects the temperature of samples in the original source, we positioned a thermocouple inside a sample capillary containing deionized water. Temperature measurements were made using the conditions used for

CAPTR experiments, but without a platinum wire electrode. Figure 4.3a shows the temperature measured inside of a capillary as a function of the temperature of the MS interface (*black triangles*). Using the original source, the temperature of the sample depends strongly on the temperature of the MS interface, which is consistent with the convective heat transfer. As the interface temperature increases from 28 to 120 ˚C, the temperature of the sample in the original source increases from 27 to 48 ˚C, which may induce thermal melting of proteins in solution.

4.4.2 *Performance of the temperature-controlled source.*

In order to control the temperature of samples prior to ionization, we constructed a temperature-controlled source that is described in the *Methods,* shown using a diagram in Figure 4.1, and shown using photographs in Figure S1. Figure 4.3a also shows the temperature of samples using the temperature-controlled source as a function of the temperature of the MS interface and the Peltier device (*colored circles*). Unlike those of the original source, the temperature of the sample in the temperature-controlled source is independent of the temperature of the MS interface.

Figure 4.3b shows the temperature of the sample as a function of the temperature of the Peltier device, using interface temperatures of 28, 60, and 120 ˚C. As indicated in Figure 4.3a, the temperature in the capillary depends strongly on the temperature of the Peltier device and is independent of that of the MS interface. Figure S2 shows that the differences between the temperatures of the Peltier device and the sample capillary are less than 1 ˚C for Peltier device temperatures from 20 to 30 ˚C and all MS-interface temperatures. Over the full range of Peltier device temperatures of 5 to 70 ˚C, the magnitude of the differences between the set temperatures of the Peltier device and the sample capillary span from +2 to −3 ˚C with increasing temperature.

These small differences are consistent with inefficient heat transfer between the sample and the Peltier device.

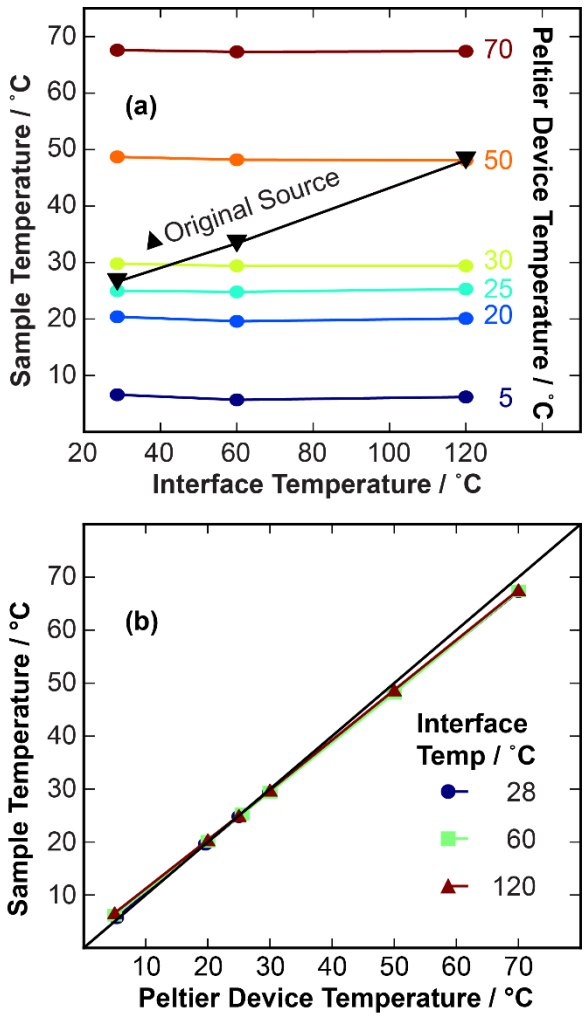

Figure 4.3. (a) Sample temperature measured with a thermocouple probe (Omega TT-T-40, Norwalk, CT) placed inside a capillary containing deionized water using the original source (*black triangles*) and using the temperature-controlled source (*colored circles*) as a function of the measured temperature of the MS interface. For the temperature-controlled source, measurements were also made for a series of set temperature for the Peltier device. (b) Results obtained

using the temperature-controlled source from (a), plotted as a function of the set temperature of the Peltier device. The black line indicates when the temperatures of the Peltier device and sample are equal.

Several approaches for controlling the temperature of samples for nanoelectrospray ionization have been reported, including the use of forced air in proximity to the sample capillary [46,47] or flowing the sample through a temperature-controlled device [48]. The present implementation is most similar to those reported by Robinson and coworkers [49] and later by Heeren and coworkers [50], in which a gold-plated sample capillary was enclosed in a stainless-steel capillary sleeve. The capillary sleeve was in thermal and electrical contact with the gold-plated capillary, which was electrically biased to provide the electrospray potential and was in thermal contact with the Peltier device. The present design uses thermally conductive and electrically insulating elastomer to establish thermal contact with the capillary, and a separate platinum wire inserted into the capillary to provide the electrospray potential. This approach provides a facile solution to ensuring independent thermal and electrical contact with the sample.

In order to further evaluate this temperature-controlled source, we measured the Ω distributions of 7+ ubiquitin from a denaturing solution as a function of the temperature of the interface using a Peltier-device temperature of 25 ˚C (Figure 4.2b). With the interface at ambient temperature, the Ω distribution is bimodal and similar to that measured using that interface temperature and the original source (bottom distribution in Figure 4.2a). As the interface temperature was increased up to 120 ˚C, the more compact feature centered around 12 nm^2 persists at approximately the same relative intensity. The retention of the compact form of 7+ ubiquitin ions when using an interface temperature of 120 ˚C suggests that the elevated interface

temperature for CAPTR is decoupled from the remainder of the experiment when using this temperature-controlled source. Note that controlling the temperature of the sample does not preclude structural isomerization in the gas phase aided by elevated gas temperatures in the interface, although no evidence for that was observed here.

Ω of cytochrome c *ions*. Using the temperature-controlled source and denaturing conditions, we first measured the arrival-time distributions of cytochrome *c* ions generated directly using nanoelectrospray as a function of *z*. Using the procedure described in the Electronic Supplementary Material, we converted the measured arrival-time distributions to apparent Ω distributions. We then calculated critical Ω values that correspond to 10%, 50%, and 90% of the cumulative distribution function (CDF), which is the integral of the apparent Ω distribution with respect to Ω. A representative Ω distribution (*solid black line*), CDF (*red line*), and the corresponding set of critical Ω values (*dashed black lines*) are shown in Figure 4.4a. Those critical Ω values for each ion are represented by the lower bars, middle points, and higher bars in Figure 4.4b, respectively. In agreement with other measurements of Ω for denatured protein ions with helium gas [10,15,51], the Ω values of cytochrome *c* ions from denaturing conditions increase with increasing *z*.

The Ω of cytochrome *c* ions from water/methanol/acetic acid (49/49/2%) [10] and water/acetonitrile/acetic acid (75/25/0-4%) [51] have been reported previously. Compared to the former study [10], the Ω determined here are 0.7% to 3.0% larger. Although these differences are comparable to the absolute errors estimated for rf-confining drift cells [10,37], there may also be contributions from the CDF data analysis used here versus the centroid of the best-fit Gaussian functions used previously. Compared to the latter study [51], the Ω determined here range from

5.5% smaller to 3.4% larger. Those differences may be attributable to some combination of differences in instrumentation, solution conditions, and data analysis.

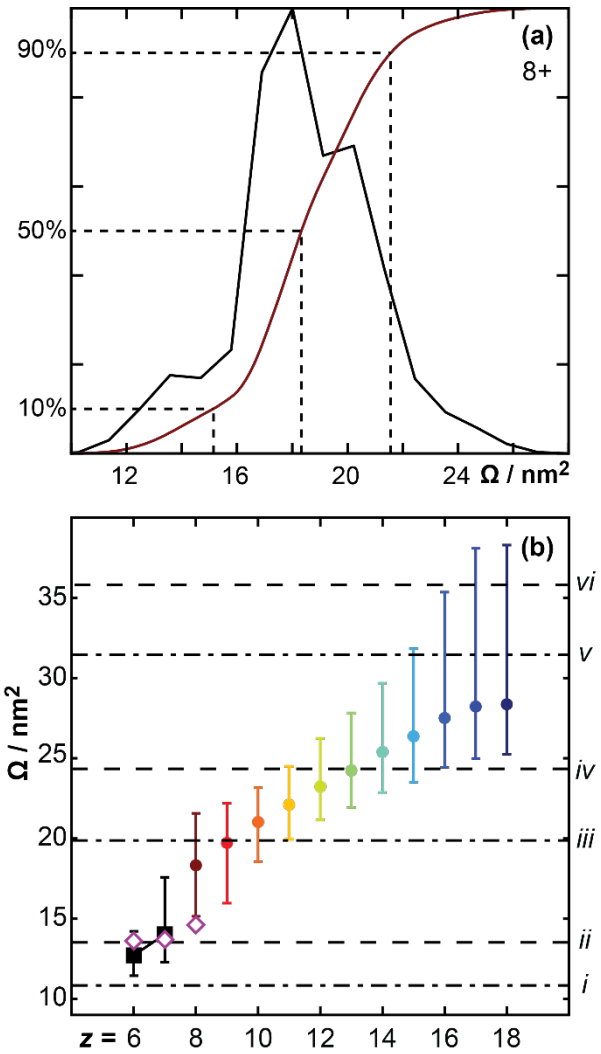

Figure 4.4. (a) Apparent Ω distribution for 8+ cytochrome *c* (*black solid line*) from denaturing conditions, and the corresponding cumulative distribution function (CDF, *red line*), which is the integral of the apparent Ω distribution with respect to Ω. Critical Ω values representing 10%, 50%, and 90% of the CDF are shown using black dashed lines. (b) Critical Ω values for all denatured (*colored circles*) and native-like (*black squares*) ions. Ω values for native-like ions that

were reported previously [12] are shown using *hollow magenta diamonds*. The horizontal dashed black lines correspond to Ω values calculated for models of cytochrome *c* (Table 1).

Using this approach, we also measured the arrival-time distributions of cytochrome *c* ions from 200 mM aqueous ammonium acetate at pH 7 (Figure 4.4b, black squares), which will be referred to as native-like ions. The 50% value of the CDF for the 7+ and 6+ native-like ions are 14.0 and 12.7 nm^2. In comparison to previous results for native-like cytochrome *c* (Figure 4.4b, magenta diamonds [12]), these values are +2.4 and −7.2% different, respectively. The 2.4% difference for the 7+ ions may not be significant, given the absolute errors estimated for rf-confining drift cells [10,37] and differences in data analysis. The −7.2% difference of the 6+ ion reported here is much more compact than observed previously, which may be the result of differences in the ionization and extents of activation in the two experiments. Furthermore, the apparent resolving powers for the ion mobility analysis of native-like ions of cytochrome *c* were previously found to be low relative to other native-like ions [37], which may accentuate differences in data analysis.

The projection approximation (PA) [43] and exact hard-sphere scattering (EHSS) [44,45] Ω for a model of native cytochrome *c* are (*i*) 10.8 and (*ii*) 13.5 nm^2, respectively (Table 5.1). These calculated values bracket the experimental results for native-like cytochrome *c*, consistent with reports that the EHSS method usually overestimates the experimental Ω of native-like ions [52] and that the PA method usually underestimates the experimental Ω of native-like ions [21,52]. Because we do not have structures for non-native forms of cytochrome *c*, we instead built linear and α-helical models that do not contain a heme group. The Ω calculated for these models (*iii* to *vi*)

span a broad range of values. Comparisons between the experimental Ω for cytochrome *c* generated from native-like and denaturing conditions (Figure 4.4b) and the theoretical Ω for models (Table 5.1) indicate that these experiments probe a diverse set of structures, from those that are compact and comparable in size to the native structure to those that are extremely extended and have minimal interactions between neighboring amino acids.

Table 4.1. Ω values calculated for models of cytochrome *c*.

	Model	**Method**	**Ω / nm^2**
i	native	PA	10.8
ii		EHSS	13.5
iii	α-helix	PA	19.9
iv		EHSS	24.3
v	linear strand	PA	31.4
vi		EHSS	35.8

4.4.3 *CAPTR of cytochrome c ions from denaturing conditions.*

The precursor ions generated using denaturing conditions were each *m*/*z* selected and subjected to CAPTR. For the remainder of the discussion, the CAPTR product ions will be referred to as "*P*→*C*", where *P* and *C* are the charge states of the precursor and product ions, respectively. Figure 4.5a shows the Ω distributions of the 18→*C* ions from denaturing conditions, which are also reproduced in Figure S3a. The Ω of the 18→*C* ions decrease with decreasing charge. From *C* = 18 to 3, there is over a 50% compaction in Ω, which is consistent with the product ions folding to form additional intramolecular interactions as charge is removed.

The Ω distributions of the highest-*C* (18 to 11) and lowest-C (4 and 3) products (Figure 4.5a) are qualitatively unimodal, *i.e.*, they exhibit a single local maximum and are relatively symmetric. Note that unimodal Ω distributions may be the result of ensembles of ions with closely related structures or more complex structural distributions with similar Ω. In contrast, the intermediate *C* products (9 to 5) exhibit multimodal Ω distributions, *i.e*, exhibit multiple local maxima and/or greater asymmetry that are consistent with greater structural diversity.

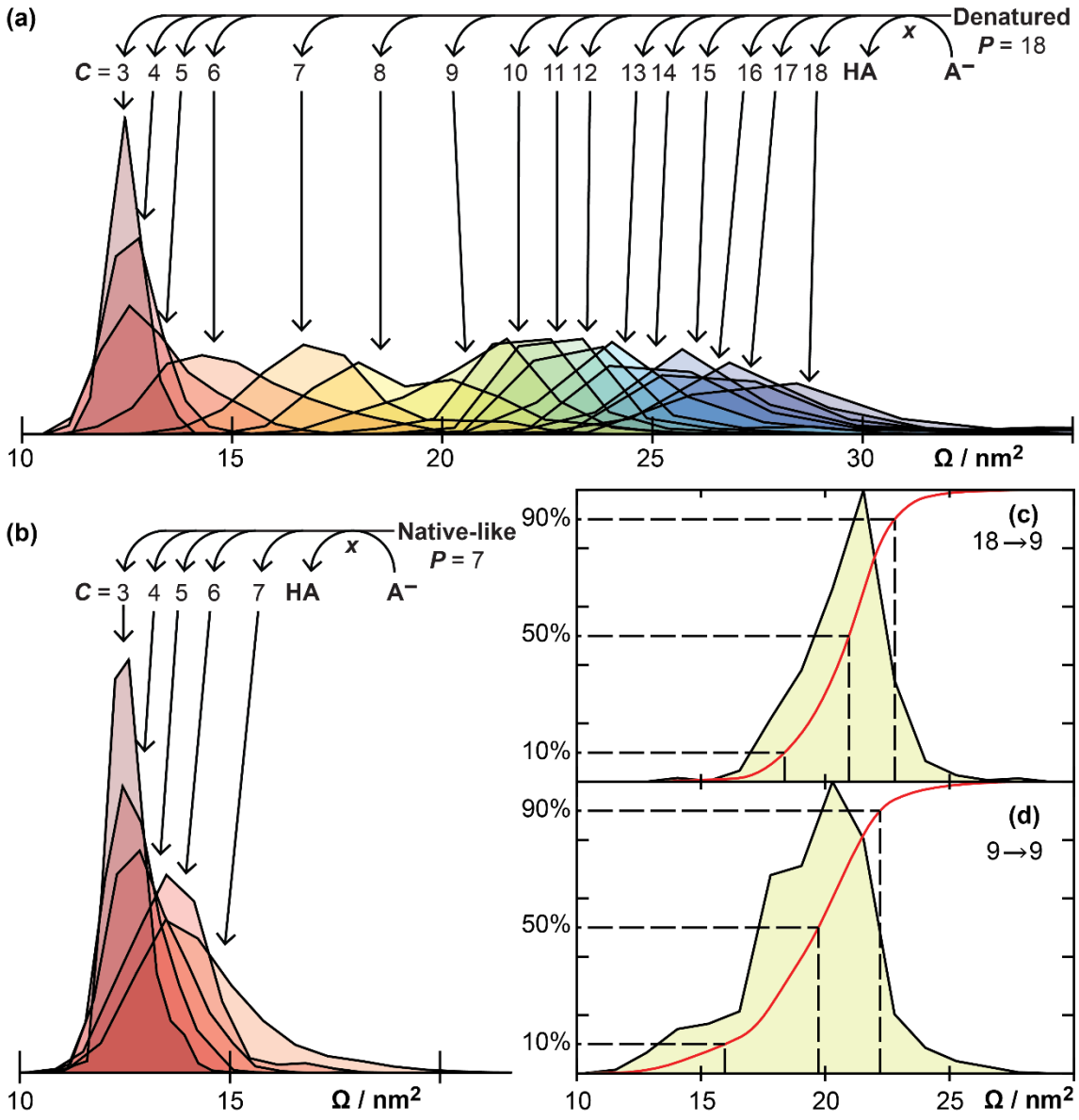

Figure 4.5. (a) Apparent Ω distributions for all 18→*C* ions of cytochrome *c* from denaturing conditions. (b) Ω distributions for all 7→*C* ions of cytochrome *c* from native-like conditions. Ω distribution (*black solid lines*), CDF (*red lines*) and critical Ω values (*black dashed lines*) for the (c) 18→9 and (d) 9→9 ions from denaturing conditions. All experiments probed ions generated using the temperature-controlled source with the temperature of the Peltier device set to 25 °C.

The Ω distributions for the 9→*C* ions from denaturing conditions are shown in Figure S3b. There are similarities between the distributions for the 18→*C* and 9→*C* ions of a given *C*, particularly for the *P*→4 and *P*→3 products. The Ω distributions for the intermediate charge state products from *P* = 18 and 9 depend on the identity of the precursor. For example, Figures 5.5c and 5.5d show the Ω distributions (*black solid lines*) of 18→9 and 9→9 ions from denaturing conditions, respectively. These Ω distributions span similar ranges and have features centered around similar Ω values, but the relative intensities of the features are clearly different. The differences in the Ω distributions are also apparent in the corresponding critical Ω values (*black dashed lines*) calculated from the CDFs (*red lines*).

Figure 4.6a shows the critical Ω values for all CAPTR precursor and product ions of cytochrome *c* from denaturing conditions. The identity of each precursor ion, *P* = 18 to 8, is indicated using a different color. The Ω distributions of the *P*→*C* ions compact to smaller Ω with each subsequent CAPTR event, which is consistent with the ions refolding to form additional intramolecular interactions as charges are removed. Although the Ω distributions depend strongly on *C*, they can also depend on *P* as highlighted for the 18→9 and 9→9 ions. At low *C* the change in Ω with each subsequent CAPTR event decreases until the difference between the Ω for the *P*→4 and *P*→3 ions is extremely small. This is consistent with the protein providing adequate shielding between those few remaining charges, suggesting that further charge reduction may not result in further compaction.

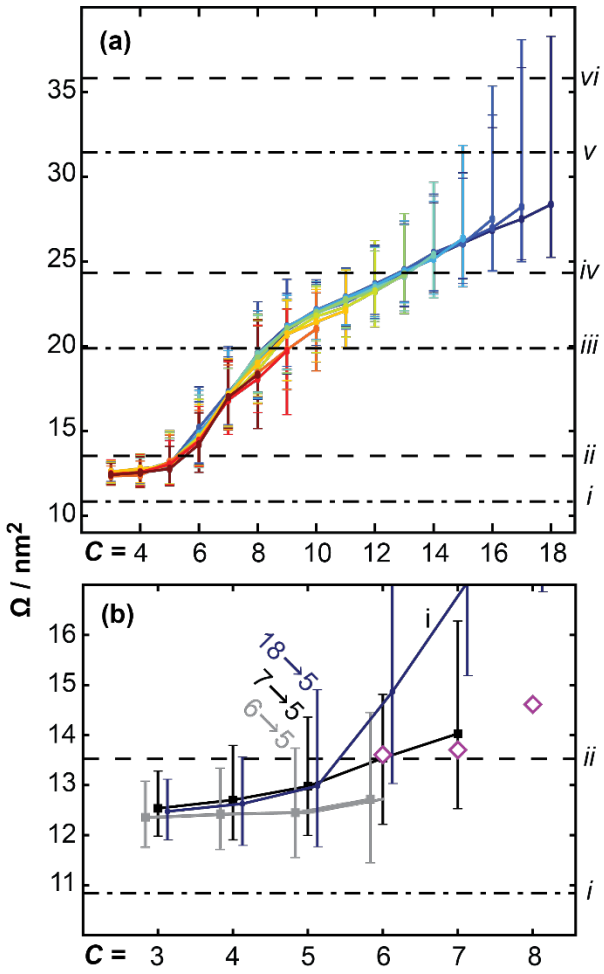

Figure 4.6. (a) Critical Ω values, which correspond to 10%, 50%, and 90% of the cumulative distribution function, for the CAPTR precursor and product ions of cytochrome *c* from denaturing conditions. The charge state of the precursor (*P*) for each set of values is indicated using a unique color. (b) Critical Ω values for native-like 7→*C* (*black squares*), native-like 6→*C* (*gray squares*) and denatured 18→*C* (*blue circles*) cytochrome *c* as a function of *C*. The three series are offset horizontally to aid in visualization, as labeled for the *P*→5 data. Ω values for native-like ions that were reported previously [12] are shown using *hollow magenta diamonds*. The horizontal dashed black lines in panels (a) and (b) correspond to Ω values calculated for models of cytochrome *c* (Table 5.1).

4.4.4 *CAPTR of cytochrome c ions from native-like conditions.*

The precursor ions generated using native-like conditions were each *m*/*z* selected and subjected to CAPTR, using the same procedure described for ions from denaturing conditions. Ω distributions for the native-like 7→*C* ions are shown in Figure 4.5b and reproduced in Figure S3c. The Ω distribution for 7+ ions from native-like conditions is smaller in magnitude and narrower in width than the distributions for the *P*→7 ions from denaturing conditions (Figures S3a and S3b). This trend continues for the 7→*C* ions from native-like conditions and the *P*→*C* ions from denaturing conditions, for *C* = 5 and 6. However, the Ω distribution for the 7→3 ions from native-like conditions are indistinguishable from those for the *P*→3 ions from denaturing conditions (Figure S3a and S3b). Relative to the Ω distributions for the ions from denaturing conditions (Figure S3a and S3b), the distributions for the ions from native-like conditions span a far narrower range of values.

The critical Ω values of native-like 7→*C* and 6→*C* ions were determined using the same procedure described for the ions from denaturing conditions and are shown in Figure 4.6b. Just as with the 7→*C* ions, the 6→*C* ions compact with decreasing *C*. The most compact products for both precursors are the *P*→3 ions, whose median Ω values are 12.4 and 12.5 nm^2 for the 7→3 and 6→3 ions, respectively. These values are 10% and 3% smaller than those for the 7+ and 6+ precursor ions, respectively. The 6→*C* ions are more compact than the corresponding 7→*C* ions, but those differences decrease with decreasing *C* until those for the two *P*→3 ions are effectively indistinguishable. This may be due to the ions compacting to similar structural populations, or different structural populations with indistinguishable Ω distributions.

The critical Ω values for the 18→*C* ions from denaturing conditions are also shown in Figure 4.6b. Although the critical Ω values for the 18→7 and 18→6 ions from denaturing conditions are significantly larger than the corresponding values for the *P*→7 and *P*→6 ions from native-like conditions, respectively, those differences decrease with decreasing *C*. Therefore, all *P*→4 and *P*→3 ions have similar critical Ω values, regardless of the Ω distribution of the precursor ion or whether the precursors were formed from denaturing or native-like conditions.

4.5 Conclusions

These experiments used CAPTR and IM to investigate the relationship between the Ω distributions and charge states of cytochrome *c* ions generated at ambient temperature from denaturing and from native-like conditions. To enable these experiments, we first developed a temperature-controlled, nanoelectrospray ionization source to control the temperature of the liquid samples, which are in close proximity to the heated atmospheric-pressure interface of the mass spectrometer in these experiments. We characterized this source using measurements of both the temperature of a liquid in the sample capillary (Figure 4.3) and the Ω distributions of 7+ ubiquitin ions from denaturing conditions (Figure 4.2b), which were sensitive to the temperature of the atmospheric-pressure interface in previous experiments using the original source (Figure 4.2a, [33]). These results all show that this temperature-controlled source decouples the temperature of the liquid sample from the temperature of the atmospheric-pressure interface.

Comparisons between the experimental (Figure 4.6) and calculated (Table 4.1) Ω indicate that CAPTR results in the formation of a diverse set of structures, from those that are compact and native-like to those that are still very extended and have minimal interactions between

neighboring amino acids. The Ω of the products depend most strongly on *C*. Most notably, the Ω distributions of all $P \rightarrow 3$ ions are very similar and are all centered near 12.4 nm^2, a value that is bracketed by the two estimates for the native model of cytochrome *c* (Table 5.1) and is slightly smaller than the Ω measured for native-like ions of cytochrome *c* without CAPTR.

Several aspects of the IM results for the CAPTR products of cytochrome *c* ions from denaturing solutions (Figures 5.5a, S3b, and 5.6a) share similarities with those reported for ubiquitin from denaturing solutions [33]. Most notably, the magnitude of the Ω distribution decreases by ~50% from the highest *C* observed to the lowest *C* observed in both cases. Furthermore, in both cases the products with the highest and lowest values of *C* exhibit Ω distributions that are unimodal, whereas those with intermediate values of *C* exhibit multiple features. However, although the relative intensities of the features observed for the $P \rightarrow 6$ ions of ubiquitin depend on *P*, similar ranges of Ω were observed for all *C*. In contrast, the ranges and relative intensities of the features in the Ω distributions for the CAPTR products of cytochrome *c* depend more strongly on *P* (Figures 5.5c, 5.5d, and 5.6a). Finally, the Ω for the lowest-*C* CAPTR products of both proteins from denaturing solutions are all consistent with the formation of compact structures. These compact ions have Ω that are similar to those measured for the corresponding native-like ions and those calculated using the corresponding native structure. Future experiments will focus on probing the similarities and differences between these compact protein ions formed through such different mechanisms, which will require complementary probes of ion structure, *e.g.*, ion chemistry [7,20,53], alternative dissociation techniques [20,31,32,54], and spectroscopy [55].

4.6 Electronic Supplementary Material.

Figures S1 to S3 and method for converting arrival-time distributions to Ω distributions. The Supporting Information is available free of charge on the internet at http://dx.doi.org/10.1007/s13361-017-1620-4

The Supporting Information is also reprinted in Appendix C.

4.7 Acknowledgments.

Research reported in this publication was supported by Eli Lilly and Company (Young Investigator Award in Analytical Chemistry to M. F. B.) and the National Institute of General Medical Sciences of the National Institutes of Health under Award Number T32GM008268 (support to K. J. L.)

4.8 References

(1) Hilton, G. R.; Benesch, J. L. P. Two Decades of Studying Non-Covalent Biomolecular Assemblies by Means of Electrospray Ionization Mass Spectrometry. *J. R. Soc. Interface* **2012**, *9* (70), 801–816.

(2) Bleiholder, C.; Do, T. D.; Wu, C.; Economou, N. J.; Bernstein, S. S.; Buratto, S. K.; Shea, J.-E.; Bowers, M. T. Ion Mobility Spectrometry Reveals the Mechanism of Amyloid Formation of Aβ(25–35) and Its Modulation by Inhibitors at the Molecular Level: Epigallocatechin Gallate and Scyllo-Inositol. *J. Am. Chem. Soc.* **2013**, *135* (45), 16926–16937.

(3) Young, L. M.; Cao, P.; Raleigh, D. P.; Ashcroft, A. E.; Radford, S. E. Ion Mobility Spectrometry–Mass Spectrometry Defines the Oligomeric Intermediates in Amylin Amyloid Formation and the Mode of Action of Inhibitors. *J. Am. Chem. Soc.* **2014**, *136* (2), 660–670.

(4) Zhou, M.; Politis, A.; Davies, R. B.; Liko, I.; Wu, K.-J.; Stewart, A. G.; Stock, D.; Robinson, C. V. Ion Mobility–mass Spectrometry of a Rotary ATPase Reveals ATP-Induced Reduction in Conformational Flexibility. *Nat. Chem.* **2014**, *6* (3), 208–215.

(5) Wyttenbach, T.; Bleiholder, C.; Bowers, M. T. Factors Contributing to the Collision Cross Section of Polyatomic Ions in the Kilodalton to Gigadalton Range: Application to Ion Mobility Measurements. *Anal. Chem.* **2013**, *85* (4), 2191–2199.
(6) Uetrecht, C.; Barbu, I. M.; Shoemaker, G. K.; van Duijn, E.; Heck, A. J. R. Interrogating Viral Capsid Assembly with Ion Mobility-Mass Spectrometry. *Nat. Chem.* **2011**, *3* (2), 126–132.
(7) Maurer, M. M.; Donohoe, G. C.; Valentine, S. J. Advances in Ion Mobility-Mass Spectrometry Instrumentation and Techniques for Characterizing Structural Heterogeneity. *Analyst* **2015**, *140* (20), 6782–6798.
(8) Shi, L.; Holliday, A. E.; Shi, H.; Zhu, F.; Ewing, M. A.; Russell, D. H.; Clemmer, D. E. Characterizing Intermediates Along the Transition from Polyproline I to Polyproline II Using Ion Mobility Spectrometry-Mass Spectrometry. *J. Am. Chem. Soc.* **2014**, *136* (36), 12702–12711.
(9) Barr, J. D.; Shi, L.; Russell, D. H.; Clemmer, D. E.; Holliday, A. E. Following a Folding Transition with Capillary Electrophoresis and Ion Mobility Spectrometry. *Anal. Chem.* **2016**, *88* (22), 10933–10939.
(10) Bush, M. F.; Hall, Z.; Giles, K.; Hoyes, J.; Robinson, C. V.; Ruotolo, B. T. Collision Cross Sections of Proteins and Their Complexes: A Calibration Framework and Database for Gas-Phase Structural Biology. *Anal. Chem.* **2010**, *82*, 9557–9565.
(11) Hogan, C. J.; Ruotolo, B. T.; Robinson, C. V.; Fernandez de la Mora, J. Tandem Differential Mobility Analysis-Mass Spectrometry Reveals Partial Gas-Phase Collapse of the GroEL Complex. *J. Phys. Chem. B* **2011**, *115* (13), 3614–3621.
(12) Allen, S. J.; Schwartz, A. M.; Bush, M. F. Effects of Polarity on the Structures and Charge States of Native-Like Proteins and Protein Complexes in the Gas Phase. *Anal. Chem.* **2013**, *85* (24), 12055–12061.
(13) Hall, Z.; Politis, A.; Bush, M. F.; Smith, L. J.; Robinson, C. V. Charge-State Dependent Compaction and Dissociation of Protein Complexes: Insights from Ion Mobility and Molecular Dynamics. *J. Am. Chem. Soc.* **2012**, *134* (7), 3429–3438.
(14) Wyttenbach, T.; Bowers, M. T. Structural Stability from Solution to the Gas Phase: Native Solution Structure of Ubiquitin Survives Analysis in a Solvent-Free Ion Mobility–Mass Spectrometry Environment. *J. Phys. Chem. B* **2011**, *115* (42), 12266–12275.
(15) Clemmer, D. E.; Hudgins, R. R.; Jarrold, M. F. Naked Protein Conformations: Cytochrome c in the Gas Phase. *J. Am. Chem. Soc.* **1995**, *117* (40), 10141–10142.
(16) Faull, P. A.; Korkeila, K. E.; Kalapothakis, J. M.; Gray, A.; McCullough, B. J.; Barran, P. E. Gas-Phase Metalloprotein Complexes Interrogated by Ion Mobility-Mass Spectrometry. *Int. J. Mass Spectrom.* **2009**, *283* (1–3), 140–148.
(17) Hilton, G. R.; Thalassinos, K.; Grabenauer, M.; Sanghera, N.; Slade, S. E.; Wyttenbach, T.; Robinson, P. J.; Pinheiro, T. J. T.; Bowers, M. T.; Scrivens, J. H. Structural Analysis of Prion Proteins by Means of Drift Cell and Traveling Wave Ion Mobility Mass Spectrometry. *J. Am. Soc. Mass Spectrom.* **2010**, *21* (5), 845–854.
(18) Beveridge, R.; Covill, S.; Pacholarz, K. J.; Kalapothakis, J. M. D.; MacPhee, C. E.; Barran, P. E. A Mass-Spectrometry-Based Framework To Define the Extent of Disorder in Proteins. *Anal. Chem.* **2014**, *86* (22), 10979–10991.
(19) Hall, Z.; Robinson, C. V. Do Charge State Signatures Guarantee Protein Conformations? *J. Am. Soc. Mass Spectrom.* **2012**, *23* (7), 1161–1168.

(20) Breuker, K.; McLafferty, F. W. Stepwise Evolution of Protein Native Structure with Electrospray into the Gas Phase, 10-12 to 102 S. *Proc. Natl. Acad. Sci. U. S. A.* **2008**, *105* (47), 18145.
(21) Benesch, J. L.; Ruotolo, B. T. Mass Spectrometry: Come of Age for Structural and Dynamical Biology. *Curr. Opin. Struct. Biol.* **2011**, *21* (5), 641–649.
(22) Schnier, P. D.; Gross, D. S.; Williams, E. R. Electrostatic Forces and Dielectric Polarizability of Multiply Protonated Gas-Phase Cytochrome c Ions Probed by Ion/Molecule Chemistry. *J. Am. Chem. Soc.* **1995**, *117* (25), 6747–6757.
(23) McLuckey, S. A.; Goeringer, D. E. Ion/Molecule Reactions for Improved Effective Mass Resolution in Electrospray Mass Spectrometry. *Anal. Chem.* **1995**, *67* (14), 2493–2497.
(24) Shelimov, K. B.; Jarrold, M. F. Conformations, Unfolding, and Refolding of Apomyoglobin in Vacuum: An Activation Barrier for Gas-Phase Protein Folding. *J. Am. Chem. Soc.* **1997**, *119* (13), 2987–2994.
(25) McLuckey, S. A.; Stephenson, J. L.; Asano, K. G. Ion/Ion Proton-Transfer Kinetics: Implications for Analysis of Ions Derived from Electrospray of Protein Mixtures. *Anal. Chem.* **1998**, *70* (6), 1198–1202.
(26) McLuckey, S. A.; Stephenson, J. L. Ion/Ion Chemistry of High-Mass Multiply Charged Ions. *Mass Spectrom. Rev.* **1998**, *17* (6), 369–407.
(27) Pitteri, S. J.; McLuckey, S. A. Recent Developments in the Ion/Ion Chemistry of High-Mass Multiply Charged Ions. *Mass Spectrom. Rev.* **2005**, *24* (6), 931–958.
(28) Stephenson Jr, J. L.; Van Berkel, G. J.; McLuckey, S. A. Ion-Ion Proton Transfer Reactions of Bio-Ions Involving Noncovalent Interactions: Holomyoglobin. *J. Am. Soc. Mass Spectrom.* **1997**, *8* (6), 637–644.
(29) Laszlo, K. J.; Bush, M. F. Analysis of Native-Like Proteins and Protein Complexes Using Cation to Anion Proton Transfer Reactions (CAPTR). *J. Am. Soc. Mass Spectrom.* **2015**, *26*, 2152–2161.
(30) Lermyte, F.; Williams, J. P.; Brown, J. M.; Martin, E. M.; Sobott, F. Extensive Charge Reduction and Dissociation of Intact Protein Complexes Following Electron Transfer on a Quadrupole-Ion Mobility-Time-of-Flight MS. *J. Am. Soc. Mass Spectrom.* **2015**, *26* (7), 1068–1076.
(31) Zhang, H.; Cui, W.; Wen, J.; Blankenship, R. E.; Gross, M. L. Native Electrospray and Electron-Capture Dissociation FTICR Mass Spectrometry for Top-Down Studies of Protein Assemblies. *Anal. Chem.* **2011**, *83* (14), 5598–5606.
(32) Lermyte, F.; Konijnenberg, A.; Williams, J. P.; Brown, J. M.; Valkenborg, D.; Sobott, F. ETD Allows for Native Surface Mapping of a 150 kDa Noncovalent Complex on a Commercial Q-TWIMS-TOF Instrument. *J. Am. Soc. Mass Spectrom.* **2014**, *25* (3), 343–350.
(33) Laszlo, K. J.; Munger, E. B.; Bush, M. F. Folding of Protein Ions in the Gas Phase after Cation-to-Anion Proton-Transfer Reactions. *J. Am. Chem. Soc.* **2016**, *138*, 9581–9588.
(34) Salbo, R.; Bush, M. F.; Naver, H.; Campuzano, I.; Robinson, C. V.; Pettersson, I.; Jørgensen, T. J. D.; Haselmann, K. F. Traveling-Wave Ion Mobility Mass Spectrometry of Protein Complexes: Accurate Calibrated Collision Cross-Sections of Human Insulin Oligomers. *Rapid Commun. Mass Spectrom.* **2012**, *26* (10), 1181–1193.
(35) Bleiholder, C.; Johnson, N. R.; Contreras, S.; Wyttenbach, T.; Bowers, M. T. Molecular Structures and Ion Mobility Cross Sections: Analysis of the Effects of He and N2 Buffer Gas. *Anal. Chem.* **2015**, *87* (14), 7196–7203.

(36) Davidson, K. L.; Oberreit, D. R.; Hogan Jr., C. J.; Bush, M. F. Nonspecific Aggregation in Native Electrokinetic Nanoelectrospray Ionization. *Int. J. Mass Spectrom.* DOI: 10.1016/j.ijms.2016.09.013.

(37) Allen, S.; Giles, K.; Gilbert, T.; Bush, M. Ion Mobility Mass Spectrometry of Peptide, Protein, and Protein Complex Ions Using a Radio-Frequency Confining Drift Cell. *Analyst* **2016**, *141*, 884–891.

(38) Williams, J. P.; Brown, J. M.; Campuzano, I.; Sadler, P. J. Identifying Drug Metallation Sites on Peptides Using Electron Transfer Dissociation (ETD), Collision Induced Dissociation (CID) and Ion Mobility-Mass Spectrometry (IM-MS). *Chem. Commun.* **2010**, *46* (30), 5458–5460.

(39) Stephenson, J. L.; McLuckey, S. A. Ion/Ion Reactions in the Gas Phase: Proton Transfer Reactions Involving Multiply-Charged Proteins. *J. Am. Chem. Soc.* **1996**, *118* (31), 7390–7397.

(40) Gunawardena, H. P.; He, M.; Chrisman, P. A.; Pitteri, S. J.; Hogan, J. M.; Hodges, B. D. M.; McLuckey, S. A. Electron Transfer versus Proton Transfer in Gas-Phase Ion/Ion Reactions of Polyprotonated Peptides. *J Am Chem Soc* **2005**, *127* (36), 12627–12639.

(41) Pettersen, E. F.; Goddard, T. D.; Huang, C. C.; Couch, G. S.; Greenblatt, D. M.; Meng, E. C.; Ferrin, T. E. UCSF Chimera--a Visualization System for Exploratory Research and Analysis. *J. Comput. Chem.* **2004**, *25* (13), 1605–1612.

(42) Bushnell, G. W.; Louie, G. V.; Brayer, G. D. High-Resolution Three-Dimensional Structure of Horse Heart Cytochrome c. *J. Mol. Biol.* **1990**, *214* (2), 585–595.

(43) von Helden, G.; Hsu, M. T.; Gotts, N.; Bowers, M. T. Carbon Cluster Cations with up to 84 Atoms: Structures, Formation Mechanism, and Reactivity. *J. Phys. Chem.* **1993**, *97* (31), 8182–8192.

(44) Shvartsburg, A. A.; Jarrold, M. F. An Exact Hard-Spheres Scattering Model for the Mobilities of Polyatomic Ions. *Chem. Phys. Lett.* **1996**, *261* (1–2), 86–91.

(45) Shvartsburg, A. A.; Mashkevich, S. V.; Baker, E. S.; Smith, R. D. Optimization of Algorithms for Ion Mobility Calculations. *J. Phys. Chem. A* **2007**, *111* (10), 2002–2010.

(46) Daneshfar, R.; Kitova, E. N.; Klassen, J. S. Determination of Protein−Ligand Association Thermochemistry Using Variable-Temperature Nanoelectrospray Mass Spectrometry. *J. Am. Chem. Soc.* **2004**, *126* (15), 4786–4787.

(47) Cong, X.; Liu, Y.; Liu, W.; Liang, X.; Russell, D. H.; Laganowsky, A. Determining Membrane Protein–Lipid Binding Thermodynamics Using Native Mass Spectrometry. *J. Am. Chem. Soc.* **2016**, *138* (13), 4346–4349.

(48) Wang, G.; Abzalimov, R. R.; Kaltashov, I. A. Direct Monitoring of Heat-Stressed Biopolymers with Temperature-Controlled Electrospray Ionization Mass Spectrometry. *Anal. Chem.* **2011**, *83* (8), 2870–2876.

(49) Benesch, J. L. P.; Sobott, F.; Robinson, C. V. Thermal Dissociation of Multimeric Protein Complexes by Using Nanoelectrospray Mass Spectrometry. *Anal. Chem.* **2003**, *75* (10), 2208–2214.

(50) Geels, R. B. J.; Calmat, S.; Heck, A. J. R.; van der Vies, S. M.; Heeren, R. M. A. Thermal Activation of the Co-Chaperonins GroES and gp31 Probed by Mass Spectrometry. *Rapid Commun. Mass Spectrom.* **2008**, *22* (22), 3633–3641.

(51) Shelimov, K. B.; Clemmer, D. E.; Hudgins, R. R.; Jarrold, M. F. Protein Structure in Vacuo: Gas-Phase Conformations of BPTI and Cytochrome c. *J. Am. Chem. Soc.* **1997**, *119* (9), 2240–2248.

(52) Jurneczko, E.; Barran, P. E. How Useful Is Ion Mobility Mass Spectrometry for Structural Biology? The Relationship between Protein Crystal Structures and Their Collision Cross Sections in the Gas Phase. *Analyst* **2011**, *136* (1), 20–28.
(53) Prentice, B. M.; McLuckey, S. A. Gas-Phase Ion/Ion Reactions of Peptides and Proteins: Acid/Base, Redox, and Covalent Chemistries. *Chem Commun* **2013**, *49* (10), 947–965.
(54) Brodbelt, J. S. Ion Activation Methods for Peptides and Proteins. *Anal. Chem.* **2016**, *88* (1), 30–51.
(55) Pagel, K.; Hyung, S.-J.; Ruotolo, B. T.; Robinson, C. V. Alternate Dissociation Pathways Identified in Charge-Reduced Protein Complex Ions. *Anal. Chem.* **2010**, *82* (12), 5363–5372

Chapter 5. Effects of Solution Structure on the Folding of Lysozyme Ions in the Gas Phase

---

This chapter is reproduced with permission from Laszlo, K. J.; Munger, E.B.; Bush M. F. "Effects of Solution Structure on the Folding of Lysozyme Ions in the Gas Phase." *The Journal of Physical Chemistry B*, **2017**. doi:10.1021/acs.jpcb.7b00783.

5.1 Abstract

The fidelity between the structures of proteins in solution and protein ions in the gas phase is critical to experiments that use gas-phase measurements to infer structures in solution. Here we generate ions of lysozyme, a 129-residue protein whose native tertiary structure contains four internal disulfide bonds, from three solutions that preserve varying extents of the original native structure. We then use cation-to-anion proton-transfer reactions (CAPTR) to reduce the charge states of those ions in the gas phase and ion mobility to probe their structures. The collision cross section (Ω) distributions of each CAPTR product depends to varying extents on the original solution, the charge state of the product, and the charge state of the precursor. For example, the Ω distributions of the 6+ ions depend strongly on the original solutions conditions and to a lesser extent on the charge state of the precursor. Energy-dependent experiments suggest that very different structures are accessible to disulfide-reduced and disulfide-intact ions, but similar Ω distributions are formed at high energy for disulfide-intact ions from denaturing and from aqueous conditions. The Ω distributions of the 3+ ions are all similar, but exhibit subtle

differences that depend more strongly on the original solutions conditions than other factors. More generally, these results suggest that specific CAPTR products may be especially sensitive to specific elements of structure in solution.

5.2 Introduction

A universal method for predicting the structures of proteins on the basis of their sequence has not yet emerged. Although the understanding of protein folding has advanced greatly in recent decades,[1–3] limitations in this understanding hinder efforts in fields as diverse as protein misfolding in human health and *de novo* protein design. In a model based on first principles, it is necessary to decouple protein intramolecular interactions from noncovalent interactions with surrounding ions and solvent molecules. Although protein-folding and protein-unfolding experiments in condensed phases have investigated pathways for specific proteins,[4] decoupling the individual contributions from solvent molecules remains challenging.[5,6] In contrast, gas-phase experiments are able to decouple intramolecular and intermolecular interactions by analyzing isolated biomolecules and complexes. Furthermore, investigations of m/z-selected complexes of biomolecules, ions, and solvent molecules enable the characterization of the effects of individual interactions with exquisite specificity.[7–10]

Electrospray ionization (ESI) from aqueous solutions with physiological ionic strengths and pH can yield "native-like" protein ions with properties that are consistent with the corresponding biomolecules in the condensed phase, including oligomeric states[11,12] and collision cross sections (Ω).[13–15] For example, recent ion mobility spectrometry and infrared action spectroscopy experiments indicate that helical and beta-sheet secondary structures of small proteins can be retained in the gas phase for low-charge ions.[16] Recollection of ions of

tobacco mosaic virus were able to infect tobacco plants[17] and ions of endospores of *Bacillus subtilis* were able to be cultured even after high-velocity impacts with surfaces,[18] establishing that ESI can even preserve biological function. Progress in native mass spectrometry[19,20] and how the structures of protein ions can evolve in the gas phase[21,22] have been reviewed elsewhere. In total, these experiments show that native-like ions can retain significant memories of their original structures in solution and that investigations of those ions can strongly complement the condensed-phase toolbox for biophysics and structural biology.

In contrast to protein ions generated from aqueous solutions, ions generated from denaturing conditions, *e.g.* organic and/or acidic solutions, typically have higher charge states (z) and Ω values that are less indicative of the native structure.[23,24] However, when these high-z and high-Ω ions from denaturing solutions are charge reduced, their resulting low-z products exhibit more compact Ω distributions.[25–30] For example, Clemmer and coworkers used ion-neutral proton-transfer reactions to simultaneously reduce all charge states of disulfide-intact and disulfide-reduced lysozyme ions generated from 1:1 water:acetonitrile with 0.2% acetic acid.[27] After ESI, all multiply protonated protein ions, $[M + zH]^{z+}$, were transferred into a chamber where they reacted with the neutral vapor of a molecule, B, with a higher gas-phase basicity:

$$[M + zH]^{z+} + B \rightarrow [M + (z-1)H]^{(z-1)+} + BH^{+} \qquad \text{(Reaction 1)}$$

Ion mobility of the ion-neutral proton-transfer reaction products showed that charge-reduced forms of disulfide-intact and disulfide-reduced lysozyme ions can have a range of Ω values that are consistent with partially-folded and highly-folded structures.[27]

Alternatively, the charge state of a protein ion may be reduced using ion/ion reactions, which benefit from more favorable thermodynamics and kinetics compared to ion/neutral

reactions.[31] Ion/ion reactions predominantly proceed though electron transfer (Reaction 2) or proton transfer (Reaction 3):

$$[M + zH]^{z+} + A^{\bullet -} \rightarrow [M + zH]^{\bullet (z-1)+} + A \qquad \text{(Reaction 2)}$$

$$[M + zH]^{z+} + A^{-} \rightarrow [M + (z-1)H]^{(z-1)+} + AH \qquad \text{(Reaction 3)}$$

Note that Reaction 2 results in formation a radical cation that will often undergo the cleavage of disulfide and other bonds (electron-transfer dissociation).[32,33] In contrast, Reaction 3 results in the formation of an even-electron cation that is charge reduced but does not undergo fragmentation.[34–36] We recently introduced cation-to-anion proton-transfer reactions (CAPTR), a method that uses Reaction 3 to yield a long series of charge-reduced product ions.[36] Differences between CAPTR and other methods for reducing the charge states of protein ions have been discussed previously.[29,36]

Recently, we used CAPTR to study the gas-phase folding of 13+ to 6+ ubiquitin ions from denaturing conditions. In those experiments, individual charge states (*P*) were each isolated using a quadrupole and reacted with anions via Reaction 3 to yield charge-reduced products of charge state *C*. Ω of those products depended strongly on *C* and were independent of *P*. However, energy-dependent measurements revealed that the structures of those ions also depended on *P*. Interestingly, the Ω values for the lowest-charge-state CAPTR products[29] were similar to those measured[37–39] and calculated[39] for the corresponding native-like ions. Subsequent experiments using CAPTR and IM to probe the effects of charge on ions of cytochrome *c* from denaturing conditions exhibited similar trends.[40] The lowest-charge-state products of cytochrome *c* ions from denaturing and native-like conditions exhibited similar Ω values.[40] In order to investigate the effects of precursor ion structure and charge state on the Ω of protein ions more generally, here we use CAPTR, IM, and post-CAPTR activation to investigate ions of lysozyme,

a 129-residue protein whose native tertiary structure contains four internal disulfide bonds. Ions were formed from three solution conditions that retain varying extents of native structure.

5.3 Methods

Lysozyme from hen egg white (Sigma Aldrich, 62970, St. Louis, MO) was prepared in three solutions, as summarized in Table 4.1. For DR conditions, aqueous solutions were heated at 90 ˚C for 20 minutes to reduce the disulfide bonds prior to the addition of acetonitrile.[27] All cations were generated using electrokinetic nanoelectrospray ionization, as described previously.[41] Experiments were performed on a Waters Synapt G2 HDMS instrument with ion/ion reaction capabilities,[42] and instrument parameters were optimized for ion/ion reactions, transmission, and minimal activation. Unless otherwise noted, the atmospheric-pressure interface of the instrument was elevated to 120 °C, which results in some heat transfer to the sample capillary.[40] Most mass spectra were acquired by operating the time-of-flight mass analyzer in "V" mode. Selected mass spectra were acquired by operating that analyzer in "W" mode, which effectively doubles the flight path and increases the resolving power.

Table 5.1. Table of Solution Conditions

	Description	Solvent and Additives
DR	Denaturing Disulfide Reduced	10 mM dithiothrietol, 0.2% acetic acid 1:1 water:acetonitrile
DI	Denaturing Disulfide Intact	0.2% acetic acid 1:1 water:acetonitrile
NI	Native-like Disulfide Intact	200 mM aqueous ammonium acetate at pH 7

Ion/ion reactions were performed as described previously.[29,36] Briefly, $[M-F]^-$ fragments of perfluoro-1,3-dimethylcyclohexane[43] were produced for 0.1 s, quadrupole selected, and

accumulated in the trap cell of the instrument. The instrument was then switched into positive ion mode for 2 to 10 s. A single charge state of lysozyme was quadrupole selected and guided into the trap cell to initiate CAPTR via Reaction 3. Residual unreacted precursor ions and CAPTR product ions were injected into an rf-confining drift cell for IM analysis.[44] IM experiments were performed with a 127 V drift voltage in 2 mbar helium, unless otherwise noted. For some low-intensity CAPTR product ions, the background was subtracted from the arrival-time distributions using a procedure described in the Supporting Information in order to remove interferences. Ion mobility arrival-time distributions were converted to Ω distributions using a method described previously.[40] Selected CAPTR products were activated by increasing the DC bias between trap and mobility cells.[29]

Ω values were calculated using the projection approximation (PA)[45] and the exact hard-sphere scattering approximation (EHSS)[46] as implemented in EHSS2/k.[47] These approximations and their relationship to momentum transfer in IM have been discussed elsewhere.[23,46] The Ω for native lysozyme is based on 50 low-energy models that are taken from the NMR-derived structural ensemble of disulfide-intact lysozyme (PDB: 1E8L).[48] The linear and α-helical models were built using Chimera[49] and the expected dihedral angles.

5.4 Results and Discussion

5.4.1 *Lysozyme ions from electrospray.*

Lysozyme ions with reduced disulfide bonds were generated from denaturing conditions (DR), whereas those with intact disulfide bonds were generated from either denaturing (DI) or native-like (NI) conditions (Table 4.1). Ions from DR conditions exhibited the highest charge states, 19+ to 10+ (Figure 4.1A), whereas those from DI (Figure 4.1B) and NI (Figure 4.1C)

conditions had comparatively fewer charges, 13+ to 8+ and 8+ to 6+, respectively. The charge-state distributions of DI and DR ions are consistent with previous results for disulfide-intact and disulfide-reduced lysozyme ions from denaturing conditions.[27,50] Each panel has an inset that expands the experimental spectrum (*black*) and shows the calculated isotopic distribution (*red*),[51–53] which confirms the presence of disulfide bonds under NI and DI conditions, and their absence under DR conditions.

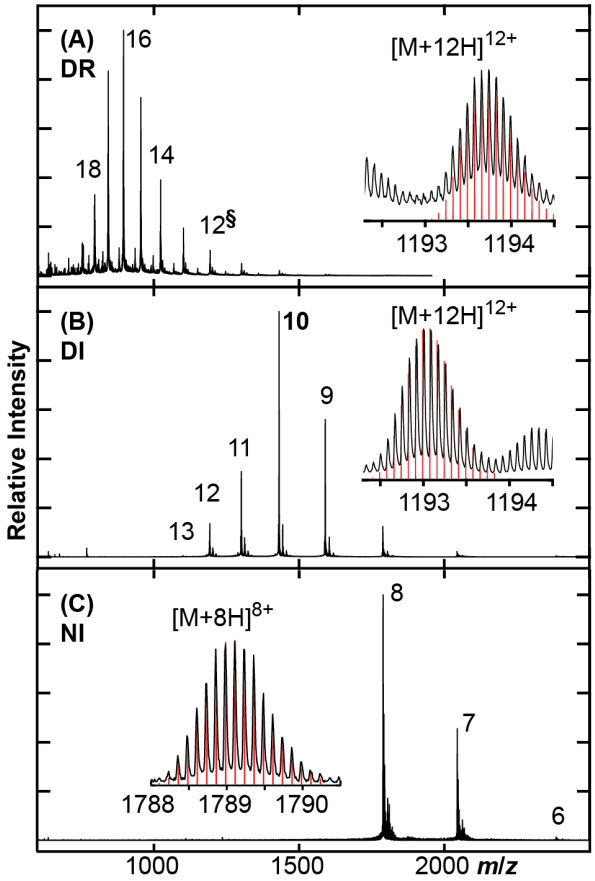

Figure 5.1. Mass spectra of lysozyme from (**A**) DR, (**B**) DI, and (**C**) NI conditions. Insets show experimental isotopic distributions (*black*) measured in "W" mode for the ions. The distributions are compared with those predicted using IDCalc[51,52] (v0.4) and the sequence of lysozyme[53] (*red vertical lines*). These isotopic distributions confirm that the four disulfide bonds remain intact under NI and DI conditions and are reduced under DR conditions.

The arrival-time distributions of these ions were measured using a rf-confining drift cell[44] that was operated with an electric field of 5 V cm^{-1} and while containing 2 mbar of He gas. The arrival-time distributions were converted to Ω distributions.[40] The median of the Ω distributions

are shown in Figure 4.2. For comparison, selected results from ion mobility experiments by Clemmer and coworkers for disulfide-intact (*white diamonds*) and disulfide-reduced (*white circles*) lysozyme ions from denaturing solutions are also shown.[27] Note that those Ω values "correspond to the peak centers for features that were clearly resolved at injection voltages of 30 or 120 V,"[27] and not the method used in the present study. Consistent with previous results,[27] the DR lysozyme ions in the present experiments also accommodate more charges from electrospray and adopt more extended conformations relative to the DI ions. The disulfide-intact ions in the previous experiments also exhibited evidence for compact conformers[27] that were not observed in these experiments, which may be attributable to differences in the ionization sources or extents of activation in the two experiments. However, the Ω values of the compact, disulfide-intact ions in Clemmer's experiments are similar to those of the NI ions in these experiments (Figure 4.2).

The weighted average Ω from previous IM results of native-like lysozyme are shown in Figure 4.2 using magenta stars.[44] In comparison to the present data measured with the atmospheric-pressure interface set to 120 ˚C, those previous results differ by 0.1 to 0.5 nm^2 for charge states 6+ to 8+. Therefore, the NI lysozyme ions appear to retain their native-like structure while the atmospheric-pressure interface is heated to 120 ˚C. Additional comparisons between the data acquired with the atmospheric-pressure interface at the two temperatures are reported in the in the Supporting Information.

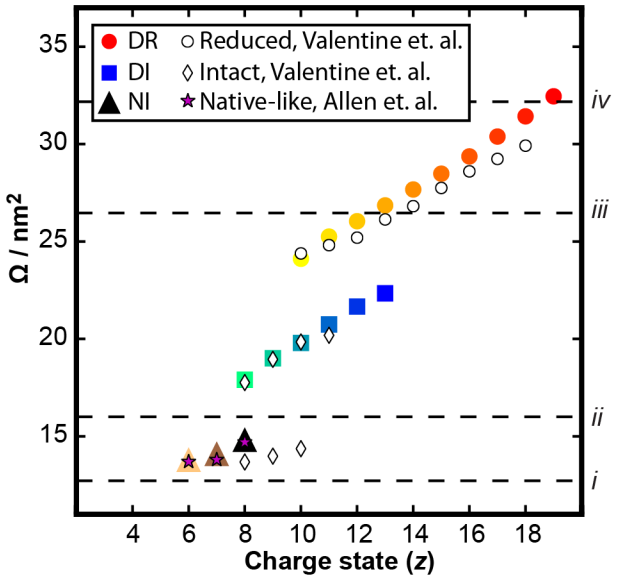

Figure 5.2. Ω values from the present and previous[27,44] studies. The median Ω of the precursor ions from DR, DI, and NI conditions in the present study are shown using solid markers with hot colors (*red* to *yellow, circles*), cool colors (*blue* to *green, squares*), and neutral colors (*black* to *beige, triangles*), respectively. Selected results for disulfide-reduced (*white circles*) and disulfide-intact (*white diamonds*) lysozyme ions from denaturing conditions reported by Clemmer and coworkers[27] are shown for comparison. The Ω values for the NI ions are similar to those reported previously for native-like ions based on field-dependent measurements (*magenta stars*).[44] Black dashed lines (*i* to *iv*) correspond to the calculated Ω values reported in Table 4.2.

5.4.2 *Comparison with calculated Ω.*

Table 4.2 reports the projection approximation (PA)[45] and exact hard-sphere scattering (EHSS)[46] Ω for three models of lysozyme, which are described in the *Methods*. In general, the PA underestimates Ω, whereas EHSS overestimates Ω.[13] As a result, these two values can be

used to bracket experimental results and provide insight into possible structures. The Ω calculated for the linear strand far exceed all values measured. The PA (*iii*) and EHSS (*iv*) Ω calculated for the α-helical model bracket the median Ω for 13+ to 18+ lysozyme ions from DR conditions (Figure 4.2). These comparisons suggest that there are significant interactions between neighboring residues even for the lysozyme ions with the largest Ω. The average Ω calculated for the native models using the PA (*i*) and of the EHSS (*ii*) methods are 12.7 and 16.0 nm^2, respectively. These values bracket the median Ω of the ions from NI conditions, consistent with these ions retaining native-like structures (Figure 4.2). In contrast, the Ω values of the DI ions are larger than those calculated for the native models and smaller than those for the α-helical model. This is consistent with the presence of disulfide bonds restricting the extent to which those ions unfold.

Table 4.2. Ω Values for Models of Lysozyme.

	Model	Method	Ω / nm^2
i	native[a]	PA	12.7 ± 0.2
ii		EHSS	16.0 ± 0.3
iii	α-helical[b]	PA	26.5 ± 0.1
iv		EHSS	32.2 ± 0.1
v	linear-strand[b]	PA	42.6 ± 0.2
vi		EHSS	48.4 ± 0.2

[a] Ω values were calculated for the 50 low-energy models in 1E8L.[48] The reported interval includes 96% of the calculated Ω values.
[b] Ω values were calculated for models that were constructed as described in the *Methods*. The reported interval was determined using Student's t-test at the 96% confidence level and 512 replicate calculations.

5.4.3 *Cation-to-anion proton-transfer reactions.*

12+ lysozyme from DR conditions (§) were quadrupole-selected and subjected to CAPTR, which yields a long series of charge-reduced products (Figure 4.3A). For the remainder of the discussion, the CAPTR products will be labeled as "*P→C"*, where "*P*" is the charge state of the precursor ion and "*C"* is the charge state of the charge-reduced product ion. Subscripts are used in some cases to indicate the solution conditions, *e.g.*, the spectrum in Figure 4.3A shows the results for the 12_{DR}→*C* ions. Unreacted precursor and CAPTR product ions are then separated by their mobilities (Figure 4.3B). The resulting arrival-time distributions are then converted to apparent Ω distributions (Figure 4.3C).[40]

The Ω distributions for the 19_{DR}→*C* ions determined using this workflow are shown in Figure 4.4A. Following most CAPTR events, the Ω distributions compact monotonically. However, the Ω distribution of the *C* = 5 to 3 ions each exhibit similar distributions centered near 13.9 nm^2. For *C* = 3 to 5 and 11 to 19, the Ω distributions are relatively unimodal and Gaussian. In contrast, for *C* = 6 to 10, the Ω distributions appear to contain multiple unresolved features.

Cumulative distribution functions, which are the cumulative sum of the Ω distributions, were calculated to aid in the comparison of Ω distributions that exhibit multiple or asymmetric features. For example, Figure 4.3C (*red solid line*) shows the Ω distribution of the 12_{DR}→6 ions from Figure 4.3B (*white box*) and the corresponding cumulative distribution function (*dashed red line*). The Ω that correspond to 10%, 50%, and 90% of the cumulative distribution illustrate the width and asymmetry of the apparent Ω distribution and will be referred to as critical Ω values.

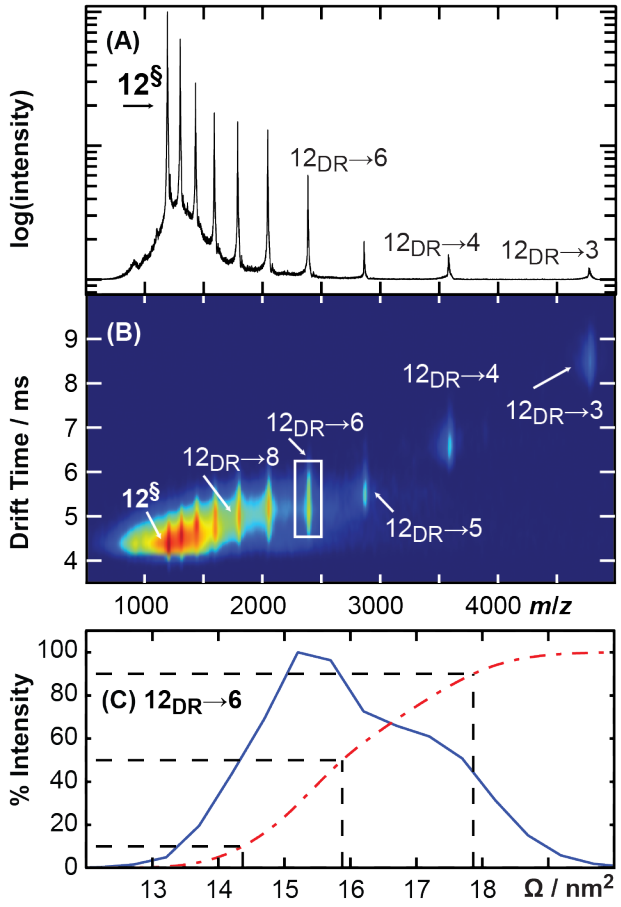

Figure 5.3. (**A**) CAPTR mass spectrum of quadrupole-selected, 12+ lysozyme (§) from DR solution conditions, *i.e.*, the 12_{DR}→*C* ions. (**B**) IM-MS of the 12_{DR}→*C* ions. (**C**) Ω distribution of the 12_{DR}→6 ions (*blue solid line*). The corresponding cumulative distribution function is shown using a *red dot dashed*

line. *Black dashed lines* intersect 10%, 50%, and 90% of the cumulative distribution function, which will be referred to as the critical values of this distribution.

Critical values were determined for the CAPTR products from each precursor that exhibited adequate abundance from DR conditions (P = 19 to 10) and are shown in Figure 4.4B. Each vertical bar spans from 10% to 90% of the corresponding cumulative distribution function of each $P \rightarrow C$. Lines connect the bars for ions of neighboring C and identical P, passing through the Ω corresponding to 50% of the corresponding cumulative distribution function of each $P \rightarrow C$. For $C \geq 5$, the critical values all decrease monotonically with decreasing C. This trend is analogous to that reported for ubiquitin from denaturing conditions based on similar experiments.[29] The lowest charge states, C = 5 to 3, exhibit narrow and compact Ω distributions around 13.9 nm^2 for all P. This result, in which the Ω distributions no longer depend on C for the lowest charge states, differs from the results for denatured ubiquitin, in which the Ω distributions of the CAPTR product ions decreased montonically with decreasing charge.[29] Finally, the critical values for the intermediate C ions, particularly C = 5 to 9, depend on the identity of P. Although the Ω distributions of the CAPTR products of lysozyme depend more strongly on P than those reported previously for ubiquitin,[29] the Ω distributions for the CAPTR products of both proteins depend far more strongly on C.

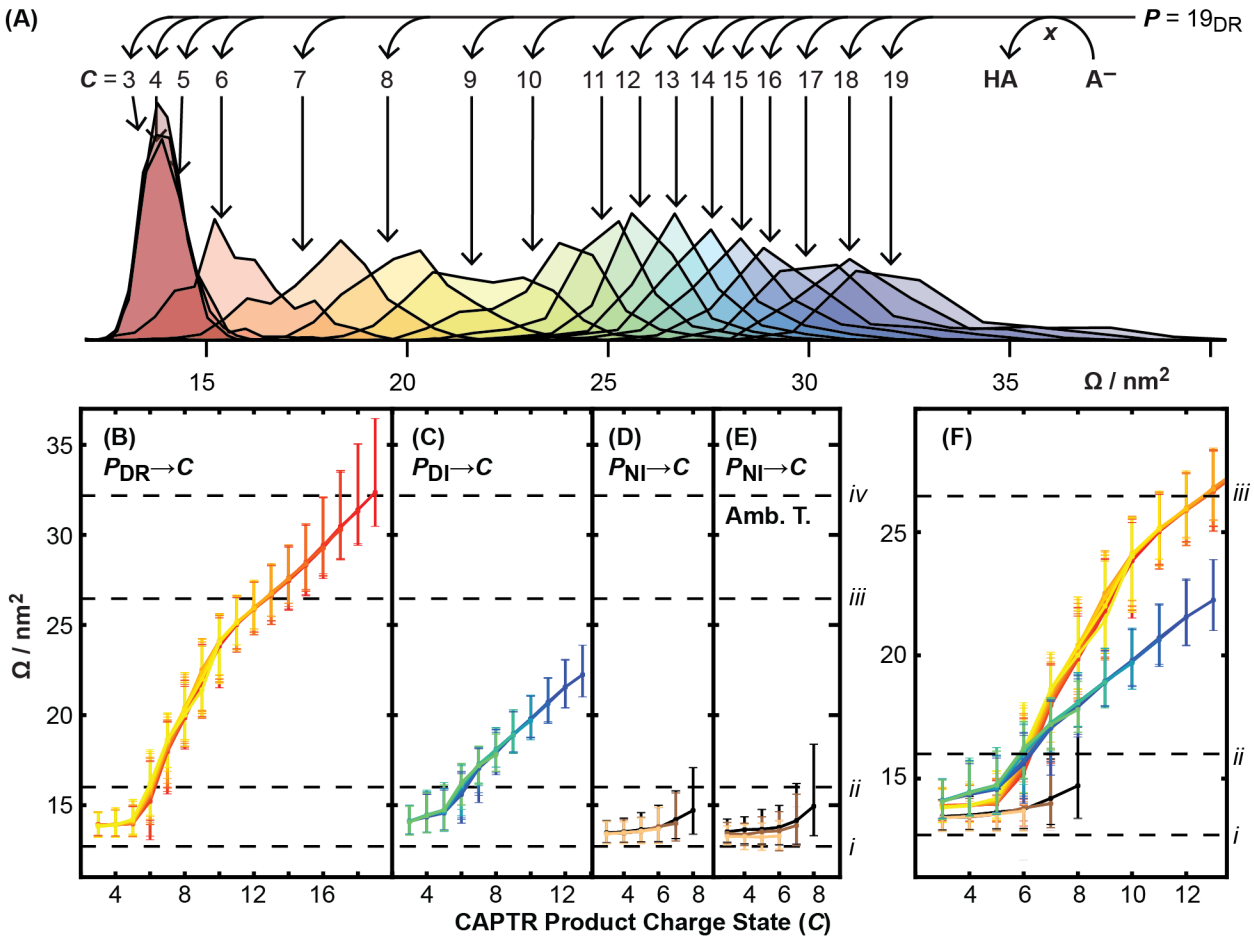

Figure 5.4. (**A**) Apparent Ω distributions of $19_{DR} \rightarrow C$ lysozyme ions. Critical values from the Ω distributions of lysozyme ions and their CAPTR products measured using (**B**) DR, (**C**) DI, and (**D**) NI condition with the atmospheric-pressure interface set to the standard temperature of 120 °C. (**E**) For NI conditions, measurements were also made with the interface at ambient temperature, which yielded similar critical values. (**F**) Comparison of C = 13 to 3 data from panels B to D. Precursor charge states of 19+ to 10+, 13+ to 8+, 8+ to 6+, and 8+ to 6+ were individually selected during the experiments reported in panels B through E, respectively, and are represented by different colors.

Horizontal dashed lines correspond to Ω values calculated for models of lysozyme (Table 4.2).

This workflow was also used for lysozyme ions from DI and NI conditions. 13+ to 8+ lysozyme from DI conditions were each isolated and subjected to CAPTR. The Ω distributions for the $12_{DI}\rightarrow C$ ions are shown in Figure S2C. Similar to the results from DR conditions, the ions compact following most CAPTR events. The critical values for all ions from DI conditions are shown in Figure 4.4C. As was the case with DR lysozyme ions, the ions compact as charge is removed, and the Ω distributions of the CAPTR product ions depend strongly on *C* for all but the lowest-*C* ions. 8+ to 6+ lysozyme from NI conditions were each isolated and subjected to CAPTR. The resulting critical Ω values, with the atmospheric-pressure interface at 120 °C and ambient temperature, are shown in Figures 4.4D and 4.4E, respectively. As charge is removed from the NI ions, they compact slightly and the median of the Ω distributions of $P_{NI}\rightarrow 3$ ions range from 13.4 to 13.47 nm^2. This compaction can also be visualized using the Ω distributions for the $8_{NI}\rightarrow C$ ions that are shown in Figure S2D. In contrast to the Ω distributions for lysozyme ions generated from DR and DI solutions (Figures 4.4B and 4.4C), those for NI lysozyme ions exhibit only modest changes in Ω. This suggests that the native-like precursors already have favorable intramolecular interactions, and that the excess charges have modest effects on their structures.

To illustrate the differences between the Ω of the CAPTR products generated from all three solutions, the critical values for the $C = 13$ to 3 ions that were plotted in Figures 4.4B to 4.4D were replotted together in Figure 4.4F. The Ω distributions for the (A) $19_{DR}\rightarrow C$, (B) $12_{DR}\rightarrow C$, (C) $12_{DI}\rightarrow C$, and (D) $8_{NI}\rightarrow C$ ions are also shown in Figure S2. For the $P\rightarrow 13$ to

$P \rightarrow 10$ ions, the Ω distributions of the DR and DI lysozyme ions are resolved from each other. This indicates that these ions have strong memories of their original structures in solution, which in turn depend on the presence or absence of disulfide bonds. Interestingly, although the Ω distributions for the $P_{DR} \rightarrow C$ ions are systematically larger than those for the $P_{DI} \rightarrow C$ ions for $C \geq 7$, the converse is true for $C \leq 5$. These difference suggest that whereas the presence of disulfide bond may limit the formation of extended structures with large Ω values for high-charge ions, they may also hinder isomerization to the most compact structures for low-charge ions.

The Ω distributions for the $P \rightarrow 3$ ions from all conditions are more similar to each other than the similarity among any other $P \rightarrow C$ ions. However, the median Ω values for the $P_{NI} \rightarrow 3$, $P_{DR} \rightarrow 3$, and $P_{DI} \rightarrow 3$ ions range from 13.40 to 13.47, 13.81 to 13.92, and 14.06 to 14.11 nm^2, respectively. Note that although these differences are smaller than the absolute accuracy estimated for these measurements,[44] most errors should be common to all of these ions since they have similar mass, similar Ω values, and identical charge states. Therefore, the relative errors should be small. Furthermore, the median Ω values for the $P_{DR} \rightarrow 3$ and $P_{DI} \rightarrow 3$ ions are all larger than those values for the $P_{NI} \rightarrow 4$ (13.44 to 13.52 nm^2) and $P_{NI} \rightarrow 5$ (13.55 to 13.64 nm^2) ions. These results suggest that IM of CAPTR products with low charge states may be still sensitive to the solution from which lysozyme ions were formed, which is different than results for cytochrome *c* ions from denaturing and native-like conditions.[40] Finally, comparisons between these results and those reported[27] for lysozyme ions following ion/neutral proton transfer reactions are discussed in the Supporting Information.

5.4.4 *Comparison of native-like and gas-phase-folded 6+ lysozyme.*

To investigate the effects of the environment in which 6+ lysozyme ions are generated, energy-dependent IM experiments were used to characterize the structures and stabilities of those

ions. In these experiments, ions are activated as a function of their kinetic energy entering the ion mobility cell; a fraction of that kinetic energy is converted to internal energy during collisions with He. An "*" is used to indicate the activated ion, *i.e.*, $P \rightarrow C^*$ indicates that the CAPTR product ion is activated. For reference, activation of most native-like ions generated from NI conditions results in the formation of additional structures that have larger Ω, which is often referred to as collision-induced unfolding.[54,55] Charge-reduced, native-like ions are more resistant to collision-induced unfolding;[56] in some cases no evidence for unfolding has been observed at energies that also results in fragmentation of covalent peptide bonds.[57]

Figures 4.5A and 4.5B show the Ω distribution of $6_{NI} \rightarrow 6^*$ ions measured with the atmospheric-pressure interface at room temperature and at 120 ˚C, respectively. At both temperatures and at low energies, the Ω distributions of the ions span from 12 to 15 nm^2 (centered around 13.5 nm^2), similar to previous results using an ambient-temperature interface and minimal activation.[44] The Ω distributions remain largely unchanged with increasing energy; there is no evidence for the formation of new structures or covalent fragmentation at the highest energies in these experiments, which were limited by the loss of signal. We propose three possible explanations for this result. (1) The energy deposited in these experiments is insufficient to overcome the barriers to isomerization. Note that collisional activation in 2 mbar of He during these experiments is less efficient than that in most collision–induced unfolding experiments, which use lower pressures of Ar. (2) The presence of four disulfide bonds affects the potential energy surface of these ions and contributes to especially high barriers to isomerization or stability of the initial native-like ions. (3) New structures are formed at high energies, but those structures yield similar Ω distributions. For reference, the Ω distributions of the $8^* \rightarrow 6$ ions of ubiquitin depend on the energy deposited into the 8+ precursor ions, even though the Ω

distributions of the 8+ ions are independent of that energy.[29] Based on these results, we are unable to differentiate contributions from these three possibilities.

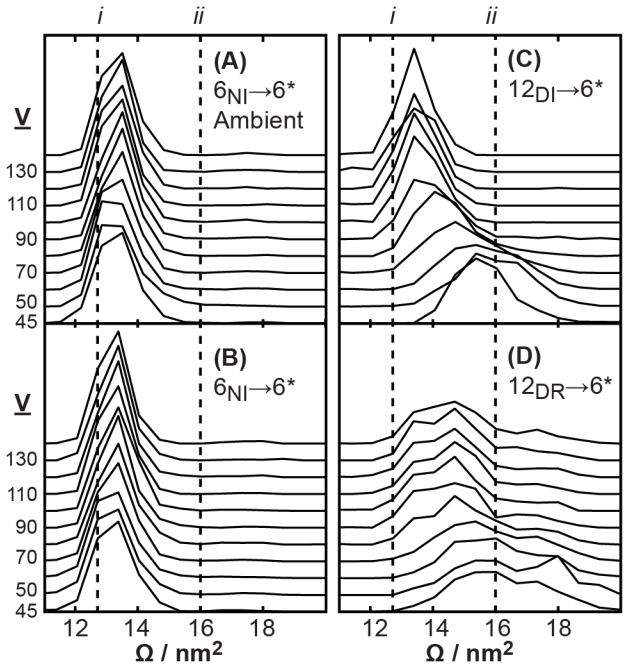

Figure 5.5. Ω distributions of the 6_{NI}→6* (**A** and **B**), 12_{DI}→6* (**C**), and 12_{DR}→6* (**D**) ions measured as a function of the bias voltage between the trap and mobility cells, which was varied from 45 to 140 V. The distributions in (A) were measured with the temperature of the atmospheric-pressure interface at ambient temperature; all other distributions were measured with the standard temperature of 120 °C. Black dashed lines (*i* and *ii*) correspond to calculated Ω values reported in Table 4.2

The 12_{DI}→6* ions (Figure 4.5C) and 12_{DR}→6* ions (Figure 4.5D) were also activated using the same range of voltages. Prior to CAPTR, the Ω distributions of 12+ lysozyme from the two solutions are resolved (Figure 4.4F). At low energy, the Ω distribution of the 12_{DI}→6* ions

ranges from 13.5 to 18 nm^2, with a maximum near 15.5 nm^2. With increasing collisional activation, the resulting Ω distributions compact. The highest energies (100 to 140 V injection) yield similar Ω distributions that range from 12 to 15 nm^2 and are centered near 13.4 nm^2. At low energy, the Ω distribution of the 12_{DR}→6* ions ranges from 13 to 20 nm^2, with features centered near 15.5 and 17.5 nm^2. With increasing energy, the Ω distributions exhibit increasing abundance near 13 nm^2, decreasing abundance near 17.5 nm^2, but similar abundance near 15.5 nm^2. At high energies, the distributions are broader than those for the other 6+ lysozyme ions analyzed using energy-dependent measurements and are consistent with the presence of multiple subpopulations of conformers over all energies. Overall these results show that the 12_{DI}→6* and 12_{DR}→6* ions compact with increasing energy, but (1) that the former ions compact more than the latter ions and (2) there is no evidence for structural convergence between these disulfide-intact and disulfide-reduced ions. The differences in the Ω distributions at the highest energies provide further evidence that the potential energy surfaces (or the regions of those surfaces populated) of lysozyme ions depend strongly on the presence or absence of disulfide bonds.

Clemmer and coworkers used collisional activation to probe the stabilities of disulfide-intact and disulfide-reduced 6+ lysozyme ions, which were generated using ion-neutral proton-transfer reactions from an ensemble of precursor ions as described in the *Introduction*.[27] The Ω distributions for those disulfide-intact lysozyme ions were independent of energy.[27] The Ω distributions for the 12_{DI}→6* ions observed here at high energies are consistent with those observed in Clemmer's experiments, whereas those observed here at low energies are larger. The Ω distributions for the disulfide-reduced lysozyme ions observed in Clemmer's experiments increased with increasing energy,[27] whereas the Ω distributions for the 12_{DR}→6* ions exhibit the opposite trend. These comparisons indicate that different regions of the potential energy surfaces

of disulfide-intact and disulfide-reduced 6+ lysozyme ions are populated in the two studies. The formation of different ions in Clemmer's experiments may be the result of differences in their precursor ions, which were an ensemble generated by electrospray,[27] or the preferential charge reduction of compact precursor ions during ion-neutral proton-transfer reactions.[50,58,59] These experiments are compared further in the Supporting Information, and all comparisons are consistent with the population of different regions of the potential energy surfaces of 6+ lysozyme in the two studies.

It is also intriguing that the $12_{DI}\rightarrow6^*$ ions at high energies compact to a Ω value similar to that of the 6+ NI ions observed here and previously[38] and the calculated Ω of native lysozyme (Table 4.2). One possibility is that a native-like structure is an important local minimum for 6+ lysozyme in the gas phase and that the $12_{DI}\rightarrow6^*$ ions isomerize to that structure. Alternatively, it is possible that the $6_{NI}\rightarrow6^*$ and $12_{DI}\rightarrow6^*$ ions have different structural distributions that coincidentally yield similar Ω distributions at high energies. Finally, it may also be the case that the $6_{NI}\rightarrow6^*$ and $12_{DI}\rightarrow6^*$ ions have all isomerized to non-native structures, which coincidentally have Ω values that are similar to those calculated for native lysozyme (Table 4.2).

5.5 Conclusions

These experiments used CAPTR and IM to investigate the relationship between the Ω distributions and charge states of lysozyme ions generated from DR, DI, and NI conditions, which maintain increasing degrees of native lysozyme in solution. For the initial ions generated from electrospray, the conditions have large effects on both their charge states (Figure 4.1) and Ω values (Figure 4.2). The Ω distributions of the CAPTR products depend strongly on the original conditions in solution and the product ion charge state. Those for the intermediate

charge states, such as C = 6 to 9, also depend to a lesser extent on the charge state of the precursor ions (Figure 4.4F). The relationship between the Ω distributions and P for these ions is stronger than that observed for ubiquitin from denaturing conditions[29] and comparable to that observed for cytochrome *c* from denaturing conditions.[40] The differences between the Ω distributions for selected 6+ ions were further characterized using energy-dependent, post-CAPTR activation of the 6_{NI}→6*, 12_{DI}→6*, and 12_{DR}→6* ions (Figure 4.5). At low energies, the Ω distributions of the three types of ions are all different. The 12_{DI}→6* ions at high energies exhibit a Ω distribution that resembles that for the 6_{NI}→6* ions over all energies, consistent with isomerization to similar native-like structures. The Ω distribution for the 12_{DR}→6* ions at high energies is very different and exhibits evidence for extended structures that were not observed for the other 6+ ions. Clearly the potential-energy surface of the 6+ ions, or at least the structures populated, depends strongly on the presence or absence of disulfide bonds.

The Ω distribution for all of the lowest charge state ions, *i.e.*, the P→3 ions, are more similar to each other than the similarity for any other P→C (Figure 4.4F and Figure S2). However, the median values for these Ω distributions still depend on the original solution conditions (Figure 4.4F). Specifically, the ranges of median Ω values for the P_{NI}→3, P_{DR}→3, and P_{DI}→3 ions range from 13.40 to 13.47, 13.81 to 13.92, and 14.06 to 14.11 nm^2, respectively. The relative size of the CAPTR products from NI conditions is further highlighted by the median Ω values for the P_{NI}→3,4,5 ions, which collectively span from 13.40 to 13.67 nm^2 and are all less than the smallest median Ω value for all of the CAPTR products from DR and DI conditions. These results indicate that despite the relatively small difference between the Ω distributions of these ions with decreasing C, those distributions may still be sensitive to the original solution conditions. This result is different than that for P→3 ions of cytochrome *c* from denaturing and

native-like conditions, which exhibited similar Ω distributions regardless of *P* and initial solutions conditions.[40]

Together, these results show that disulfide bonds have significant effects on the structures and dynamics of protein ions in the gas phase, analogous to their importance in condensed phases. These results are consistent with disulfide bonds preferentially stabilizing native-like structures in the gas phase. However, the extent to which similar Ω distributions for different CAPTR products are the result of similar structural distributions remains unclear. Future tandem experiments that probe aspects of secondary and tertiary structure, such as gas-phase hydrogen deuterium exchange,[21,58,60] spectroscopy,[16] or electron-mediated dissociation,[21,33] may provide additional insights into gas-phase folding motifs and the extent of fidelity between the structures of proteins in solution and in the gas phase.

5.6 Supporting Information.

Method for background subtraction, effects of interface temperature, comparison with 6+ lysozyme ions formed via ion-neutral charge reduction,[27] Figure S1, and Figure S2. The Supporting Information is available free of charge on the ACS Publications website at DOI: http://dx.doi.org/10.1021/acs.jpcb.7b00783. The Supporting Information is also reprinted in Appendix D.

5.7 Acknowledgments.

Research reported in this publication was supported by the American Society for Mass Spectrometry (Research Award to M. F. B.), Eli Lilly and Company (Young Investigator Award

in Analytical Chemistry to M. F. B.), and the National Institute of General Medical Sciences of the National Institutes of Health under Award Number T32GM008268 (support to K. J. L.)

5.8 References

(1) Kiss, G.; Çelebi-Ölçüm, N.; Moretti, R.; Baker, D.; Houk, K. N. Computational Enzyme Design. *Angew. Chem.* **2013**, *52* (22), 5700–5725.
(2) Moretti, R.; Fleishman, S. J.; Agius, R.; Torchala, M.; Bates, P. A.; Kastritis, P. L.; Rodrigues, J. P. G. L. M.; Trellet, M.; Bonvin, A. M. J. J.; Cui, M.; et al. Community-Wide Evaluation of Methods for Predicting the Effect of Mutations on Protein–protein Interactions. *Proteins Struct. Funct. Bioinforma.* **2013**, *81* (11), 1980–1987.
(3) Dill, K. A.; Ozkan, S. B.; Shell, M. S.; Weikl, T. R. The Protein Folding Problem. *Annu. Rev. Biophys.* **2008**, *37* (1), 289–316.
(4) Borgia, A.; Williams, P. M.; Clarke, J. Single-Molecule Studies of Protein Folding. *Annu. Rev. Biochem.* **2008**, *77* (1), 101–125.
(5) Fersht, A. R. From the First Protein Structures to Our Current Knowledge of Protein Folding: Delights and Scepticisms. *Nat. Rev. Mol. Cell Biol.* **2008**, *9* (8), 650–654.
(6) Englander, S. W.; Mayne, L. The Nature of Protein Folding Pathways. *Proc. Natl. Acad. Sci. U. S. A.* **2014**, *111* (45), 15873–15880.
(7) Bush, M. F.; Prell, J. S.; Saykally, R. J.; Williams, E. R. One Water Molecule Stabilizes the Cationized Arginine Zwitterion. *J. Am. Chem. Soc.* **2007**, *129* (44), 13544–13553.
(8) Czar, M. F.; Jockusch, R. A. Sensitive Probes of Protein Structure and Dynamics in Well-Controlled Environments: Combining Mass Spectrometry with Fluorescence Spectroscopy. *Curr. Opin. Struct. Biol.* **2015**, *34*, 123–134.
(9) Rodgers, M. T.; Armentrout, P. B. Cationic Noncovalent Interactions: Energetics and Periodic Trends. *Chem. Rev.* **2016**, *116* (9), 5642–5687.
(10) Servage, K. A.; Silveira, J. A.; Fort, K. L.; Russell, D. H. Cryogenic Ion Mobility-Mass Spectrometry: Tracking Ion Structure from Solution to the Gas Phase. *Acc. Chem. Res.* **2016**, *49* (7), 1421–1428.
(11) Zhou, M.; Sandercock, A. M.; Fraser, C. S.; Ridlova, G.; Stephens, E.; Schenauer, M. R.; Yokoi-Fong, T.; Barsky, D.; Leary, J. A.; Hershey, J. W.; et al. Mass Spectrometry Reveals Modularity and a Complete Subunit Interaction Map of the Eukaryotic Translation Factor eIF3. *Proc. Natl. Acad. Sci. U. S. A.* **2008**, *105*, 18139–18144.
(12) Shoemaker, G. K.; van Duijn, E.; Crawford, S. E.; Uetrecht, C.; Baclayon, M.; Roos, W. H.; Wuite, G. J. L.; Estes, M. K.; Prasad, B. V. V.; Heck, A. J. R. Norwalk Virus Assembly and Stability Monitored by Mass Spectrometry. *Mol. Cell. Proteomics* **2010**, *9* (8), 1742–1751.
(13) Jurneczko, E.; Barran, P. E. How Useful Is Ion Mobility Mass Spectrometry for Structural Biology? The Relationship between Protein Crystal Structures and Their Collision Cross Sections in the Gas Phase. *Analyst* **2011**, *136* (1), 20–28.
(14) Benesch, J. L.; Ruotolo, B. T. Mass Spectrometry: Come of Age for Structural and Dynamical Biology. *Curr. Opin. Struct. Biol.* **2011**, *21* (5), 641–649.

(15) Hall, Z.; Politis, A.; Robinson, C. V. Structural Modeling of Heteromeric Protein Complexes from Disassembly Pathways and Ion Mobility-Mass Spectrometry. *Structure* **2012**, *20* (9), 1596–1609.
(16) Seo, J.; Hoffmann, W.; Warnke, S.; Bowers, M. T.; Pagel, K.; von Helden, G. Retention of Native Protein Structures in the Absence of Solvent: A Coupled Ion Mobility and Spectroscopic Study. *Angew. Chem. Int. Ed.* **2016**, *55*, 14173–14176.
(17) Siuzdak, G.; Bothner, B.; Yeager, M.; Brugidou, C.; Fauquet, C. M.; Hoey, K.; Change, C.-M. Mass Spectrometry and Viral Analysis. *Chem. Biol.* **1996**, *3* (1), 45–48.
(18) Barney, B. L.; Pratt, S. N.; Austin, D. E. Survivability of Bare, Individual Bacillus Subtilis Spores to High-Velocity Surface Impact: Implications for Microbial Transfer through Space. *Planet. Space Sci.* **2016**, *125*, 20–26.
(19) Ruotolo, B. T.; Robinson, C. V. Aspects of Native Proteins Are Retained in Vacuum. *Curr. Opin. Chem. Biol.* **2006**, *10* (5), 402–408.
(20) Leney, A. C.; Heck, A. J. R. Native Mass Spectrometry: What Is in the Name? *J. Am. Soc. Mass Spectrom.* **2017**, *28* (1), 5–13.
(21) Breuker, K.; McLafferty, F. W. Stepwise Evolution of Protein Native Structure with Electrospray into the Gas Phase, 10−12 to 102 S. *Proc. Natl. Acad. Sci. U. S. A.* **2008**, *105* (47), 18145–18152.
(22) Meyer, T.; Gabelica, V.; Grubmüller, H.; Orozco, M. Proteins in the Gas Phase. *Wiley Interdiscip. Rev. Comput. Mol. Sci.* **2013**, *3* (4), 408–425.
(23) Wyttenbach, T.; Bleiholder, C.; Bowers, M. T. Factors Contributing to the Collision Cross Section of Polyatomic Ions in the Kilodalton to Gigadalton Range: Application to Ion Mobility Measurements. *Anal. Chem.* **2013**, *85*, 2191–2199.
(24) Clemmer, D. E.; Hudgins, R. R.; Jarrold, M. F. Naked Protein Conformations: Cytochrome c in the Gas Phase. *J. Am. Chem. Soc.* **1995**, *117* (40), 10141–10142.
(25) Shelimov, K. B.; Jarrold, M. F. "Denaturation" and Refolding of Cytochrome c in Vacuo. *J. Am. Chem. Soc.* **1996**, *118* (42), 10313–10314.
(26) Valentine, S. J.; Counterman, A. E.; Clemmer, D. E. Conformer-Dependent Proton-Transfer Reactions of Ubiquitin Ions. *J. Am. Soc. Mass Spectrom.* **1997**, *8* (9), 954–961.
(27) Valentine, S. J.; Anderson, J. G.; Ellington, A. D.; Clemmer, D. E. Disulfide-Intact and -Reduced Lysozyme in the Gas Phase: Conformations and Pathways of Folding and Unfolding. *J. Phys. Chem. B* **1997**, *101* (19), 3891–3900.
(28) Lermyte, F.; Łącki, M. K.; Valkenborg, D.; Gambin, A.; Sobott, F. Conformational Space and Stability of ETD Charge Reduction Products of Ubiquitin. *J. Am. Soc. Mass Spectrom.* **2016**, *28*, 69–76.
(29) Laszlo, K. J.; Munger, E. B.; Bush, M. F. Folding of Protein Ions in the Gas Phase after Cation-to-Anion Proton-Transfer Reactions. *J. Am. Chem. Soc.* **2016**, *138* (30), 9581–9588.
(30) Jhingree, J. R.; Beveridge, R.; Dickinson, E. R.; Williams, J. P.; Brown, J. M.; Bellina, B.; Barran, P. E. Electron Transfer with No Dissociation Ion Mobility–mass Spectrometry (ETnoD IM–MS). The Effect of Charge Reduction on Protein Conformation. *Int. J. Mass Spectrom.* **2017**, DOI: 10.1016/j.ijms.2016.08.006.
(31) McLuckey, S. A.; Stephenson, J. L. Ion/Ion Chemistry of High-Mass Multiply Charged Ions. *Mass Spectrom. Rev.* **1998**, *17* (6), 369–407.

(32) Chrisman, P. A.; Pitteri, S. J.; Hogan, J. M.; McLuckey, S. A. SO2−· Electron Transfer Ion/Ion Reactions with Disulfide Linked Polypeptide Ions. *J. Am. Soc. Mass Spectrom.* **2005**, *16* (7), 1020–1030.
(33) Lermyte, F.; Konijnenberg, A.; Williams, J. P.; Brown, J. M.; Valkenborg, D.; Sobott, F. ETD Allows for Native Surface Mapping of a 150 kDa Noncovalent Complex on a Commercial Q-TWIMS-TOF Instrument. *J. Am. Soc. Mass Spectrom.* **2014**, *25* (3), 343–350.
(34) Stephenson, J. L.; McLuckey, S. A. Ion/Ion Proton Transfer Reactions for Protein Mixture Analysis. *Anal. Chem.* **1996**, *68* (22), 4026–4032.
(35) Gunawardena, H. P.; He, M.; Chrisman, P. A.; Pitteri, S. J.; Hogan, J. M.; Hodges, B. D. M.; McLuckey, S. A. Electron Transfer versus Proton Transfer in Gas-Phase Ion/Ion Reactions of Polyprotonated Peptides. *J. Am. Chem. Soc.* **2005**, *127* (36), 12627–12639.
(36) Laszlo, K. J.; Bush, M. F. Analysis of Native-Like Proteins and Protein Complexes Using Cation to Anion Proton Transfer Reactions (CAPTR). *J. Am. Soc. Mass Spectrom.* **2015**, *26*, 2152–2161.
(37) Salbo, R.; Bush, M. F.; Naver, H.; Campuzano, I.; Robinson, C. V.; Pettersson, I.; Jørgensen, T. J. D.; Haselmann, K. F. Traveling-Wave Ion Mobility Mass Spectrometry of Protein Complexes: Accurate Calibrated Collision Cross-Sections of Human Insulin Oligomers. *Rapid Commun. Mass Spectrom.* **2012**, *26* (10), 1181–1193.
(38) Allen, S. J.; Schwartz, A. M.; Bush, M. F. Effects of Polarity on the Structures and Charge States of Native-Like Proteins and Protein Complexes in the Gas Phase. *Anal. Chem.* **2013**, *85* (24), 12055–12061.
(39) Bleiholder, C.; Johnson, N. R.; Contreras, S.; Wyttenbach, T.; Bowers, M. T. Molecular Structures and Ion Mobility Cross Sections: Analysis of the Effects of He and N2 Buffer Gas. *Anal. Chem.* **2015**, *87* (14), 7196–7203.
(40) Laszlo, K. J.; Buckner, J. H.; Munger, E. B.; Bush, M. F. Native-like and Denatured Cytochrome c Ions Yield Cation-to-Anion Proton-Transfer Reaction Products with Similar Collision Cross Sections. *J. Am. Soc. Mass Spectrom.* In Press, DOI: 10.1007/s13361-017-1620-4.
(41) Davidson, K. L.; Oberreit, D. R.; Hogan Jr., C. J.; Bush, M. F. Nonspecific Aggregation in Native Electrokinetic Nanoelectrospray Ionization. *Int. J. Mass Spectrom.* **2017**, DOI: 10.1016/j.ijms.2016.09.013.
(42) Williams, J. P.; Brown, J. M.; Campuzano, I.; Sadler, P. J. Identifying Drug Metallation Sites on Peptides Using Electron Transfer Dissociation (ETD), Collision Induced Dissociation (CID) and Ion Mobility-Mass Spectrometry (IM-MS). *Chem. Commun.* **2010**, *46* (30), 5458–5460.
(43) Stephenson, J. L.; McLuckey, S. A. Ion/Ion Reactions in the Gas Phase: Proton Transfer Reactions Involving Multiply-Charged Proteins. *J. Am. Chem. Soc.* **1996**, *118* (31), 7390–7397.
(44) Allen, S.; Giles, K.; Gilbert, T.; Bush, M. Ion Mobility Mass Spectrometry of Peptide, Protein, and Protein Complex Ions Using a Radio-Frequency Confining Drift Cell. *Analyst* **2016**, *141*, 884–891.
(45) von Helden, G.; Hsu, M. T.; Gotts, N.; Bowers, M. T. Carbon Cluster Cations with up to 84 Atoms: Structures, Formation Mechanism, and Reactivity. *J. Phys. Chem.* **1993**, *97* (31), 8182–8192.

(46) Shvartsburg, A. A.; Jarrold, M. F. An Exact Hard-Spheres Scattering Model for the Mobilities of Polyatomic Ions. *Chem. Phys. Lett.* **1996**, *261* (1–2), 86–91.
(47) Shvartsburg, A. A.; Mashkevich, S. V.; Baker, E. S.; Smith, R. D. Optimization of Algorithms for Ion Mobility Calculations. *J. Phys. Chem. A* **2007**, *111* (10), 2002–2010.
(48) Schwalbe, H.; Grimshaw, S. B.; Spencer, A.; Buck, M.; Boyd, J.; Dobson, C. M.; Redfield, C.; Smith, L. J. A Refined Solution Structure of Hen Lysozyme Determined Using Residual Dipolar Coupling Data. *Protein Sci.* **2001**, *10* (4), 677–688.
(49) Pettersen, E. F.; Goddard, T. D.; Huang, C. C.; Couch, G. S.; Greenblatt, D. M.; Meng, E. C.; Ferrin, T. E. UCSF Chimera--a Visualization System for Exploratory Research and Analysis. *J. Comput. Chem.* **2004**, *25* (13), 1605–1612.
(50) Gross, D. S.; Schnier, P. D.; Rodriguez-Cruz, S. E.; Fagerquist, C. K.; Williams, E. R. Conformations and Folding of Lysozyme Ions in Vacuo. *Proc. Natl. Acad. Sci. U. S. A.* **1996**, *93* (7), 3143–3148.
(51) IDCalc -- Isotope Distribution Calculator https://proteome.gs.washington.edu/software/IDCalc/ (accessed Jun 23, 2016).
(52) Kubinyi, H. Calculation of Isotope Distributions in Mass Spectrometry. A Trivial Solution for a Non-Trivial Problem. *Anal. Chim. Acta* **1991**, *247* (1), 107–119.
(53) Uniprot entry P00698 http://www.uniprot.org/uniprot/P00698.
(54) Ruotolo, B. T.; Hyung, S.-J.; Robinson, P. M.; Giles, K.; Bateman, R. H.; Robinson, C. V. Ion Mobility–Mass Spectrometry Reveals Long-Lived, Unfolded Intermediates in the Dissociation of Protein Complexes. *Angew. Chem. Int. Ed.* **2007**, *46* (42), 8001–8004.
(55) Freeke, J.; Bush, M. F.; Robinson, C. V.; Ruotolo, B. T. Gas-Phase Protein Assemblies: Unfolding Landscapes and Preserving Native-like Structures Using Noncovalent Adducts. *Chem. Phys. Lett.* **2012**, *524*, 1–9.
(56) Hall, Z.; Politis, A.; Bush, M. F.; Smith, L. J.; Robinson, C. V. Charge-State Dependent Compaction and Dissociation of Protein Complexes: Insights from Ion Mobility and Molecular Dynamics. *J. Am. Chem. Soc.* **2012**, *134* (7), 3429–3438.
(57) Pagel, K.; Hyung, S.-J.; Ruotolo, B. T.; Robinson, C. V. Alternate Dissociation Pathways Identified in Charge-Reduced Protein Complex Ions. *Anal. Chem.* **2010**, *82* (12), 5363–5372.
(58) Cassady, C. J.; Carr, S. R. Elucidation of Isomeric Structures for Ubiquitin [M+12H]12+ Ions Produced by Electrospray Ionization Mass Spectrometry. *J. Mass Spectrom.* **1996**, *31* (3), 247–254.
(59) Valentine, S. J.; Counterman, A. E.; Clemmer, D. E. Conformer-Dependent Proton-Transfer Reactions of Ubiquitin Ions. *J. Am. Soc. Mass Spectrom.* **1997**, *8* (9), 954–961.
(60) Khakinejad, M.; Kondalaji, S. G.; Donohoe, G. C.; Valentine, S. J. Ion Mobility Spectrometry-Hydrogen Deuterium Exchange Mass Spectrometry of Anions: Part 2. Assessing Charge Site Location and Isotope Scrambling. *J. Am. Soc. Mass Spectrom.* **2016**, *27* (3), 451–461.

Chapter 6. Interpreting the Collision Cross Sections of Native-Like Protein Ions: Insights from Cation-to-Anion Proton-Transfer Reactions

---

This chapter is reproduced with permission from Laszlo, K. J.; Bush, M. F. "Interpreting the Collision Cross Sections of Native-Like Protein Ions: Insights from Cation-to-Anion Proton-Transfer Reactions" **2017**, manuscript in preparation

6.1 Abstract

The effects of charge state on structures of native-like serum albumin, streptavidin, avidin, and alcohol dehydrogenase were probed using cation-to-anion proton-transfer reactions (CAPTR), ion mobility, mass spectrometry, and complementary energy-dependent experiments. The CAPTR products all have collision cross section (Ω) values that are within 5.5% of the original precursors. The first CAPTR event for each precursor yields products that have smaller Ω values and frequently exhibit the greatest magnitude of change in Ω resulting from a single CAPTR event. To investigate how the structure of the precursors affect the structures of the products, ions were activated as a function of energy prior to CAPTR. In each case, the Ω distributions of the activated precursors increase with increasing energy, but the Ω distributions of the CAPTR products are significantly more compact than the activated precursors. To investigate the stabilities of the CAPTR products, the products were activated immediately prior to ion mobility. These results show that additional structures with smaller or larger Ω can be populated and that the structures and stabilities of these ions depend most strongly on the identity of the protein and the charge state of the product, rather than the charge state of the

precursor or the number of CAPTR events. Together, these results indicate that the excess charges initially present on native-like ions have a modest, but statistically significant, effect on their Ω values. Therefore, potential contributions from charge state should be considered when using experimental Ω values to elucidate structures in solution.

6.2 Introduction

Native-like ions are generated using electrospray ionization of proteins, nucleic acids, lipids, and other biological molecules in aqueous solutions with biologically relevant pH and ionic strength.[1–3] These ions can retain noncovalent interactions in the gas phase that were present in the original solution.[1,4] The stoichiometry and relative abundance of these noncovalent complexes can be probed using mass spectrometry (MS).[1] Advances in ion mobility (IM) have enabled accurate measurements of collision cross sections (Ω) of ions of proteins and their noncovalent complexes.[5–7] As a result, there is increasing interest in using IM-MS measurements in structural biology and biophysics.[8,9] For example, IM-MS measurements have provided significant contributions to the fields of amyloid[10,11] and serpinopathy[12] formation, virus capsid assembly,[13,14] small heat shock protein subunit dynamics,[15] and ATPase function.[16]

The charge states of native-like ions appear to be independent of the magnitude and polarity of their charge states in solution, and instead appear to depend on the ionization mechanism.[17,18] Therefore, it is important to consider the effects of charge state in the interpretation of experimental Ω values for biological molecules in the gas phase. The Ω values of many native-like ions of larger proteins and protein complexes can depend weakly on z.[5,18,19] In contrast, stronger relationships between Ω and z have been reported for native-like ions of

smaller proteins,[20,21] prion and intrinsically disordered proteins,[22,23] and proteins generated from solutions with "supercharging" reagents,[24] as well as protein ions from denaturing solutions.[25,26] Thus, it is unclear from IM-MS measurements alone the extent to which the z of a native-like ion affects its structure, and whether low-z ions have "more native" structures. As a result, several approaches to report Ω with respect to z have been implemented that each implicitly assume different relationships between z and the structure of a native-like ion, including reporting a Ω for each z measured,[5,18] reporting an average Ω,[27] and extrapolating to the Ω of a "zero-charge" protein.[28] Those difference lead to ambiguities in how Ω measurements should restrict possible structural models.

Several studies have investigated the relationship between Ω and z for native-like protein cations by reducing the magnitude of z. Modest charge reduction caused by addition of a base to the solution prior to ionization or reacting the ions with a neutral with a higher gas-phase basicity revealed that the Ω of the charge-reduced ions are similar to those produced under typical native MS conditions and depend weakly on z.[18,29,30] In contrast, there have been reports of significant compaction for lower-z products of native-like ions based on traveling-wave ion mobility spectrometry (TWIMS) and more extensive charge reduction enabled by ion/ion reactions.[31,32] Charge reduction in those experiments was the result of competitive proton transfer and electron transfer reactions:

$$[M_n + zH]^{z+} + A^{\bullet -} \rightarrow [M_n + zH]^{\bullet (z-1)+} + A \qquad \text{(Reaction 1)}$$

$$[M_n + zH]^{z+} + A^{-} \rightarrow [M_n + (z-1)H]^{(z-1)+} + AH \qquad \text{(Reaction 2)}$$

These competitive reaction products complicate data interpretation because the m/z difference between the products were not resolvable, and Reaction 1 results in the formation of radical

cations that may undergo additional chemistry and concomitant changes to the identity and/or structure of the product.[33]

Recently, we used cation-to-anion proton-transfer reactions (CAPTR), which yields a long series of charge-reduced product ions originating from quadrupole-selected precursor ions,[34] to reduce positive charge states of cytochrome *c*[35] and lysozyme[36] ions generated from native-like, aqueous conditions. The CAPTR products were then analyzed using an rf-confining drift cell,[19] which enables absolute measurements of mobilities that are indistinguishable from those determined using electrostatic drift tubes.[5,19,37] The lowest-*z* CAPTR products had Ω values that were up to 10.6% and 8.4% smaller than those for the highest-*z* precursors of native-like cytochrome *c*[35] and lysozyme,[36] respectively. For comparison, CAPTR of the highest-*z* ions generated from denaturing conditions results in the formation of low-*z* products with Ω values that are roughly twofold smaller than those of the precursors.[26,35,36] The objective of this study is to use CAPTR, IM-MS, and complementary energy-dependent experiments to determine the effect of *z* on the Ω of native-like ions of large proteins and protein complexes. The results indicate that the range in Ω measurements over many *z* should be considered to restrain potential structures of those ions in the context of structural biology, rather than the precision of a single *z*.

6.3 Methods

6.3.1 *Samples and Ionization.*

All proteins were purchased from Sigma Aldrich and dissolved into the buffer, which was aqueous 200 mM ammonium acetate at pH 7. For serum albumin, streptavidin, and alcohol dehydrogenase, Micro Bio-Spin 6 columns (Bio-Rad, Hercules, CA) were used to exchange the

buffer and remove nonvolatile salts from the original solution. Final electrospray solutions contained 5 to 20 μM protein. Nanoelectrospray sample capillaries were prepared and loaded as described previously.[38] The inlet to the mass spectrometer was heated to 120 ºC; under these conditions there is some convective heat transfer to the sample capillary.[26,35]

Cation-to-Anion Proton-Transfer Reactions. Experiments were performed using a modified Waters Synapt G2 HDMS equipped with a glow-discharge ionization source[39] for anion generation (Figure 6.1). Briefly, perfluoro-1,3-dimethylcyclohexane (PDCH)[40] vapor was introduced into nitrogen gas that was passed through a sharpened glow-discharge ionization needle. Anions were generated for 0.1 s, during which time the fragment $[PDCH\text{-}F]^-$ at *m*/*z* 381 was quadrupole selected and accumulated in the trap cell.[34] Following anion accumulation, the instrument was switched into positive ion mode for 2 to 10 s for protein cation transmission. Example relative potentials for cation transmission are shown in Figure 6.1. To initiate CAPTR, quadrupole-selected precursor ions were trapped with the stored anions. Both unreacted precursor and CAPTR product ions were then analyzed using IM-MS.

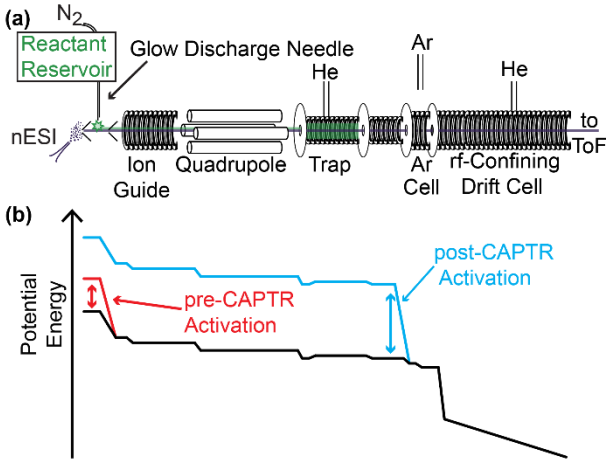

Figure 6.1. (a) Instrument diagram of Waters Synapt G2 HDMS mass spectrometer, modified for ion/ion reactions and absolute mobility

measurements.[19] (b) Typical potentials used for cation transmission (*black*). For pre-CAPTR activation experiments, the bias between the first two ion optics in the atmospheric-pressure interface was increased (*red*). For post-CAPTR activation experiments, ions were injected as a function of energy into a region immediately prior to the rf-confining drift cell was pressured with argon gas (*cyan*), as described in *Methods*.

6.3.2 *Ion Mobility.*

IM separations were performed using an rf-confining drift cell,[19] which replaced the traveling-wave IM cell of the original instrument. The drift velocity of ions in this cell is the product of their mobility (K) and the applied drift field,[19,37] similar to electrostatic drift cells. IM experiments were performed in 2 mbar of helium, unless otherwise noted. K values for the CAPTR product ions were determined from drift times measured using a drift voltage of 212 V that were corrected for the transport time to the time-of-flight mass analyzer. The method used to correct the drift times, a discussion of the associated errors, and comparisons with field-dependent methods (Figures S1 to S3) are included in the Supporting Information. Values of K were then converted to Ω using the Mason-Schamp equation:[41]

$$\Omega = \frac{3ez}{16N}\left(\frac{2\pi}{\mu k_B T}\right)^{1/2}\frac{1}{K} \qquad \text{(Equation 6.1)}$$

where e is the elementary charge, z is charge state, N is the neutral gas number density, μ is reduced mass, k_B is Boltzmann's constant, and T is temperature. A discussion of how the drift voltage may affect Ω measurements can be found the Supporting Information

6.3.3 *Pre- and Post-CAPTR Activation.*

Selected experiments were performed in which ions were activated as they enter the atmospheric-pressure interface of the instrument (pre-CAPTR activation) or the drift cell (post-CAPTR activation). The relative potentials in those experiments are indicated in Figure 6.1. For post-CAPTR activation, the drift cell was modified by adding an additional aperture to the front of the rf-confining drift cell,[19] establishing a short pressurized region with independent gas control that is analogous to the "helium cell" of the traveling-wave IM cell of a Synapt G2 HDMS instrument.[7] During post-CAPTR experiments, 15 ml min^{-1} of argon gas was introduced into this region. The flow rate of helium to the drift cell was adjusted so that the total pressure of argon and helium was 2 mbar.

6.3.4 *Ω Calculations.*

Ω for serum albumin (PDB: 4F5S),[42] streptavidin (PDB: 4Y5D),[43] avidin (PDB: 1AVD),[44] and alcohol dehydrogenase (PDB: 5ENV)[45] were calculated using the projection approximation[46] and exact hard-sphere scattering[47] methods as implemented in EHSS2/k.[48] Prior to the Ω calculations, all noncovalent additions to the protein(s) in the deposited structures, including water molecules and metal ions, were deleted and Chimera[49] was used to complete side chains and add hydrogen atoms.

6.4 Results and Discussion

Ω values determined using IM measurements of native-like ions are used to restrain models for proteins and protein complexes in solution. Therefore, an accurate understanding of the effects of charge state on the structures of gas-phase protein ions is important for

interpreting the results of native IM-MS experiments in the context of structural biology and biophysics. Here, the effects of *z* on the Ω values of native-like ions were investigated using CAPTR, IM-MS, and energy-dependent experiments. Serum albumin (67 kDa, monomer), streptavidin (53 kDa, homotetramer), avidin (64 kDa, homotetramer), and alcohol dehydrogenase (147 kDa, homotetramer) were selected based on their use as model systems[50–52] and as calibration standards[5,19] for native IM-MS. Streptavidin and avidin are homologs, but avidin is glycosylated, and as a consequence, has a larger mass.[53,54]

IM-MS was used to characterize the CAPTR products originating from two to four of the most abundant charge states of serum albumin, streptavidin, avidin, and alcohol dehydrogenase. For example, Figure 6.2 shows representative data for serum albumin. First, native-like ions were generated using electrospray ionization (Figure 6.2a). From those ions, the 17+ cations were quadrupole selected (Figure 6.2b) and subjected to CAPTR (Figure 6.2c). In CAPTR, multiply charged protein cations are reacted with $[PDCH-F]^-$ anions to yield a long series of charge-reduced products via Reaction 2. CAPTR products will be referred to as "*P*→*C*" where "*P*" is the charge state of the precursor and "*C*" is the charge state of the CAPTR product. Following CAPTR, product ions and residual precursor ions were injected into an rf-confining drift cell[19,37] and separated on the basis of their mobility in helium gas (Figure 6.2d). The arrival-time distributions were then used to determine apparent Ω distributions, as described in the *Methods* and Supporting Information.

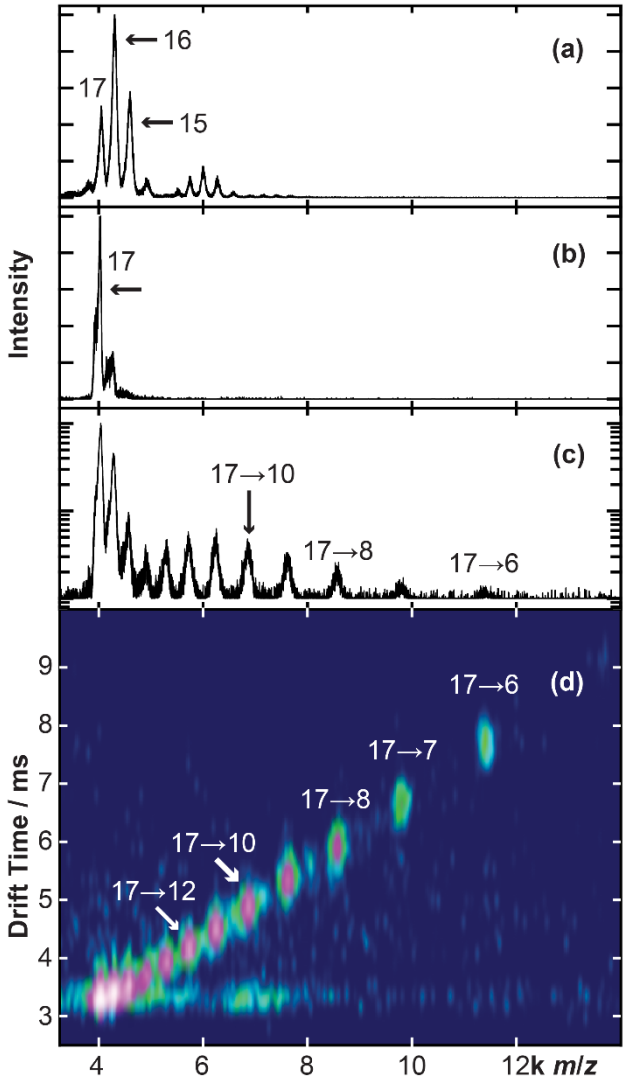

Figure 6.2. (a) Mass spectrum of native-like serum albumin. Additional peaks centered around *m*/*z* 6,000 correspond to non-specific dimers of serum albumin. (b) Quadrupole-selected 17+ serum albumin. (c) CAPTR of the selected ions results in a series of charge-reduced products (17→*C*). Intensities are plotted logarithmically. (d) Plot of the IM-MS data for the 17→*C* ions. Colors in this panel are proportional to a nested logarithm function of the intensity, i.*e.* $\log_{10}(\log_{10}(\text{intensity}))$, to aid in visualization of the data.

The Ω values determined using this approach are shown in Figure 6.3. These values are bracketed by those calculated using the PA and EHSS methods, which are respectively used as the lower and upper bounds of the plot. This bracketing is consistent with previous reports that these methods typically underestimate and overestimate the Ω values for native-like ions, respectively.[20] Significantly, the CAPTR products do not exhibit evidence for a large-scale structural collapses with decreasing *z*, as reported for the CAPTR products of high-*z* protein ions generated from denaturing conditions.[26,35,36] Note that all experimental Ω values reported in this work include the 95% confidence intervals, based on three replicate measurements and *t*-statistics. Visual analysis of the data in Figure 6.3 suggests that after the first few CAPTR events for a given protein, the Ω values for ions of a given *C* originating from different *P* are similar and the differences are likely not significant. The general trends in the Ω values for each protein as a function of *C* appears to be general to all precursors of a given protein, which creates a larger sample size and increases the significance of those trends.

The Ω values of the serum albumin precursor ions are 43.0 ± 1.1, 42.1 ± 1.0, and 41.7 ± 1.5 nm^2 for the 17+, 16+, and 15+ ions, respectively (Figure 6.3a). These values are 3.3 to 4.4% larger than those reported previously,[18] indicating that relative to previous experiments the ions in these experiments may have partially unfolded prior to CAPTR. Following the first CAPTR event, the Ω of the products are 2% to 3% smaller than those of the corresponding precursor ions. The most compact CAPTR product ions are 3% to 5.5% more compact than their respective precursor ion. Interestingly, the Ω values for all $P \rightarrow 14$ to 6 ions vary by only ±1.2%. Although all CAPTR product ions are more compact than the corresponding precursor ion, most of the change in Ω occurs during the first one to three CAPTR events.

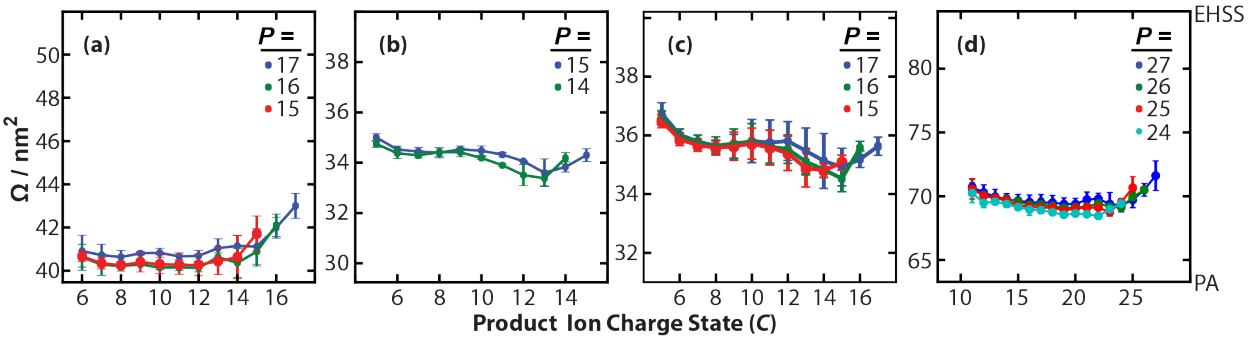

Figure 6.3. Ω values of the $P \rightarrow C$ ions of (a) serum albumin, (b) streptavidin, (c) avidin and (d) alcohol dehydrogenase, where "*P*" is the charge state of the precursor and "*C*" is the charge state of the CAPTR product. The bars span the 95% confidence interval for each value, and the upper and lower limits of each panel correspond to the Ω values calculated using the PA and EHSS methods, as described in *Methods* and summarized in Table S1. The different colors are used indicate ions from different *P*.

For streptavidin, the Ω values of the precursor ions are 34.3 ± 0.5 and 34.2 ± 0.4 nm^2 for the 15+ and 14+ ions, respectively (Figure 6.3b). The $P \rightarrow 13$ ions were the most compact CAPTR products, but the Ω values of those products were less than 2.5% smaller than the original precursor ions. The $15 \rightarrow 5$ and $14 \rightarrow 5$ ions had Ω of 35.0 ± 0.3 and 34.7 ± 0.2 nm^2, respectively, which were the largest of all the CAPTR products for each precursor. For avidin, the Ω values of the 17+ to 15+ precursor ions are 0.9 to 1.8% smaller than those reported previously,[18] consistent with these ions retaining their native-like conformations. The Ω of 17+ avidin was 35.6 ± 0.6 nm^2. The most-compact product was formed following two CAPTR events (34.9 ± 1.2 nm^2), but the Ω of the products of the subsequent CAPTR events increase

slightly until the value of 36.7 ± 0.7 nm^2 determined for the 17→5 ions. Analogous trends were observed for the 16→*C* and 15→*C* ions, and the Ω values for all of the CAPTR products of avidin are within 4% of the precursor ions. The relationship between Ω and *z* for avidin is similar that observed for streptavidin, which suggests that the presence of glycans has a minor effect on how avidin ions respond to changes in charge state.

For alcohol dehydrogenase, the Ω values of the precursor ions are 70.4 ± 2.3, 69.1 ± 0.5, 69.3 ±1.8, and 68.0 ± 0.6 nm^2 for the 27+ to 24+ ions, respectively (Figure 6.3d). These values differ by 0.2%, −1.6%, −1.3% and −3.3%, respectively, relative to those reported previously.[18] The value for the 24+ precursor is notably small, suggesting that these ions may be more compact than those investigated previously.[18] Relative to each precursor, the Ω values of the products of the first two to three CAPTR events decrease and are up to 3.6% smaller than the respective precursors. In contrast, the Ω values of the subsequent CAPTR events increase and have values that are up to 1.3% larger than the precursors. The Ω values for *P*→11 ions, which was the lowest *C* observed, ranged from 69.4 ± 1.3 to 68.8 ± 1.5 nm^2, which correspond to a −1.4% to +1.3% change in Ω relative to the respective precursor. Therefore, the differences in the Ω of the precursor ions are larger than the differences for the lowest-*C* products observed.

The CAPTR products of native-like serum albumin, streptavidin, avidin, and alcohol dehydrogenase all have Ω values that are within 5.5% of their original precursors. The first CAPTR event for each precursor yields products that have smaller Ω values and frequently exhibit the greatest magnitude of change in Ω resulting from a single CAPTR event. The Ω values of the products of the subsequent CAPTR events exhibit either small decreases or increases in Ω. The Ω values of the CAPTR products, relative to Ω value of the precursor, span from −5.5% to −2.9% for serum albumin, −2.3% to 2.1% for streptavidin, −2.9% to 4.0% for

avidin, and −3.6% to 1.3% for alcohol dehydrogenase. The maximum decreases in Ω with decreasing charge are smaller than the decreases reported based on CAPTR and rf-confining drift cell analysis of lower-mass (8.6 to 14 kDa) protein ions[26,35,36] and reported based on other charge reduction approaches using ion/ion chemistry and traveling-wave IM of alcohol dehydrogenase[32] and pyruvate kinase (230 kDa).[31] It should also be noted that some of the native-like precursor ions in this study had slightly larger Ω values than reported previsouly,[18] which may be attributable to destabilization of the precursor ions concomitant with heating in the sample capillary[35] or during transport through the elevated-temperature, atmospheric-pressure interface.[55] The destabilization of the precursor ions under these conditions is supported by arrival-time distributions of 27+ alcohol dehydrogenase measured as a function of the bias voltage between the first two ion optics in the atmospheric-pressure interface at ambient temperature and at 120 °C; ions under the latter conditions unfold at lower voltages (Figure S5). Therefore, it is possible that the small decreases observed for the initial CAPTR events are consistent with the refolding of partially disrupted structures. To investigate how the structures of the precursors affect the structures of the CAPTR products, we performed additional energy-dependent experiments that will be discussed in *Pre-CAPTR Activation*.

The origin of the small increase in Ω with decreasing *z* for some ions is not obvious. One possibility is that there is a systemic error in our measurements. Possible biases based on the strength of the electric field in the IM cell are discussed at length in the Supporting Information. Alternatively, similar phenomena have been described before. In order to explain the subtle increase in Ω for very low charge states of cytochrome *c* formed by ion/ion proton-transfer reactions, Badman and co-workers proposed that the loss of protons disrupts some hydrogen bonds, resulting in structures that are more flexible and less compact.[53] The loss of

some stabilizing interactions after charge reduction is also consistent with the enhanced ultraviolet photodissociation observed for the ion/ion proton transfer products of native-like ions, which the authors attribute to fraying in the terminal regions of the charge-reduced products relative to the native-like precursors.[54] Additionally, each CAPTR event is exothermic and the internal energy of CAPTR products may increase over the course of several reactions. For comparison, we estimated that CAPTR events are exothermic by at least 200 kJ/mol per reaction.[34] To investigate how activation of the products affect their structures, we performed additional energy-dependent experiments that will be discussed in *Post-CAPTR Activation*.

More generally, the results of these CAPTR experiments indicate that the excess charges on native-like ions with large masses have a relatively small (less than 5.5%) effect on their Ω. This finding is consistent with the conclusions drawn from modest charge-reduction using solution additives[18,29] and ion/neutral reactions.[29] In contrast, two studies using traveling-wave IM to analyze ions with a comparable extent of charge reduction reported significant compaction with decreasing *z*.[31,32] Results from these studies[18,29,31,32] are compared further in Figure S4, Table S2, and the associated discussion in the Supporting Information. Differences between the two measurements that may explain the differences in the data include the mechanism of charge reduction and the type of IM cell used.

Pre-CAPTR Activation. To probe the effects of the structures of the precursors on the structures of the CAPTR products, native-like ions were analyzed as a function of the bias voltage between the first two ion optics in the atmospheric-pressure interface. Increasing the bias voltage will increase the extent of collisional activation in the interface. The activated species in these experiments is indicated with an "*", *i.e.*, $P^* \rightarrow C$. Note that in our previous pre-CAPTR activation experiments, ions were activated as a function of their injection energy into

the helium-filled trap cell where CAPTR is performed.[26] For these larger ions with more degrees of freedom, collisions with helium at the kinetic energies accessible on this instrument were inadequate to induce changes in Ω. One disadvantage of the current approach is that activation, which can also result in loss of charge,[48] is performed prior to quadrupole selection.

Figure 6.4a shows the Ω distributions of 15+ serum albumin as a function of the activation voltage. With increasing energy, the distribution increases monotonically to values centered near 50 nm^2. Figures 6.4b-d show the Ω distributions of the 15*→9, 15*→7, and 15*→6 ions as a function of the activation voltage. With increasing activation voltage, the Ω distributions indicate that the CAPTR products of the activated precursor ions are more compact than the activated precursor ions and similar to the minimally activated precursor ions. The pre-CAPTR activation results for the 15*→*C* ions of streptavidin, 17*→*C* ions of avidin, and 27*→*C* ions of alcohol dehydrogenase are shown in Figure S6. In each case, the Ω distributions of the activated precursors increase with increasing energy, but the Ω distributions indicate that the CAPTR products are significantly more compact than the activated precursors. Interestingly, there is no evidence for the formation of CAPTR products with Ω distributions that are more compact than the minimally-activated precursor ions.

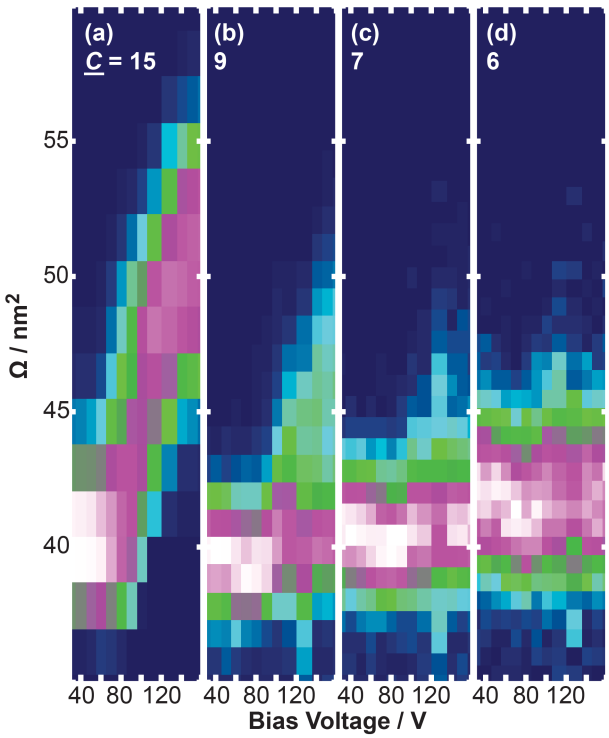

Figure 6.4. Ω distributions of 15*→*C* ions of serum album that were activated prior to CAPTR, where the "*" indicates the collisionally activated ion. Data is shown as a function of the voltage bias between the first two optics in the atmospheric-pressure interface (Figure 6.1b). Note that these distributions were determined using a lower drift voltage than used to acquire the data summarized in Figure 6.3, which may bias these apparent Ω distributions to slightly larger values as discussed in the Supporting Information. Results from pre-CAPTR activation of 15+ streptavidin, 17+ avidin, and 27+ alcohol dehydrogenase are shown in Figure S6.

In most cases with adequate energy and time, slow heating of a protein ion (including activation under multiple collision conditions) results in the loss of a monomeric subunit that retains a disproportionally large fraction of the total charge relative to the masses of the two

products.[58,59] This asymmetric charge partitioning has been attributed to a dissociation mechanism in which the unfolding of a single subunit and charge migration to that subunit work in concert to reduce the Coulombic energy of the complex prior to dissociation.[58,60,61] This model suggests that the increase in Ω for the activated precursors is the result of unfolding of a single protein.[62] Because the unfolded region will have a disproportionally large fraction of the total charge, this region may be the origin of a disproportionally large fraction of the protons transferred during these experiments. The results from these pre-CAPTR activation experiments therefore suggests that the CAPTR products fold to more compact structures that enable additional noncovalent interactions, consistent with their lower charge states and reduced Coulombic energy. This finding may also have implications in the interpretation of Ω measurements of surface-induced dissociation product ions, which generally have lower charge states and compact Ω than those produced via collisional activation.[63] Consequentially, if there were unfolded intermediates following SID, they may compact due to their low *z*. The folding in these pre-CAPTR activation experiments appears to be analogous to that reported for the CAPTR products of unfolded ubiquitin,[26] cytochrome *c*,[35] and lysozyme[36] ions generated from denaturing conditions. In all these cases, the Ω of the lowest-*C* products are similar to those of the corresponding native-like ions, thus these protein ions fold in the gas-phase to sizes similar to the corresponding native-like structure. However, beyond Ω, the degree to which refolded CAPTR product ions and native-like ions share similar structures remains uncertain.

Post-CAPTR Activation. To investigate the stabilities of CAPTR products, the products were activated as a function of their kinetic energy prior to IM. The activated ions in these experiments are indicated with an "*", *i.e.*, $P \rightarrow C^*$. Note that in our previous post-CAPTR activation experiments, ions were activated as a function of their injection energy into a helium-

filled drift cell.[26,36] As per the pre-CAPTR experiments, collisions with helium were inadequate to induce changes in Ω. Instead, ions were injected as a function of their kinetic energy into a small cell positioned at the entrance to the drift cell (see *Methods*) that was filled with argon to enable more efficient conversion from translational to internal degrees of freedom. One disadvantage of this approach is that the drift cell will contain a mixture of helium and argon gases and will have a net flow of gas along the longitudinal axis. Therefore, the IM results will be reported in terms of drift time instead of Ω.

Figure 6.5a shows the arrival-time distributions for 15→13* serum albumin as a function of the laboratory frame energy, which is the product of *C* and the voltage used to inject the ions into the argon-filled cell. At the lowest energy, the distribution is centered near 7.4 ms and unimodal, which is consistent with the peak shape for experiments performed without the additional cell. With increasing energies to ~780 eV, the distributions shift to smaller values centered near 7.2 ms that are consistent with the formation of more compact structures. Then with increasing energies to ~1500 eV, the distributions shift to larger values centered near 8.9 ms. That distribution persists with increasing energy, consistent with the formation of a quasi-equilibrium of structures in these experiments.[64] The results of the 16→13* ions are shown in Figure S7a and are nearly identical to those for the 15→13* ions.

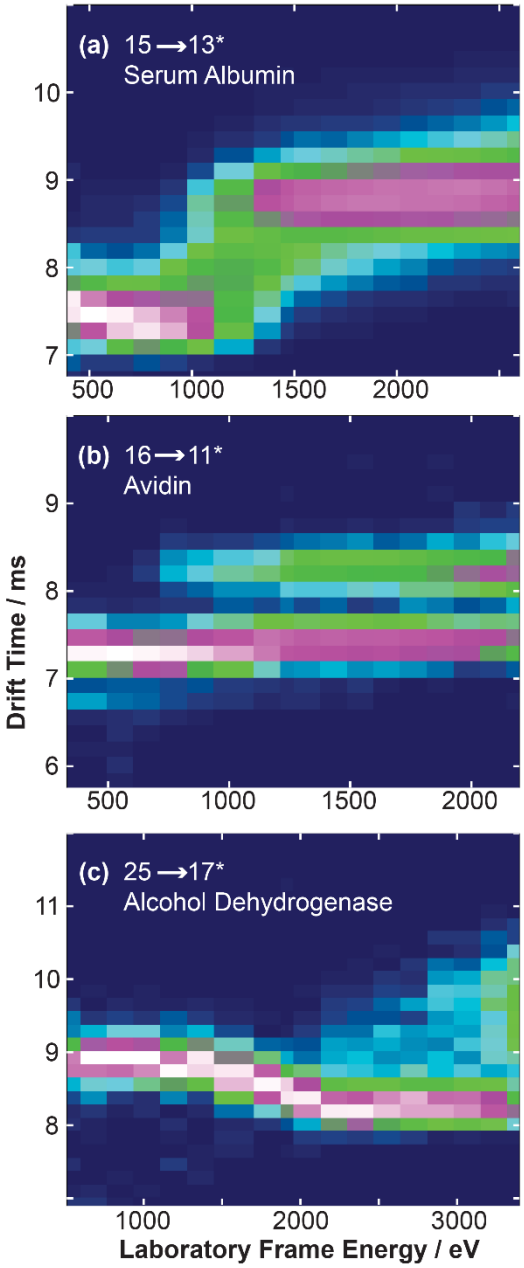

Figure 6.5. Post-CAPTR activation of (a) 15→13* serum albumin, (b) 16→11* avidin, and (c) 25→17* alcohol dehydrogenase, where "*" indicates the collisionally activated ion. The data show the arrival-time distributions plotted as colors, against the laboratory-frame energy used to inject the CAPTR products into the argon-filled cell. Results for 16→13* serum albumin, 17→11* avidin, and 27→17* alcohol dehydrogenase are shown in Figure S7.

Results for 16→11* avidin are shown in Figures 6.5b. At low energies, the arrival-time distributions are unimodal and centered near 7.3 ms. With energies of at least 750 eV, an additional feature near 8.3 ms appears. The relative intensity of the larger Ω feature increases with energy until both features exhibit similar intensities at the highest energies. These results are qualitatively similar those obtained from collision-induced unfolding of 11+ avidin that was generated from solution containing triethylammonium, which also yielded a bimodal arrival-time distribution at the highest energies.[65] The results for the 17→11* ions (Figure S7b) are nearly identical to those for the 16→11* ions. Results for 25→17* alcohol dehydrogenase are shown in Figures 6.5c. At low energies, the arrival-time distributions are unimodal and centered near 8.9 ms. With energies increasing to ~1800 eV, the distributions shift to smaller values centered near 8.2 ms that are consistent with the formation of much more compact structures. From 2000 eV to 2500 eV, the distributions become significantly broader until an additional feature centered near 9.7 ms appears and persists with increasing energy. The results for the 27→17* ions (Figure S7c) are nearly identical to those for the 25→17* ions.

The results in Figures 6.5 and S7 demonstrate that the structures of CAPTR products can depend on the extent of activation. Depending on the identity of the ion and the extent of activation, new structures with smaller or larger Ω can be formed. For *P*→13* serum albumin, *P*→11* avidin, and *P*→17* alcohol dehydrogenase and a given energy, the arrival-time distribution appears to be independent of *P*. This suggests that the structures and stabilities of these ions depend most strongly on the identity of the protein and *C*, rather than *P* or the number of CAPTR events. These results are consistent with the CAPTR products of native-like ions retaining elements of native-like structure, rather than the exothermicity of each CAPTR

event fully annealing the structures. These results suggest that the structure of native-like CAPTR products depend weakly on *P*, and are consistent with the all of the precursor ions having similar, native-like structures or that CAPTR products isomerize to similar structures. These data support the hypothesis that the structures of native-like ions generated from ESI of 200 mM aqueous ammonium acetate conditions are all similar and depend weakly on *z*. Consequentially, the error of Ω measurements and the range of Ω measured should be considered when using Ω to restrict possible structural models.

6.5 Conclusions

The effects of charge state on structures of native-like serum albumin, streptavidin, avidin, and alcohol dehydrogenase were probed using CAPTR, IM-MS, and complementary energy-dependent experiments. The CAPTR products all have Ω values that are within 5.5% of their original precursors and provide no evidence for large-scale structural collapses resulting from charge reduction (Figure 6.3). The first CAPTR event for each precursor yields products that have smaller Ω values and frequently exhibit the greatest magnitude of change in Ω resulting from a single CAPTR event. The Ω values of the products of the subsequent CAPTR events exhibit either small decreases or increases in Ω. The maximum decrease in Ω, relative to the original precursor, is −5.5% for serum albumin, −2.3% for streptavidin, −2.9% for avidin, and −3.6% for alcohol dehydrogenase. These maximum decreases in Ω with decreasing charge are smaller than those reported based on CAPTR and rf-confining drift cell analysis of lower-mass (8.6 to 14 kDa) protein ions[26,35,36] and based on alternative charge reduction approaches and traveling-wave IM of native-like alcohol dehydrogenase[32] and pyruvate kinase (230 kDa).[31]

To investigate how the structure of the precursors affect the structures of the CAPTR products, ions were activated in the atmospheric-pressure interface as a function of energy prior to CAPTR (Figures 6.4 and S6). In each case, the Ω distributions of the activated precursors increase with increasing energy, but the Ω distributions of the CAPTR products are significantly more compact than the activated precursors. To investigate the stabilities of the CAPTR products, selected products were activated as a function of energy immediately prior to IM (Figures 6.5 and S7). These results shown that new structures with smaller or larger Ω can be formed with increasing extents of activation. Interesting, the similarity in the results for a given protein and *C* suggests that the structures and stabilities of these ions depend most strongly on the identity of the protein and *C*, rather than *P* or the number of CAPTR events.

The ions in these experiments were generated from aqueous solutions containing 200 mM ammonium acetate at pH 7, which is one of the most common sample solutions for native IM-MS experiments. Therefore, these results support the hypothesis that elements of solution structure are retained in typical native IM-MS experiments and the use of Ω values for characterizing the structures of proteins and protein complexes in solution. Although these results indicate that the excess charges initially present on native-like ions have a modest effect on their Ω values, the changes in Ω values as a function of *C* can be statistically significant. For instance, all avidin $P \rightarrow 5+$ ions are statistically different from the precursor ions, *i.e.* $P = 17+$ to 15+, but are not statistically different from the $P \rightarrow 11+$ ions. This finding indicates that potential contributions from charge should be considered when using experimental Ω values to restrain or filter models of candidate structures in solution; simply using the precision of the measurements may considerably underestimate the true uncertainty. Lower-*z* ions typically adopt smaller ranges of Ω values, which is appealing for structure elucidation. Unfortunately, limiting analysis

to a subset of ions will inherently bias results and may systematically exclude subpopulations of extended structures from ensembles that were present in solution, which will preferentially adopt higher charge states during ionization. Analysis of lower-*z* ions may also obfuscate when structures were altered at some point during analysis (Figure 6.5). Consequentially, the error in Ω measurements as well as the range of Ω measured should be used to restrict structural models. Together, these results indicate that advancing the molecular understanding of the structures that give rise to the small difference in Ω values observed will be important for increasing the accuracy of models generated using restraints from native IM-MS experiments.

6.6 Supporting Information.

The Supporting Information is available in Appendix E.

Figures S1 to S7, Tables S1 to S2, Converting Drift Times to Ω and Consideration of Error, Comparisons with Ω Values Reported for Other Charge-Reduced, Native-Like Ions

6.7 Acknowledgments.

Research reported in this publication was supported by the American Society for Mass Spectrometry (Research Award to M. F. B.), Eli Lilly and Company (Young Investigator Award in Analytical Chemistry to M. F. B.), and the National Institute of General Medical Sciences of the National Institutes of Health under Award Number T32GM008268 (support to K. J. L.).

6.8 References

(1) Hilton, G. R.; Benesch, J. L. P. Two Decades of Studying Non-Covalent Biomolecular Assemblies by Means of Electrospray Ionization Mass Spectrometry. *J. R. Soc. Interface* **2012**, *9* (70), 801–816.

(2) Ma, X.; Lai, L. B.; Lai, S. M.; Tanimoto, A.; Foster, M. P.; Wysocki, V. H.; Gopalan, V. Uncovering the Stoichiometry of Pyrococcus Furiosus RNase P, a Multi-Subunit Catalytic Ribonucleoprotein Complex, by Surface-Induced Dissociation and Ion Mobility Mass Spectrometry. *Angew. Chem. Int. Ed.* **2014**, *53* (43), 11483–11487.

(3) Cong, X.; Liu, Y.; Liu, W.; Liang, X.; Russell, D. H.; Laganowsky, A. Determining Membrane Protein–Lipid Binding Thermodynamics Using Native Mass Spectrometry. *J. Am. Chem. Soc.* **2016**, *138* (13), 4346–4349.

(4) Zhou, M.; Sandercock, A. M.; Fraser, C. S.; Ridlova, G.; Stephens, E.; Schenauer, M. R.; Yokoi-Fong, T.; Barsky, D.; Leary, J. A.; Hershey, J. W.; et al. Mass Spectrometry Reveals Modularity and a Complete Subunit Interaction Map of the Eukaryotic Translation Factor eIF3. *Proc Natl Acad Sci U A* **2008**, *105*, 18139–18144.

(5) Bush, M. F.; Hall, Z.; Giles, K.; Hoyes, J.; Robinson, C. V.; Ruotolo, B. T. Collision Cross Sections of Proteins and Their Complexes: A Calibration Framework and Database for Gas-Phase Structural Biology. *Anal. Chem.* **2010**, *82*, 9557–9565.

(6) Ruotolo, B. T.; Benesch, J. L.; Sandercock, A. M.; Hyung, S. J.; Robinson, C. V. Ion Mobility-Mass Spectrometry Analysis of Large Protein Complexes. *Nat Protoc* **2008**, *3*, 1139–1152.

(7) Giles, K.; Williams, J. P.; Campuzano, I. Enhancements in Travelling Wave Ion Mobility Resolution. *Rapid Commun Mass Spectrom* **2011**, *25*, 1559–1566.

(8) Benesch, J. L.; Ruotolo, B. T. Mass Spectrometry: Come of Age for Structural and Dynamical Biology. *Curr. Opin. Struct. Biol.* **2011**, *21* (5), 641–649.

(9) Lanucara, F.; Holman, S. W.; Gray, C. J.; Eyers, C. E. The Power of Ion Mobility-Mass Spectrometry for Structural Characterization and the Study of Conformational Dynamics. *Nat. Chem.* **2014**, *6* (4), 281–294.

(10) Bleiholder, C.; Do, T. D.; Wu, C.; Economou, N. J.; Bernstein, S. S.; Buratto, S. K.; Shea, J.-E.; Bowers, M. T. Ion Mobility Spectrometry Reveals the Mechanism of Amyloid Formation of Aβ(25–35) and Its Modulation by Inhibitors at the Molecular Level: Epigallocatechin Gallate and Scyllo-Inositol. *J. Am. Chem. Soc.* **2013**, *135* (45), 16926–16937.

(11) Young, L. M.; Cao, P.; Raleigh, D. P.; Ashcroft, A. E.; Radford, S. E. Ion Mobility Spectrometry–Mass Spectrometry Defines the Oligomeric Intermediates in Amylin Amyloid Formation and the Mode of Action of Inhibitors. *J. Am. Chem. Soc.* **2014**, *136* (2), 660–670.

(12) Ekeowa, U. I.; Freeke, J.; Miranda, E.; Gooptu, B.; Bush, M. F.; Pérez, J.; Teckman, J.; Robinson, C. V.; Lomas, D. A. Defining the Mechanism of Polymerization in the Serpinopathies. *Proc. Natl. Acad. Sci.* **2010**, *107* (40), 17146–17151.

(13) Shepherd, D. A.; Holmes, K.; Rowlands, D. J.; Stonehouse, N. J.; Ashcroft, A. E. Using Ion Mobility Spectrometry–Mass Spectrometry to Decipher the Conformational and Assembly Characteristics of the Hepatitis B Capsid Protein. *Biophys. J.* **2013**, *105* (5), 1258–1267.

(14) Uetrecht, C.; Barbu, I. M.; Shoemaker, G. K.; van Duijn, E.; Heck, A. J. R. Interrogating Viral Capsid Assembly with Ion Mobility–mass Spectrometry. *Nat. Chem.* **2011**, *3* (2), 126–132.
(15) Baldwin, A. J.; Lioe, H.; Hilton, G. R.; Baker, L. A.; Rubinstein, J. L.; Kay, L. E.; Benesch, J. L. P. The Polydispersity of αB-Crystallin Is Rationalized by an Interconverting Polyhedral Architecture. *Structure* **2011**, *19* (12), 1855–1863.
(16) Zhou, M.; Politis, A.; Davies, R. B.; Liko, I.; Wu, K.-J.; Stewart, A. G.; Stock, D.; Robinson, C. V. Ion Mobility–mass Spectrometry of a Rotary ATPase Reveals ATP-Induced Reduction in Conformational Flexibility. *Nat. Chem.* **2014**, *6* (3), 208–215.
(17) Heck, A. J. R.; van den Heuvel, R. H. H. Investigation of Intact Protein Complexes by Mass Spectrometry. *Mass Spectrom. Rev.* **2004**, *23* (5), 368–389.
(18) Allen, S. J.; Schwartz, A. M.; Bush, M. F. Effects of Polarity on the Structures and Charge States of Native-Like Proteins and Protein Complexes in the Gas Phase. *Anal. Chem.* **2013**, *85* (24), 12055–12061.
(19) Allen, S. J.; Giles, K.; Gilbert, T.; Bush, M. F. Ion Mobility Mass Spectrometry of Peptide, Protein, and Protein Complex Ions Using a Radio-Frequency Confining Drift Cell. *Analyst* **2016**, *141* (3), 884–891.
(20) Jurneczko, E.; Barran, P. E. How Useful Is Ion Mobility Mass Spectrometry for Structural Biology? The Relationship between Protein Crystal Structures and Their Collision Cross Sections in the Gas Phase. *Analyst* **2010**, *136* (1), 20–28.
(21) Salbo, R.; Bush, M. F.; Naver, H.; Campuzano, I.; Robinson, C. V.; Pettersson, I.; Jørgensen, T. J. D.; Haselmann, K. F. Traveling-Wave Ion Mobility Mass Spectrometry of Protein Complexes: Accurate Calibrated Collision Cross-Sections of Human Insulin Oligomers. *Rapid Commun. Mass Spectrom.* **2012**, *26* (10), 1181–1193.
(22) Hilton, G. R.; Thalassinos, K.; Grabenauer, M.; Sanghera, N.; Slade, S. E.; Wyttenbach, T.; Robinson, P. J.; Pinheiro, T. J. T.; Bowers, M. T.; Scrivens, J. H. Structural Analysis of Prion Proteins by Means of Drift Cell and Traveling Wave Ion Mobility Mass Spectrometry. *J. Am. Soc. Mass Spectrom.* **2010**, *21* (5), 845–854.
(23) Beveridge, R.; Covill, S.; Pacholarz, K. J.; Kalapothakis, J. M. D.; MacPhee, C. E.; Barran, P. E. A Mass-Spectrometry-Based Framework To Define the Extent of Disorder in Proteins. *Anal. Chem.* **2014**, *86* (22), 10979–10991.
(24) Sterling, H. J.; Daly, M. P.; Feld, G. K.; Thoren, K. L.; Kintzer, A. F.; Krantz, B. A.; Williams, E. R. Effects of Supercharging Reagents on Noncovalent Complex Structure in Electrospray Ionization from Aqueous Solutions. *J. Am. Soc. Mass Spectrom.* **2010**, *21* (10), 1762–1774.
(25) Shelimov, K. B.; Clemmer, D. E.; Hudgins, R. R.; Jarrold, M. F. Protein Structure in Vacuo: Gas-Phase Conformations of BPTI and Cytochrome c. *J. Am. Chem. Soc.* **1997**, *119* (9), 2240–2248.
(26) Laszlo, K. J.; Munger, E. B.; Bush, M. F. Folding of Protein Ions in the Gas Phase after Cation-to-Anion Proton-Transfer Reactions. *J. Am. Chem. Soc.* **2016**, *138*, 9581–9588.
(27) van Duijn, E.; Barendregt, A.; Synowsky, S.; Versluis, C.; Heck, A. J. R. Chaperonin Complexes Monitored by Ion Mobility Mass Spectrometry. *J. Am. Chem. Soc.* **2009**, *131* (4), 1452–1459.
(28) Hogan, C. J.; Ruotolo, B. T.; Robinson, C. V.; Fernandez de la Mora, J. Tandem Differential Mobility Analysis-Mass Spectrometry Reveals Partial Gas-Phase Collapse of the GroEL Complex. *J. Phys. Chem. B* **2011**, *115* (13), 3614–3621.

(29) Bornschein, R.; Hyung, S.-J.; Ruotolo, B. Ion Mobility-Mass Spectrometry Reveals Conformational Changes in Charge Reduced Multiprotein Complexes. *J. Am. Soc. Mass Spectrom.* **2011**, *22* (10), 1690–1698.
(30) Hall, Z.; Politis, A.; Bush, M. F.; Smith, L. J.; Robinson, C. V. Charge-State Dependent Compaction and Dissociation of Protein Complexes: Insights from Ion Mobility and Molecular Dynamics. *J. Am. Chem. Soc.* **2012**, *134* (7), 3429–3438.
(31) Campuzano, I. G.; Schnier, P. Coupling Electrospray Corona Discharge, Charge Reduction and Ion Mobility Mass Spectrometry: From Peptides to Large Macromolecular Protein Complexes. *Int. J. Ion Mobil. Spectrom.* **2013**, *16* (1), 51–60.
(32) Lermyte, F.; Williams, J. P.; Brown, J. M.; Martin, E. M.; Sobott, F. Extensive Charge Reduction and Dissociation of Intact Protein Complexes Following Electron Transfer on a Quadrupole-Ion Mobility-Time-of-Flight MS. *J. Am. Soc. Mass Spectrom.* **2015**, *26*, 1068–1076.
(33) Tureček, F.; Julian, R. R. Peptide Radicals and Cation Radicals in the Gas Phase. *Chem. Rev.* **2013**, *113* (8), 6691–6733.
(34) Laszlo, K. J.; Bush, M. F. Analysis of Native-Like Proteins and Protein Complexes Using Cation to Anion Proton Transfer Reactions (CAPTR). *J. Am. Soc. Mass Spectrom.* **2015**, *26*, 2152–2161.
(35) Laszlo, K. J.; Buckner, J. H.; Munger, E. B.; Bush, M. F. Native-like and Denatured Cytochrome c Ions Yield Cation-to-Anion Proton-Transfer Products with Similar Collision Cross Sections. *J. Am. Soc. Mass Spectrom.* **2017**, DOI: 10.1007/s13361-017-1620-4.
(36) Laszlo, K. J.; Munger, E. B.; Bush, M. F. Effects of Solution Structure on the Folding of Lysozyme Ions in the Gas-Phase. *J. Phys. Chem. B* **2017**, *121*, 2759–2766.
(37) Allen, S. J.; Bush, M. F. Radio-Frequency (RF) Confinement in Ion Mobility Spectrometry: Apparent Mobilities and Effective Temperatures. *J. Am. Soc. Mass Spectrom.* **2016**, *27*, 2054–2063.
(38) Davidson, K. L.; Oberreit, D. R.; Hogan Jr., C. J.; Bush, M. F. Nonspecific Aggregation in Native Electrokinetic Nanoelectrospray Ionization. *Int. J. Mass Spectrom.* **2017**, DOI: 10.1016/j.ijms.2016.09.013.
(39) Williams, J. P.; Brown, J. M.; Campuzano, I.; Sadler, P. J. Identifying Drug Metallation Sites on Peptides Using Electron Transfer Dissociation (ETD), Collision Induced Dissociation (CID) and Ion Mobility-Mass Spectrometry (IM-MS). *Chem. Commun.* **2010**, *46* (30), 5458–5460.
(40) Stephenson, J. L.; McLuckey, S. A. Ion/Ion Proton Transfer Reactions for Protein Mixture Analysis. *Anal. Chem.* **1996**, *68* (22), 4026–4032.
(41) Mason, E. A.; McDaniel, E. W. *Transport Properties of Ions in Gases*; Wiley: New York, 1988.
(42) Bujacz, A. Structures of Bovine, Equine and Leporine Serum Albumin. *Acta Crystallogr. D Biol. Crystallogr.* **2012**, *68* (10), 1278–1289.
(43) Terai, T.; Kohno, M.; Boncompain, G.; Sugiyama, S.; Saito, N.; Fujikake, R.; Ueno, T.; Komatsu, T.; Hanaoka, K.; Okabe, T.; et al. Artificial Ligands of Streptavidin (ALiS): Discovery, Characterization, and Application for Reversible Control of Intracellular Protein Transport. *J. Am. Chem. Soc.* **2015**, *137* (33), 10464–10467.

(44) Pugliese, L.; Coda, A.; Malcovati, M.; Bolognesi, M. Three-Dimensional Structure of the Tetragonal Crystal Form of Egg-White Avidin in Its Functional Complex with Biotin at 2·7 Å Resolution. *J. Mol. Biol.* **1993**, *231* (3), 698–710.
(45) Plapp, B. V.; Charlier Jr., H. A.; Ramaswamy, S. Mechanistic Implications from Structures of Yeast Alcohol Dehydrogenase Complexed with Coenzyme and an Alcohol. *Arch. Biochem. Biophys.* **2016**, *591*, 35–42.
(46) von Helden, G.; Hsu, M. T.; Gotts, N.; Bowers, M. T. Carbon Cluster Cations with up to 84 Atoms: Structures, Formation Mechanism, and Reactivity. *J. Phys. Chem.* **1993**, *97* (31), 8182–8192.
(47) Shvartsburg, A. A.; Jarrold, M. F. An Exact Hard-Spheres Scattering Model for the Mobilities of Polyatomic Ions. *Chem. Phys. Lett.* **1996**, *261* (1–2), 86–91.
(48) Shvartsburg, A. A.; Mashkevich, S. V.; Baker, E. S.; Smith, R. D. Optimization of Algorithms for Ion Mobility Calculations. *J. Phys. Chem. A* **2007**, *111* (10), 2002–2010.
(49) Pettersen, E. F.; Goddard, T. D.; Huang, C. C.; Couch, G. S.; Greenblatt, D. M.; Meng, E. C.; Ferrin, T. E. UCSF Chimera--a Visualization System for Exploratory Research and Analysis. *J. Comput. Chem.* **2004**, *25* (13), 1605–1612.
(50) Deng, L.; Broom, A.; Kitova, E. N.; Richards, M. R.; Zheng, R. B.; Shoemaker, G. K.; Meiering, E. M.; Klassen, J. S. Kinetic Stability of the Streptavidin–Biotin Interaction Enhanced in the Gas Phase. *J. Am. Chem. Soc.* **2012**, *134* (40), 16586–16596.
(51) Freeke, J.; Bush, M. F.; Robinson, C. V.; Ruotolo, B. T. Gas-Phase Protein Assemblies: Unfolding Landscapes and Preserving Native-like Structures Using Noncovalent Adducts. *Chem. Phys. Lett.* **2012**, *524*, 1–9.
(52) Eschweiler, J. D.; Martini, R. M.; Ruotolo, B. T. Chemical Probes and Engineered Constructs Reveal a Detailed Unfolding Mechanism for a Solvent-Free Multidomain Protein. *J. Am. Chem. Soc.* **2017**, *139* (1), 534–540.
(53) Livnah, O.; Bayer, E. A.; Wilchek, M.; Sussman, J. L. Three-Dimensional Structures of Avidin and the Avidin-Biotin Complex. *Proc. Natl. Acad. Sci.* **1993**, *90* (11), 5076–5080.
(54) Bayer, E. A.; Wilchek, M. Application of Avidin-Biotin Technology to Affinity-Based Separations. *J. Chromatogr.* **1990**, *510*, 3–11.
(55) Li, J.; Taraszka, J. A.; Counterman, A. E.; Clemmer, D. E. Influence of Solvent Composition and Capillary Temperature on the Conformations of Electrosprayed Ions: Unfolding of Compact Ubiquitin Conformers from Pseudonative and Denatured Solutions. *Int. J. Mass Spectrom.* **1999**, *185–187*, 37–47.
(56) Zhao, Q.; Schieffer, G. M.; Soyk, M. W.; Anderson, T. J.; Houk, R. S.; Badman, E. R. Effects of Ion/Ion Proton Transfer Reactions on Conformation of Gas-Phase Cytochrome c Ions. *J. Am. Soc. Mass Spectrom.* **2010**, *21* (7), 1208–1217.
(57) Holden, D. D.; Brodbelt, J. S. Ultraviolet Photodissociation of Native Proteins Following Proton Transfer Reactions in the Gas Phase. *Anal. Chem.* **2016**, *88* (24), 12354–12362.
(58) Jurchen, J. C.; Williams, E. R. Origin of Asymmetric Charge Partitioning in the Dissociation of Gas-Phase Protein Homodimers. *J. Am. Chem. Soc.* **2003**, *125* (9), 2817–2826.
(59) Wysocki, V. H.; Joyce, K. E.; Jones, C. M.; Beardsley, R. L. Surface-Induced Dissociation of Small Molecules, Peptides, and Non-Covalent Protein Complexes. *J. Am. Soc. Mass Spectrom.* **2008**, *19* (2), 190–208.

(60) Wanasundara, S. N.; Thachuk, M. Free Energy Barrier Estimation for the Dissociation of Charged Protein Complexes in the Gas Phase. *J. Phys. Chem. A* **2009**, *113* (16), 3814–3821.
(61) Sciuto, S. V.; Liu, J.; Konermann, L. An Electrostatic Charge Partitioning Model for the Dissociation of Protein Complexes in the Gas Phase. *J. Am. Soc. Mass Spectrom.* **2011**, *22* (10), 1679.
(62) Ruotolo, B. T.; Hyung, S.-J.; Robinson, P. M.; Giles, K.; Bateman, R. H.; Robinson, C. V. Ion Mobility–Mass Spectrometry Reveals Long-Lived, Unfolded Intermediates in the Dissociation of Protein Complexes. *Angew. Chem. Int. Ed.* **2007**, *46* (42), 8001–8004.
(63) Zhou, M.; Dagan, S.; Wysocki, V. H. Impact of Charge State on Gas-Phase Behaviors of Noncovalent Protein Complexes in Collision Induced Dissociation and Surface Induced Dissociation. *Analyst* **2013**, *138* (5), 1353–1362.
(64) Pierson, N. A.; Valentine, S. J.; Clemmer, D. E. Evidence for a Quasi-Equilibrium Distribution of States for Bradykinin [M + 3H]3+ Ions in the Gas Phase. *J. Phys. Chem. B* **2010**, *114* (23), 7777–7783.
(65) Bornschein, R. E.; Niu, S.; Eschweiler, J.; Ruotolo, B. T. Ion Mobility-Mass Spectrometry Reveals Highly-Compact Intermediates in the Collision Induced Dissociation of Charge-Reduced Protein Complexes. *J. Am. Soc. Mass Spectrom.* **2015**, *27* (1), 41–49.

Chapter 7. On The Relationship Between Native-like and Gas-Phase-Folded Poly-Ubiquitin Ions

---

This chapter is reproduced with permission from Laszlo, K. J.; Gadzuk-Shea, M. M.; Heard, S. C.; Buckner, J. H.; Bush, M. F. "On The Relationship Between Native-like and Gas-Phase-Folded Poly-Ubiquitin" **2017**, manuscript in preparation

7.1 Abstract

Protein structure in solution depends on protein intramolecular interactions, and interactions with solvent and other solvated ions and molecules. Those interactions fold proteins into larger order structures, which can often be divided into separate domains. In these experiments, we use gas-phase Cation to Anion Proton Transfer Reactions (CAPTR) to provide insight into the role protein intramolecular interactions play in defining protein domain structure at low charge states (z). Poly-ubiquitin ion are used as model multi-domain proteins with 1 to 4 domains (Ub_1 to Ub_4), and ions are generated from denaturing and native-like conditions. Collision cross sections (Ω) of the CAPTR product ions are measured using ion mobility. Results from ions from native-like conditions show that the Ω of the product ions are weakly related to the product ion charge state (C). In contrast, the Ω of product ions from denaturing conditions strongly depend on C, and to a lesser extent on the precursor charge state (P). The Ω dependence on P increases at intermediate C for Ub_2, Ub_3, and Ub_4. Coarse grained models were developed to help interpret the domain structure of the lowest C CAPTR product ions from denaturing conditions. Energy dependent Ω measurements were performed on native-like poly-ubiquitin ions for comparison to the Ω of CAPTR product ions from denaturing conditions. In general,

these results show that domain structure for native-like ions can be maintained at low *z*, and that the Ω of the lowest *z* CAPTR product ions of Ub_1, Ub_2, and Ub_3 from denaturing conditions are consistent with the domain structure of the respective protein in solution.

7.2 Introduction

Advances in the understanding of the structures and stabilities of gas-phase protein ions have enabled structural biology measurements of gas-phase protein ions.[1–9] For protein ions generated via electrospray ionization (ESI), ion mobility (IM)[10] and hydrogen/deuterium exchange[11] measurements show that solution-phase structures isomerize to stable-gas-phase structures over several seconds to minutes. Due to the low dielectric constant of vacuum, electrostatic interactions can result in subtle isomerization to kinetically trapped protein structures younger than several seconds.[12] Measurements of these kinetically trapped structures generated from native conditions, *i.e.* 200 mM ammonium acetate, pH 7, etc., have revealed that secondary,[13,14] tertiary,[15–17] and quaternary structures[9,18] can be retained in the gas-phase.

However, protein ions generated via ESI generate a distribution of charge states (*z*), which can affect gas-phase structures[19] and the results of gas-phase measurements.[20] For instance, ions generated via ESI from denaturing solution conditions generate a wide distribution of *z* and collision cross sections (Ω),[21,22] whereas ions generated from native conditions yield a much narrower *z* and Ω range.[23,24] Consequently, a great deal of interest has been place in the relationship between *z* and the structure of gas-phase ions. That relationship can be directly interrogated by modulating *z* via ion/neutral[24–26] and ion/ion proton transfer[19,27–29] reactions, shown below as Reactions 1 and 2, respectively:

$$[M_n + zH]^{z+} + A \rightarrow [M_n + (z-1)H]^{(z-1)+} + AH^+ \qquad \text{(Reaction 1)}$$

$$[M_n + zH]^{z+} + A^- \rightarrow [M_n + (z-1)H]^{(z-1)+} + AH \qquad \text{(Reaction 2)}$$

Ion/ion proton transfer reactions generally benefit from favorable kinetics and thermodynamics compared to ion/neutral reactions,[30] however they are more challenging to implement. Several studies have investigated the structures and stabilities of the low *z* product ions from these reactions using collisional activation and ion mobility,[31] as well as ultraviolet photodissociation.[32]

Recently, we have implemented cation-to-anion proton transfer reactions to monitor the Ω of denatured and native-like protein ions as a function of their charge state using ion mobility-mass spectrometry (IM-MS).[17,19,29,33] Initial experiments measuring the Ω of denatured Ub_1 ions revealed that the Ω of CAPTR products depended on the product ion charge state.[19] Nonetheless, energy-dependent collisional activation of those CAPTR product ions revealed that the ions had different structural populations, despite having similar Ω distributions. Ω measurements of the CAPTR product ions of several native-like protein and protein complex ions have shown that the Ω of those ions depend less on *z* than that of denatured protein ions, and that the stoichiometry of those ions is retained at low *z*.[17,29,33] Moreover, the Ω of the lowest-*z* CAPTR products of protein ions from denaturing and native like solution conditions yield ions with similar Ω distributions.

Energy-dependent collisional activation of the CAPTR products of denatured and di-sulfide intact lysozyme ions revealed that the ions compact to Ω consistent with the Ω of the corresponding native-like ion.[17] In contrast, analogous energy-depend experiments on the CAPTR product of denatured and disulfide reduced lysozyme revealed that those ions compacted overall, but yielded Ω distributions different than their disulfide-intact and native-like counterparts. Thus, the native disulfide bonds of lysozyme may be stabilizing the native-like tertiary structure of lysozyme or structures of a similar size in the gas-phase.

Recent experiments have employed collisional activation to probe the tertiary domain structure of gas-phase native-like protein ions, using C-to-N linked poly-ubiquitin chains as a model system.[15,16] Those results concluded that structural transitions observed following collisional activation of native-like ions can be used to determine the number of domains in the tertiary structure of a gas-phase protein ion or the location of drug binding sites. Here, we measure the Ω of native-like and denatured poly-ubiquitin ions and their CAPTR product ions, and develop coarse grained models to interpret possible domain structures for those ions. Ω measurements of the CAPTR products of native-like poly-ubiquitin show that domain structure is maintained at low *z,* and that of denatured poly-ubiquitin ions larger than Ub_1 reveal multiple gas-phase folding pathways. Comparing those results to coarse grained models shows that the ions fold domain structures consistent with their solution phase structures. Further collisional activation investigates the structures of the native-like ions compared to the low *z* CAPTR product ions of denatured poly-ubiquitin ions.

7.3 Methods

For experiments performed under denaturing conditions, ubiquitin (Ub_1), di-, tri-, and tetra- ubiquitin (C-to-N terminally linked; Ub_2, Ub_3, and Ub_4, respectively) were purchased from Boston Biochem (Cambridge, MA). To denature these proteins, the proteins were prepared in a solution of 70% methanol 30% water, that was adjusted to pH 2 with trifluoroacetic acid. For experiments performed under native-like conditions, ubiquitin and tri-ubiquitin were purchased from Boston Biochem, and linear di-, and tetra- ubiquitin were purchased from Enzo Life Science (Farmingdale, NY). Proteins were prepared in a solution of 200 mM aqueous ammonium acetate at pH 7. Nano-ESI was used to generate protein cations. Borosilicate glass

capillaries were pulled to a ~1 to 3 μm tip on one end using a Sutter Instruments Model P-97 micropipette puller (Novato, CA), and sample solutions were inserted into the opposite end of the capillary. Electrical contact with the solution for electrospray ionization was maintained by inserting a platinum wire into the sample solution in the capillary. IM-MS experiments were performed on a Waters Synapt G2 HDMS instrument with ion/ion reaction capabilities,[34] and instrument parameters were optimized for ion/ion reactions, transmission, and minimal activation. The atmospheric-pressure interface of the instrument was elevated to 120 °C, unless otherwise noted. Native-like ions for CAPTR experiments were generated using a temperature-controlled nESI source,[33] and solution temperatures were held at 25 ˚C. During other experiments, the temperature of the sample capillary was not controlled and depended on the extent of convective heat transfer from the atmospheric-pressure interface.[19,33]

Ion/ion reactions were performed as described previously.[19,33,35] Briefly, quadrupole selected $[M-F]^-$ fragments of perfluoro-1,3-dimethylcyclohexane[36] were produced for 0.1 s, and accumulated in the trap cell of the instrument. Importantly, $[M-F]^-$ reacts exclusively by proton transfer,[30,35,36] and has not been observed to react via electron transfer. The instrument was then switched into positive ion mode for 2 to 10 s. A single charge state of the protein was quadrupole selected and guided into the trap cell to initiate CAPTR. Residual unreacted precursor ions and CAPTR product ions were injected into an rf-confining drift cell[37] for IMS analysis. Arrival-time distributions were measured using a 127 V drift voltage and 2 mbar helium, unless otherwise noted. For the arrival-time distributions of some low-abundance CAPTR product ions, a background subtraction was used to remove chemical noise and noise resulting from ion-neutral collisions in the time-of-flight mass analyzer.[17] Arrival-time distributions were converted to Ω

distributions via a method previously described.[17,19] The Ω of the native-like precursor ions (white markers, Figure 7.1) were determined using a field-dependent method.[24]

7.3.1 *Projection approximation (PA) and exact hard-spheres scattering (EHSS) Calculations.*

Ω values were calculated using the PA[38] and EHSS[39,40] methods in order to bracket possible Ω values. PDB entries for the native structures for ubiquitin and di-ubiquitin (1UBQ[41] and 3AXC,[42] respectively) were modified using Chimera[43] to fix sidechains and add hydrogens. α-helical and linear models of all four poly-ubiquitins were built using Chimera using the appropriate lengths and dihedral angles.[43]

7.3.2 *Coarse Grained Modelling.*

Coarse grained models were generated by estimating protein domains as spherical beads. The density of each bead was equivalent to the mass of ubiquitin divided by the volume of a sphere with the same Ω as the average Ω of native-like ubiquitin.[44] The distance between the beads was optimized with respect to the average experimental Ω of native di-ubiquitin over all *z*, and therefore adjacent spheres have some overlap. The ratio of the distance between adjacent beads and the radius of those beads was held constant over all domain models. PA Ω were calculating by generating 1024 random orientations of the 3D structures, projecting these structures to three orthogonal planes, and estimating the projected area using Monte Carlo integration with 10 000 points. The projected areas were then averaged to determine the Ω.

7.4 Results and Discussion

Previous experiments with cytochrome *C*[33] and lysozyme[17] indicated the CAPTR product ions from denatured and native-like solutions had similar Ω at the lowest-*z* ions. In said lysozyme study, we observed that the four disulfide bonds that largely define the tertiary structure of lysozyme in solution also stabilized the native structure in the gas-phase. Here, we develop coarse-grained models to investigate the tertiary domain structure of native-like poly-ubiquitins and the CAPTR products of denatured poly-ubiquitins. Results from these experiments also provide insights into the relationship between precursor ion charge state, product ion charge state, and Ω.

7.4.1 *Ion Mobility of Poly-Ubiquitin Ions from Denaturing and Native-Like Conditions.*

Figure S1a shows a mass spectrum of denatured Ub_1. Figure S1b show the corresponding IM-MS spectrum, where the ions were separated by their mobilities in helium. Arrival-time distributions for each ion were extracted, and converted to a Ω distribution, as described in the *Methods* section. Figure 7.1 shows the median Ω ($\widetilde{\Omega}$) for Ub_1, Ub_2, Ub_3, and Ub_4 generated from nESI under denaturing conditions as a function of charge state. nESI of the poly-ubiquitins from denaturing solutions generated wide *z* distributions and extended structures with large $\widetilde{\Omega}$ values. nESI of denatured Ub_1 generated charge states from 6+ to 13+, which ranged in $\widetilde{\Omega}$ from 12.8 to 20.0 nm^2, consistent with previous results.[19] The larger poly-ubiquitins exhibited comparatively higher *z* and $\widetilde{\Omega}$ than Ub_1, consistent with these ions also having extended structures in the gas-phase.

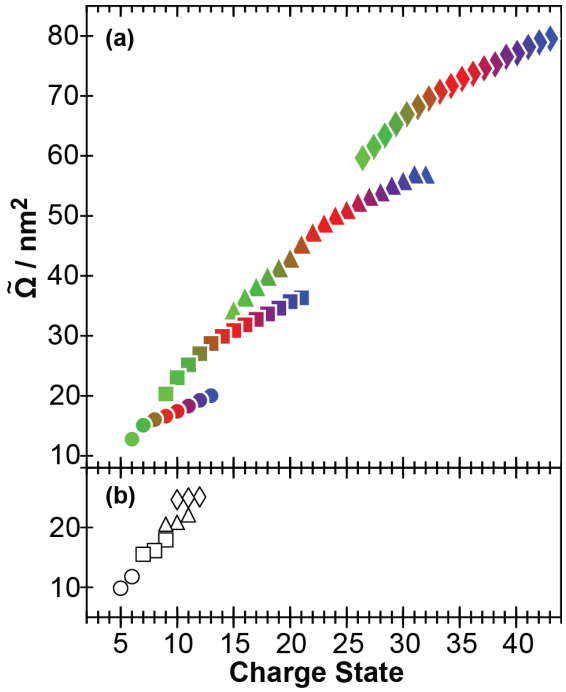

Figure 7.1. Median collision cross section with helium ($\tilde{\Omega}$) as a function of charge state for Ub_1 (*circles*), Ub_2 (*squares*), Ub_3 (*triangles*), and Ub_4 (d*iamonds*) generated from nESI under denaturing (a) and native-like (b) conditions. Measurements made under native-like solution conditions were analyzed using a field-dependent method with the MS interface at ambient temperature, and measurements made under denaturing solution conditions represent the $\tilde{\Omega}$ using a single-field strength method with the MS interface at 120 ˚C.

The $\tilde{\Omega}$ values for native-like poly-ubiquitin are shown in Figure 7.1b. For each successively larger poly-ubiquitin there is a corresponding increase in their *z* distribution and $\tilde{\Omega}$. In comparison to denatured poly-ubiquitin, these ions have relatively lower charge states, narrower charge-state distributions, and much smaller $\tilde{\Omega}$. nESI of Ub_1 generated charge states 5+ and 6+, and $\tilde{\Omega}$ values of 9.85 respectively 11.8 nm^2, respectively. These values differ from

previous results of native-like Ub_1 which exhibited Ω of 9.72 to 10 nm^2 for 4+ and 6+ ions;[44] under the conditions used in this experiment 4+ Ub_1 was too low in intensity to yield a $\tilde{\Omega}$. The differences in $\tilde{\Omega}$ for 6+ Ub_1 in the present study compared to the previous work are likely due to different amounts of collisional activation between the two experiments. Consequently, the 6+ ion in the present experiment has likely unfolded in the gas phase. Ub_2, Ub_3, and Ub_4 had *z* distributions of 7+ to 9+, 9+ to 11+ and 11+ to 13+, respectively, and $\tilde{\Omega}$ values that ranged from 15.5 to 17.9 nm^2, 20.6 to 22.1 nm^2, and 24.6 to 25.1 nm^2, respectively. Thus, relative to those ions generated under denaturing conditions, these native-like ions structures have remained folded after transfer to the gas phase.

7.4.2 *Interpreting the $\tilde{\Omega}$ of Poly-Ubiquitin Ions.*

The effective density of the native-like poly-ubiquitin ions range from 0.63 to 0.68 g cm^{-3}. These values were calculated using the volume of the sphere that would reproduce the experimental $\tilde{\Omega}$, average over all *z*, and are consistent with previous estimates of the density of native-like protein ions.[46,47] Alternatively, estimating the density of the ions by the including the drag enhancement factor, $\xi = 1.36$,[48] yields densities from 1.02 to 1.09 g cm^{-3}, which is generally consistent with previous measurements using a similar analysis of native-like protein ions.[48] All further discussions of density in this manuscript will include consideration of the drag-enhancement factor, as it calculates a higher density, and therefore provides the rigorous comparison to the density of the solvent excluded region of a protein, which has been previously estimated to range from 1.20 to 1.47 g cm^{-3}.[49,50] Therefore, the native-like ions in Figure 7.1b have not collapsed to high-density structures which is consistent with the retention of domain structure.

In order to evaluate the possible domain structures and arrangements of poly-ubiquitin ions, we have employed atomic and coarse-grained models for comparison. Atomic models for Ub_1 and Ub_2 were generated from entries in the PDB according to the *Methods* section, and their Ω values were calculated using the PA and EHSS; atomic models were unavailable for Ub_3 and Ub_4. Additionally, coarse-grained models were generated with linear, planar, and close-packing arrangements of spherical beads. Briefly, all beads are spherical and assumed to have the same density as that of native-like Ub_1 from previous measurements.[44] The distance between adjacent beads was determined by optimizing the distance between two Ub_1-sized beads to the average Ω of native-like Ub_2. Using this approach, the center-to-center spacing between beads was 74.6% of the diameter of those beads. Note for two-bead structures, the three models are equivalent, and for three beadπ structures, the planar and close-packing models are equivalent.

The Ω for all models are shown in Figure 7.2 relative to that Ω of a 1.2 g cm^{-3} beads, which provides a facile way to evaluate experimental Ω values against these model structures. The relative Ω of the linear model increases with increasing numbers of beads, and appears to be asymptotic with a maximum. The planar model increases in relative Ω at a much slower rate than that of the linear model. This is due to the beads being more tightly packed than that of the linear structure, and consequently more domain overlap for these structures (Figure S2). In contrast to the other two models, the close-packing model slightly compacts overall. This is because this arrangement has the greatest amount of bead overlap, and therefore the smallest volume, which leads more compact Ω values (Figure S3).

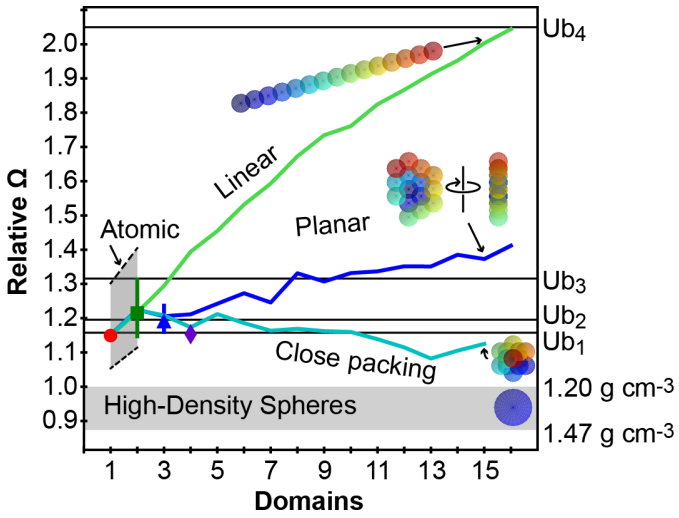

Figure 7.2. Ω relative to the Ω of a sphere with a density of 1.2 g cm^{-3} as a function of the number of beads (domains). The relative Ω values for coarse-grained models in linear (*light green*), planar (*blue*), and close-packing (*cyan*) arrangements are shown as a function of the number of beads. Proportional images of all three coarse-grained models with a 15-bead structure, and a sphere with a density of 1.2 g cm^{-3}are also shown. Regions corresponding to possible Ω based on atomic modelling (Table 7.1) and a high-density spherical structure (1.2 to 1.47 g cm^{-3}) are indicated with gray boxes. Average experimental native-like Ω values of Ub_1 (*red circle*) from previous measurments,[44] Ub_2 (*dark green square*), Ub_3 (*blue triangle*), Ub_4 (*purple diamond*), are shown with vertical bars corresponding to the range of values. The average $\widetilde{\Omega}$ of the lowest *C* denatured CAPTR product ions, *i.e.* $Ub_1^{DP\rightarrow 3}$, $Ub_2^{DP\rightarrow 4}$, $Ub_3^{DP\rightarrow 5}$ and $Ub_4^{DP\rightarrow 13}$, for each poly-ubiquitin are shown as horizontal black lines.

Figure 7.2 also includes markers that correspond to the average Ω of the native-like ions for previous measurements of Ub_1,[44] the present measurements of Ub_2, Ub_3, and Ub_4. As a result

of the coarse-grained models being optimized using the Ω measurements of Ub_1 and Ub_2, conclusions many only be drawn regarding Ub_3 and Ub_4. The Ω of Ub_3 and Ub_4 are consistent with three- and four-domain closed-packing structures, respectively. However, the native-like Ω values for Ub_1 and Ub_2 do agree with their atomic models, respectively. Notably, the relative Ω for the native-like poly-ubiquitins are also consistent with higher domain structures with similar relative Ω values, which consequently are also possible conclusions.

7.4.3 *Effects of Charge State on the Ions from Native-Like Conditions.*

Previous Ω measurements of large multi-domain protein complex ions have indicated significant compaction at low *z*.[50] To examine whether domain structure of these native-like ions is lost at low *z*, we performed CAPTR on several charge states of native-like poly-ubiquitin ions and measured the Ω of the ions with respect to changes in *z*. To generate CAPTR product ions, individual charge states were quadrupole selected and reacted with $[PDCH\text{-}F]^-$. This produces a long series of charge-reduced CAPTR product ions (Figure S1c), which were separated by their mobilities using an rf-confining drift cell containing 2 mbar of He gas (Figure S1d). For the remainder of the discussion, ions will be described using the following notation, "$Ub_n^{DP\rightarrow C}$", where *n* is the length of the poly-ubiquitin chain, *P* is the precursor charge state, *C* is the product ion charge state, and D or N will be used to differentiate ions from denaturing or native-like solution conditions.

$\widetilde{\Omega}$ values for native-like CAPTR product ions are shown in Figure 7.3. Precursor charge state $\widetilde{\Omega}$ for Ub_1 to Ub_4 ions range from ±1.3%, ±5.7%, ±1.0%, and ±5.6%, respectively, relative to the corresponding field-dependent $\widetilde{\Omega}$ values shown in Figure 7.1b. These differences may be attributable to the different extents of ion activation in the MS interface of the instrument due to the elevated temperature in the CAPTR experiments.

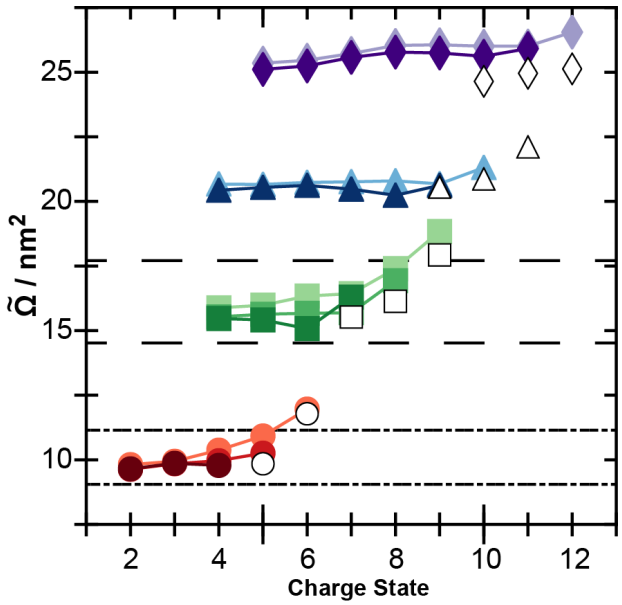

Figure 7.3. $\widetilde{\Omega}$ of native-like Ub_1 (*circles*), Ub_2 (*squares*), Ub_3 (*triangles*), and Ub_4 (*diamonds*) ions as a function of charge state. Native-like ions determined via a field-dependent method with the MS interface at ambient temperature are shown using white markers. CAPTR precursor and product ions are shown using colored markers, were analyzed using a single field-strength methodology with a 212 V across the drift cell, and generated using a temperature controlled nESI source with the sample at 25 ˚C and the MS interface at 120 ˚C.[17,19,33] Horizontal lines correspond to the Ω for PA and EHSS values for native structures of Ub_1 (*dot-dashed line*) and Ub_2 (*dashed lined*), respectively (Table 7.1).

For Ub_1, CAPTR product ions decreased in $\widetilde{\Omega}$ from $P \rightarrow 2$ between 0.6 % to 22.0% relative to *P*. The large compaction of 22.0% was for the 6+ charge state is likely because this ion has unfolded in the gas-phase, as noted previously. In contrast, the 5+ and 4+ ions are much more compact, and have therefore remained folded. These results indicate a weak relationship

between *C* and $\widetilde{\Omega}$ for native-like ion, which is similar to results we have previous reported for native-like proteins[17,33] and protein complexes.[29] $Ub_2^{NP\rightarrow4}$, $Ub_3^{NP\rightarrow4}$, and $Ub_4^{NP\rightarrow5}$ ions, which were the lowest *C* measured for Ub_2, Ub_3, and Ub_4, respectively, changed between -17.9 to -5.9%, -3.0 to 0.4%, -4.5 to -2.8% relative to *P*, respectively. The large -17.9% change in $\widetilde{\Omega}$ for $Ub_2^{N9\rightarrow4}$, may indicate this precursor ion had unfolded in the gas-phase, analogous to 6+ Ub_1.

In general, these results confirm that, with the exceptions of 6+ $Ub_1$and 9+ Ub_2, these native-like poly-ubiquitin ions have remained folded in their globular structures upon transfer to the gas-phase, and are generally unaffected by changes in *z*. Therefore, solution-phase domain structure is maintained at low *z*.

7.4.4 *Effects of Charge State on the Ions from Denaturing Conditions.*

Figure 4a to 4d show the Ω distributions of CAPTR product ions of Ub_1, Ub_2, Ub_3, and Ub_4 generated from denaturing conditions, respectively. Unlike the native-like ions, which exhibited unimodal Ω distributions, many Ω distributions were multimodal. To represent the width and asymmetry of the apparent Ω distributions, vertical bars spanning from 10% to 90% of the corresponding cumulative distribution function (CDF) are included in Figure 7.4a to 7.4d. Lines connecting ions of adjacent *C* intersect each vertical bar at the $\widetilde{\Omega}$ value (50% of the CDF), and different colors represent ions of different *P*. Figure 7.4a to 7.4d also includes lines corresponding to the Ω values for the PA[38] and EHSS[39,40] values for native and α-helical structures. Additionally, the y limits on each panel correspond to the range between the PA for a sphere with a density of 1.2 g cm^{-3} and a linear structure for each respective poly-ubiquitin (Table 7.1).

Table 7.1. Ω Values for Protein Structures.

Protein	Method	Native	α-Helix	Linear	Sphere 1.20 g cm^{-3}	Sphere 1.47 g cm^{-3}
Ub_1	PA	9.05[a]	14.52	22.92	8.57	7.49
	EHSS	11.15[a]	17.71	26.11		
Ub_2	PA	15.18[b]	28.23	45.54	13.6	11.9
	EHSS	19.08[b]	34.6	51.9		
Ub_3	PA		42.0	68.2	17.8	15.6
	EHSS		51.5	77.7		
Ub_4	PA		55.6	90.8	21.6	18.9
	EHSS		68.4	103.8		

In general, the highest *C* ions have Ω between those expected for an α-helix and a linear structure. Consequently, even the highest *C* ions have some interactions between adjacent amino acid residues. Additionally, each ion exhibits about a 50% compaction from the highest *C* to the lowest *C*, in stark contrast to the previously discussed native-like ions. The Ω distributions for Ub_2, Ub_3, and Ub_4 depended on *P* more than any previously measured protein ions, which is further discussed and quantitated in the section "*Do CAPTR Products "Remember" their Original Identity?*

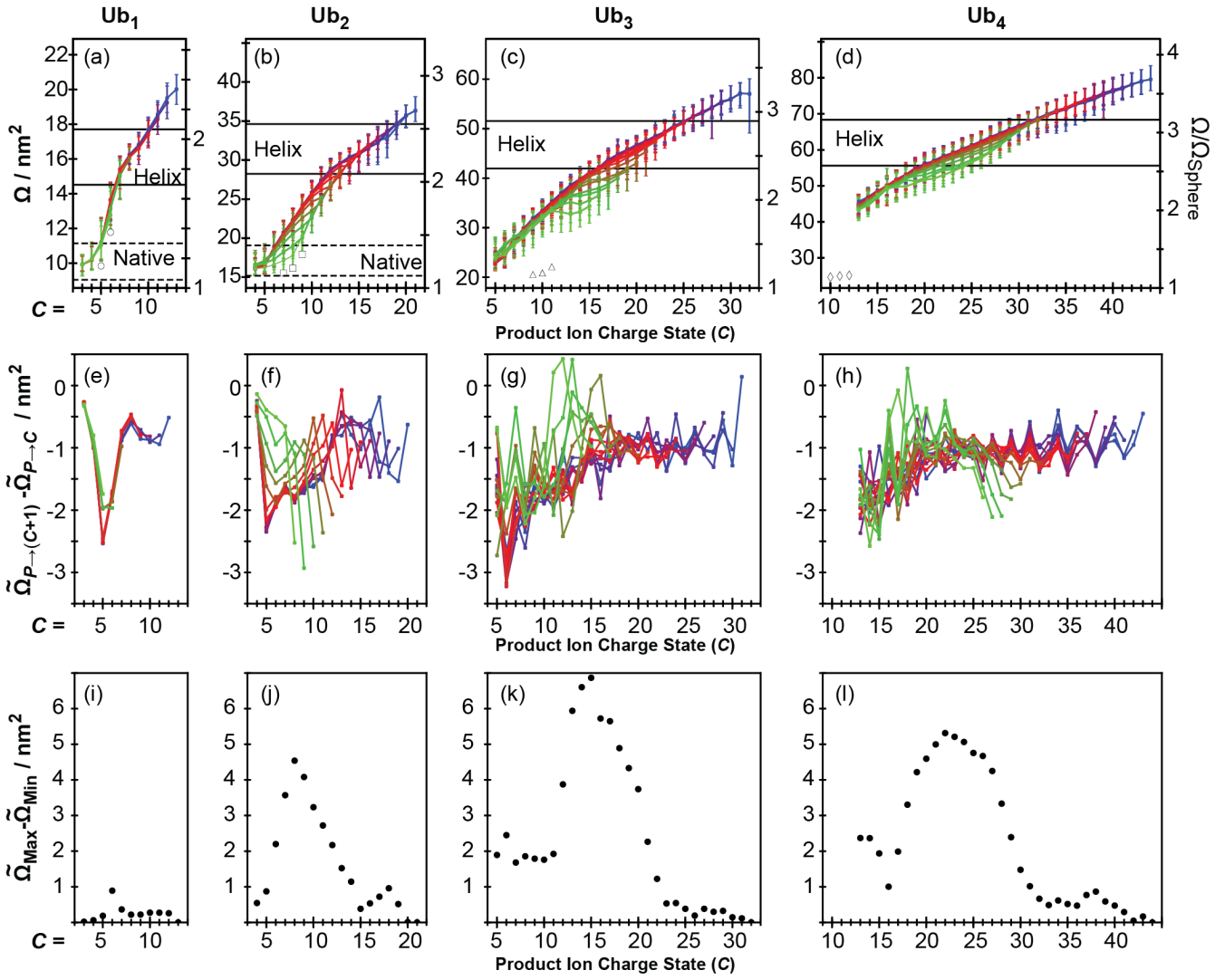

Figure 7.4. Ω distributions of CAPTR product ions of denatured (a) Ub_1, (b) Ub_2, (c) Ub_3, (d) Ub_4; Ω values relative to the Ω of a 1.2 g cm^{-3} using the PA are shown in the right y-axis. Upper and lower bars correspond to 10% and 90% of the Ω distributions corresponding CDF, and the lines connecting adjacent *C* pass through $\tilde{\Omega}$. Ions of different *P* are shown using different colors. Native-like Ω, shown using white markers, correspond to the same values as those shown in Figure 7.1b. Lines corresponding to the Ω region between PA[38] and EHSS[39,40] values for native (*dashed black*) and α-helical (*solid black*) structures,

respectively are shown. The bounds on these panels are defined by the Ω of a 1.2 g cm^{-3} sphere and the PA of the poly-ubiquitin linear structure (Table 7.1). Panels e to h show the change in $\widetilde{\Omega}$ per reaction for Ub_1, Ub_2, Ub_3, and Ub_4, respectively. Colors indicate ions of different *P*. Panels i to l show the range in $\widetilde{\Omega}$ for each *C* for Ub_1, Ub_2, Ub_3, and Ub_4, respectively.

Precursor charge states 13+ to 6+ of Ub_1 were selected for CAPTR. The $Ub_1^{DP\rightarrow 4}$ and $Ub_1^{DP\rightarrow 3}$ ions have Ω distributions that agree with the native PA and EHSS values, as well as previous native-like measurements of Ub_1 ,[44] which indicate that these ions have compacted to sizes similar to that of the native-like ion. Overall, these results show a significant compaction from a $\widetilde{\Omega}$ of 20.0 nm^2 at 13+ to $\widetilde{\Omega}$ ranging from 9.91 to 9.93 nm^2 at $P_{Ub_1}\rightarrow 3$.

Figure 7.4b shows the Ω distributions of CAPTR product ions of denatured Ub_2 ions, where *P* = 21+ to 9+. Several aspects of the Ub_1CAPTR results in Figure 7.4a are shared by that of Ub_2. For instance, the lowest *C* measured have Ω values that agree with the PA and EHSS values of the native structure and the average $\widetilde{\Omega}$ of the corresponding native-like ions. Additionally, there is a significant compaction in Ω from the highest *C* (21+, 36.3 nm^2) to the lowest *C* ($Ub_2^{DP\rightarrow 4}$, 16.0 to 16.6 nm^2), which generally agrees with the native-like measurements shown as white markers.

Figures 7.4c show analogous data for denatured Ub_3; native PA and EHSS values are not included because there are not entries for linear Ub_3 and Ub_4 in the PDB. Unlike denatured Ub_1 and Ub_2, the CAPTR products of denatured Ub_3 fold to Ω more extended than their native-like counterparts. At the lowest *C* measured, $Ub_3^{DP\rightarrow 5}$, $\widetilde{\Omega}$ ranges from 22.7 to 24.6 nm^2, which are higher than the Ω for the native-like precursor ions by ~10 to 20%.

Ub_4 exhibited properties most similar to Ub_3 (Figure 7.4d). As *C* decreases, the ions compact to smaller Ω ranges, and Ω depends on *P* for some intermediate *C*. Unlike the other poly-ubiquitins, we were unable to transmit Ub_4 CAPTR product ions with charge states equal to or lesser than the charge states of the corresponding native-like ions. This may be because those ions have such low mobilities that they are unable to be injected into the rf-confining drift cell with 2.0 mbar of He. Thus, the lowest *C* measured ions of Ub_4 have likely not compacted to a folded gas-phase conformation. Consequently, additional CAPTR events would likely generate more compact Ω distributions.

The right-hand side of Figures 7.4a to 7.4d also includes the relative Ω value established in Figure 7.2 to evaluate the structures of the ions. Interestingly, none of the CAPTR product ions fold to Ω distributions consistent with a density of 1.2 g cm^{-3} (≤1.0 on this scale). The average $\widetilde{\Omega}$ for the lowest charge state CAPTR product ions (*i.e.* $Ub_1^{DP\rightarrow 3}$, $Ub_2^{DP\rightarrow 4}$, $Ub_3^{DP\rightarrow 5}$ and $Ub_4^{DP\rightarrow 13}$) are also shown in Figure 7.2. Those results indicate that the denatured product ions of Ub_1 and Ub_2 are consistent with the ions folding to one and two domain structures, respectively. The CAPTR product ions of Ub_3 are consistent with the ions folding to a linear arrangement of three beads, which is the largest of the three coarse-grained models. In contrast, the CAPTR product ions of Ub_4 are consistent with a linear arrangement of sixteen beads, although as noted previously, those experiments are likely limited by transmission of low *C* ions that would likely be more compact than those shown. The data is also consistent with those denatured CAPTR product ions folding to other geometries with additional beads because they have similar Ω values as structures with few beads. For example, the single domain structures have similar Ω to the close-packing models with 7 to 10 beads, and therefore the structures cannot be differentiated using these models. Consequently, these experimental Ω values are consistent with Ub_1, Ub_2, and

Ub_3 folding to gas-phase structures with domain structures analogous to their solution-phase counterparts, although there are other interpretations consistent with the data.

7.4.5 *When have CAPTR Products Fully Folded in the Gas Phase?*

Previous measurements of denatured CAPTR product ions have indicated that at low *C*, Ω weakly depends on *C* and therefore the ions have folded to compact gas-phase structures. To evaluate the extent to which the denatured poly-ubiquitins in Figures 7.4a to 7.4d have folded to those compact structures, the change in $\widetilde{\Omega}$ following each CAPTR event is plotted in Figures 7.4e to 7.4h.

Figure 7.4e shows the change in the $\widetilde{\Omega}$ of Ub_1 with respect to changes in *C*, where ions of different *P* are indicated using different colors. From *C*=13 to 8 the denatured Ub_1 ions change by an average of 0.74 nm^2 per CAPTR event, and ions from different *P* are indistinguishable from one another. The magnitude of the rate increases for $Ub_1^{DP\rightarrow 7}$ and $Ub_1^{DP\rightarrow 6}$ for all ions, then decreases again for $Ub_1^{DP\rightarrow 5}$ and $Ub_1^{DP\rightarrow 4}$. That decrease in the change in Ω indicates the ions' $\widetilde{\Omega}$ becomes less affected by changes in *C*, and therefore, the ions have reached a folded gas-phase conformation. Additionally, these results indicate the changes in $\widetilde{\Omega}$ following each reaction of denatured Ub_1 are independent of *P*.

In contrast to those denatured Ub_1 results, the changes in $\widetilde{\Omega}$ of Ub_2 depend more on *P* (Figure 7.4f). CAPTR product ions from *P* = 21 to 13 generally behave like the Ub_1 data in 4e, in that the ions modestly change in $\widetilde{\Omega}$ for the first several CAPTR events, the changes accelerate at intermediate *C,* and decrease following the last reaction. In contrast, changes in $\widetilde{\Omega}$ of CAPTR product ions from *P* < 13 depend on *P*, and exhibit less of a clear trend. Overall, the largest change in $\widetilde{\Omega}$ occurs during the reaction from $Ub_2^{DP\rightarrow 6}$ to $Ub_2^{DP\rightarrow 5}$. Nonetheless, all ions change in

$\widetilde{\Omega}$ by less than 0.5 nm^2 in the reaction from $Ub_2^{DP\,\rightarrow 5}$ to $Ub_2^{DP\,\rightarrow 4}$, which indicates the ions have folded to a compact gas-phase conformation. Therefore, at low *z* all ions appear to achieve a folded structure, despite folding through different pathways.

Figure 7.4g shows analogous data for Ub_3, which are generally similar to that of Ub_2. High charge states of Ub_3 change by ~1 nm^2 for *C* = 31+ to 17+, that rate increases from 17+ to 6+, and then decreases at *C* = 5+. In contrast to Ub_1 and Ub_2, which exhibited changes in $\widetilde{\Omega}$ of less than 0.5 nm^2 during the last CAPTR event, Ub_3 exhibits a greater change in $\widetilde{\Omega}$ at the lowest *C* measured, *i.e.* the reaction from $Ub_3^{DP\,\rightarrow 6}$ to $Ub_3^{DP\,\rightarrow 5}$. Therefore, Ub_3 may compact more following further CAPTR events than that of Ub_1 or Ub_2. However, the change in $\widetilde{\Omega}$ in the reaction from $Ub_3^{DP\,\rightarrow 6}$ to $Ub_3^{DP\,\rightarrow 5}$ did decrease for most ions compared to the $Ub_3^{DP\,\rightarrow 7}$ to $Ub_3^{DP\,\rightarrow 6}$reaction. Therefore, the $\widetilde{\Omega}$ of these ions may be within 1-2 reactions from the analogous folded gas-phase conformations observed for Ub_1 and Ub_2 ions. As previously discussed, the lowest *C* products agree with the largest coarse-grained model with three beads. Consequently, if additional reactions caused the protein to compact by 1-2 nm^2, the $\widetilde{\Omega}$ of lower *z* ions may agree with one of the other coarse-grained models.

Changes in $\widetilde{\Omega}$ as a function of CAPTR product ion charge state for Ub_4 are shown in Figure 7.4h. Ub_4 behaves similar to that of Ub_2 and Ub_3, in that the changes in Ω are modest at high *C*, then accelerate at lower *C*. Unlike that of the smaller poly-ubiquitins, there is not a significant decrease in the rate of change observed at the lowest *C* measured. As stated previously, we were unable to measure the Ω of Ub_4 CAPTR product ions at charge states as low as their native-like counterparts due to low ion transmission. Therefore, the analogous decrease in $\widetilde{\Omega}$ was likely not observed due to those transmission issues. Consequently, the lowest *C* ions of

denatured Ub_4 ion observed would likely continue to significantly compact with further reactions, and is therefore not a compact gas-phase folded structure.

The magnitude of the change in Ω with respect to *C* for all poly-ubiquitins are similar. This suggests that changes in Ω with respect to *C* are independent of the size of the protein. Thus, a single CAPTR event induces a structural change in the local environment of the reaction, as opposed to larger isomerization involving the entire protein. Do CAPTR Products "Remember" their Original Identity?

7.4.6 *Do CAPTR Products "Remember" their Original Identity?*

Although previous studies of the Ω distributions of CAPTR products of denatured proteins have exhibited some dependence on *C*, [17,33] none have exhibited a dependence as strong as those for Ub_2, Ub_3, and Ub_4. Previous results for denatured Ub_1 showed that ions of different *P* folded to different structural populations, despite the products having similar Ω distributions. In contrast, the Ω of Ub_2, Ub_3, and Ub_4 depend on *C*, particularly for intermediate *C*. Figures 7.4i to 7.4l show the range in $\widetilde{\Omega}$ as a function of *C* to evaluate their relationship.

Figure 7.4i shows the range of the $\widetilde{\Omega}$ observed for each *C* of denatured Ub_1. The results indicate that $Ub_1^{DP\rightarrow 6}$ has the largest range of $\widetilde{\Omega}$ values, and is therefore the most structurally diverse. However, the ions range in $\widetilde{\Omega}$ by less than 1 nm^2, which is relatively modest compared to the width of the apparent Ω distributions in Figure 7.4a. Nonetheless, it is interesting that the reaction of $Ub_1^{DP\rightarrow 6}$ to $Ub_1^{DP\rightarrow 5}$ also corresponds to the charge state with the greatest change in $\widetilde{\Omega}$ with respect to *C* (Figure 7.2e). This observation is generally consistent with previous CAPTR Ω measurements of $Ub_1^{DP\rightarrow 6}$.[19] In those previous experiments, we also performed energy-dependent collisional activation experiments that showed that although the Ω of CAPTR products were independent of *P*, the structures of those products depended on *P*. Therefore, CAPTR product

ions originating from different *P* fold through different pathways, and consequently we expect that the structures of those products do depend on *P*. Moreover, even small ranges in $\widetilde{\Omega}$ (< 1 nm^2) may indicate significant differences in structural populations of CAPTR product ions, despite narrow $\widetilde{\Omega}$ ranges at low *C*.

Analogous data for Ub_2, Ub_3, and Ub_4 are shown in Figure 7.4j to 7.4l. In contrast to the $\widetilde{\Omega}$ ranges for Ub_1, all three of these proteins exhibit much higher $\widetilde{\Omega}$ ranges, particularly for intermediate charge states. For instance, Ub_2 ions between $Ub_2^{DP\rightarrow 14}$ to $Ub_2^{DP\rightarrow 6}$ have average $\widetilde{\Omega}$ values that range more than 1 nm^2 (Figure 7.4f), which exceeds all ranges of $\widetilde{\Omega}$ for a given *C* for all denatured Ub_1 CAPTR product ions. Compared to Ub_1, these much stronger $\widetilde{\Omega}$ dependences on *P* for Ub_2, Ub_3, and Ub_4 indicate that ions from different *P* fold through different pathways, without the need for energy-dependent measurements. Interestingly, at the lowest *C* ions measured, $Ub_2^{DP\rightarrow 5}$ and $Ub_2^{DP\rightarrow 4}$, have average $\widetilde{\Omega}$ ranges less than 1 nm^2. This indicates that these ions are converging to similar Ω distributions at low *C*, which is independent of *P*. In contrast, both Ub_3 and Ub_4 exhibit $\widetilde{\Omega}$ ranges of ~2 nm^2 at the lowest *C* values, which indicates these large poly-ubiquitin have a wider range of structures at the lowest *C* measured.

In general, these results show that $\widetilde{\Omega}$ depend significantly on *P* for Ub_2, Ub_3, and Ub_4. That dependency may be the result of different folding pathways, and therefore ions of different *P* fold though different intermediate structures. Consequently, ions have some memory of their initial structures. Interestingly, for *C* that exhibit a Ω dependence on *P*, there is a general trend that ions with lower *P* have more compact Ω distributions (Figure 7.4a to 7.4d). This may be because (a) precursor ions with lower *P* have more compact Ω distributions, and therefore their products are more compact, (b) more compact precursor ions react faster than more extended structures for ions of the same *P*, which also leads to more compact product ions, which has been

observed for ion/neutral reactions,[21] or that (c) CAPTR product ions heat during each CAPTR event such that over many events the ions isomerize to more extended gas-phase structures for a given *C*.

7.4.7 *How are Collisionally Activated Native-Like Ions Related to Denatured CAPTR Product Ions?*

The Ω distributions in Figure 7.4A to 7.4D show that the CAPTR ions from denatured Ub_1, Ub_2, and Ub_3 with the same charge states as that of their native-like counterparts have different Ω distributions. To investigate the relationship between these seemingly disparate data sets energy-dependent collisional activation was performed on native-like ions. With sufficient collisional activation, the native-like ions can isomerize, which may be monitored using IM. Consequently, these measurements can monitor if the energy-dependent native-like Ω distributions have features similar to that of the denatured CAPTR product ions.

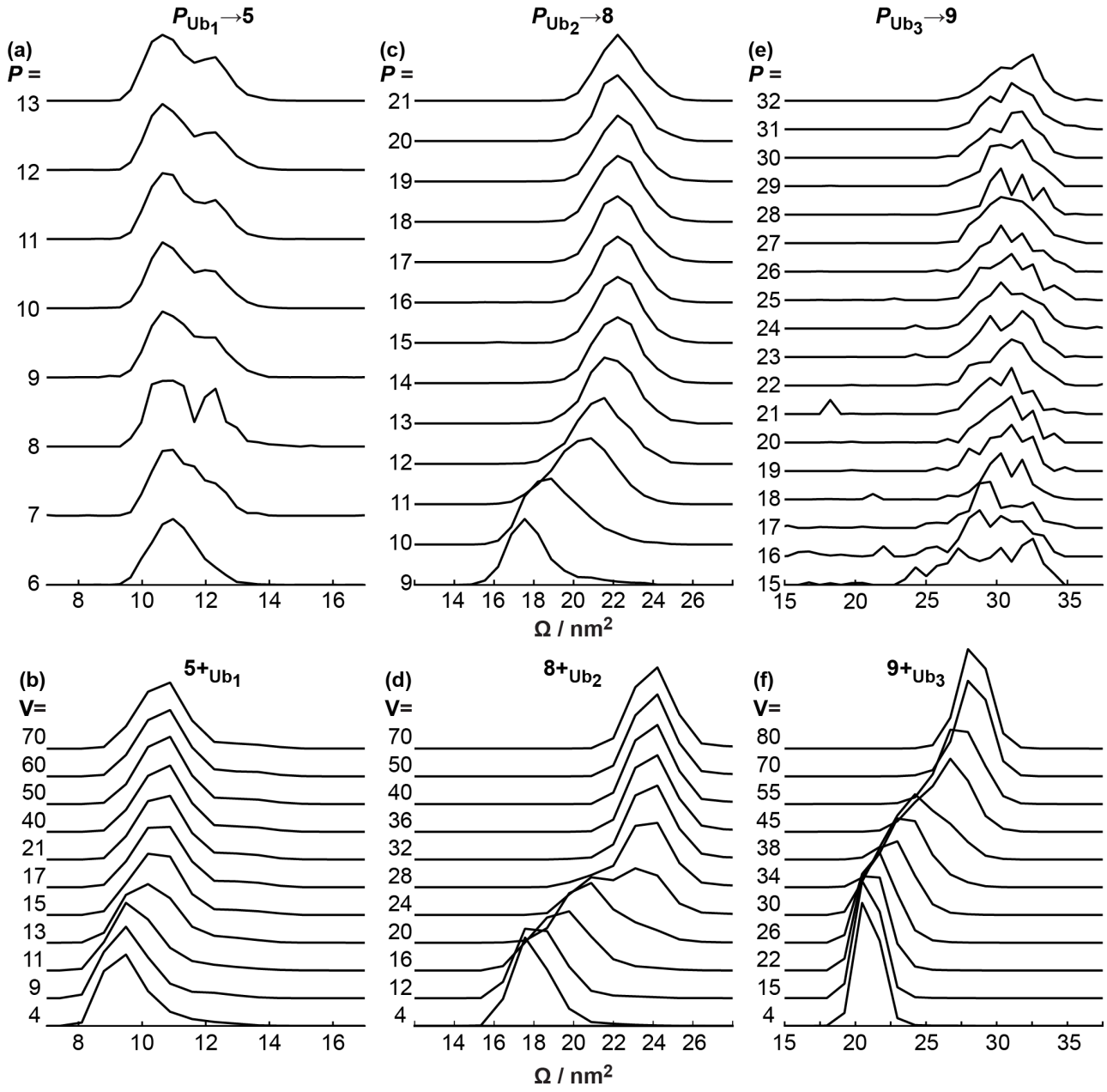

Figure 7.5. Ω distributions of CAPTR product ions of (a) $Ub_1^{DP\rightarrow 5}$, (c) $Ub_2^{DP\rightarrow 8}$, and (e) $Ub_3^{DP\rightarrow 9}$, and energy dependent collisional activation of (b) Ub_1^{N5}, (d) Ub_2^{N8}, and (f) Ub_3^{N9}. Time was converted to Ω using a single-field strength method with a 212 V drop across the drift cell.

Figure 7.5a and 7.5b show the Ω distributions of denatured $Ub_1^{DP\rightarrow 5}$ as a function of *P* and Ub_1^{N5+} as a function of collisional activation voltage. For the CAPTR product ions, the Ω distributions generally include two features, near 11.0 nm^2 and 12.5 nm^2, and span a Ω range of 9.5 to 13.5 nm^2. The intensity of these two features is approximately constant from *P* = 13 to 8, whereas the feature at 10.5 nm^2 is much more intense than the latter feature for $Ub_1^{D7\rightarrow 5}$ and $Ub_1^{DP6\rightarrow 5}$. At low energies, the native-like Ub_1^{N5+} is more compact than that of any denatured $Ub_1^{DP\rightarrow 5}$ ions, and has a single feature around 9.5 nm^2. With about 11 V to 15 V of collisional activation, this distribution shifts to a single feature around 11 nm^2. Thus, the collisionally activated Ub_1^{N5} ion has a Ω distribution that significantly overlaps with the Ω distribution of the gas-phase folded $Ub_1^{DP\rightarrow 5}$ ion. There are two explanations to this data: (1) the two Ω distributions include completely unique structural distribution that have similar sizes and consequently have overlapping Ω distributions, or (2) the two Ω distribution have structural populations in common with one another, in addition to their own unique structural populations. Thus, it may be the case that although these ions were generated via very different methods from very different solution conditions, they may have populations occupying a similar local-minimum on the gas-phase energy surface of 5+ Ub_1.

Results comparing the Ω distribution of denatured $Ub_2^{DP\rightarrow 8}$ and energy-dependent native-like Ub_2^{N8+}, are shown in Figure 7.5c and 7.5d. The $Ub_2^{DP\rightarrow 8}$ Ω distributions are dependent on *P*, which is discussed in the section '*Ω of denatured poly-ubiquitins and their CAPTR product ions'*. At low *P* the Ω are unimodal and have a single feature near 17.5 nm^2. As *P* increases, the Ω distribution transitions to a single feature centered near 22.0 nm^2. The low energy Ub_2^{N8+} Ω distribution and the $Ub_2^{D9\rightarrow 8}$ Ω distribution are indistinguishable from one another. Thus, these two Ω distributions may include similar structural distributions, or ions with similar sizes and Ω.

In contrast, the high energy Ub_2^{N8+} Ω distributions are unimodal and centered around 24 nm^2, and overlap less with high *P* ions of $Ub_2^{DP\ \rightarrow 8}$ distribution. Consequentially, these two ion populations may have unresolved structures in common, in addition to unique structural populations.

Ub_3 Ω distributions for $Ub_3^{DP\ \rightarrow 9}$ and Ub_3^{N9+} ions are shown in Figure 7.5e and 7.5f, respectively. In general, these ions do not have overlapping Ω distributions, with the exceptions of the $Ub_3^{D15\ \rightarrow 9}$ and high energy Ub_3^{N9+}. The $Ub_3^{DP\ \rightarrow 9}$ Ω distributions has low signal to noise ratio, and it is difficult to characterize how many features are in a given Ω distribution. Thus, unlike Ub_1, and Ub_2, which had many Ω distributions that overlapped, only two for Ub_3 do overlap. As a result, it appears that there is a high barrier for the native-like ion to interconvert to structures with Ω distributions overlapping with some corresponding CAPTR product ions.

As noted earlier, there are not any charge states in common between the denatured CAPTR product ions of Ub_4 and native-like Ub_4. Figure S6 shows energy dependent Ub_4^{N11+} and Ub_4^{N12+} Ω distributions and denatured $Ub_4^{DP\ \rightarrow 13}$ Ω distributions. In general, comparisons of the data are similar to those that can be made for Ub_3. However, because these ions are of different charge state, conclusions relating the data are difficult.

In general, these Ω distributions in Figure 7.5 show various extents of overlapping Ω populations between CAPTR product ions, and energy-dependent native-like ions. Additional Ω distributions comparing sizes of denatured CAPTR products and energy-dependent native-like ions of 6+ Ub_1, 9+ Ub_2, and 10+ Ub_3 may be found in Figure S4. Overall, these results may be explained with three possibilities: (1) ions with similar Ω distributions share common structures, and thus the relationship between gas-phase and solution-phase folded ions may be directly compared. Further experiments to probe residue-level structure may help determine the extent to

which protein-solvent interactions, or lack thereof, are involved in protein folding. (2) Alternatively, similar Ω distributions may not have any structures in common, in which case we are able to study different portions of an ions potential energy surface. (3) Likewise, in cases where the distributions do not overlap, these experiments are able to generate different conformations of an ion that are unable to interconvert. Consequentially, further studies may be able to study different portions of an ions potential energy surface. Additionally, it is unclear whether the CAPTR product ions have annealed to local energetic minima, or whether they would isomerize with increasing collisional activation. Future post-CATPR collisional activation of these ions may provide further insight into how the gas-phase folded CAPTR product ions relate to their native-like counterparts.

7.5 Conclusions

The Ω of poly-ubiquitin ions and their CAPTR product ions were measured from denaturing and native-like conditions, and the domain structures of those ions were interpreted using coarse-grained models. Precursor ions from denaturing conditions yielded a wide distribution of *z* and Ω compared to their native-like counterparts. The CAPTR products of native-like poly-ubiquitin ions yielded Ω values similar to their respective precursor ion, with the exception of 6+ Ub_1 and 9+ Ub_2. These results indicate that the domain structure of those ions remains intact even at low *z*.

The Ω distributions of CAPTR product ions of poly-ubiquitin from denaturing conditions yielded more compact Ω distributions for most ions, similar to previous results with protein ions from denaturing conditions. The Ω distributions of Ub_2, Ub_3, and Ub_4 ions with intermediate *C* were much more dependent on *P* than any previous CAPTR study, and there was a general trend

that ions from lower *P* yielded more compact Ω distributions than ions from higher *P*. The rate of compaction with respect to changes in *C* accelerated at intermediate *C*, relative to high *C*, then decrease again at the lowest *C*. Moreover, the magnitude of those changes were similar for all poly-ubiquitin lengths, indicating that the isomerizations are independent of protein size, and consequentially are due to localized isomerizations. Additionally, the range in $\widetilde{\Omega}$ for ions of a given *C* was used to quantify the structural diversity of ions from different *P*. The lowest *C* ions for each poly-ubiquitin had an average $\widetilde{\Omega}$ value consistent with the protein folding to a domain structure similar to that of the native-like ion, with the exception of Ub_4, which was limited due to poor transmission of the lowest mobility ions.

Finally, Ω distributions collisionally activated native-like Ub_1 and Ub_2 overlapped with some Ω distributions of the CAPTR products of those ions from denaturing conditions. Analogous experiments comparing those of Ub_3 indicated less overlap between the energy-dependent native-like Ω distributions and CAPTR product ions from denaturing conditions. Consequentially, in cases where there is significant Ω overlap the ions may have similar structural population. In contrast, for Ω distributions with little or no overlap, these data may be used to probe different portions of an ions gas-phase energy surface. These results would greatly benefit from future energy-dependent collisional activation experiments investigating the structures of the CAPTR product ions from denaturing conditions.

7.6 Supporting Information.

Figures S1 to S5 and Table 1 are available in Appendix F.

7.7 Acknowledgments.

Research reported in this publication was supported by Eli Lilly and Company (Young Investigator Award in Analytical Chemistry to M. F. B.) and the National Institute of General Medical Sciences of the National Institutes of Health under Award Number T32GM008268 (support to K. J. L.)

7.8 References

(1) Hilton, G. R.; Benesch, J. L. P. Two Decades of Studying Non-Covalent Biomolecular Assemblies by Means of Electrospray Ionization Mass Spectrometry. *J. R. Soc. Interface* **2012**, *9* (70), 801–816.

(2) Ruotolo, B. T.; Benesch, J. L.; Sandercock, A. M.; Hyung, S. J.; Robinson, C. V. Ion Mobility-Mass Spectrometry Analysis of Large Protein Complexes. *Nat Protoc* **2008**, *3*, 1139–1152.

(3) Benesch, J. L.; Ruotolo, B. T. Mass Spectrometry: Come of Age for Structural and Dynamical Biology. *Current Opinion in Structural Biology* **2011**, *21* (5), 641–649.

(4) Lanucara, F.; Holman, S. W.; Gray, C. J.; Eyers, C. E. The Power of Ion Mobility-Mass Spectrometry for Structural Characterization and the Study of Conformational Dynamics. *Nat Chem* **2014**, *6* (4), 281–294.

(5) Bleiholder, C.; Do, T. D.; Wu, C.; Economou, N. J.; Bernstein, S. S.; Buratto, S. K.; Shea, J.-E.; Bowers, M. T. Ion Mobility Spectrometry Reveals the Mechanism of Amyloid Formation of Aβ(25–35) and Its Modulation by Inhibitors at the Molecular Level: Epigallocatechin Gallate and Scyllo-Inositol. *J. Am. Chem. Soc.* **2013**, *135* (45), 16926–16937.

(6) Shepherd, D. A.; Holmes, K.; Rowlands, D. J.; Stonehouse, N. J.; Ashcroft, A. E. Using Ion Mobility Spectrometry–Mass Spectrometry to Decipher the Conformational and Assembly Characteristics of the Hepatitis B Capsid Protein. *Biophysical Journal* **2013**, *105* (5), 1258–1267.

(7) Uetrecht, C.; Barbu, I. M.; Shoemaker, G. K.; Duijn, E. van; Heck, A. J. R. Interrogating Viral Capsid Assembly with Ion Mobility–mass Spectrometry. *Nature Chemistry* **2011**, *3* (2), 126–132.

(8) Baldwin, A. J.; Lioe, H.; Hilton, G. R.; Baker, L. A.; Rubinstein, J. L.; Kay, L. E.; Benesch, J. L. P. The Polydispersity of αB-Crystallin Is Rationalized by an Interconverting Polyhedral Architecture. *Structure* **2011**, *19* (12), 1855–1863.

(9) Zhou, M.; Sandercock, A. M.; Fraser, C. S.; Ridlova, G.; Stephens, E.; Schenauer, M. R.; Yokoi-Fong, T.; Barsky, D.; Leary, J. A.; Hershey, J. W.; et al. Mass Spectrometry Reveals Modularity and a Complete Subunit Interaction Map of the Eukaryotic Translation Factor eIF3. *Proc. Natl. Acad. Sci. U.S.A.* **2008**, *105*, 18139–18144.

(10) Myung, S.; Badman, E. R.; Lee, Y. J.; Clemmer, D. E. Structural Transitions of Electrosprayed Ubiquitin Ions Stored in an Ion Trap over ~10 Ms to 30 S†. *J. Phys. Chem. A* **2002**, *106* (42), 9976–9982.
(11) Freitas, M. A.; Hendrickson, C. L.; Emmett, M. R.; Marshall, A. G. Gas-Phase Bovine Ubiquitin Cation Conformations Resolved by Gas-Phase Hydrogen/Deuterium Exchange Rate and extent1. *International Journal of Mass Spectrometry* **1999**, *185–187*, 565–575.
(12) Breuker, K.; McLafferty, F. W. Stepwise Evolution of Protein Native Structure with Electrospray into the Gas Phase, 10−12 to 102 S. *Proc Natl Acad Sci U S A* **2008**, *105* (47), 18145–18152.
(13) Seo, J.; Hoffmann, W.; Warnke, S.; Bowers, M. T.; Pagel, K.; von Helden, G. Retention of Native Protein Structures in the Absence of Solvent: A Coupled Ion Mobility and Spectroscopic Study. *Angew Chem Int Ed Engl* **2016**, *55* (45), 14173–14176.
(14) González Flórez, A. I.; Mucha, E.; Ahn, D.-S.; Gewinner, S.; Schöllkopf, W.; Pagel, K.; von Helden, G. Charge-Induced Unzipping of Isolated Proteins to a Defined Secondary Structure. *Angew. Chem. Int. Ed.* **2016**, *55* (10), 3295–3299.
(15) Zhong, Y.; Han, L.; Ruotolo, B. T. Collisional and Coulombic Unfolding of Gas-Phase Proteins: High Correlation to Their Domain Structures in Solution. *Angew. Chem.* **2014**, n/a-n/a.
(16) Eschweiler, J. D.; Martini, R. M.; Ruotolo, B. T. Chemical Probes and Engineered Constructs Reveal a Detailed Unfolding Mechanism for a Solvent-Free Multidomain Protein. *J. Am. Chem. Soc.* **2017**, *139* (1), 534–540.
(17) Laszlo, K. J.; Munger, E. B.; Bush, M. F. Effects of Solution Structure on the Folding of Lysozyme Ions in the Gas Phase. *J. Phys. Chem. B* **2017**, *121* (13), 2759–2766.
(18) Uetrecht, C.; Versluis, C.; Watts, N. R.; Roos, W. H.; Wuite, G. J. L.; Wingfield, P. T.; Steven, A. C.; Heck, A. J. R. High-Resolution Mass Spectrometry of Viral Assemblies: Molecular Composition and Stability of Dimorphic Hepatitis B Virus Capsids. *PNAS* **2008**.
(19) Laszlo, K. J.; Munger, E. B.; Bush, M. F. Folding of Protein Ions in the Gas Phase after Cation-to-Anion Proton-Transfer Reactions. *J. Am. Chem. Soc.* **2016**, *138*, 9581–9588.
(20) Freeke, J.; Bush, M. F.; Robinson, C. V.; Ruotolo, B. T. Gas-Phase Protein Assemblies: Unfolding Landscapes and Preserving Native-like Structures Using Noncovalent Adducts. *Chemical Physics Letters* **2012**, *524*, 1–9.
(21) Clemmer, D. E.; Hudgins, R. R.; Jarrold, M. F. Naked Protein Conformations: Cytochrome c in the Gas Phase. *J. Am. Chem. Soc.* **1995**, *117* (40), 10141–10142.
(22) Wyttenbach, T.; Bowers, M. T. Structural Stability from Solution to the Gas Phase: Native Solution Structure of Ubiquitin Survives Analysis in a Solvent-Free Ion Mobility–Mass Spectrometry Environment. *J. Phys. Chem. B* **2011**, *115* (42), 12266–12275.
(23) Bush, M. F.; Hall, Z.; Giles, K.; Hoyes, J.; Robinson, C. V.; Ruotolo, B. T. Collision Cross Sections of Proteins and Their Complexes: A Calibration Framework and Database for Gas-Phase Structural Biology. *Analytical Chemistry* **2010**, *82*, 9557–9565.
(24) Allen, S. J.; Schwartz, A. M.; Bush, M. F. Effects of Polarity on the Structures and Charge States of Native-Like Proteins and Protein Complexes in the Gas Phase. *Anal. Chem.* **2013**, *85* (24), 12055–12061.
(25) Valentine, S. J.; Counterman, A. E.; Clemmer, D. E. Conformer-Dependent Proton-Transfer Reactions of Ubiquitin Ions. *Journal of the American Society for Mass Spectrometry* **1997**, *8* (9), 954–961.

(26) Bornschein, R.; Hyung, S.-J.; Ruotolo, B. Ion Mobility-Mass Spectrometry Reveals Conformational Changes in Charge Reduced Multiprotein Complexes. *J. Am. Soc. Mass Spectrom.* **2011**, *22* (10), 1690–1698.
(27) McLuckey, S. A.; Stephenson, J. L. Ion/Ion Chemistry of High-Mass Multiply Charged Ions. *Mass Spectrom. Rev.* **1998**, *17* (6), 369–407.
(28) Lermyte, F.; Łącki, M. K.; Valkenborg, D.; Gambin, A.; Sobott, F. Conformational Space and Stability of ETD Charge Reduction Products of Ubiquitin. *J. Am. Soc. Mass Spectrom.* **2016**, 1–8.
(29) Laszlo, K. J.; Bush, M. F. Effects of Charge State on the Structures of Native-Like Protein Ions: Results From Cation to Anion Proton Transfer Reactions (CAPTR). *Submitted to Analytical Chemistry*.
(30) Gunawardena, H. P.; He, M.; Chrisman, P. A.; Pitteri, S. J.; Hogan, J. M.; Hodges, B. D. M.; McLuckey, S. A. Electron Transfer versus Proton Transfer in Gas-Phase Ion/Ion Reactions of Polyprotonated Peptides. *J. Am. Chem. Soc.* **2005**, *127* (36), 12627–12639.
(31) Bornschein, R. E.; Niu, S.; Eschweiler, J.; Ruotolo, B. T. Ion Mobility-Mass Spectrometry Reveals Highly-Compact Intermediates in the Collision Induced Dissociation of Charge-Reduced Protein Complexes. *J. Am. Soc. Mass Spectrom.* **2015**, *27* (1), 41–49.
(32) Holden, D. D.; Brodbelt, J. S. Ultraviolet Photodissociation of Native Proteins Following Proton Transfer Reactions in the Gas Phase. *Anal. Chem.* **2016**, *88* (24), 12354–12362.
(33) Laszlo, K. J.; Buckner, J. H.; Munger, E. B.; Bush, M. F. Native-Like and Denatured Cytochrome c Ions Yield Cation-to-Anion Proton Transfer Reaction Products with Similar Collision Cross-Sections. *J. Am. Soc. Mass Spectrom.* **2017**, 1–10.
(34) Williams, J. P.; Brown, J. M.; Campuzano, I.; Sadler, P. J. Identifying Drug Metallation Sites on Peptides Using Electron Transfer Dissociation (ETD), Collision Induced Dissociation (CID) and Ion Mobility-Mass Spectrometry (IM-MS). *Chem. Commun.* **2010**, *46* (30), 5458–5460.
(35) Laszlo, K. J.; Bush, M. F. Analysis of Native-Like Proteins and Protein Complexes Using Cation to Anion Proton Transfer Reactions (CAPTR). *J. Am. Soc. Mass Spectrom.* **2015**, *26*, 2152–2161.
(36) Stephenson, J. L.; McLuckey, S. A. Ion/Ion Reactions in the Gas Phase: Proton Transfer Reactions Involving Multiply-Charged Proteins. *J. Am. Chem. Soc.* **1996**, *118* (31), 7390–7397.
(37) Allen, S.; Giles, K.; Gilbert, T.; Bush, M. Ion Mobility Mass Spectrometry of Peptide, Protein, and Protein Complex Ions Using a Radio-Frequency Confining Drift Cell. *Analyst* **2016**, *141*, 884–891.
(38) von Helden, G.; Hsu, M. T.; Gotts, N.; Bowers, M. T. Carbon Cluster Cations with up to 84 Atoms: Structures, Formation Mechanism, and Reactivity. *J. Phys. Chem.* **1993**, *97* (31), 8182–8192.
(39) Shvartsburg, A. A.; Jarrold, M. F. An Exact Hard-Spheres Scattering Model for the Mobilities of Polyatomic Ions. *Chemical Physics Letters* **1996**, *261* (1–2), 86–91.
(40) Shvartsburg, A. A.; Mashkevich, S. V.; Baker, E. S.; Smith, R. D. Optimization of Algorithms for Ion Mobility Calculations. *J. Phys. Chem. A* **2007**, *111* (10), 2002–2010.
(41) Vijay-Kumar, S.; Bugg, C. E.; Cook, W. J. Structure of Ubiquitin Refined at 1.8Åresolution. *Journal of Molecular Biology* **1987**, *194* (3), 531–544.
(42) Rohaim, A.; Kawasaki, M.; Kato, R.; Dikic, I.; Wakatsuki, S. Structure of a Compact Conformation of Linear Diubiquitin. *Acta Cryst D, Acta Cryst Sect D, Acta Crystallogr D,*

Acta Crystallogr Sect D, Acta Crystallogr D Biol Crystallogr, Acta Crystallogr Sect D Biol Crystallogr **2012**, *68* (2), 102–108.

(43) Pettersen, E. F.; Goddard, T. D.; Huang, C. C.; Couch, G. S.; Greenblatt, D. M.; Meng, E. C.; Ferrin, T. E. UCSF Chimera--a Visualization System for Exploratory Research and Analysis. *J Comput Chem* **2004**, *25* (13), 1605–1612.

(44) Salbo, R.; Bush, M. F.; Naver, H.; Campuzano, I.; Robinson, C. V.; Pettersson, I.; Jørgensen, T. J. D.; Haselmann, K. F. Traveling-Wave Ion Mobility Mass Spectrometry of Protein Complexes: Accurate Calibrated Collision Cross-Sections of Human Insulin Oligomers. *Rapid Communications in Mass Spectrometry* **2012**, *26* (10), 1181–1193.

(45) Kaddis, C. S.; Lomeli, S. H.; Yin, S.; Berhane, B.; Apostol, M. I.; Kickhoefer, V. A.; Rome, L. H.; Loo, J. A. Sizing Large Proteins and Protein Complexes by Electrospray Ionization Mass Spectrometry and Ion Mobility. *Journal of the American Society for Mass Spectrometry* **2007**, *18* (7), 1206–1216.

(46) Bush, M. F.; Hall, Z.; Giles, K.; Hoyes, J.; Robinson, C. V.; Ruotolo, B. T. Collision Cross Sections of Proteins and Their Complexes: A Calibration Framework and Database for Gas-Phase Structural Biology. *Analytical Chemistry* **2010**, *82*, 9557–9565.

(47) Hogan, C. J.; Mora, J. F. de la. Ion Mobility Measurements of Nondenatured 12–150 kDa Proteins and Protein Multimers by Tandem Differential Mobility Analysis–Mass Spectrometry (DMA-MS). *J. Am. Soc. Mass Spectrom.* **2011**, *22* (1), 158–172.

(48) Quillin, M. L.; Matthews, B. W. Accurate Calculation of the Density of Proteins. *Acta Crystallographica Section D Biological Crystallography* **2000**, *56* (7), 791–794.

(49) Fischer, H.; Polikarpov, I.; Craievich, A. F. Average Protein Density Is a Molecular-Weight-Dependent Function. *Protein Science* **2004**, *13* (10), 2825–2828.

(50) Campuzano, I. G.; Schnier, P. Coupling Electrospray Corona Discharge, Charge Reduction and Ion Mobility Mass Spectrometry: From Peptides to Large Macromolecular Protein Complexes. *Int. J. Ion Mobil. Spec.* **2013**, *16* (1), 51–60.

Chapter 8. Effect of Charge State, Partial Charge Distribution, and Structure on Momentum Transfer Collision Cross Sections of Protein Ions

---

This chapter is reproduced with permission from Laszlo, K. J.; Bush, M. F. "Effect of Charge State, Partial Charge Distribution, and Structure on Momentum Transfer Collision Cross Sections of Protein Ions" **2017**, manuscript in preparation

8.1 Abstract

Momentum transfer collision cross sections (Ω) of gas-phase ions are commonly measured using ion mobility-mass spectrometry, and are increasingly being used in structural biology applications. To verify Ω against other established structural biology tools, like NMR and x-ray crystallography, several software tools have been designed to estimate Ω from atomic structures. However, many of these software tools neglect long-range ion-neutral interactions, which change as a function of ion charge state (z) to simplify the computational costs of the calculation. Those limitations make structural interpretations of Ω challenging over several z, like those produced via electrospray ionization (ESI). Recent advances in these software tools and computer hardware are now placing more advanced "Trajectory Method" (TM) calculations, which include the ion-neutral interaction potential, within reach. Here, we calculate Ω_{TM} for several structural models of the proteins ubiquitin, di-ubiquitin, and alcohol dehydrogenase to investigate the extent that changes in the ion-induced dipole interaction may affect Ω over many z, and provide guidelines on how to best assign partial charges to atomic protein structural

models. In general, we find that this interaction is insignificant over the narrow *z* range generated via ESI of globular protein ions generated from native-like solutions. Furthermore, we find that this term can account for the small changes in Ω measured for the highest *z* protein ions generated from denatured and supercharging conditions.

8.2 Introduction

To verify ion mobility (IM) momentum transfer collision cross section (Ω) measurements to other structural biology measurements, *i.e.* NMR and x-ray crystallography, several algorithms have been developed to estimate Ω from input atomic structures.[1–6] The most widely used algorithms are the projection approximation (PA),[1] exact hard sphere scattering (EHSS),[2,3] and the trajectory method (TM).[4,5] The projection approximation involves orientationally averaging the projected area of an ion-neutral interaction. This method is computationally inexpensive and generally underestimates experimental Ω values. The EHSS simulates hard-sphere elastic collisions between the input ion structure and neutral gas and calculates momentum transfer from the gas to the ion to estimate a Ω. This method is also computationally inexpensive and generally overestimates experimental Ω values. As a result, the PA and EHSS values may be used to bracket possible Ω for a given structure.[7–9]

One challenge with these approaches is that both are independent of the charge state of an ion (*z*). In most ion mobility-mass spectrometry (IM-MS) experiments, ions are generated from electrospray ionization (nESI), which generates a distribution of charge states for each analyte. Therefore, multiple Ω values are measured for a single analyte. For protein ions generated from denaturing conditions (organic solvents, low pH, etc.), Ω strongly depends on *z*.[10] In contrast, the Ω of high *z* protein ions generated from supercharging solution conditions (organic solvents, low

pH, 15% propylene carbonate, etc.), depend less on *z* than their lower *z* counterparts.[11] Similarly, the Ω of the lowest *z* ions generated from ion/ion proton transfer reactions of proteins ions from denaturing solution conditions[8,9] and protein[9] and protein complex[12] ions from native-like solution conditions (aqueous, pH 7, etc.) depend weakly on *z*. Similar results were found of low *z* ions generated via nESI of native-like protein solutions containing triethylamine.[13] Consequentially, the extent to which changes in *z* initiate structural isomerization versus how changes in *z* affect momentum transfer between the neutral bath gas and ion is unclear.

In contrast to the PA and EHSS, the TM[4,5] accounts for changes in the charge state of an ion. The TM is the most computationally expensive of the three algorithms, and simulates many ion-neutral collisions and calculates momentum transfer, similar to the EHSS. Unlike the EHSS, the TM includes the potential energy of the ion-neutral interaction. The potential energy of the ion-neutral interaction is described using a Lennard-Jones interaction, which is attractive at long distances and repulsive at short distances, and an ion-induced dipole interaction, which is attractive at all distances.[4] Consequentially, an increase that the ion-induced dipole interaction will increases momentum transfer from the neutral collision partner to the ion. Moreover, each atom in the input structure for TM calculations also includes a partial charge parameter to calculate the ion-induced dipole interaction. Due to how computationally expensive the TM is, it is seldom used to estimate the Ω of large ions, like protein and protein complex ions.[14] However, advances in computer hardware and faster implementations of the TM, like that of IMoS,[15–17] have decreased the time to calculate TM values for these large structures.

Here, we have performed TM calculations on atomic structures of ubiquitin (Ub_1), di-ubiquitin (Ub_2), and alcohol dehydrogenase (ADH) using several different methods of assigning partial charges to each structure and as a function of charge state (*z*). The results herein provide

insight into how the ion-induced dipole interaction in the TM may affect Ω_{TM} values, and the extent to which changes in experimental Ω (Ω_{Exp}) may be attributed to changes in the ion-induced dipole interaction. Furthermore, Ω_{TM} data for the different partial charge distribution (PCD) methods provide guidelines on how future TM calculations of protein ions may be performed to yield Ω_{TM} in close agreement with Ω_{Exp}.

8.3 Experimental Methods

8.3.1 *nESI-IM-MS.*

Experimental Ω data were measured on a Waters Synapt G2 HDMS instrument modified with a radio-frequency confining drift cell for absolute Ω measurement.[18] Ub_1 was purchased from Boston Biochem, and C-to-N terminally linked Ub_2 was purchased from Enzo Life Science (Farmingdale, NY). Those proteins were dissolved into a denaturing solution of 70% methanol 30% water, which was adjusted to pH 2.0 with trifluoroacetic acid. The final concentration for Ub_1 and Ub_2 were 20 μM and 10 μM, respectively. For supercharging experiments, 15% by volume of propylene carbonate was added to these solutions, as described previously.[11] The final protein concentration for supercharging experiments was 11.6 μM and 8.5 μM for Ub_1 and Ub_2, respectively.

Nano-electrospray ionization (nESI) was used to generate protein cations. Borosilicate glass capillaries were pulled to a ~1 to 3 μm tip on one end using a Sutter Instruments Model P-97 micropipette puller (Novato, CA), and a platinum wire and sample solutions were inserted into the opposite end of the capillary to achieve electrical contact. The atmospheric pressure interface of the instrument was elevated to 120 °C. With this elevated source temperature, some heat is transferred to the sample capillary, as shown previously.[7,19] Ion mobility experiments

were performed using a radio-frequency confining drift cell[20] with a 212 V drift voltage in 2 mbar helium. Ion mobility arrival-time distributions were converted to Ω distributions via a method previously described.[8,19]

8.3.2 *Model Building.*

Structural models of the native protein were generated by modifying the PDB entries of Ub_1 (1UBQ), Ub_2 (3AXC), and ADH (5ENV). Side-chains were fixed and hydrogens were added using Chimera v1.11.2.[21] These models were energetically relaxed via a steepest descent energy minimization in Chimera using partial charges assigned by the Amber force field.[22] Energy minimization was performed using 100 steepest descent steps, and 10 conjugate gradient steps with a 0.02 Å step size for each step. Examples of the native and energy-relaxed models can be found in Figure S1. α-helical and linear structures of Ub_1 and Ub_2 were built using Chimera and the corresponding dihedral angles.

8.3.3 *Partial Charge Distributions.*

Atomic partial charges were defined using six different partial charge distribution (PCD) methods, which are summarized in Table 8.1. In the center of mass model (CoM), a point charge was placed at the center of mass for the structural model equal to the charge state of the ion, and the partial charge of every atom was set to 0.0 *e*. In the Even model, every atom was given the same partial charge, such that the sum of all the partial charges is equal to the charge state of the ion.

Table 8.1. Description of PCD methods

PCD Method	Description
CoM	Charge is placed at the center of mass of the protein (CoM). All atomic partial charges are 0.0 *e*
Even	All atoms are given the same partial charge
FF-Even	Atoms are given charges using Amber force field. Charge is adjusted by adding the same partial charge to every atom
FF-Protonation	Atoms are given charges using Amber force field. Charge is adjusted by adding a charge of 1.0 *e* to the most negative atom.
FF-Shuffle	Charges from FF-Even model are randomly re-assigned to new atoms
Random	Atoms are given a random partial charge, such that the standard deviation of the PCD is equal to that of the FF-Even Model

Alternatively, the Amber force field[22] (FF) was used to assign PCDs using Chimera.[21] Charge was increased from those calculations using two approaches. In the FF-Even method, the initial partial charge on every atom was determined by the FF, and the charge state was increased by adding the same amount of partial charge to every atom. Cation protonation was simulated in the FF-Protonation PCD method by assigning the most negative z atoms a partial charge 1.0 e higher than that assigned by the FF, where z is the charge state of the ion. Note, a proton was not added to the structure in this PCD method. However, using Amber to calculate partial charges generates several atoms with the same partial charge, which adds ambiguity to which atom is the most negative. Consequently, for cases where there were fewer remaining charges to be assigned than atoms with the most negative charge, the charges were assigned randomly. This process was repeated five times to yield five different partial charge assignments per charge state to sample different protonation states, and all calculated Ω for a given z were averaged.

Lastly, two randomized PCDs were generated. To examine how the location of partial charges effect Ω_{TM} calculations, the partial charge distributions in the FF-Even method were randomly reassigned to new atoms; this will be referred to as the FF-Shuffle PCD method. The final PCD method randomly selected partial charge assignments such that the width of the random partial charge distribution had the same standard deviation as the FF-Even method. In this "Random" PCD method, a random number set, *A*, of *n* random numbers with a standard deviation of 1 was generated, where *n* is the number of atoms in the structure divided by 2. This random number set was then multiplied by the standard deviation, σ, of the FF-Even method, thus making the two partial charge distribution have effectively equivalent standard deviations. The absolute value of *A* was then joined with the product of -1 and the absolute value of *A*; these operations yield a distribution with a standard deviation nearly equivalent to that of the neutral FF-Even partial charge distribution, and a sum of zero. The operations are summarized below:

$$B = |\sigma * A| \bigcup -1 * |\sigma * A|$$

For structures with an odd number of atoms, *A* contained (*n*-1)/2 values, and an additional value of "0.0" was added to *B*. Values in *B* were then randomly assigned to atoms, and charge was increased by adding the same partial charge to every atom, such that the sum of all partial charges was equal to the integer charge state of the ion. For the FF-Shuffle and Random PCD methods, 12 to 15 partial charge assignments were calculated for every charge state in order to yield a reasonable distribution of the sample space.

8.3.4 *Ω Calculations.*

Trajectory method (TM) calculations were performed using IMoS v1.06.[15–17] An example of the settings used in the calculations are shown in the Supporting Information. For the native

structure, 15 to 20 replicates for each charge state were ran. For α-helical and linear structures, 20 to 75 replicates for each partial charge assignment were ran. Each replicate included 10000 gas trajectories in 199.98 pascals of helium at 301.15 K. The random number seed for each replicate was randomly reassigned to be a number between 0 and 4096. Lennard Jones parameters were equivalent to those in MobCal.[4,5] Additionally, Ω were calculated for all models using the projection approximation (PA)[1] and exact hard sphere scattering (EHSS)[2,3] Ω calculations were ran on all structural models (Table 8.1).

8.4 Results and Discussion

Figure 8.1a shows apparent experimental Ω distributions as a function of charge state for Ub_1 and Ub_2 from denaturing and supercharging. Vertical bars indicate the width of the apparent experimental Ω distribution (10% and 90% of the corresponding cumulative distribution function), and the markers indicate the median experimental Ω value ($\widetilde{\Omega}_{\mathrm{Exp}}$, 50% of the corresponding cumulative distribution function). In agreement with other IM studies of denatured protein ions,[11,19,23,24] Ω_{Exp} generally increases with increasing charge for each data set.

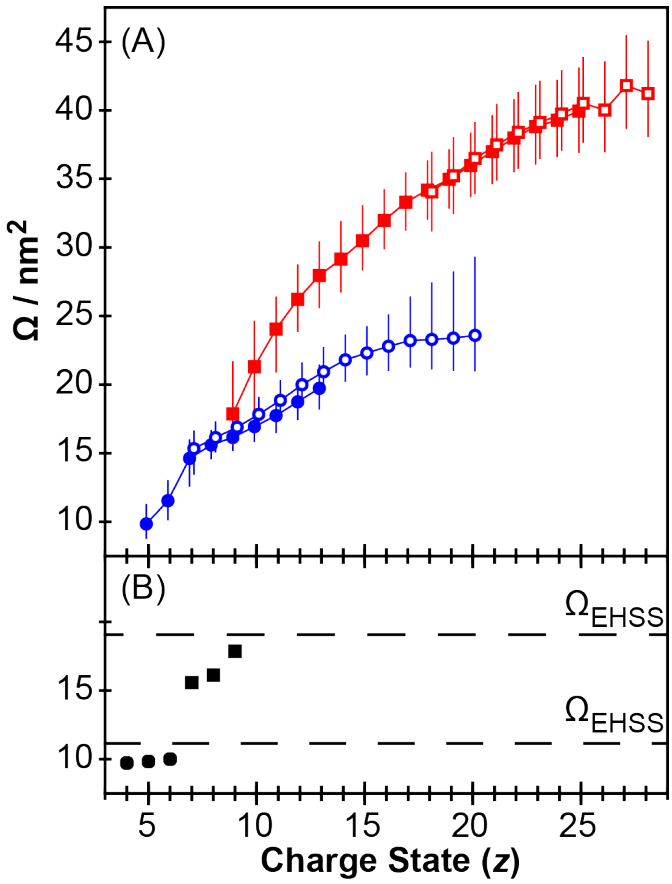

Figure 8.1. (A) Ω distributions as a function of charge state for Ub_1 (*blue circles*) and Ub_2 (*red squares*) from denaturing (*solid*) and supercharging (*hollow markers*). Vertical bars indicate the width of the apparent Ω distribution (10% and 90% of the corresponding cumulative distribution function), and the markers indicate the $\widetilde{\Omega}_{Exp}$ value. (B) Previously reported Ω_{Exp} of Ub_1[25] and Ub_2[9] ion from native-like conditions. Horizontal dashed black lines correspond to Ω_{EHSS} for these ions based on the native structural models of these proteins (Table 8.1).

Denatured Ub_1 $\widetilde{\Omega}_{Exp}$ values range from 9.85 to 19.7 nm^2 for z = 5+ to 13+. When Ub_1 ions were generated via nESI under supercharging conditions, the highest charge state observed was 20+, which is an increase of seven charge states relative to denaturing conditions.

Supercharged Ub_1 $\widetilde{\Omega}_{Exp}$ values range from 15.3 to 23.6 nm^2 for z = 7+ to 20+. Ω_{Exp} values of native-like Ub_1 ions generated under native conditions (200 mM ammonium acetate, pH 7, etc.) are shown in Figure 8.1b, and ranged from 9.72 to 10 nm^2 from z = 4+ to 6+. Denatured Ub_2 $\widetilde{\Omega}_{Exp}$ values range from 17.9 to 39.9 nm^2 for z = 9+ to 25+, and supercharged Ub_2 range in $\widetilde{\Omega}$ from 34.0 to 41.8 for z = 18+ to 28+; only three additional charge states were detected under these supercharging conditions relative to the denaturing solution conditions. Interestingly, the maximum $\widetilde{\Omega}_{Exp}$ for supercharged Ub_2 was measured for 27+, and not the highest charge state measured, 28+, which had a $\widetilde{\Omega}$ of 41.2 nm^2. Ω_{Exp} values of native-like Ub_2 ions are also included in Figure 8.1b, and ranged from 15.6 to 17.9 nm^2. At the highest charge states generated from supercharging conditions of both proteins, Ω depends weakly on z and slowly increases with increasing z.

Ω values for Ub_1 and Ub_2 from all three solution conditions depend on z. That dependence is highest for intermediate charge states from denaturing and supercharging conditions, and is weaker for low z native-like ions and the highest z supercharged ions. The observed change in Ω with respect to z may be caused by either (1) structural isomerization or (2) changes in the ion-induced dipole interaction between the ion and neutral gas. Consequently, decoupling these effects and their contribution to the observed Ω can be a significant challenge in using Ω for structural biology measurements. Here, we investigate the contribution of the ion-induced dipole interactions, which may be studied computationally by comparing Ω_{EHSS} to Ω_{TM}. Previous work with the TM has been used on many small ions,[4,26] as well as several larger protein ions.[14] We also explore different methods of applying PCDs to protein ions in compact and extended conformations for TM calculation to inform future calculations.

8.4.1 *How do partial charge distributions effect Ω_{TM}?*

TM calculations were performed on the native model of Ub_1 (Figure S1A) with 1+ to 22+ charges, which spans the *z* range of ions generated via ion/ion proton transfer reactions at low *z,*[9,19] to "supercharged" ions at high *z,* like those in Figure 8.1a. Figure 8.2A shows the Ω_{TM} values calculated for these charge states using the six PCD methods described in the *Experimental Methods* section (Table 8.1). This data is also shown in Figure S2A, and includes the Ω_{PA} value. Additionally, all Ω_{PA} and Ω_{EHSS} for all proteins and structural models may be found in Table 8.2. Each marker includes vertical bars spanning to the 95% confidence interval, which are also reported following every value for the remainder of the discussion. Overall, the Ω_{TM} of each PCD method increases with increasing *z*, due to an increase in the ion-induced dipole interaction.

Table 8.2. Calculated Ω_{PA} and Ω_{EHSS} values for all structural models.

Protein	Method	Native [c]	Energy-relaxed [c]	α-Helix [c]	Linear [c]
Ubiquitin	PA:	9.05 ± 0.01 [a]	8.36 ± 0.01	14.52 ± 0.02 [a]	22.92 ± 0.03 [a]
	EHSS:	11.15 ± 0.01 [a]	10.17 ± 0.01	17.71 ± 0.06 [a]	26.11 ± 0.08 [a]
Di-ubiquitin	PA:	15.18 ± 0.01 [a]	13.76 ± 0.01	28.23 ± 0.06 [a]	45.54 ± 0.09 [a]
	EHSS:	19.08 ± 0.02 [a]	17.15 ± 0.02	34.6 ± 0.2 [a]	51.9 ± 0.2 [a]
Alcohol Dehydrogenase	PA:	63.28 ± 0.04 [b]	58.40 ± 0.04		
	EHSS:	84.50 ± 0.07 [b]	77.72 ± 0.06		

[a]Value reported previously[9]
[b]Value reported previously[12]
[c]Ω values were calculated for models that were constructed as described in the *Methods*.
The reported interval was determined using Student's t-test at the 95% confidence level and 512 replicate calculations.

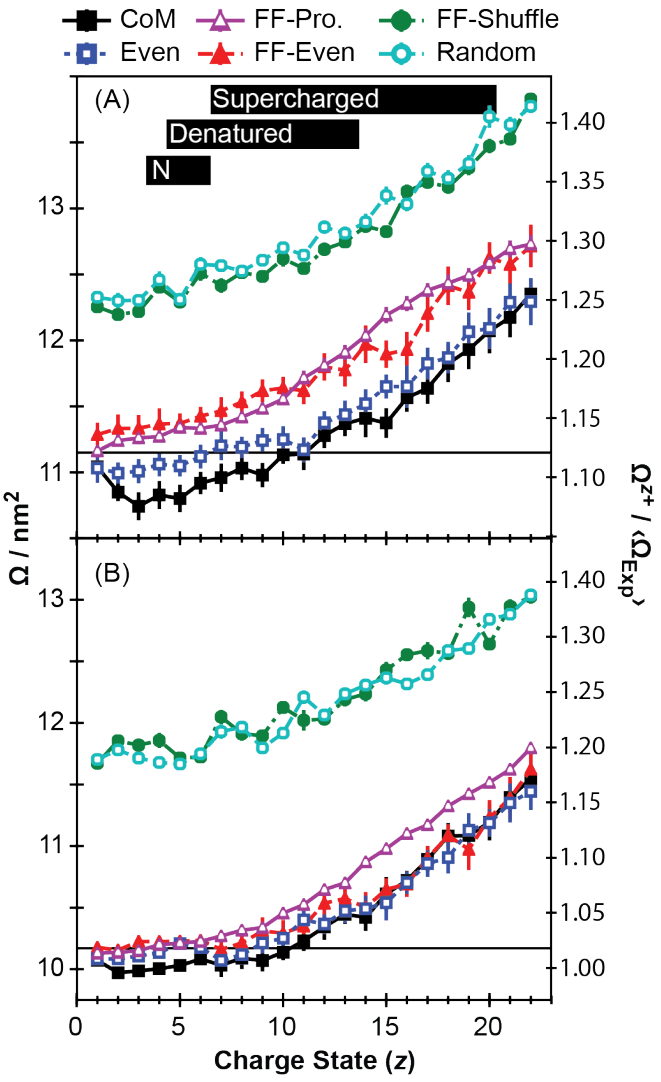

Figure 8.2. (A) Ω_{TM} using the native model of Ub_1 (Figure S1A) with helium as a function of charge state. (B) Ω_{TM} using the relaxed model of Ub_1 (Figure S1B) with helium as a function of charge state. In both panels, the ratio of Ω_{TM} to $\langle\Omega_{Exp}\rangle$ from Figure 8.1b is shown on the right-hand axis, and Ω_{EHSS} values for both structural models are included as black horizontal lines (Table 8.2). Error bars indicate the 95% confidence interval. Descriptions of the PCD methods can be found in the *Methods* section and Table 8.1.

Using the CoM and Even PCD methods, the PCD of the ions are simulated as a single point charge, or as many point charges, respectively. These models yield the smallest Ω_{TM} values of any PCD method. Moreover, the two PCD methods yield very similar Ω_{TM} values. The CoM and Even PCD methods both yield a Ω_{TM} value of 11.0 ± 0.1 nm^2 for 1+, and a Ω_{TM} for 22+ of 12.4 ± 0.1 nm^2 and 12.3 ± 0.2 nm^2, respectively.

The FF-Even and FF-Protonation methods yield higher Ω_{TM} values than the CoM and Even methods. The FF-Even values range in Ω_{TM} from 11.3 ± 0.1 nm^2 at 1+ to 12.7 ± 0.2 nm^2 at 22+. Similarly, the FF-Protonation method ranges in Ω_{TM} from 11.2 ± 0.04 nm^2 to 12.7 ± 0.07 nm^2 from 1+ to 22+, respectively. The similarity between these two data sets at low *z* is due to the nearly identical partial charge assignments at low *z*, as discussed in the *Experimental Methods* section. In contrast, the more localized charges in the FF-Protonation method generally yields higher Ω_{TM} at high *z*, in agreement with previous studies that showed that more localized charges on fullerenes yielded larger Ω values than more dispersed partial charge assignments.[26]

The FF-Shuffle and Random PCD methods systematically yielded much larger Ω_{TM} values than any of the other PCD methods. The FF-Shuffle PCD method yield Ω values from 12.3 ± 0.03 nm^2 to 13.8 ± 0.05 nm^2 from charge states 1+ to 22+, and the Random PCD method yielded Ω_{TM} from 12.3 ± 0.04 nm^2 to 13.8 ± 0.05 nm^2 over the same *z* range. The FF-Shuffle method yields Ω_{TM} about 1 nm^2 greater than the FF-Even at any given *z*, despite the two PCD methods having the same set of partial charge values. Therefore, the origin of the difference in Ω_{TM} between these two methods is due to the placement of the partial charges on the structure. An illustrative example of this may be found in Figure S3, where panels A and B show the Coulombic surface of 1+ FF-Even and panels C and B show a replicate of 1+ FF-Shuffle. The Coulombic surface in FF-Shuffle are generally greater in magnitude than that of FF-Even, due to

some partial charges with the same polarity being randomly assigned atoms geometrically near one another. This induces a greater dipole in the approaching helium and consequently results in greater momentum transfer and a larger Ω_{TM} for the FF-Shuffle.

Analogous data for the native model of Ub_2 are shown in Figure S4A using the CoM, Even, FF-Even, and FF-Protonation PCD method. Similar to that of Ub_1, the Even, FF-Even, and FF-Protonation method increase in Ω over the range of *z* studied, 1+ to 29+. Additionally, the general order of the relative Ω_{TM} for the FF-Protonation, FF-Even, and Even PCD methods is the same as for Ub_1, where FF-Protonation > FF-Even > Even.

In contrast to the Ω_{TM} results for Ub_1, the CoM method for Ub_2 yields smaller Ω_{TM} overall. This is attributable to the center of mass being between the two domains of the protein in free space (Figure S1E). These results provide insight into how future TM calculations may be optimized by mathematically decomposing structures into structural domains, and placing charges proportional to the mass of each domain at the center.[27–29] By placing a partial charge in the center of mass for each domain, the ion-induced dipole interactions may be calculated for each point charge instead of each atom, thus reducing the computational cost of TM calculations.

Overall, the differences between these six PCD methods may be rationalized by considering differences in the charge on the surface. PCD methods that yield higher surface charges induce stronger dipoles in the neutral collision partner, which lead to larger Ω_{TM} values. This agrees with previous studies that noted that point charges on fullerenes results in greater momentum transfer and greater Ω_{TM} than that of diffuse charges.[26] This hypothesis can further explain why the CoM and Even PCD methods yield the smallest Ω_{TM}, and why FF-Protonation leads to greater Ω than FF-Even at high *z*. Consequentially, PCD methods that model the charges on the surface of ions, like FF-Even, will yield more accurate Ω_{TM} values. Furthermore, future

TM calculations calculating long-range ion-induced dipole interactions with point charges located at the center of mass for different protein domains may enable faster TM calculations.

8.4.2 *Do Ion-Induced Dipole Interactions Affect Native-like Ω measurements?*

The Ω_{EHSS} and Ω_{TM} values for the native model of Ub_1 were higher than previous measurements of native-like Ub_1, which yielded experimental Ω values of 9.72 to 10.0 nm^2 from charge states 4+ to 6+.[25] To investigate how the ion-induced dipole interaction affects the measurement of Ω of native-like ions, we performed an energy-relaxation on the native model using Chimera. Ω_{EHSS} (Table 8.1) of this energy-relaxed model agree well with the previous Ω measurement.[25] Consequently, Ω_{TM} of these energy-relaxed models are more comparable to Ω_{Exp} values and the effects of ion-induced dipole interactions on Ω_{Exp} may be determined. Images of the model before (Figure S1A) and after energy relaxation (Figure S1B) may be found in the Supplementary Information.

Figure 8.2B shows the Ω_{TM} values calculated from the energy-relaxed Ub_1 structural model; this data is also shown with the Ω_{PA} value for the relaxed Ub_1 model in Figure S2C. The lowest *z* ions for the CoM, Even, FF-Even, and FF-Protonation PCD method are in agreement with the native-like Ω from previous measurements,[25] as well as Ω_{EHSS}, which indicates the ion-induced dipole interaction is negligible for these low *z* ions. Interestingly, the CoM, Even, FF-Even, and FF-Protonated PCD methods agree much more with one another for the relaxed model than those calculated for the native model. This is may be attributable to charge solvation during the energy relaxation leading to fewer differences between the Coulombic surface of these PCD methods. In contrast, the FF-Shuffle and Random PCD methods still yield higher Ω values than the other PCD methods because of their higher-magnitude surface charge relative to the other PCD methods.

Figure S2D shows the Ω_{TM} relative to the 1+ ion for each PCD method. Each PCD increases by approximately 10% to 12.5% percent from 1+ to 22+. The Ω_{TM} over the *z* range of native-like charge states, 4+ to 6+, changes by very little and agrees with the Ω_{EHSS} for this structure. These results indicate that each PCD similarly increases in Ω_{TM} with respect to *z*.

To investigate how changes in *z* affect the potential energy of the interaction between the ion and neutral, we calculated the potential energy of the ion-helium interaction as a function of distance from the center of mass for the energy-minimized structural model of 1+ Ub_1 using the FF-Even method. These data are shown with respect two three orthogonal axes in Figure S5. Figure S6 shows the difference in the minimum of the potential energy vectors between of a *z*+ ion and that of the 1+ ion in meV and kJ/mol. With increasing charge, the magnitude of the difference between the minimum of the *z*+ potential relative to that of the 1+ gets larger, and is reflective of an increased ion-induced dipole interaction. The difference between the 22+ and the 1+ ion ranges from -7.88×10^{-7} kJ/mol to -9.85×10^{-7} kJ/mol. Interestingly, the changes in the potential as a function of *z* are roughly ~6 orders of magnitude smaller than the magnitude of the potentials themselves. Although the change in potential energy between the ion and helium with increasing *z* is small, those changes result is significant changes in Ω_{TM} from 1+ to 22+ for Ub_1. However, there are only insignificant changes in Ω_{TM} from 1+ to 6+, which includes the range of *z* typically generated for Ub_1 from nESI of native-like solution conditions. Consequentially, these results indicate that the change in the ion-induced dipole interaction does not affect typical Ω measurements over the narrow *z* range measured in native-like experiments.

Ω_{TM} data for energy-relaxed Ub_2 using the CoM, Even, FF-even, and FF-Protonation PCD methods are shown in Figure S4C. Images of the native model before and after energy relaxation shows the two domains have moved closer to one another following the energy

relaxation (Figure S1E to S1H). Like that of energy-relaxed Ub_1, the data agree more closely with the average Ω_{Exp} from previous experiments (right axis) at low z than compared to the native structural model. Additionally, the low z data also agree with Ω_{EHSS} (Table 8.1). The PCD methods agree more with each other than compared to the native structural model. The Ω_{TM} for all four PCD methods shown increase with increasing z, indicating the ion-induced dipole interaction becomes significant at high charge states. Figure S4D shows the Ω_{TM} relative to the Ω_{TM} of the 1+ ion for each PCD method. The change in Ω_{TM} from 1+ to 29+ varies by about 8% to 10%. However, the Ω_{TM} varies by less than 2% relative to the 1+ ions for ions of $z = 10$ or less, which indicates the ion-induced dipole interaction has a negligible effect of Ω measurements over the native-like charge states of 8+ to 10+.

Many structural biology applications of IM-MS involve measurements of non-covalently bound protein complex ions. Consequently, we have used ADH, a 147 kDa homotetramer, to study ion-induced dipole effects on the Ω_{TM} of protein complex ions. Previous Ω_{Exp} measurements of ADH have been made from native-like conditions,[13] supercharging conditions,[30] and ion/ion proton transfer reactions of native-like ions.[12] In total, those measurements yielded Ω values for 11+ to 37+ ADH ions. Figure S7A and S7C shows the Ω_{TM} as a function of z from 1+ to 400+ for the native and energy-relaxed structures of ADH using the 'FF-Even' PCD method; these figures also include a inset which shows the data from 1+ to 40+. Figure S1I to S1L show images of the native and energy-relaxed models. Like that of Ub_1 and Ub_2, the ion compacts following the energy-relaxation. Additionally, the energy-relaxed structural model from 1+ to 40+ structure is in much better agreement with previous experiments[13] of native-like ADH than compared to the native structural model; the ratio of Ω_{TM}

to the average Ω_{Exp} ($\langle\Omega_{Exp}\rangle$) from those previous experiments can be found on the right-hand axis of Figure S7A and S7C.

Unlike Ub_1 and Ub_2, whose Ω_{TM} depends on z within the range of experimentally measured z, the Ω_{TM} of ADH weakly depends on z over the range of experimentally measured z, *i.e.* 11+ to 37+. Additionally, there is not a clear trend in the relationship between z and Ω for those charge states. (Figure S7B and S7D), and all Ω_{TM} for this range of z agree with the Ω_{EHSS} calculation. This indicates the ion-induced dipole interaction has an insignificant effect on Ω_{TM} over this range of z. Ω_{TM} values differ significantly from the Ω_{EHSS} value at very high z, *i.e.* $z >$ 70, which is much higher than experimentally measured ADH ion.

To compare the Ω_{TM} of all three energetically-relaxed structural models, Figure 8.3 shows Ω_{TM} values relative to the 1+ ion using the FF-Even PCD method as a function of the logarithm of m/z. The m/z range studied for Ub_1 and Ub_2 was approximately m/z 390 to 8 565 and m/z 581 to 16 823, respectively. Interestingly, both Ub_1 and Ub_2 exhibit significant increases in Ω_{TM} relative to the 1+ ion between m/z 1000 to 1100. In contrast, the Ω_{TM} of ADH sharply increases around m/z 3,000. These trends may be rationalized by considering the ratio of z to the radius of a sphere with the same Ω as the average Ω_{EXP} (Figure S8A), because the potential energy of the ion-helium interaction is a function of the distance of the helium to the ion. Figures S8b and S8c also show the charge per unit of surface area and charge per unit of volume of a sphere with the same Ω of the ion, respectively, which agree less with the trends in Figure 8.3.

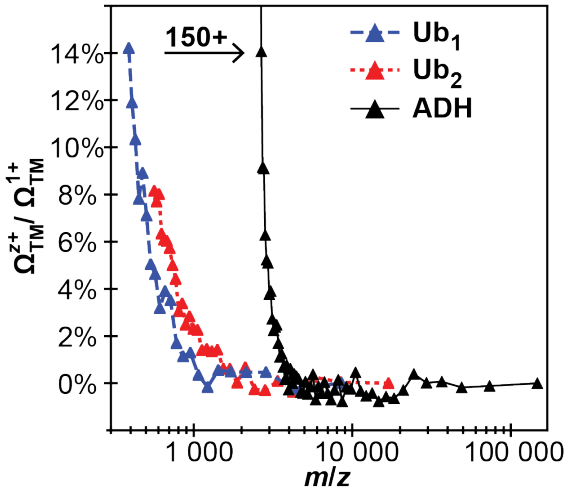

Figure 8.3. Ω_{TM} of energy-relaxed Ub_1 (*blue*), Ub_2 (*red*), and ADH (*black*) using FF-Even relative to the respective 1+ ions as a function of *m*/*z*. *m*/*z* is plotted logarithmically to aid in visualizing the data. Full data sets for energy-relaxed Ub_1, Ub_2, and ADH may be found in Figure 8.2b, S4C, and S5C, respectively.

In general, these results show that the ion-induced dipole interaction between native-like globular protein ions and helium have an insignificant effect on Ω measurements over the *z* range generated by electrospray ionization of typical native-like solution conditions, *i.e.* 200 mM aqueous ammonium acetate. The compact native and energy-relaxed structural models have many protein intra-actions that reduce the amount of exposed charges when using the FF-Even and FF-Protonation PCD methods for TM calculations, which reduces the effect of this long-range interaction. Consequently, EHSS calculations, which neglect this interaction, are relatively well suited to approximate experimental Ω. Importantly, Ω_{EHSS} of the native structural models over estimate Ω_{Exp}. When those models are energetically relaxed by a steepest descent approach, the Ω_{EHSS} of the energy-relaxed models are in much better agreement with native-like Ω_{Exp}

measurements. However, even after energy relaxation, Ω_{TM} was up to 10% larger than experimental Ω values. Consequently, future work to parameterize Ω_{PA} and Ω_{EHSS} values of the native-like models, which underestimate and overestimate experimental Ω, respectively, may be used to predict experimental Ω.

8.4.3 *Origin of changes in Ω at high z.*

The Ω_{TM} results for energetically-relaxed Ub_1 and Ub_2 indicate that changes in the ion-induced dipole interaction can only account for up to 12.5% change in Ω_{Exp}, which is much less than the greater than 2x increase observed in Ω over all *z* (Figure 8.1a). Therefore, the Ω measurements from intermediate to high *z* must be the result of structural isomerization to extended structures and ion-induced dipole interactions between the ion and helium. α-helical and linear structural models of Ub_1 and Ub_2 were constructed to investigate the effect of ion-induced dipole interactions on Ω measurements of extended protein structures.

Figure S2E and S2G show Ω_{TM} values for the six PCD methods for α-helical, and linear structures for Ub_1. Both extended Ub_1 structural models exhibit increases in Ω_{TM} from 1+ to 22+ for each PCD method, except for the linear model using the CoM PCD method. Similar to the compact structures previously discussed, the FF-Shuffle and Random PCD methods are systematically higher than all other PCD methods due to the closer proximity of like-charges. Ω_{TM} values generally decrease between the FF-Protonation, FF-Even, and Even PCD method due to differences in exposed partial charges. The CoM PCD method behaves uniquely for both the α-helical and linear structures and indicates that the CoM PCD method poorly estimates the true PCD for ions with these extended structures, unlike that of the compact Ub_1 Ω_{TM} data. Analogous data for Ub_2 is also shown in Figures S4E and S4G, except for the FF-Shuffle and Random models, and these data follow the same trends as that of Ub_1. In general, Ω_{TM} depends

more strongly on the choice of PCD method for the extended structures of Ub_1 and Ub_2 than compared to the compact structures previously discussed.

Figures S2F and S2H show the ratio of Ω_{TM} for an ion relative to the Ω_{TM} of the 1+ ion for that PCD method for the α-helical and linear structural models of Ub_1, respectively; data for α-helical and linear Ub_2 are shown in Figures S4F to S4H. In contrast to the data for the compact structures of Ub_1, which changed in Ω_{TM} by 10% to 15%, the α-helical and linear structures change in Ω by a maximum of 1% to 6% from 1+ to 22+, for the Even, FF-Even, and FF-Protonated method. Therefore, although the choice of PCD matters more for extended structures than for compact structures, Ω depends more weakly on *z* for these extended structures than compared to the native and energy-relaxed structures over the same range of *z*.

Figure 8.4a includes the FF-Even data for all structural models of Ub_1, and the Ω_{Exp} of Ub_1 from Figure 8.1 for direct comparison. As previously discussed, the models increase in Ω_{TM} in the following order: energy-relaxed model, native model, α-helical model, and linear model. Notably, the high *z* supercharged ions of Ub_1 depend weakly on *z* from 17+ to 20+, similar to that of the linear structural model.

Figure 8.4b shows the Ω relative to the Ω of the 20+ ion for both linear structural model of Ub_1 using the FF-Even PCD method and experimental supercharged Ub_1 data from Figure 8.1A. From z = 7+ to 16+, the two data sets yield very different relative Ω values, due to the structure in the experimental data changing with *z*. However, from z = 17+ to 20+, the two data sets yield similar Ω_{TM} values relative to the 20+. As a result, for those high *z* ions, the ion-induced dipole interaction alone can account for the observed Ω_{Exp} values in lieu of conformational changes. Analogous data for Ub_2 may be found in Figure S9.

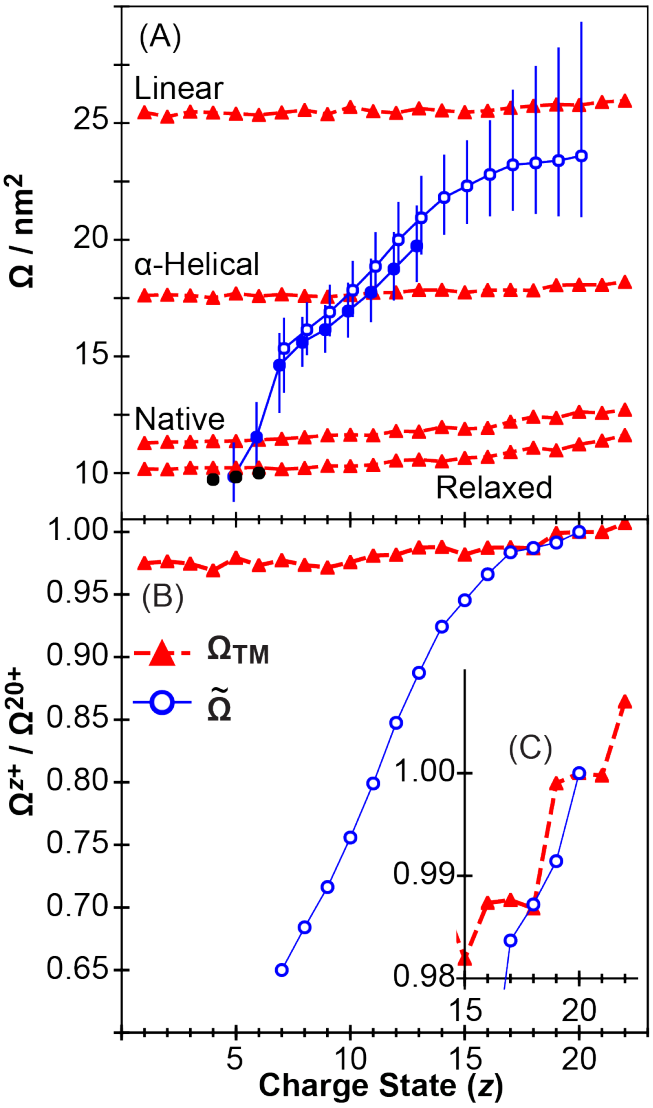

Figure 8.4. (A) All experimental Ub_1 data from Figure 8.1 including denatured (*solid blue*), supercharged (*hollow blue*) and native (*black*) data as a function of charge state. Ω_{TM} using the FF-Even method for all structural models are also shown (*red triangles*). (B) Difference in Ω between the 20+ ion and other charge states for linear Ub_1 (*red triangles*, Figure S2G) using the FF-Even method, and supercharged Ub_1 (*hollow blue*, Figure 8.1A). Inset shows z = 15 to 22 in panel A with scaled y axis.

In general, choice of PCD matters much more for extended structures at high *z* than compared to compact structures at low *z*. Furthermore, Ω is weakly related to *z* for these extended models than compared to the previously discussed compact models, but the *z* range over which Ω_{TM} changes correspond to the high *z* where these structures may be adopted by gas-phase ions. These results also show that ion-induced dipole interaction effects can account for differences in the experimentally measured Ω values of supercharged denatured protein ions.

8.5 Conclusions

Recent improvements in ion mobility and mass spectrometry have produced a need for tools to develop structural models, ways to estimate Ω for those models, and an understanding of the important parameters for a given structural model. Here, we have used the TM and EHSS to evaluate the contribution of ion-induced dipole interactions on compact and extended structural models of several proteins, which varied from 8.6 to 147 kDa. Those results indicate that ion-induced dipole interactions do not significantly affect Ω measurements of globular protein and protein complexes over the range of *z* generated under native-like solution conditions (*i.e.* 200 mM ammonium acetate, pH 7, etc.). Likewise, those ion-induced dipole interactions also do not affect Ω measurements of lower *z* protein and protein complex ions, like those generated from gas-phase ion/ion proton transfer reactions[7–9,12,31,32] or via the addition of basic compounds to nESI solutions.[13,33] For globular protein systems, Ω_{EHSS} calculations provide reasonable approximations of experimental Ω values. Moreover, the Ω_{TM} and Ω_{EHSS} values of energetically relaxed atomic models from x-ray crystallography data agree much more with Ω_{Exp} than the "native" models used here. Furthermore, development of software tools to place point charges in

the center of mass of deconvoluted protein domains could lead to significant increases in the computation speed of TM calculations.

Our data also show that partial charge distributions that reasonably reflect the partial charge distributions on the surface of ion are critical to yield Ω_{TM} values in agreement with Ω_{Exp} for native-like proteins, unlike those that are randomly assigned. Consequently, PCD models that yield Coulombic surfaces like the Even, FF-Even, and FF-Protonation PCD methods yield similar Ω_{TM} values for compact structures. In contrast, extended structures that have many more exposed charges, depend much more on the choice of PCD. This finding will be critical to evaluate Ω of extended structural models that may not yield aßccurate Ω_{EHSS} data. For instance, Ω_{TM} may be appropriate for estimating the Ω of extended structures of native-like ions, like those of intrinsically disordered or prion proteins or denatured protein structures. Moreover, the ion-induced dipole interactions can account for changes in Ω_{TM} at the highest *z* denatured ions in lieu of structural changes.

8.6 Supporting Information.

The Supporting Information is available in Appendix G, which contains the TM calculation settings used in IMoS, and Figure S1 to S9.

8.7 Acknowledgments.

Research reported in this publication was supported by the American Society for Mass Spectrometry (Research Award to M. F. B.), and Eli Lilly and Company (Young Investigator Award in Analytical Chemistry to M. F. B.).

8.8 References

(1) von Helden, G.; Hsu, M. T.; Gotts, N.; Bowers, M. T. Carbon Cluster Cations with up to 84 Atoms: Structures, Formation Mechanism, and Reactivity. *J. Phys. Chem.* **1993**, *97* (31), 8182–8192.

(2) Shvartsburg, A. A.; Jarrold, M. F. An Exact Hard-Spheres Scattering Model for the Mobilities of Polyatomic Ions. *Chem. Phys. Lett.* **1996**, *261* (1–2), 86–91.

(3) Shvartsburg, A. A.; Mashkevich, S. V.; Baker, E. S.; Smith, R. D. Optimization of Algorithms for Ion Mobility Calculations. *J. Phys. Chem. A* **2007**, *111* (10), 2002–2010.

(4) Mesleh, M. F.; Hunter, J. M.; Shvartsburg, A. A.; Schatz, G. C.; Jarrold, M. F. Structural Information from Ion Mobility Measurements: Effects of the Long-Range Potential. *J. Phys. Chem.* **1996**, *100* (40), 16082–16086.

(5) Shvartsburg, A. A.; Hudgins, R. R.; Dugourd, P.; Jarrold, M. F. Structural Elucidation of Fullerene Dimers by High-Resolution Ion Mobility Measurements and Trajectory Calculation Simulations. *J. Phys. Chem. A* **1997**, *101* (9), 1684–1688.

(6) Bleiholder, C.; Wyttenbach, T.; Bowers, M. T. A Novel Projection Approximation Algorithm for the Fast and Accurate Computation of Molecular Collision Cross Sections (I). Method. *Int. J. Mass Spectrom.* **2011**, *308* (1), 1–10.

(7) Laszlo, K. J.; Buckner, J. H.; Munger, E. B.; Bush, M. F. Native-Like and Denatured Cytochrome c Ions Yield Cation-to-Anion Proton Transfer Reaction Products with Similar Collision Cross-Sections. *J. Am. Soc. Mass Spectrom.* **2017**, 1–10.

(8) Laszlo, K. J.; Munger, E. B.; Bush, M. F. Effects of Solution Structure on the Folding of Lysozyme Ions in the Gas Phase. *J. Phys. Chem. B* **2017**, *121* (13), 2759–2766.

(9) Laszlo, K. J.; Gadzuk-Shea, M. M.; Heard, S.; Buckner, J. H.; Bush, M. F. On The Relationship Between Native-like and Gas-Phase-Folded Poly-Ubiquitin Ions. **2017**, In Preparation.

(10) Clemmer, D. E.; Hudgins, R. R.; Jarrold, M. F. Naked Protein Conformations: Cytochrome c in the Gas Phase. *J. Am. Chem. Soc.* **1995**, *117* (40), 10141–10142.

(11) Going, C. C.; Williams, E. R. Supercharging with M-Nitrobenzyl Alcohol and Propylene Carbonate: Forming Highly Charged Ions with Extended, Near-Linear Conformations. *Anal. Chem.* **2015**, *87* (7), 3973–3980.

(12) Laszlo, K. J.; Bush, M. F. Effects of Charge State on the Structures of Native-Like Protein Ions: Results From Cation to Anion Proton Transfer Reactions (CAPTR). *Submitt. Anal. Chem.*

(13) Allen, S. J.; Schwartz, A. M.; Bush, M. F. Effects of Polarity on the Structures and Charge States of Native-Like Proteins and Protein Complexes in the Gas Phase. *Anal. Chem.* **2013**, *85* (24), 12055–12061.

(14) Jurneczko, E.; Barran, P. E. How Useful Is Ion Mobility Mass Spectrometry for Structural Biology? The Relationship between Protein Crystal Structures and Their Collision Cross Sections in the Gas Phase. *Analyst* **2011**, *136* (1), 20–28.

(15) Larriba, C.; Hogan, C. J. Ion Mobilities in Diatomic Gases: Measurement versus Prediction with Non-Specular Scattering Models. *J. Phys. Chem. A* **2013**, *117* (19), 3887–3901.

(16) Larriba-Andaluz, C.; Hogan, C. J. Collision Cross Section Calculations for Polyatomic Ions Considering Rotating Diatomic/Linear Gas Molecules. *J. Chem. Phys.* **2014**, *141* (19), 194107.

(17) Larriba-Andaluz, C.; Fernández-García, J.; Ewing, M. A.; Hogan, C. J.; Clemmer, D. E. Gas Molecule Scattering & Ion Mobility Measurements for Organic Macro-Ions in He versus N2 Environments. *Phys. Chem. Chem. Phys.* **2015**, *17* (22), 15019–15029.
(18) Allen, S.; Giles, K.; Gilbert, T.; Bush, M. Ion Mobility Mass Spectrometry of Peptide, Protein, and Protein Complex Ions Using a Radio-Frequency Confining Drift Cell. *Analyst* **2016**, *141*, 884–891.
(19) Laszlo, K. J.; Munger, E. B.; Bush, M. F. Folding of Protein Ions in the Gas Phase after Cation-to-Anion Proton-Transfer Reactions. *J. Am. Chem. Soc.* **2016**, *138* (30), 9581–9588.
(20) Allen, S. J.; Bush, M. F. Radio-Frequency (RF) Confinement in Ion Mobility Spectrometry: Apparent Mobilities and Effective Temperatures. *J. Am. Soc. Mass Spectrom.* **2016**, *27*, 2054–2063.
(21) Pettersen, E. F.; Goddard, T. D.; Huang, C. C.; Couch, G. S.; Greenblatt, D. M.; Meng, E. C.; Ferrin, T. E. UCSF Chimera--a Visualization System for Exploratory Research and Analysis. *J. Comput. Chem.* **2004**, *25* (13), 1605–1612.
(22) Case, D. A.; Babin, V.; Berryman, J. T.; Betz, R. M.; Cai, Q.; Cerutti, D. S.; Cheatham, III, T. E.; Darden, T. A.; Duke, R. E.; Gohlke, H.; et al. *AMBER 14*; University of California, San Francisco., 2014.
(23) Valentine, S. J.; Counterman, A. E.; Clemmer, D. E. Conformer-Dependent Proton-Transfer Reactions of Ubiquitin Ions. *J. Am. Soc. Mass Spectrom.* **1997**, *8* (9), 954–961.
(24) Wyttenbach, T.; Bowers, M. T. Structural Stability from Solution to the Gas Phase: Native Solution Structure of Ubiquitin Survives Analysis in a Solvent-Free Ion Mobility–Mass Spectrometry Environment. *J. Phys. Chem. B* **2011**, *115* (42), 12266–12275.
(25) Salbo, R.; Bush, M. F.; Naver, H.; Campuzano, I.; Robinson, C. V.; Pettersson, I.; Jørgensen, T. J. D.; Haselmann, K. F. Traveling-Wave Ion Mobility Mass Spectrometry of Protein Complexes: Accurate Calibrated Collision Cross-Sections of Human Insulin Oligomers. *Rapid Commun. Mass Spectrom.* **2012**, *26* (10), 1181–1193.
(26) Young, M. N.; Bleiholder, C. Molecular Structures and Momentum Transfer Cross Sections: The Influence of the Analyte Charge Distribution. *J. Am. Soc. Mass Spectrom.* **2017**, 1–9.
(27) Kundu, S.; Melton, J. S.; Sorensen, D. C.; Phillips Jr., G. N. Dynamics of Proteins in Crystals: Comparison of Experiment with Simple Models. *Biophys. J.* **2002**, *83* (2), 723–732.
(28) Kundu, S.; Sorensen, D. C.; Phillips, George N. Automatic Domain Decomposition of Proteins by a Gaussian Network Model. *Proteins Struct. Funct. Bioinforma.* **2004**, *57* (4), 725–733.
(29) Politis, A.; Park, A. Y.; Hyung, S.-J.; Barsky, D.; Ruotolo, B. T.; Robinson, C. V. Integrating Ion Mobility Mass Spectrometry with Molecular Modelling to Determine the Architecture of Multiprotein Complexes. *PLOS ONE* **2010**, *5* (8), e12080.
(30) Allen, S. J. Personal Communication.
(31) Campuzano, I. G.; Schnier, P. Coupling Electrospray Corona Discharge, Charge Reduction and Ion Mobility Mass Spectrometry: From Peptides to Large Macromolecular Protein Complexes. *Int. J. Ion Mobil. Spectrom.* **2013**, *16* (1), 51–60.
(32) Lermyte, F.; Williams, J. P.; Brown, J. M.; Martin, E. M.; Sobott, F. Extensive Charge Reduction and Dissociation of Intact Protein Complexes Following Electron Transfer on a

Quadrupole-Ion Mobility-Time-of-Flight MS. *J. Am. Soc. Mass Spectrom.* **2015**, *26* (7), 1068–1076.

(33) Bornschein, R.; Hyung, S.-J.; Ruotolo, B. Ion Mobility-Mass Spectrometry Reveals Conformational Changes in Charge Reduced Multiprotein Complexes. *J. Am. Soc. Mass Spectrom.* **2011**, *22* (10), 1690–1698.

APPENDIX A

Gas-Phase Basicity of $[PDCH–F]^-$

Perfluoro-1,3-dimethylcyclohexane (PDCH) has many conformers that depend on the conformation of the ring (chair versus boat) and the configuration of its two carbon stereocenters. Only the chair conformation of the ring was considered here due to the preference of that form for cyclohexane. The methyl groups may be arranged *cis* or *trans* to each other. The *trans* conformation has one axial methyl group and one equatorial methyl group, while the *cis* conformation may have either two axial or two equatorial groups. Due to steric hindrances, only the *trans*/*axial*/*equatorial* and *cis*/*equatorial*/*equatorial* were considered. Between those two arrangements there are 21 unique fluorine atoms. For each unique fluorine, structures were generated for $[PDCH–F_{unique}]^-$ and $[PDCH–F_{unique}+H]$, in which a proton was added to the vacated position. These structures were energy minimized and vibrational frequencies were calculated using B3LYP/6-31++G(d,p) as implemented in Gaussian 09 [1].

Those calculations were then used to estimate the gas-phase basicity (GB) of each conformer of $[PDCH–F]^-$:

$$[\mathrm{PDCH-F}]^- + \mathrm{H}^+ \rightarrow [\mathrm{PDCH-F+H}] \qquad \mathrm{GB} = -\Delta G$$

GB corresponds to the relative total free energies (electronic and thermal) of the reactants and products at standard conditions:

$$GB = -G_{Total}([PDCH - F + H]) + \left\{G_{Total}([PDCH - F]) - \frac{5}{2}RT\right\}$$

For these calculations, we only considered reactions in which the reactant and product have similar geometries. Therefore, the values calculated here are diabatic gas-phase basicities.

The smallest gas-phase basicity calculated using this approach was 1310 kJ/mol. Interestingly, this value is the diabatic gas-phase basicity for the lowest-energy conformer of $[PDCH–F]^-$. This value is significantly greater than the upper limit estimated for the gas-phase basicity of the protein ions in these experiments (1080 kJ/mol, see main text). Therefore, the transfer of a proton from the reactant protein cation to $[PDCH–F]^-$ should be >200 kJ/mol exothermic for each CAPTR event. It is likely that many conformers of $[PDCH–F]^-$ are generated by the glow discharge ionization source. The remaining 20 unique pairs considered in this work all have larger diabatic gas-phase basicities (1324–1501 kJ/mol). Therefore, the transfer of a proton from the reactant protein cation to these conformers of $[PDCH–F]^-$ would be even more exothermic.

The two lowest-energy structures of $[PDCH–F]^-$ and [PDCH–F+H] are shown below and correspond to the loss of a fluorine from one of the carbon stereocenters (carbons 1 & 3). The preference for the loss of those fluorine atoms is consistent with increased negative hyperconjugation to the trifluoromethyl substituent of the carbon 3 relative to the fluorine substituent of the other carbon atoms. Note that the loss of fluorine from carbon 3 and the increased negative hyperconjugation causes the trifluoromethyl group of $[PDCH–F]^-$ to shift onto the plane of the ring. For the purposes of this study, it was assumed that upon proton abstraction the trifluoromethyl group returns to an axial position.

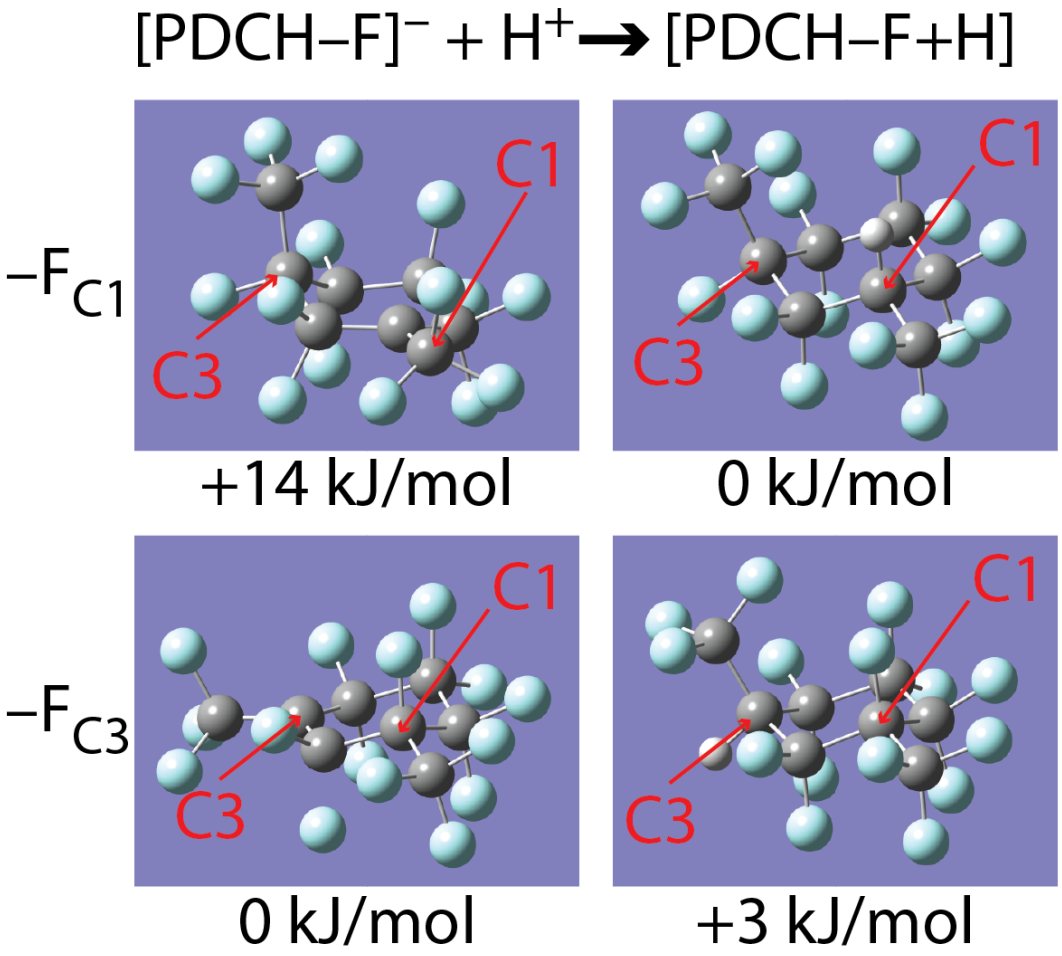
[PDCH–F]⁻ + H⁺ → [PDCH–F+H]
–F C1
C1
C3
+14 kJ/mol
C1
C3
0 kJ/mol
–F C3
C1
C3
0 kJ/mol
C1
C3
+3 kJ/mol

Simulating Native Mass Spectra in Figure 3

Initial native mass spectra were simulated using in-house software implemented using Python, NumPy, and SciPy. Our model assumes that (1) charge state distributions are Gaussian, (2) m/z peaks are Gaussian, and (3) all charge states have the same average m. The analyst provides five initial parameters: (1) m, (2) m/z resolving power, (3) average charge state, (4) width of the charge state distribution, and (5) intensity. These parameters, or a subset of these parameters, are then optimized using a Levenberg−Marquardt least-squares algorithm to minimize the difference between the experimental and simulated spectra. This process yields both optimized parameters and the resulting simulated spectra.

Derivation of Equations 2 & 3

The resolution between two peaks is defined by:

$$Resolution = R = \frac{\frac{m_x}{z_x} - \frac{m_y}{z_y}}{2(\sigma_x + \sigma_y)} \quad \text{(Equation 1)}$$

where *m, z* and σ are the mass, charge, and standard deviation for component *x* and *y* of the mixture as indicated. Guilhaus has shown previously that assuming the widths of peak widths in ToF are due to kinetic energy distribution before ToF acceleration [2]:

$$\frac{m/z}{\Delta m/z} = \frac{U_0 + qV}{\Delta U_0} \quad \text{(Equation S1)}$$

Where U_0 is the initial translational energy of an ion prior to acceleration, q is the charge of an ion in coulombs, V is the accelerating voltage in the pusher region. The ion charge, in coulombs, is related to the charge state by the relation:

$$z = \frac{-q}{e} \quad \text{(Equation S2)}$$

Thus, the width of a peak in *m*/*z* is inversely related to *z*:

$$\frac{1}{\Delta m/z} \propto z \quad \text{(Equation S3)}$$

Therefore, the relative increase in peak width between two different charge states may be described as the ratio, where n is the number of proton transfer reactions:

$$\frac{\sigma_{z^*-n}}{\sigma_{z^*}} = \frac{\Delta(m/z)_{z^*-n}}{\Delta(m/z)_{z^*}} = \frac{z^*}{z^*-n} \quad \text{(Equation 2)}$$

Assuming the centroid of the peaks are changing solely based on charge state, and peak widths vary according to *z* in Equation 2, Equation 2 may be inserted into Equation 1 to yield resolution as a function of the number of proton transfer reactions:

$$R_{CAPTR}(n) = \frac{\frac{m_x}{(z_x^*-n)} - \frac{m_y}{(z_y^*-n)}}{2\left[\sigma_x^*\left(\frac{z_x^*}{z_x^*-n}\right) + \sigma_y^*\left(\frac{z_y^*}{z_y^*-n}\right)\right]} \quad \text{(Equation 3)}$$

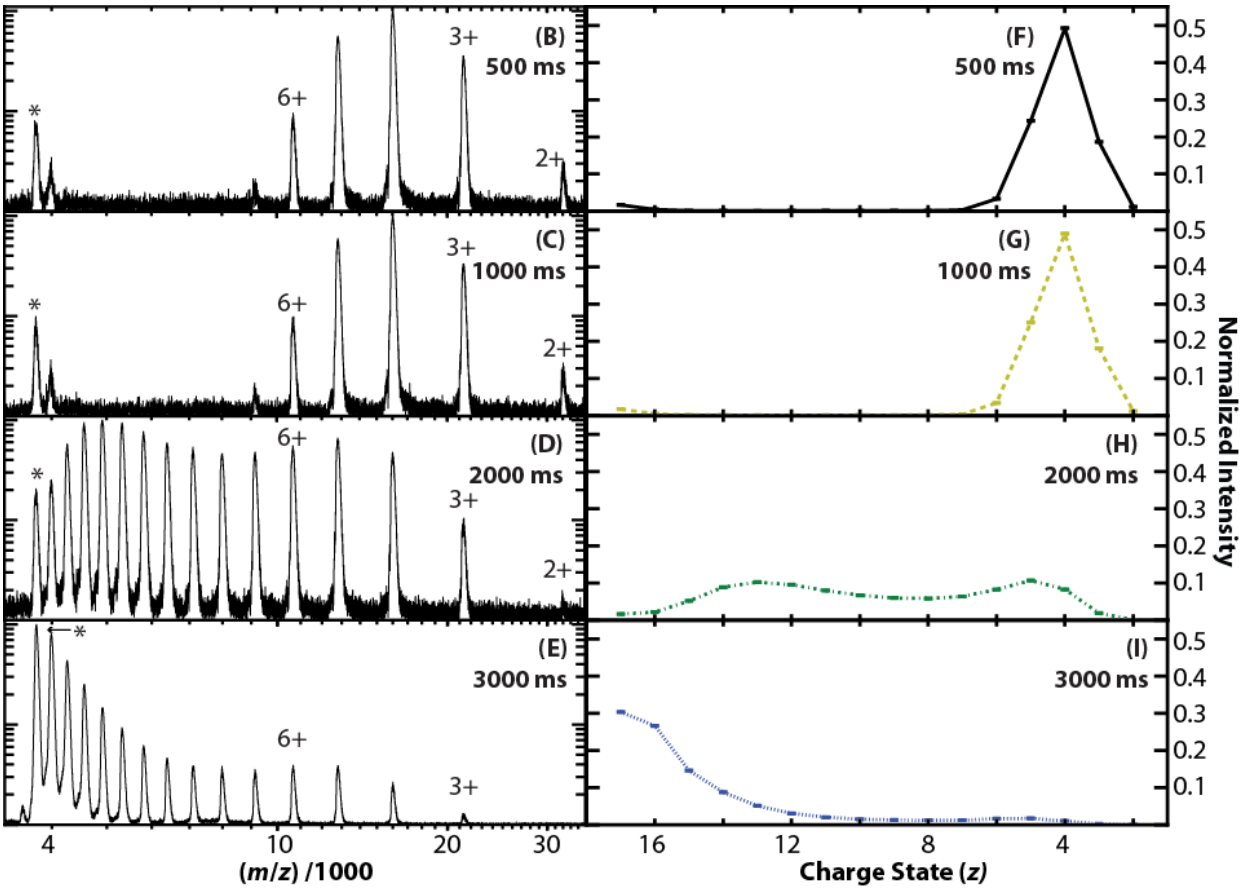

Figure S1. (B–E) CAPTR spectra of 17+ avidin measured as a function of cation transmission time. These spectra are identical to those shown in Figure 2B–E of the main text. (F–I) Normalized intensities the ion counts detected for each peak in the spectra shown in B–E, respectively.

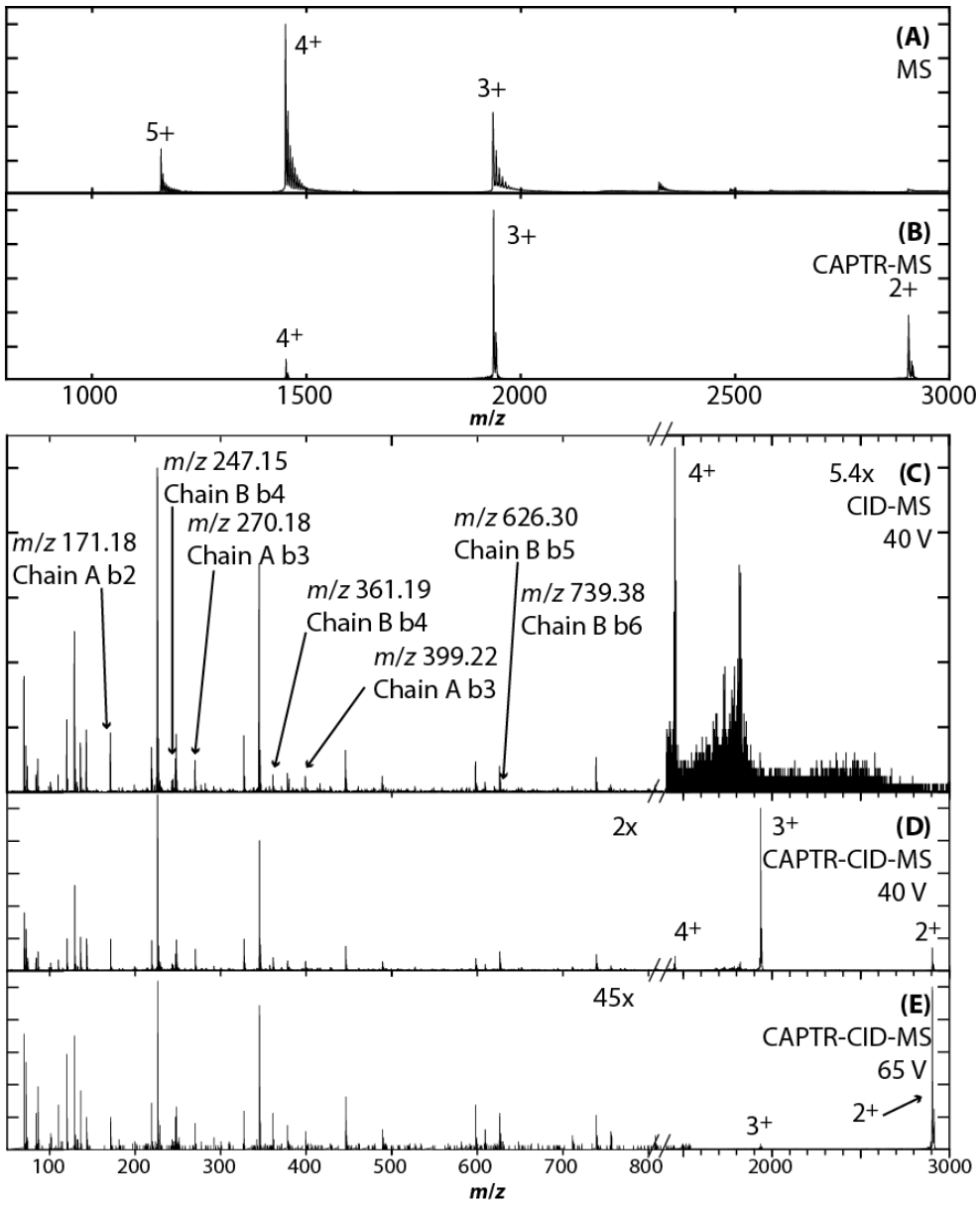

Figure S2: (A) MS of denatured insulin (5.8 kDa, monomer). Significant Na^+ adduction is observed, however only protonated precursor ions were quadrupole filtered for the subsequent spectra. (B) CAPTR of 4+ insulin monomer. (C) Collision induced dissociation (CID) of 4+ insulin with 40 V acceleration yields b^+ and y^+ fragments. No fragments corresponding to cleavage of a disulfide bond were detected. Two product ions with masses similar to possible c^+ and $z^{+\bullet}$ product ions were detected, but are attributed to CID pathways since no anions were present for electron transfer. (D) CAPTR of 4+ insulin followed by 40 V injection into the

transfer collision cell. This spectrum is virtually identical to C, therefore all fragment ions are attributed to CID pathways. (E) CAPTR of 4+ insulin followed by CID with 65 V injection into the transfer collision cell. This higher acceleration voltage was used to mitigate the effects of lower charge state ions experience lower center-of-mass collision energies for a given injection voltage than higher charge state ions. The resulting fragments are identical to those observed in C and D, albeit at lower overall intensities.

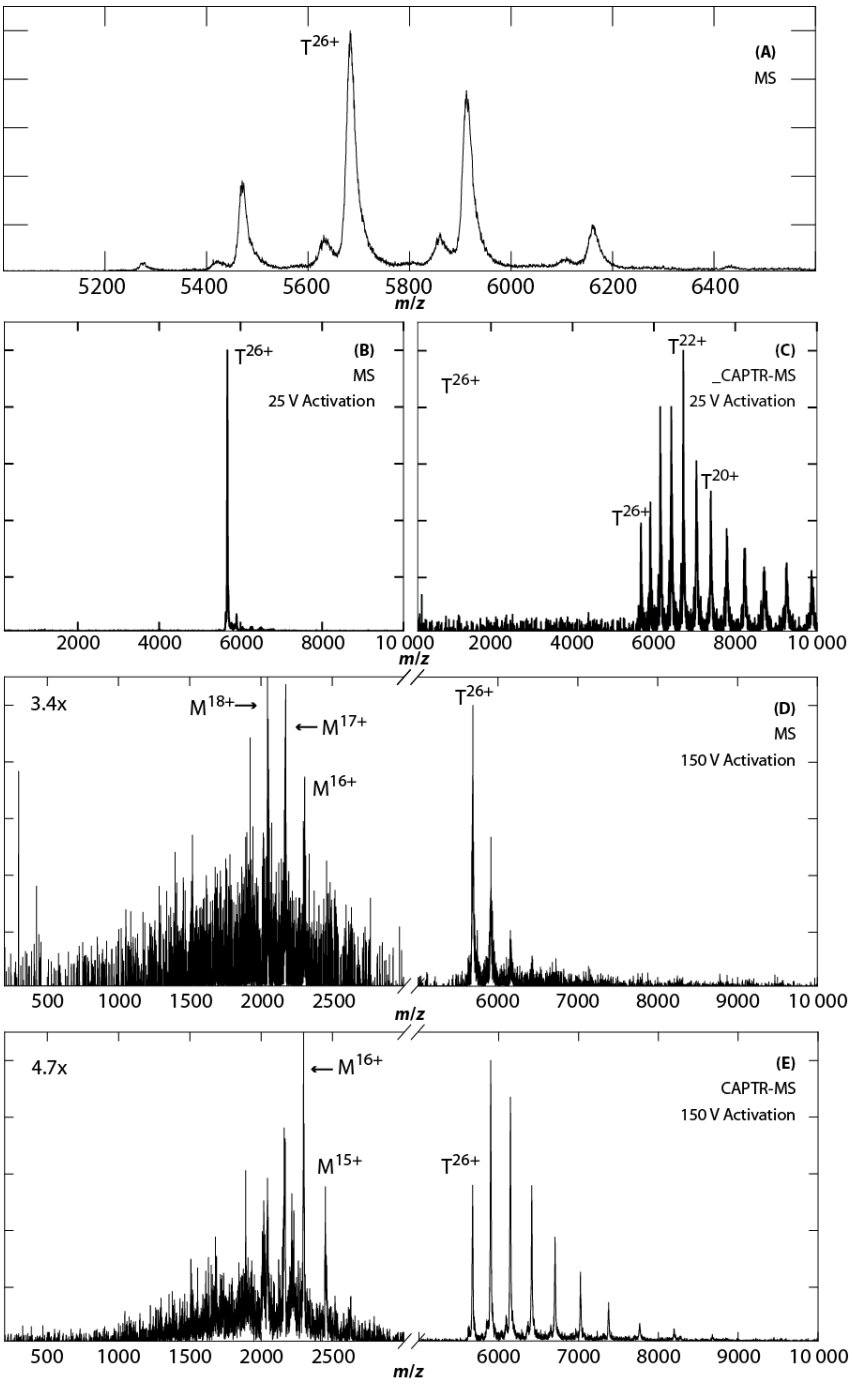

Figure S3: (A) Mass spectrum of alcohol dehydrogenase tetramer. 26^{+} tetramer (T^{26+}) quadrupole selected for further experiments. (B) 25 V acceleration of T^{26+} does not yield any CID ions. (C) 25 V acceleration of T^{26+} following CAPTR does not yield any characteristic ETD fragments (c^{+} and $z^{+\bullet}$ions) or CID ions. For comparison, 15 V of activation has previously been

shown to release fragments from the ETnoD products of native ADH following ETD on a similar instrument [3]. (D) 150 V acceleration of T^{26+} results in ejection of highly charged monomer (M). 150 V acceleration of T^{26+} following CAPTR results in ejection of highly charged monomer; however the charge state distribution of the monomer is shifted to slightly lower *z*, indicating some CAPTR products are undergoing monomer loss. No c^+ or $z^{+\bullet}$ ions were detected.

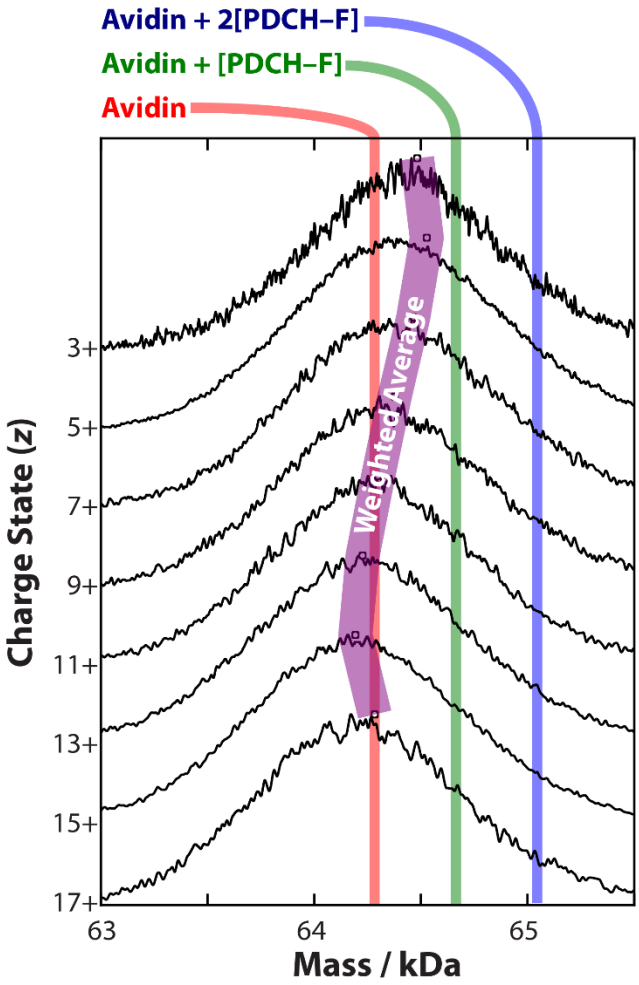

Figure S4: CAPTR products of avidin plotted on a mass axis. The weighted average of the 17+ distribution is shown as a vertical red line. The adduction of 1 and 2 $[PDCH–F]^-$ fragments (381 Da) are shown as the vertical green and blue lines respectively. The weighted average of the CAPTR products is plotted with small circles and a purple line. At low *z*, the mass distribution of the peaks increase slightly (~200 Da), indicating that a fraction of the product ions bind a very small numbers of anions.

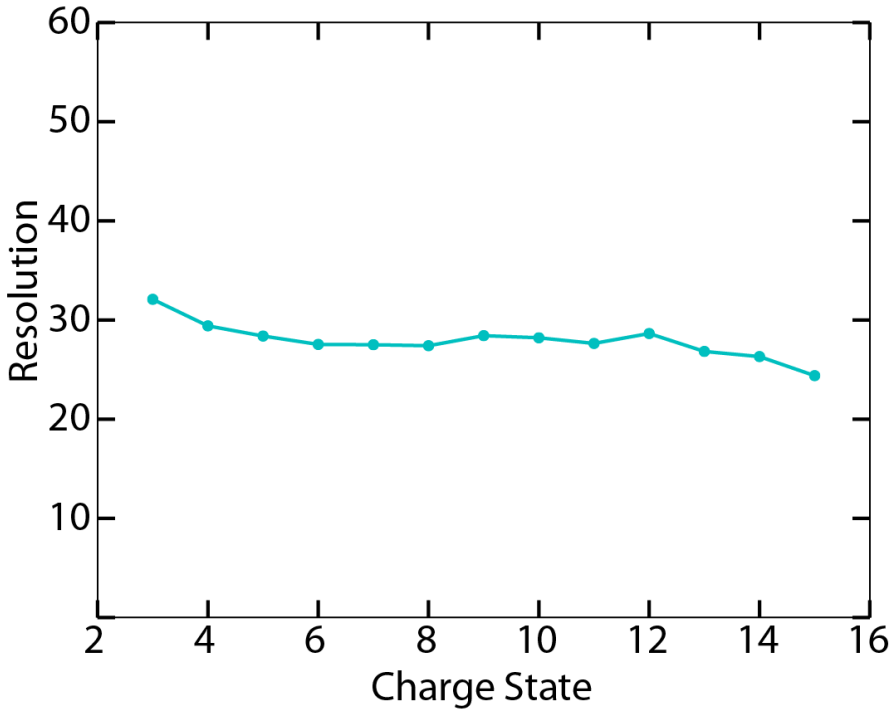

Figure S5: Resolution between $(BSA + zH)^{z+}$ and $(enolase + zH)^{z+}$ from measured individually (Figures 4B and 4C) as a function of charge state. Only charge states that were common to both proteins are compared.

References

(1) Frisch, M. J.; Trucks, G. W.; Schlegel, H. B.; Scuseria, G. E.; Robb, M. A.; Cheeseman, J. R.; Scalmani, G.; Barone, V.; Mennucci, B.; Petersson, G. A.; et al. *Gaussian 09, Revision D.1*; Gaussian, Inc.: Wallingford, CT, 2009.

(2) Guilhaus, M. Principles and Instrumentation in Time-of-Flight Mass Spectrometry. *J. Mass Spectrom.* **1995**, *30* (11), 1519–1532.

(3) Lermyte, F.; Williams, J. P.; Brown, J. M.; Martin, E. M.; Sobott, F. Extensive Charge Reduction and Dissociation of Intact Protein Complexes Following Electron Transfer on a Quadrupole-Ion Mobility-Time-of-Flight MS. *J. Am. Soc. Mass Spectrom.* **2015**, *26* (7), 1068–1076.

APPENDIX B

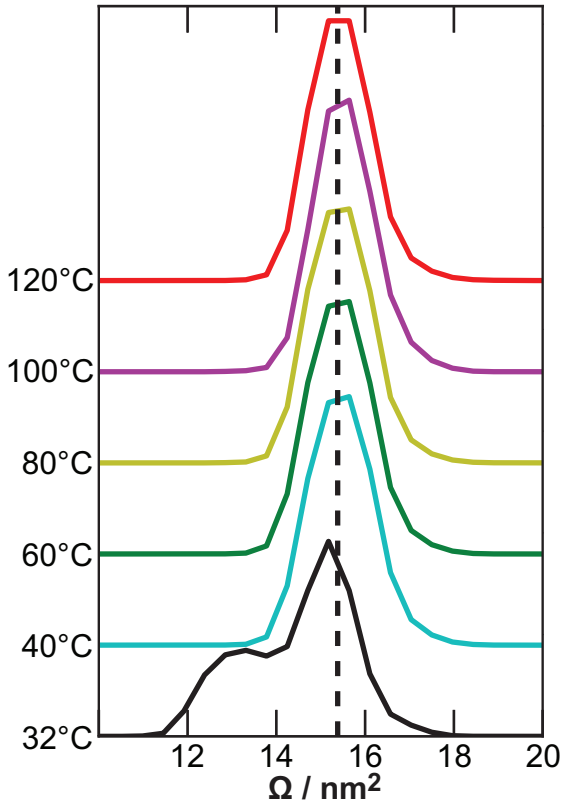

Figure S1: The *P→7* Ω distributions in Figure 3 exhibit a monomodal arrive-time distribution corresponding to a Ω of 15.4 nm^2. Previous results showed distributions spanning 9 to 17 nm^2, some of which exhibited multi-modal distributions.[1–4] One explanation for the single,

monomodal feature is that these experiments used a source temperature of 120 °C, which may activate the proteins during ionization or in solution due to convective heat transfer. Figure S1 shows the Ω distribution of 7+ ubiquitin as a function of source temperature. The vertical black dashed line indicates the average Ω of $P \rightarrow 7$ ion in Figure 4. At 32°C, the ion has a bimodal distribution from 12 to 17 nm^2, and shifts to a monomodal distribution centered around 15.4 nm^2 with the source held at 40°C. This is generally consistent with previous experiments in which increasing the inlet capillary from 25 to 132 °C resulted in the formation 7+ ubiquitin ions that exhibited a Ω distribution[1] similar to that observed here.

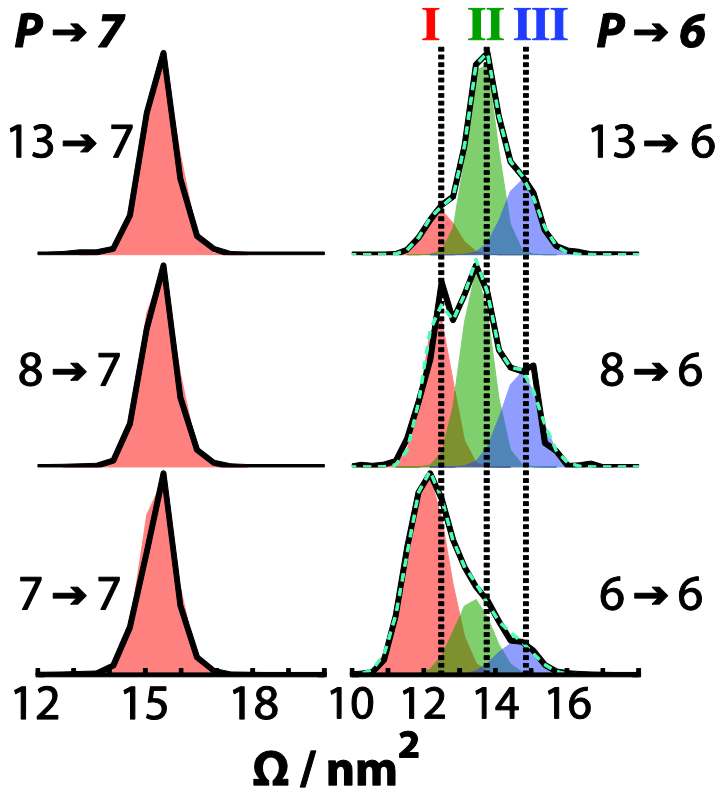

Figure S2. Ω distributions of selected $P \rightarrow 7$ and $P \rightarrow 6$ ubiquitin ions as a function of the charge state of the precursor ion (P). The data for the $P \rightarrow 7$ ions is the same as that used to determine the centroid Ω reported in Figure 4. The data for the $P \rightarrow 6$ ion is the same at the reported in Figure 5A to 5C using a trap injection voltage of 45 V. The $P \rightarrow 7$ Ω distribution are well-described using a single Gaussian function. The Ω distributions of the $P \rightarrow 6$ ions were assigned using three Gaussian functions; the sum of the three functions is shown with a dashed cyan line. The centroids for the all $P \rightarrow 7$ Gaussian functions, and the three $P \rightarrow 6$ Gaussian functions for P = 13+ to 6+ (Figure 4) were averaged and those four averages are shown using dashed black lines.

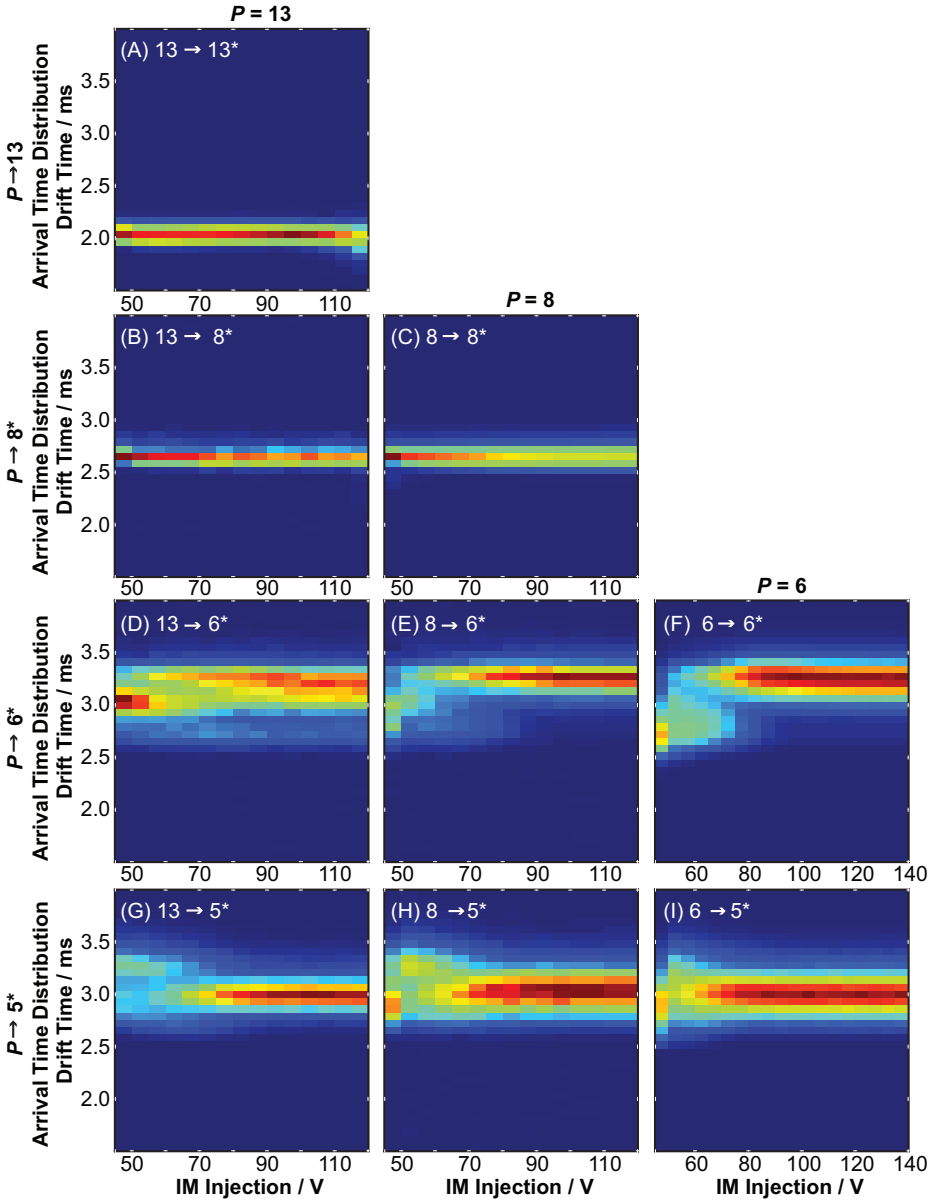

Figure S3. Arrival-time distributions for selected CAPTR product ions from precursor charge states (*P*) 13+, 8+, and 6+ ubiquitin plotted against injection voltage into mobility cell.

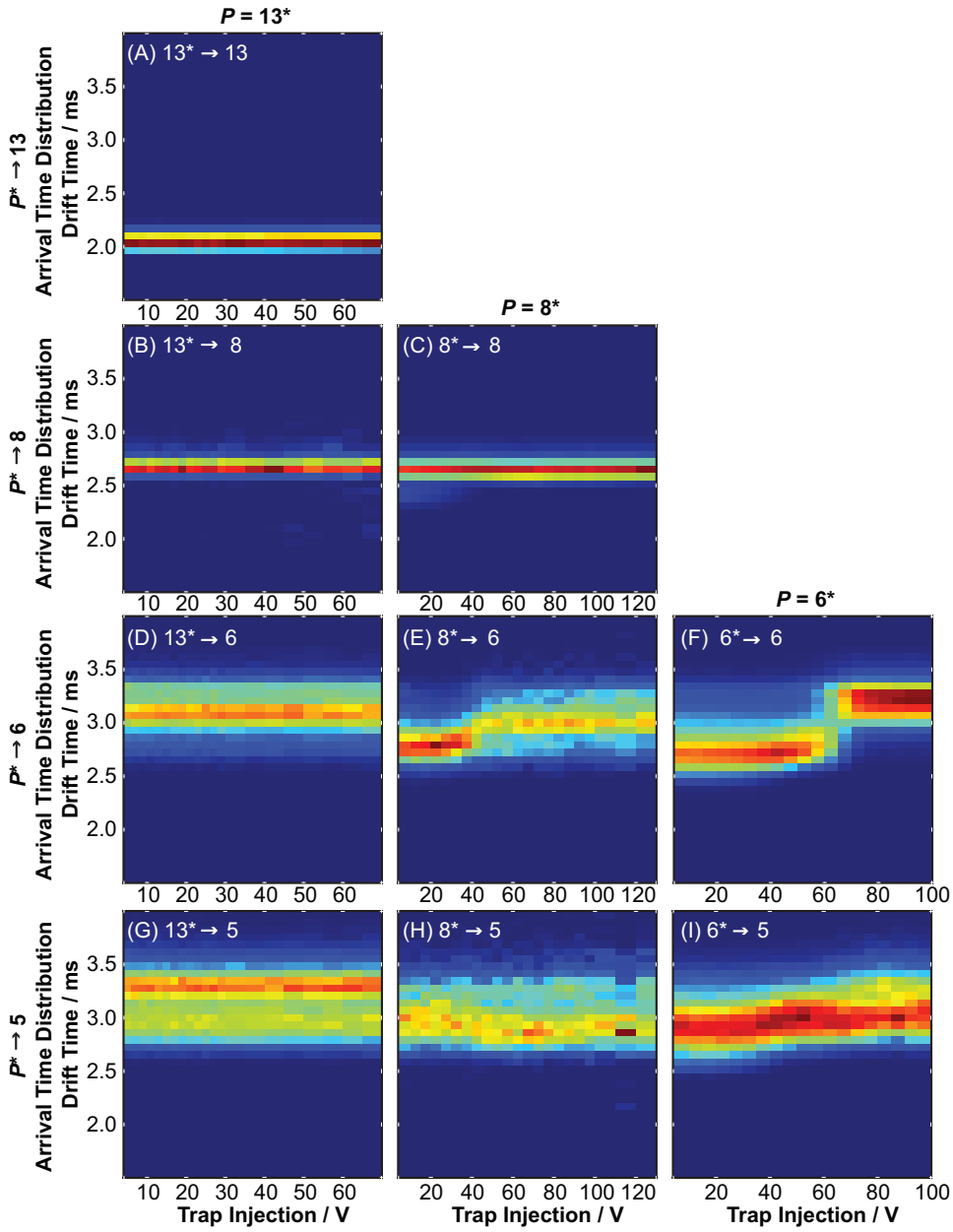

Figure S4. Arrival-time distributions of $P \rightarrow 13$, $P \rightarrow 8$, $P \rightarrow 6$, and $P \rightarrow 5$ ubiquitin product ions (P) and from precursor charge states 13+, 8+, and 6+ when activated entering the trap cell.

Consideration of Spontaneous Charge Loss: One challenge for interpreting these results is that ions adducted with any additional salt clusters may undergo the spontaneous loss or gain of charge following IM separation and prior to mass analysis. This is attributed to the ion ejecting either positively or negatively charged salt/solvent clusters when provided adequate collisional activation. These ions would therefore have the mobility of a *P* ion during the IM separation, but the *m*/*z* of a (*P*-1)+ or (*P*+1) ion during mass analysis.[5,6] For these experiments we can estimate how significant these pathways are by comparing the intensities of the quadrupole selected peak, *P*, and the corresponding anion ejected peak, (*P*+1). For the data collected, the 13+ precursor ion showed no sign of anion loss to generate a 14+ cation. However, when the 8+ ion was selected, there is a low-intensity signal corresponding to a 9+ cation at high collision energies. With the highest collisional activation into the trap cell, the 9+ to 8+ ratio was 0.0026, indicating the loss of an anion is not a dominant pathway in these experiments. We expect the rate of anion loss to be less than the rate of cation loss, however these values are expected to be on a similar order of magnitude.

Determining Collision Cross Sections:

Measured drift times (t_D) in these experiments depend on the mobility dependent drift time (t_K) and the transport time of ions from the exit of the mobility cell to the time-of-flight mass analyzer (t_0):

$$t_D = t_K + t_0 \quad \text{(Equation S1)}$$

where the t_K is defined as:

$$t_k = \frac{\text{mobility cell length}}{KE} \quad \text{(Equation S2)}$$

where K is the mobility of the ion and E is the electric field in the mobility cell

Measuring the drift time of nESI generated ubiquitin cations (identical denaturing conditions) at 10 electric fields from 104 to 354 V drop across the 25.2 cm mobility cell was used to determine t_0. t_0 has both a *m*/*z* dependent ($t_{m/z}$) and independent term (t_{ind}), which is related to instrumental parameters. t_{ind} is defined as:

$$t_{ind} = t_0 - t_{m/z} \quad \text{(Equation S3)}$$

$t_{m/z}$ is defined as:[7]

$$t_{m/z} = \frac{c\sqrt{m/z}}{1000} \quad \text{(Equation S4)}$$

where *c* is an instrument specific parameter (the 'enhanced dude cycle delay coefficient' on the Synapt G2). The average of t_{ind} from field dependent measurements was treated as a constant for CAPTR-IM experiments. For example, the average t_{ind} for charge states 13+ through 9+ ubiquitin was 0.04 ms, with a standard deviation of 0.005 ms.

CAPTR-IM experiments were performed at 1.5 Torr Helium with a 127 V drop across the mobility cell (unless otherwise noted). For CAPTR precursor and product ions, t_0 was calculated by summing t_{ind} and $t_{m/z}$, using the *m*/*z* value of each respective ion. For example, for ubiquitin charge states 13+ through 3+ $t_{m/z}$ ranged from 0.04 to 0.08. t_0 and measured t_D were

then used to calculate K of CAPTR product ions and residual precursors (Equation S2). Collision cross section (Ω) values were determined from the experimental K using the Mason-Schamp equation:[8]

$$\Omega = \frac{3ez}{16N}\left(\frac{2\pi}{\mu k_B T}\right)^{1/2}\frac{1}{K} \qquad \text{(Equation 1)}$$

where *e* is the fundamental charge, N is the number density of the drift gas, μ is the reduced mass of the ion and drift gas, k_B is the Boltzmann constant, and T is the drift-gas temperature

References

(1) Li, J.; Taraszka, J. A.; Counterman, A. E.; Clemmer, D. E. Influence of Solvent Composition and Capillary Temperature on the Conformations of Electrosprayed Ions: Unfolding of Compact Ubiquitin Conformers from Pseudonative and Denatured Solutions. *Int. J. Mass Spectrom.* **1999**, *185–187*, 37–47.

(2) Wyttenbach, T.; Bowers, M. T. Structural Stability from Solution to the Gas Phase: Native Solution Structure of Ubiquitin Survives Analysis in a Solvent-Free Ion Mobility–Mass Spectrometry Environment. *J. Phys. Chem. B* **2011**, *115* (42), 12266–12275.

(3) Shi, H.; Atlasevich, N.; Merenbloom, S. I.; Clemmer, D. E. Solution Dependence of the Collisional Activation of Ubiquitin [M + 7H]7+ Ions. *J. Am. Soc. Mass Spectrom.* **2014**, *25* (12), 2000–2008.

(4) Shi, H.; Clemmer, D. E. Evidence for Two New Solution States of Ubiquitin by IMS–MS Analysis. *J. Phys. Chem. B* **2014**, *118* (13), 3498–3506.

(5) Freeke, J.; Bush, M. F.; Robinson, C. V.; Ruotolo, B. T. Gas-Phase Protein Assemblies: Unfolding Landscapes and Preserving Native-like Structures Using Noncovalent Adducts. *Chem. Phys. Lett.* **2012**, *524*, 1–9.

(6) Sobott, F.; McCammon, M. G.; Robinson, C. V. Gas-Phase Dissociation Pathways of a Tetrameric Protein Complex. *Int. J. Mass Spectrom.* **2003**, *230* (2–3), 193–200.

(7) Ruotolo, B. T.; Benesch, J. L.; Sandercock, A. M.; Hyung, S. J.; Robinson, C. V. Ion Mobility-Mass Spectrometry Analysis of Large Protein Complexes. *Nat Protoc* **2008**, *3*, 1139–1152.

(8) Mason, E. A.; McDaniel, E. W. *Transport Properties of Ions in Gases*; Wiley: New York, 1988.

APPENDIX C

This Appendix is reproduced with permission from the Supporting Information of Laszlo, K. J.; Buckner J. H.; Munger, E.B.; Bush, M.F.; "Native-Like and Denatured Cytochrome c Ions Yield Cation-to-Anion Proton Transfer Reaction Products with Similar Collision Cross-Sections." *Journal of The American Society for Mass Spectrometry*, **2017**, doi:10.1007/s13361-017-1620-4.

Converting Arrival-Time Distributions to Ω Distributions:

Measured drift times (t_D) in ion mobility experiments depend on the mobility-dependent drift time (t_K) and the transport time of ions from the exit of the drift cell to the time-of-flight mass analyzer (t_0):

$$t_D = t_K + t_0 \qquad \text{(Equation S1)}$$

where the t_K is defined as:

$$t_K = \frac{(\text{drift cell length})^2}{KV} \qquad \text{(Equation S2)}$$

where K is the mobility of the ion and V is the voltage drop across the drift cell. t_0 is defined as:

$$t_0 = t_{ind} + t_{m/z} \qquad \text{(Equation S3)}$$

where $t_{m/z}$ is defined as [1]:

$$t_{m/z} = \frac{c\sqrt{m/z}}{1000} \qquad \text{(Equation S4)}$$

where c is an instrument specific parameter (the 'enhanced duty cycle delay coefficient' on the Synapt G2) [1]. Using these relationships Equation S1 can be expressed as:

$$t_K = \frac{(\text{drift cell length})^2}{K\text{V}} = t_\text{D} - \left(t_\text{ind} + \frac{c\sqrt{m/z}}{1000}\right) \quad \text{(Equation S5)}$$

In the present experiments, t_{ind} is determined through field-dependent measurements of precursor ions, using a previously described method [2]. Equation S5 can be rearranged to yield:

$$\frac{1}{K} = \frac{\left[t_\text{D} - \left(t_\text{ind} + \frac{c\sqrt{m/z}}{1000}\right)\right] * \text{V}}{(\text{drift cell length})^2} \quad \text{(Equation S6)}$$

The mobility of an ion can be converted to a collision cross section (Ω) using the Mason-Schamp equation [3]:

$$\Omega = \frac{3ez}{16\text{N}}\left(\frac{2\pi}{\mu k_\text{B} T}\right)^{1/2}\frac{1}{K} \quad \text{(Equation S7)}$$

Inserting Equation S6 into Equation S7 yields:

$$\Omega = \frac{3ez}{16\text{N}}\left(\frac{2\pi}{\mu k_\text{B} T}\right)^{1/2}\frac{\left[t_\text{D} - \left(t_\text{ind} + \frac{c\sqrt{m/z}}{1000}\right)\right] * \text{V}}{(\text{drift cell length})^2} \quad \text{(Equation S8)}$$

where *e* is the fundamental charge, *z* is the charge state, N is the number density of the drift gas, μ is the reduced mass of the ion and drift gas, k_B is the Boltzmann constant, and T is the drift-gas temperature. Using this relationship, experimental t_D may be converted to Ω.

Cumulative distribution functions (CDF) for each Ω were then calculated, and the critical Ω values corresponding to 10%, 50%, and 90% of the CDF were used to describe the Ω in Figure 4B and Figure 6. Examples of Ω distributions, the corresponding CDFs, and the critical Ω values are shown in Figure 4A, 5C, and 5D.

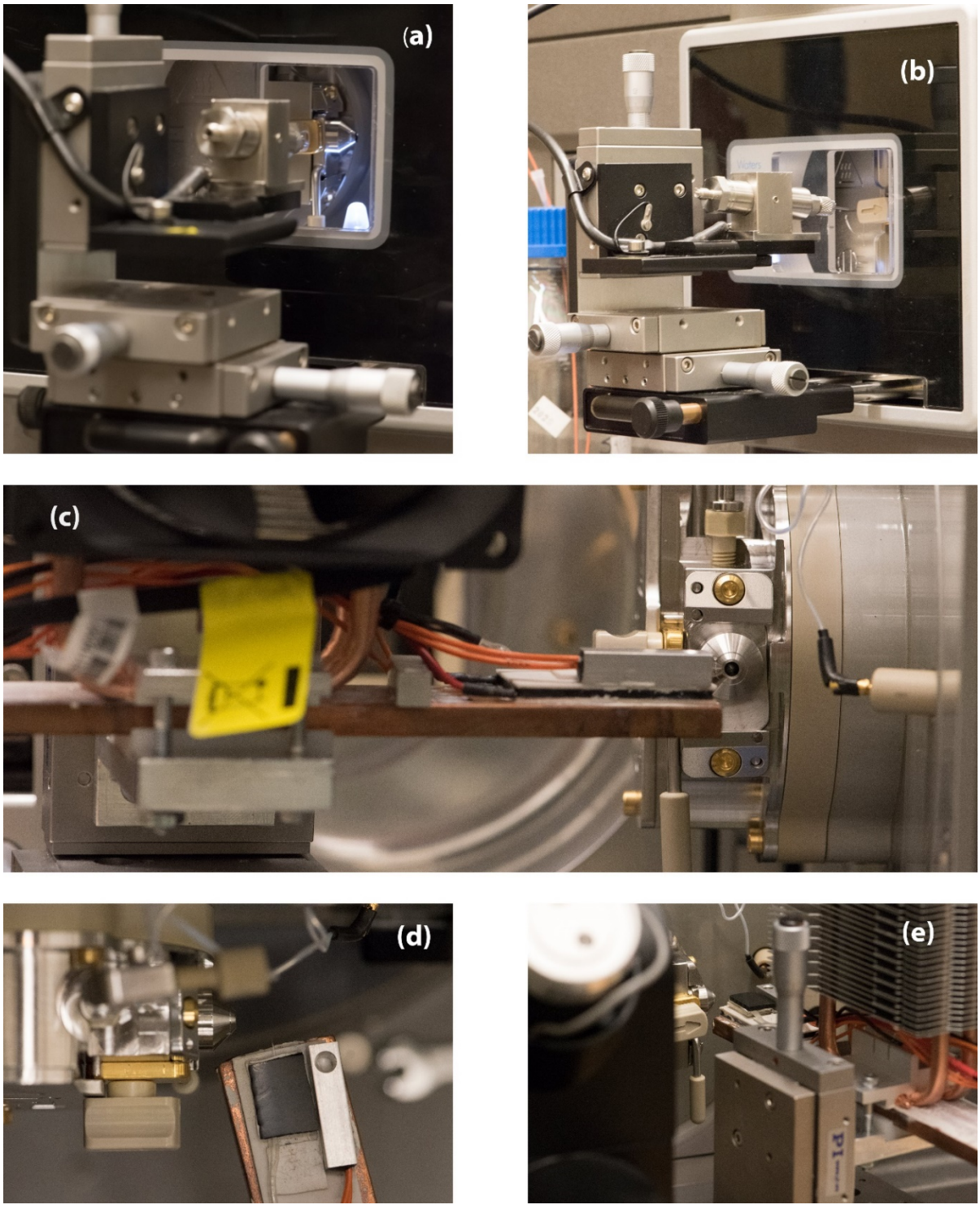

Figure S1. (a−b) Pictures of the original nanoelectrospray ionization source. Note that the translational stage is pulled away from the enclosure to reveal all of the components of the source. (c−e) Pictures of the new temperature-controlled, nanoelectrospray ionization source.

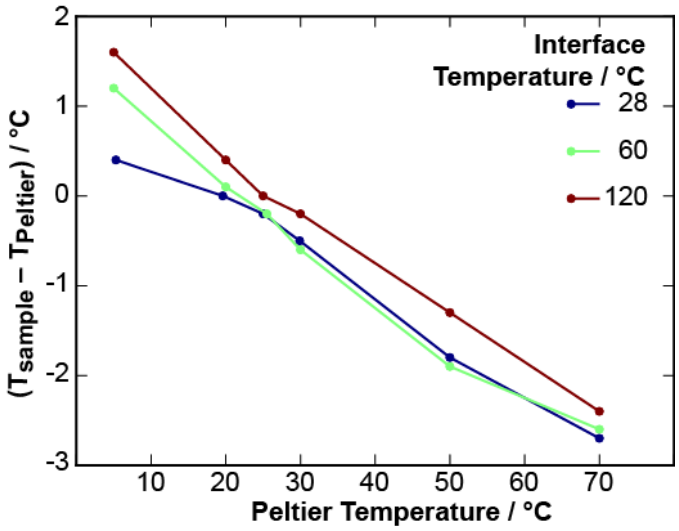

Figure S2. Difference between the temperature of the sample and the set temperature of the Peltier device.

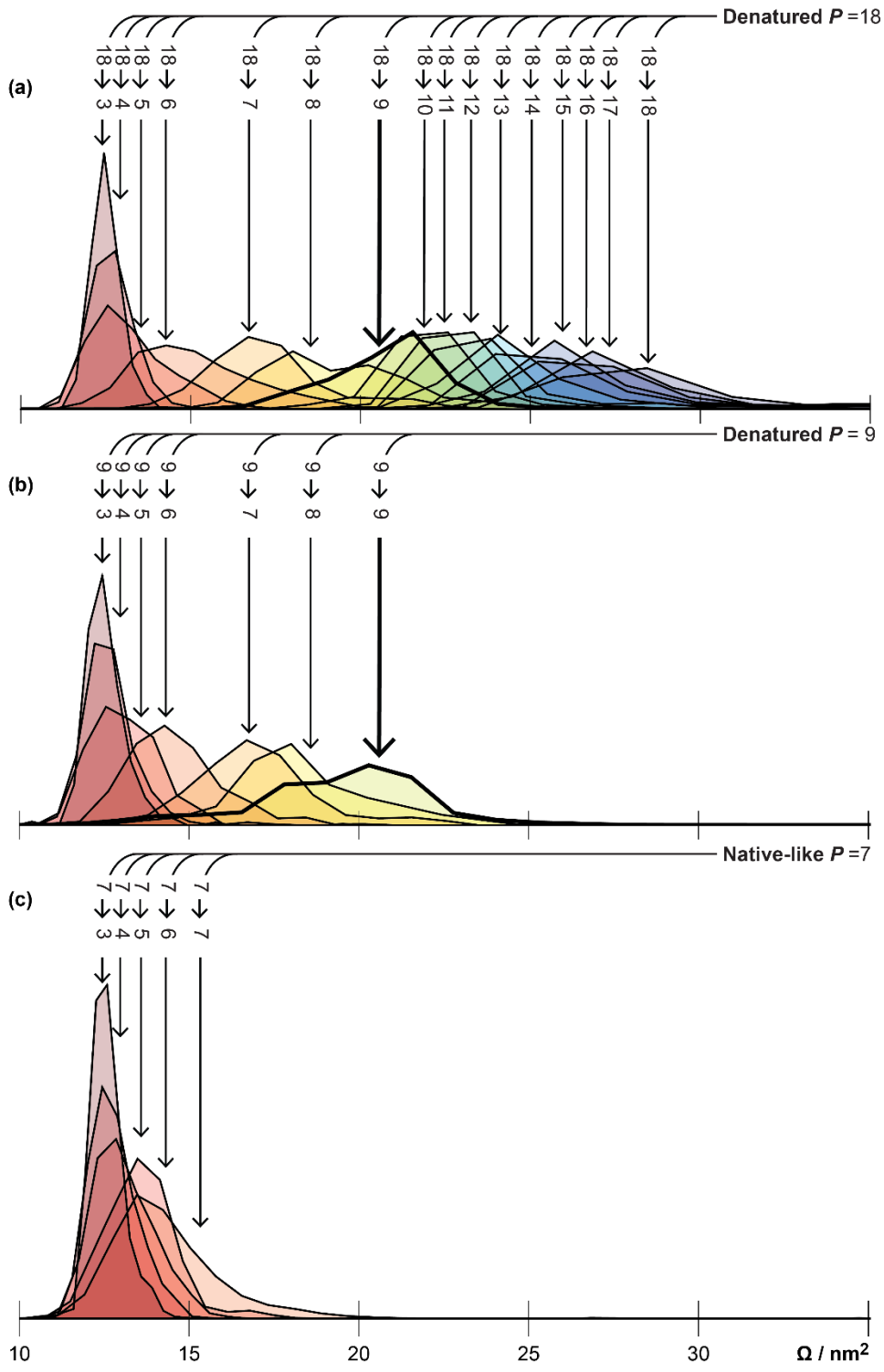

Figure S3. Ω distributions of (a) denatured 18→*C*, (b) denatured 9→*C*, and (c) native-like 7→*C* ions. Bolded 18→9 and 9→9 Ω distributions are reprinted in Figure 5c and 5d.

References

1. Ruotolo, B.T., Benesch, J.L., Sandercock, A.M., Hyung, S.J., Robinson, C.V.: Ion mobility-mass spectrometry analysis of large protein complexes. Nat Protoc. 3, 1139–52 (2008).
2. Allen, S., Giles, K., Gilbert, T., Bush, M.: Ion Mobility Mass Spectrometry of Peptide, Protein, and Protein Complex Ions using a Radio-Frequency Confining Drift Cell. Analyst. 141, 884–891 (2016).
3. Mason, E.A., McDaniel, E.W.: Transport Properties of Ions in Gases. Wiley, New York (1988).

APPENDIX D

Description of Background Subtraction.

Despite low pressures in the time-of-flight (ToF) mass analyzer, some ions may undergo collisions with neutrals in the flight tube, and therefore collide with the detector at a time unrelated to their *m*/*z*. The number of ions this occurs to is proportional to amount of ions in the flight tube, which is greatest when the most intense charge states exit the IM cell and enter the ToF. As a result, a peak corresponding to scattered ions was observed in the arrival-time distributions of the lowest intensity CAPTR product ions. In order to remove this interference, we implemented the following background subtraction.

The interfering high intensity ions were typically only the precursor charge state, but also included the first and second CAPTR product ions, or other chemical noise, *e.g.*, ions of salt clusters. The arrival-time distributions for these high intensity ions were summed together (ATD_0), and the first (median, t_m) and second (width, σ) moments of this distribution were calculated. The sum of ATD_0 elements from t_m-2σ to t_m+2σ was then related to the sum of the

CAPTR ion arrival-time distribution (ATD_{CAPTR}) by the scaler *A*, which is defined as:

$$A = \frac{\sum_{i=t_m-2\sigma}^{t_m+2\sigma}[ATD_{CAPTR}]_i}{\sum_{i=t_m-2\sigma}^{t_m+2\sigma}[ATD_0]_i} \quad \text{(Equation S1)}$$

The product of the precursor arrival-time distribution and *A* was then subtracted element-wise from the CAPTR product ion arrival-time distribution to yield the background subtracted CAPTR arrival-time distribution (ATD'_{CAPTR}):

$$[ATD'_{CAPTR}]_i = [ATD_{CAPTR}]_i - A\,[ATD_0]_i \quad \text{(Equation S2)}$$

Where t_m-2σ ≤*i* ≤t_m+2σ.

An example of these operations are shown in Figure S1. Figure S1A shows the arrival-time distribution of *P* = 10 ion from DI conditions, which has its maximum at about 4 ms; the intensity of the arrival-time distribution was scaled by *A*, according to Equation S1. The green dashed vertical lines in Figure S1 correspond to t_m-2σ and t_m+2σ of the 10+ ion. Figures S1B to S1D show data for the 10_{DI}→6 ion with respect to time on the upper x-axis, and with respect to Ω on the lower x-axis; note the upper time axis is aligned with Figure S1A. Figure S1B shows the arrival-time distribution of 10_{DI}→6 from the same denaturing conditions, which has a maximum at about 4 ms and 5.4 ms. These features correspond to scattered precursor ions, and the 10_{DI}→6 distribution, respectively. Figure S1C shows the background subtracted arrival-time distributions of 10_{DI}→6, according to Equation S2; this Ω distribution is identical to that of Figure 3C. Note that although the intensity of some of the arrival-time distribution is negative, the net change from t_m-2σ and t_m+2σ is 0, as per the definition of Equation S1. Figure S1D shows the cumulative distribution of the background subtracted arrival-time distribution shown in Figure S1C, this cumulative distribution function is identical to that shown in Figure 3C. The black dotted lines correspond to 10%, 50% and 90% intensity, and the corresponding Ω values, which are plotted in Figure 4.

Effects of the temperature of the atmospheric-pressure interface.

The Ω values for 8+, 7+ and 6+ NI lysozyme ions generated while the atmospheric interface was at ambient temperature are 14.9, 13.7, and 13.3 nm^2, respectively (Figure 2). The Ω of these ions were determined previously using field-dependent IM measurements, 2.7 mbar of helium, three technical replicates, and the centroids determined from the Gaussian function that has the smallest residual sum of squares with the experimental arrival-time distributions, which yielded values of 14.6, 13.7, and 13.6 nm^2 for these ions (Figure 2, magenta).[1] Analysis of a single arrival-time distribution measured during that study[1] using the present method[2] yields median of 14.8, 13.8 and 13.2 nm^2 for the 8+, 7+ and 6+ ions, respectively. This comparison suggests that both methods yield similar Ω values. Measurements were also made with the atmospheric-pressure interface at 120 °C. This elevated temperature is that normally used for CAPTR experiments and was selected to minimize the buildup of byproducts of glow-discharge ionization.[3] The mean Ω for precursor charge states 8+, 7+, and 6+ are 14.7, 14.0 and 13.7 nm^2, respectively (Figure 4D). These values are similar to those determined using the unheated atmospheric-pressure interface. Therefore, the NI lysozyme ions appear to retain their native-like structure while the atmospheric-pressure interface is heated to 120 ˚C.

Comparison with ion-neutral proton-transfer reactions. Foundational experiments by Clemmer and coworkers simultaneously charge-reduced a wide range of charge states of lysozyme using ion-neutral proton-transfer reactions, as described in the *Introduction*.[4] Analogous to those results, the CAPTR products of lysozyme from DR and DI conditions also exhibit more compact Ω distributions than the corresponding precursor ions (Figure 4B and 4C). The additional results for lysozyme from NI conditions (Figure 4D and 4E) provide a comparison for native-like lysozyme, which enables the conclusion that the lowest-charge state CAPTR products all fold to compact Ω distributions that are similar to that expected for native lysozyme, independent of solution conditions, precursor charge state, and the presence of the native disulfide bonds. The most significant difference in this study is that the precursor ions were each isolated individually and that additional, lower charge-state products were also formed. Therefore, our results build upon those previous measurements by measuring differences in the Ω distributions of CAPTR products of the same C that originate from different P, for wide ranges of P and C.

Comparison with activation of 6+ lysozyme ions formed via ion-neutral charge reduction.

Clemmer and coworkers used collisional activation to probe the stabilities of disulfide-intact and disulfide-reduced 6+ lysozyme ions that were generated via gas-phase ion-neutral proton-transfer of an ensemble of precursor ions generated from electrospray ionization, as described in the *Introduction*.[4] Those disulfide-intact 6+ ions had a Ω near 13.5 nm^2 at low energy, and exhibited a similar arrival-time distribution at high energies.[4] In the present study, the Ω distribution of the disulfide-intact $12_{DI}\rightarrow6$ ions are shifted to significantly larger values under low-energy conditions, but the Ω distribution of the $12_{DI}\rightarrow6^*$ at the highest energy is centered near 13.4 nm^2 (Figure 5C). This suggests that elements of the extended structure of the 12+ precursor ion are preserved during CAPTR, but that following collisional activation, the $12_{DI}\rightarrow6^*$ product ions isomerize to a lower-energy, gas-phase structure that may be similar to that formed in Clemmer's ion-neutral proton-transfer experiments. Extended structures were not observed at low energy in Clemmer's experiments.

The disulfide-reduced 6+ ions in those previous ion/neutral experiments had a Ω near 13.4 nm^2, and additional conformers with Ω near 14.5 and 16.3 nm^2 were also observed at high energies.[4] The Ω distribution of the $12_{DR}\rightarrow6$ ions in these experiments are broad and generally centered near 15.5 nm^2, but with increasing energy, the distribution shifts to smaller values, particularly in the region from 13 to 14 nm^2 (Figure 5D). These result is consistent with the formation of some of the conformers in both experiments. However, evidence for significantly larger structures (~17.5 nm^2) persist over all energies in the present experiments. Analogous extended conformers of disulfide-reduced 6+ lysozyme were not observed in Clemmer's experiments, even though the precursors ions (prior to charge reduction) in those experiments included a broad range of charge states (z = 10 to 17) than that used in the present experiments (z

= 12). Furthermore, the present results show that the $12_{DR} \rightarrow 6$ ions exhibit an overall compaction with increasing energy, whereas the 6+ product ions of the ion-neutral proton-transfer reactions unfold to more extended structures with increasing energy.[4] Based on the Ω distributions at low and high energies, it is clear that there are significant differences between the structures of 6+ lysozyme produced in the two experiments. These differences may be attributable to differences in the charge state of the precursors, which were an ensemble of 10+ to 17+ lysozyme,[4] or the preferential charge reduction of compact precursor ions during ion-neutral proton-transfer reactions.[5–7]

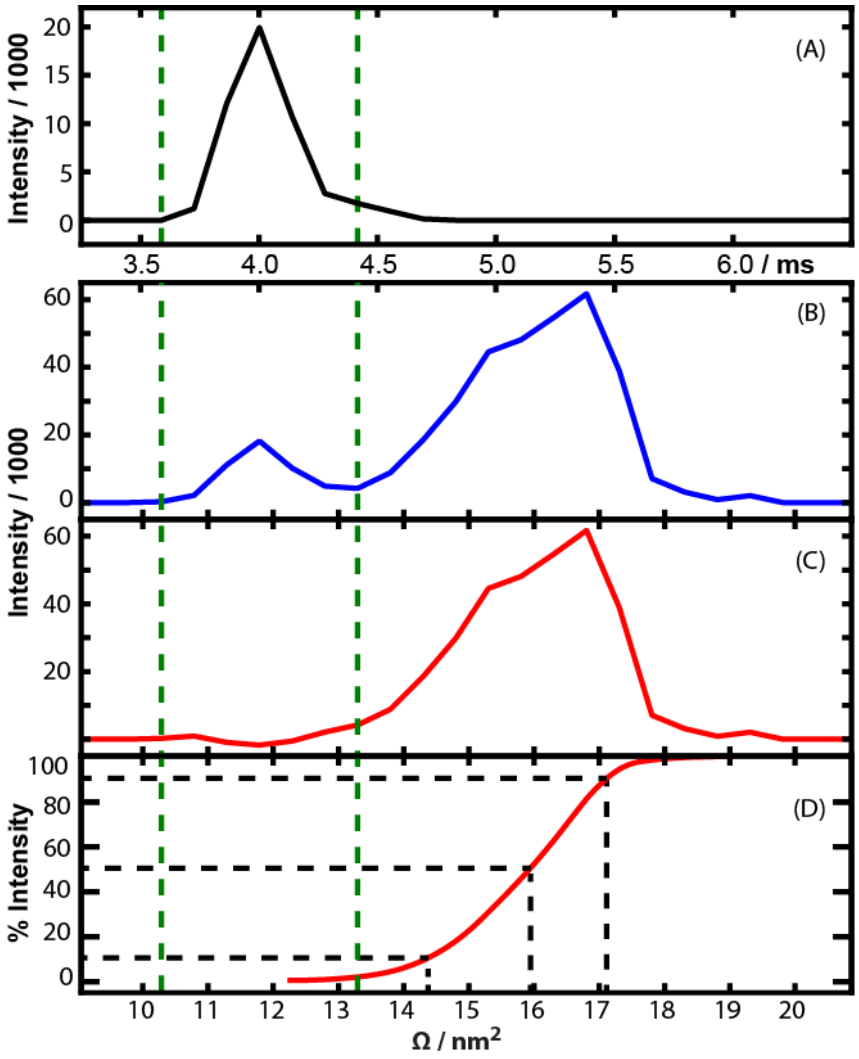

Figure S1. (A) Arrival-time distribution for 10+ lysozyme from denaturing conditions (ATD_0), multiplied by the scalar defined in Equation S1. Vertical dashed green lines correspond to t_m-2σ and t_m+2σ. (B-D) Data correspond to the 10_{DI}→6 ion from denaturing conditions and are relative to both the upper time x-axis, as well as the lower Ω x-axis. (B) Ω distribution of 10_{DI}→6 ion prior to background subtraction (ATD_{CAPTR}). (C) Background subtracted 10_{DI}→6 ion (ATD'_{CAPTR}). (D) Cumulative distribution function of C. Dashed black lines correspond to 10, 50, and 90% percent of the Ω distribution and the corresponding Ω values.

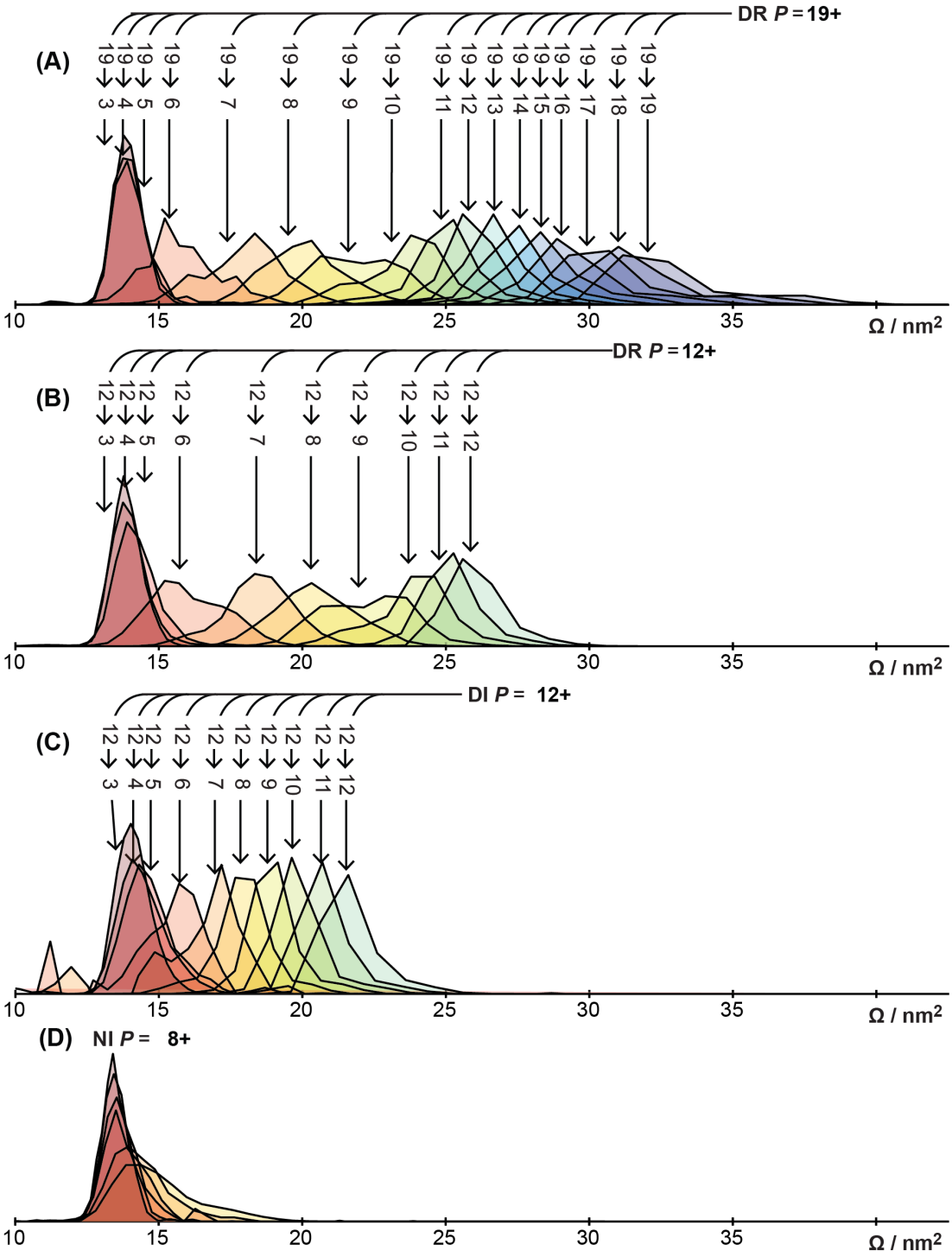

Figure S2. Ω distribution of (**A**) the $19_{DR}\rightarrow C$ ions, (**B**) the $12_{DR}\rightarrow C$ ions, the (**C**) $12_{DI}\rightarrow C$ ions, and (**D**) the $8_{NI}\rightarrow C$ ions. All distributions were determined with the atmospheric-pressure interface at 120 ˚C.

APPENDIX E

This Appendix is reproduced with permission the Supporting Information of Laszlo, K. J.; Bush, M. F. "Interpreting the Collision Cross Sections of Native-Like Protein Ions: Insights from Cation-to-Anion Proton-Transfer Reactions" **2017**, manuscript in preparation

Table S1. Calculated Ω Values.

Protein	PDB[a]	Method	Ω / nm^2 [b]
Serum Albumin	4F5S	PA	39.46 ± 0.03
		EHSS	51.99 ± 0.05
Streptavidin	4Y5D	PA	29.25 ± 0.02
		EHSS	38.11 ± 0.03
Avidin	1AVD [c]	PA	31.00 ± 0.02
		EHSS	40.21 ± 0.03
Alcohol Dehydrogenase	5ENV	PA	63.28 ± 0.04
		EHSS	84.50 ± 0.07

[a] Ω values were calculated for models that were constructed as described in the *Methods*, based on these deposited structures.
[b] The reported interval was determined using Student's t-test at the 95% confidence level and 512 replicate calculations.
[c] This crystal structure of avidin does not contain glycans, unlike the native protein. For context, the mass of the model used for the calculations is 55,143 Da, whereas a mass of 64 kDa is typically observed for avidin in native mass spectrometry experiments.

Converting Drift Times to Ω and Consideration of Error

Measured drift times (t_D) in these ion mobility (IM) experiments depend on the mobility-dependent drift time through the mobility cell (t_K) and the transport time of the ion from the exit of the drift cell to the time-of-flight mass analyzer (t_0):

$$t_D = t_K + t_0 \quad \text{(Equation S1)}$$

As validated previously for RF-confining drift cells, t_K depends on the length of the drift cell, the mobility of the ion, K, and the voltage drop across the drift cell, V (the drift voltage):

$$t_K = \frac{(\text{drift cell length})^2}{KV} \quad \text{(Equation S2)}$$

Combining Equations S1 and S2 yields:

$$t_D = \frac{(\text{drift cell length})^2}{KV} + t_0 \quad \text{(Equation S3)}$$

Therefore, the mobility of an ion can be determined by analyzing the rate at which drift time changes as a function of 1/V, and t_0 may be determined from the y-intercept of this plot.[1,2] Additional details of field dependent measurements, including sources of the observed random errors (~2%), are discussed elsewhere.[1–3]

Collision cross section (Ω) values are determined using K and the Mason-Schamp equation:[4]

$$\Omega = \frac{3ez}{16N}\left(\frac{2\pi}{\mu k_B T}\right)^{1/2}\frac{1}{K} \quad \text{(Equation 1)}$$

where e is the fundamental charge, N is the number density of the drift gas, μ is the reduced mass of the ion and drift gas, k_B is the Boltzmann constant, and T is the drift-gas temperature.

The transport time from the mobility cell to the mass analyzer, t_0, includes m/z-dependent ($t_{m/z}$) and m/z-independent (t_{ind}) contributions:

$$t_0 = t_{ind} + t_{m/z} \quad \text{(Equation S4)}$$

The value for $t_{m/z}$ can be estimated using:[5]

$$t_{m/z} = \frac{c\sqrt{m/z}}{1000} \qquad \text{(Equation S5)}$$

where *c* is an instrument-specific parameter (the 'enhanced duty cycle delay coefficient' on the Synapt G2).[5]

The CAPTR products were analyzed using 1.5 Torr of helium gas and a drift voltage of 212 V. This method was described previously for the analysis of the CAPTR products of ubiquitin ions.[6] Briefly, values for t_D were determined from the Gaussian function that has the smallest residual sum of squares with the experimental arrival-time distribution. Values for t_0 were first estimated from those determined for the precursor ions using a field-dependent method, and were then corrected for differences in *m*/*z* using Equation S5.

To validate this method, field-dependent measurements of the CAPTR products of avidin were made using five drift voltages ranging from 104 to 304 V. Figure S1 shows t_0 determined from subsets of the field-dependent data and that determined using the single field-strength method. When all five field strengths are considered (104 – 304 V, *royal blue*), the apparent t_0 decreases at low *z*. Additionally, the quality of the linear regression decreases with decreasing *z*, resulting in larger errors for those charge states. Excluding the results measured using the lowest voltage, the apparent t_0 increases and the error decreases at low *z* (*yellow*). When only the highest three field strengths are considered, this trend continues (*red*). Therefore, the use of low drift voltages appears to bias to lower t_0 values for low-*z* ions. Figure S1 also includes t_0 determined using the single field-strength analysis (*dark blue*). These data are within the uncertainties of the previous determinations. To visualize the effects of the value of t_0, Figure S2 shows the Ω values determined using each approach. For the 16→6 ions, which were the lowest charge state observed, the field-dependent analysis using all five drift voltages yields

a Ω value of 38.4 nm^2, the field-dependent analysis using the three highest drift voltages yields a Ω value of 36.2 nm^2, the single field-strength analysis of 104 V yields a Ω value of 37.6 nm^2, and the single field-strength analysis of 212 V yields a Ω value of 36.0 nm^2. Thus, this analysis validates this method for determining t_0 when interpreting t_D measured using a drift voltage of 212 V and indicates that inclusion of results measuring using very low field strengths results in a systematic and positive bias of the Ω values.

To evaluate the origin of the bias for low-*z* ions at low field strengths, Figure S3 shows the apparent Ω distribution for the 16→6 ions, based on five single field-strength determinations. The distributions determined using drift voltages of 161, 212, and 304 V are all reasonably symmetric and have similar centroids (particularly given the limited sampling of the distributions). The distribution determined using a drift voltage of 127 V is biased to slightly larger values. The distribution determined using a drift voltage of 104 V is further biased to even larger values and is skewed. Based on these results, we propose that the origin of this effect is that low mobility ions have a disproportionally long residence time near the entrance to the mobility cell where the low field strength is partially countered by the net flow of gas towards the entrance aperture to the drift cell.

These experiments show that careful consideration must be taken when using IM to analyze a wide range of mobilities. In particular, avoiding extremely low field strengths aids efficient transfer of ions into the drift cell, which in turn results in Gaussian arrival-time distributions and reduced errors. Furthermore, these results validate the use of single field-strength analysis of CAPTR product ions and that the values of t_0 are realistic and within the uncertainties of values determined using field-dependent measurements. Furthermore, errors in t_0 and other uncertainties in these experiments adds approximately 1% error to these

experiments relative to those for typical field-dependent measurements (~2%).[1–3] The total random error in the present experiments is therefore approximately ±2.2%, which is the square root of the sum of squares of both sources of random error.

The IM-MS data in these experience often exhibit noise that is attributed to scattering in the time-of-flight mass analyzer. Scattered ions will exhibit the same drift times as unscattered ions, but will appear across a broad range of *m*/*z*. Scattering after the reflectron will result in noise at higher *m*/*z* and scattering before the reflectron may result in noise at lower *m*/*z*, because ions with lower kinetic energies will have shorter residence times in the reflectron. Unreacted precursor ions exhibit the shortest drift times and often the greatest relative intensity, and therefore, yield the most scattered ions. When the arrival-times of those scattered ions are well resolved from the arrival-times of a CAPTR product of interest, a single Gaussian function was used to characterize the distribution of the CAPTR product. When the arrival-times of those scattered ions are not well resolved, the distribution was characterized using two Gaussian functions. During optimization, the centroid and width of one of the functions was held constant at the values determined for the precursor ion. The t_D value for the analyte was then determined from the centroid of the other optimized function. This approach acts as a background subtraction of any scattered precursor ions.

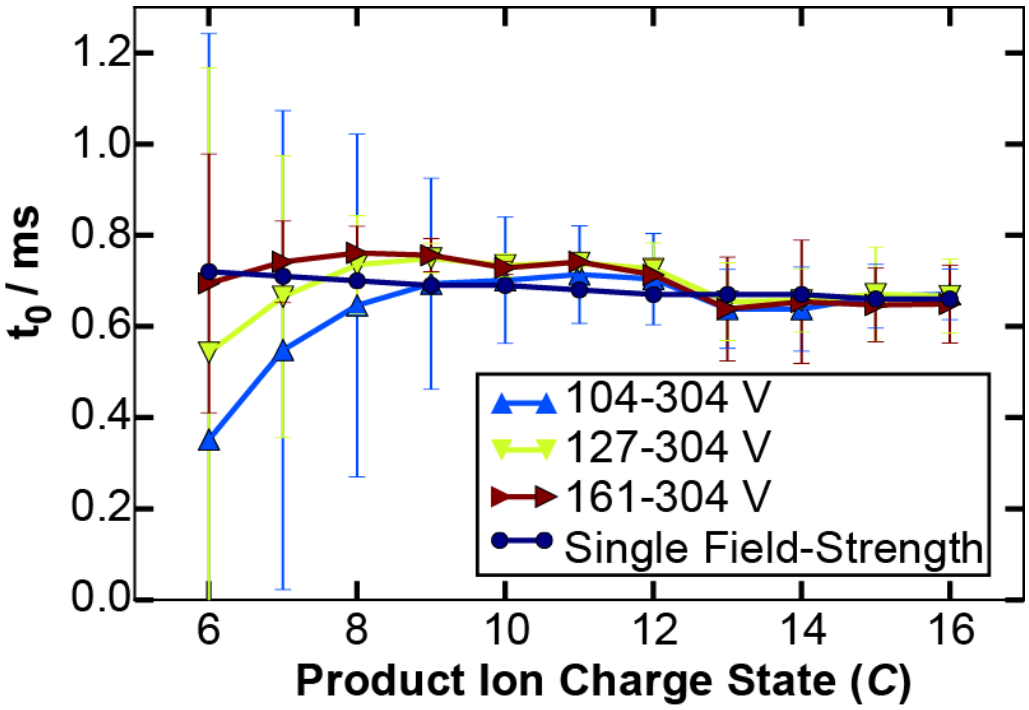

Figure S1. Estimated transport time of avidin ions between the drift cell and the mass analyzer as a function of charge state. Values were calculated based on data obtained using different ranges of drift voltages and the single field-strength method as discussed in *Converting Drift Times to Ω and Consideration of Error*. Error bars were propagated from linear regression of the plots of 1/V versus t_D.

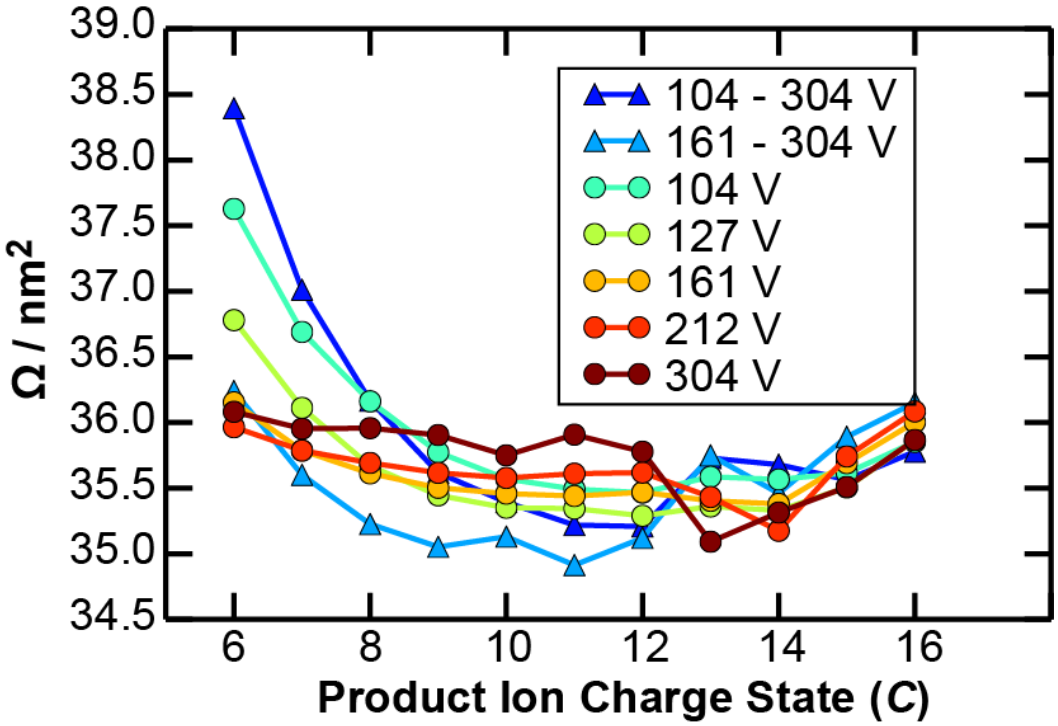

Figure S2. Apparent Ω values of 16→*C* avidin ions resulting from a series of field-dependent (*triangles*) and single field-strength (*circles*) determinations.

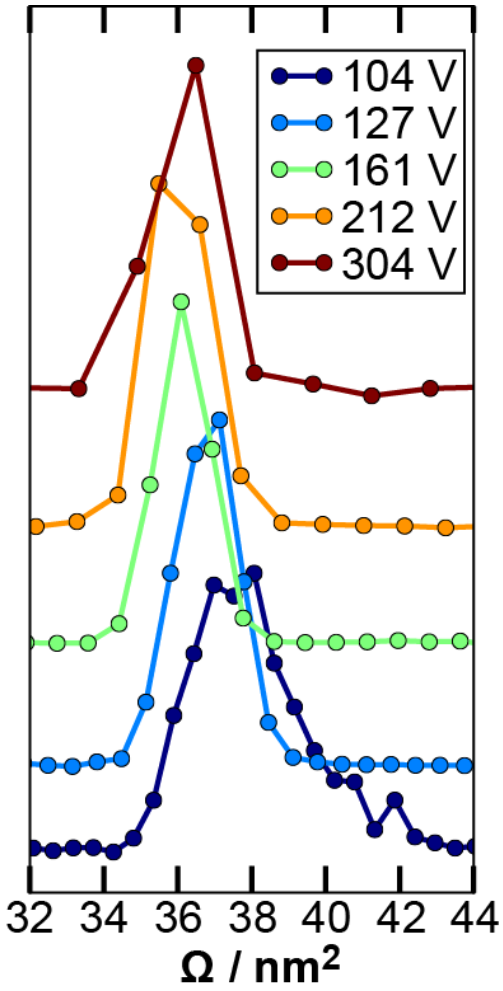

Figure S3. Apparent Ω distributions for 16→6 avidin based on measurement using drift voltages of 104 V (*dark blue*), 127 V (*light blue*), 161 V (*light green*), 213 V (*orange*), and 304 V (*maroon*).

Comparisons with Ω Values Reported for Other Charge-Reduced, Native-Like Ions

Figure S4a compares Ω values determined here and reported previously for alcohol dehydrogenase. As discussed in the main text, the Ω values for native-like alcohol dehydrogenase and its CAPTR products initially decrease with decreasing charge, then plateau, and finally increase following the final CAPTR events (*blue triangles*). Ω values have also been reported for alcohol dehydrogenase generated from electrospray of solutions containing 200 mM ammonium acetate at pH 7.0 (*black circles*),[7] 200 mM ammonium acetate with 10 mM triethylamine at pH 7.0 (*cyan diamonds*),[7] and 100 mM ammonium acetate at pH 6.9 with exposure to nebulized 1,5-diazabicyclo[4,3,0]non-5-ene (DBU, *green squares*).[8] The addition of a weak base enables the formation of additional ions with lower charge states. Relative to the CAPTR experiments, the ions in those charge-reduction experiments[7,8] exhibit a narrower range of charge states (18 to 27 versus 11 to 27) and a smaller range of Ω values for the highest-*z* ions. Interestingly, after the initial charge reduction, the CAPTR products and the additional ions observed with the addition of a weak base[7,8] all exhibit modest increases in Ω with decreasing charge state, but those increases occur far earlier for the latter. Some of the differences between the Ω reported here and these previous experiments may be attributable the single-field strength analysis and heated atmospheric-pressure interface in the present experiments.

Ω values have also been reported for the products of native-like alcohol dehydrogenase ions that were reacted with 1,4-dicyanobenzene radical anions.[9] Those Ω values (*red inverted triangles*) decrease significantly with decreasing charge state, implying significant structural collapse. Although those experiments[9] and these CAPTR experiments both use ion/ion chemistry and were performed on similar instruments, there are two significant differences. First, reactions with radical anions can yield charge-reduced products via proton transfer

(Reaction 2) or electron transfer (Reaction 1), which will result in the formation of a radical cation that can undergo further reactions.[10] Thus, the charge-reduced products in the two experiments are not necessarily the same ions. Second, the products in the previous experiments were analyzed using traveling-wave IM,[9] whereas the products in these CAPTR experiments were analyzed using an rf-confining drift cell.[1]

Figure S4b compares Ω values determined here and reported previously for pyruvate kinase. Ω values were determined for the CAPTR products of 33+, 34+, 35+, and 36+ pyruvate kinase generated from 200 mM ammonium acetate at pH 7.0 and are reported as a function of *C* and averaged across all *P* (*blue triangles*). Note that these Ω values are based on measurements using a drift voltage of 127 V, which likely biases the Ω of low-*C* ions to slightly higher values (see *Converting Drift Times to Ω and Consideration of Error*). These values and those determined for ions generated from generated from electrospray of solutions containing 200 mM ammonium acetate at pH 7.0 (*black circles*),[7] 200 mM ammonium acetate with 10 mM triethylamine at pH 7.0 (*cyan diamonds*),[7] and 100 mM ammonium acetate at pH 6.9 with exposure to nebulized DBU (*green squares*),[8] all indicate that pyruvate kinase does not undergo significant structural collapse with decreasing charge state. In contrast, Ω values reported for pyruvate kinase ions that were generated in close proximity to a corona discharge probe (*purple inverted triangles*) decrease 19% with deceasing charge state, which suggests that pyruvate kinase undergoes significant structural collapse with decreasing charge state.[11] In addition to the differences in the charge reduction method, those experiments used traveling-wave IM using a ramped wave amplitude. Accordingly, the authors state in that manuscript “The authors are well aware that ion movement through a TWIM device is complex even when a single TWIM amplitude is utilised, and since all TWIM measurements were performed using a TWIM

amplitude ramp (3–8 V), we describe our reported Ω He values as purely tentative; only limited structural assignments are inferred *vide infra*."[11]

Both studies that reported significant structural compaction with decreasing charge state used traveling-wave IM.[9,11] rf-confining drift cells, such as that used in this study,[1] have been shown to yield Ω values similar to those determined using electrostatic drift tubes[2] and provide a more direct determination of Ω than traveling wave IM. The conditions for the traveling-wave experiments described above are summarized in Table S2, so that they may be directly compared to the present measurements. Notably, the results

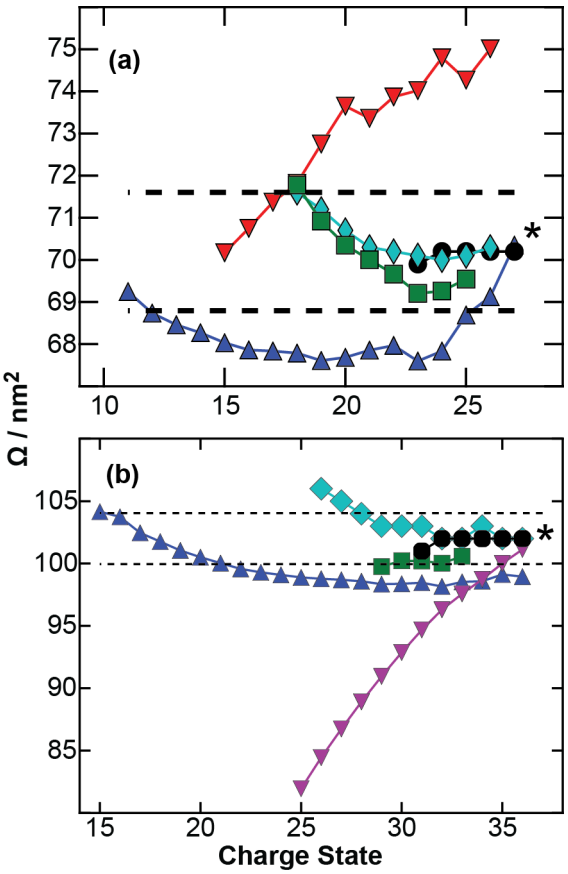

Figure S4. (a) Ω values for alcohol dehydrogenase ions. Results from CAPTR (*blue triangles*) are based on the average of the values for the products from each precursor. For comparison, values are also plotted for ions generated from electrospray of solutions containing 200 mM ammonium acetate at pH 7.0 (*black circles*),[7] 200 mM ammonium acetate with 10 mM triethylamine at pH 7.0 (*cyan diamonds*),[7] 100 mM ammonium acetate at pH 6.9 with exposure to nebulized 1,5-diazabicyclo[4,3,0]non-5-ene (DBU, *green squares*),[8] and 100 mM ammonium acetate at pH 6.9 and reacted with 1,4-dicyanobenzene radical anions (*red inverted triangles*).[9] (b) Ω values for pyruvate kinase ions. Results from CAPTR (*blue triangles*) are describe in *Comparisons with* Ω *Values Reported for Other Charge-Reduced, Native-Like Ions*. For comparison, values are also plotted for ions generated from electrospray of solutions containing 200 mM ammonium acetate at pH 7.0 (*black circles*),[7] 200 mM ammonium acetate with 10 mM triethylamine at pH 7.0 (*cyan diamonds*),[7] 100 mM ammonium acetate at pH 6.9 with exposure to nebulized DBU (*green squares*),[8] and 100 mM ammonium acetate in close proximity to a corona discharge probe (*purple inverted triangles*). Dashed horizontal lines indicate ±2% of the data point marked with an asterisk (*).

Table S2. Traveling-wave IM calibration parameters for previously reported values in Figure S4. Abbreviations refer to the following proteins: avidin (AVD), alcohol dehydrogenase (ADH), and pyruvate kinase (PK) were commonly used in addition to concanvilin A (ConA, tetramer, 103 kDa), glutamate dehydrogenase (GDH, hexamer, 336 kDa), and β-galactosidase (β-GAL, 468 kDa, tetramer). Calibrant and analyte mobilities were estimated based on available calibration data sets, and the reported experimental parameters and data.

	Bornschien et. al.[8]	**Lermyte et. al.**[9]	**Bornschien et. al.**[8]	**Campuzano & Schnier**[11]
Analyte	**ADH**	**ADH**	**PK**	**PK**
Calibrants	AVD, ADH, PK, ConA, GDH	ADH	AVIDIN, ADH, PK, ConA, GDH	ADH, PK, GDH, β-GAL
Wave Height / V	30−35	30	30−35	3−8 (Ramped)
Wave Velocity / m/s	500−600	1000	500−600	190−200
Pressure / mbar	3.5	4.3	3.5	0.2
Calibrant Mobilities / $m^2/s \cdot V$	0.79−1.16	0.88−0.99	0.79−1.16	0.79−0.99
Analyte Mobilities / $m^2/s \cdot V$	0.71−1.02	0.61−0.99	0.83−0.93	0.83−1.01

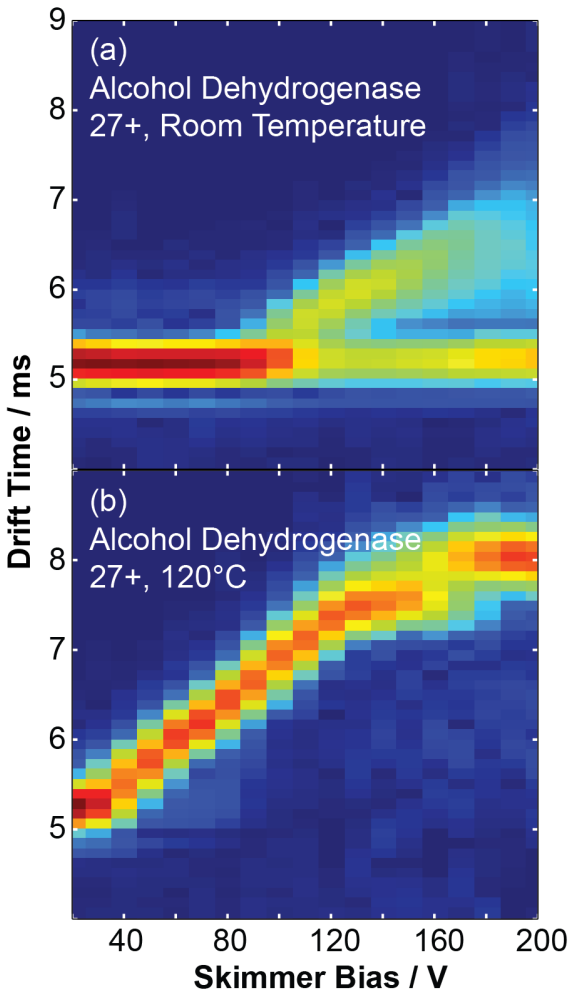

Figure S5. Arrival-time distributions of 27+ alcohol dehydrogenase measured as a function of the voltage bias between the first two optics of the atmospheric-pressure interface, which was operated at (a) ambient temperature and (b) 120 °C. At the two temperatures, 27+ alcohol dehydrogenase exhibits the onset of unfolding with bias voltages of 90 and 30 V, respectively. The lower threshold observed when the atmospheric-pressure interface is operated at the higher temperature is consistent with convective heat transfer to the sample destabilizing the structure in solution[6,12] and/or the higher gas temperature increasing the extent of activation during transfer into the vacuum system.

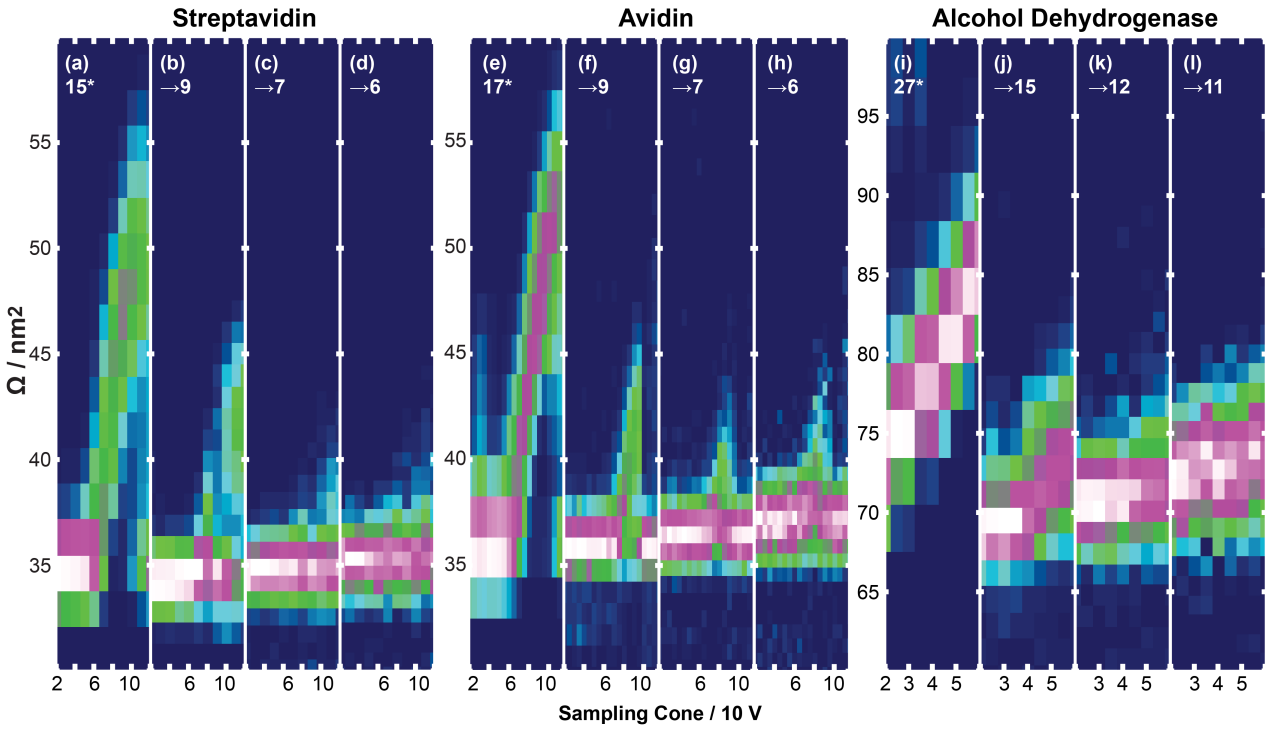

Figure S6. Ω distributions of the 15*→*C* ions of streptavidin (a-d), 17*→*C* ions of avidin (e-h), and 27*→*C* ions of alcohol dehydrogenase (i-l) that were activated prior to CAPTR. Data is shown as a function of the voltage bias between the first two optics in the atmospheric-pressure interface (Figure 1b). Results from pre-CAPTR activation of 15+ serum albumin are shown in Figure S6.

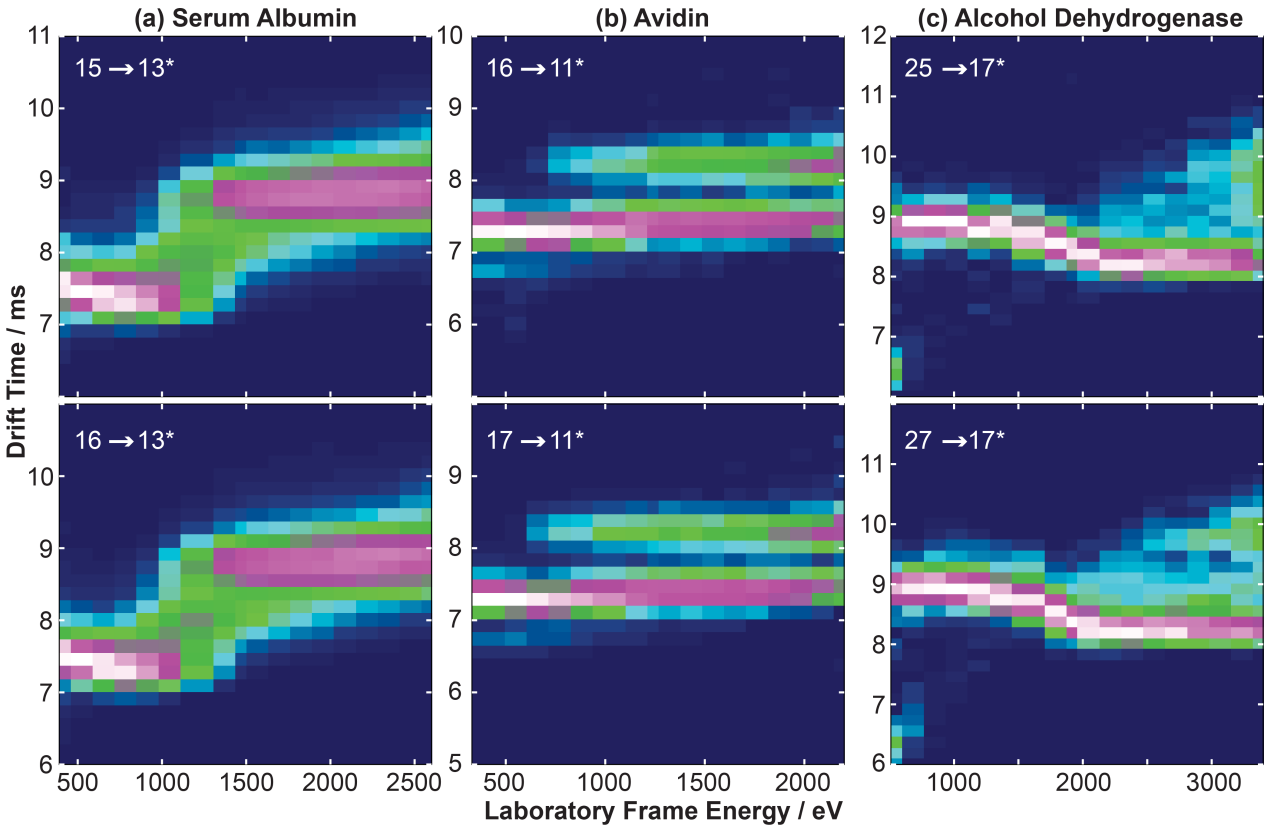

Figure S7. Post-CAPTR activation of (a) serum albumin, (b) avidin, and (c) alcohol dehydrogenase. The data show the arrival-time distributions plotted as colors, against the laboratory-frame energy used to inject the CAPTR product ions into the argon-filled cell, as described in *Methods*.

References

(1) Allen, S. J.; Giles, K.; Gilbert, T.; Bush, M. F. Ion Mobility Mass Spectrometry of Peptide, Protein, and Protein Complex Ions Using a Radio-Frequency Confining Drift Cell. *Analyst* **2016**, *141* (3), 884–891.

(2) Allen, S. J.; Bush, M. F. Radio-Frequency (RF) Confinement in Ion Mobility Spectrometry: Apparent Mobilities and Effective Temperatures. *J. Am. Soc. Mass Spectrom.* **2016**, *27*, 2054–2063.

(3) Bush, M. F.; Hall, Z.; Giles, K.; Hoyes, J.; Robinson, C. V.; Ruotolo, B. T. Collision Cross Sections of Proteins and Their Complexes: A Calibration Framework and Database for Gas-Phase Structural Biology. *Anal. Chem.* **2010**, *82*, 9557–9565.

(4) Mason, E. A.; McDaniel, E. W. *Transport Properties of Ions in Gases*; Wiley: New York, 1988.

(5) Ruotolo, B. T.; Benesch, J. L.; Sandercock, A. M.; Hyung, S. J.; Robinson, C. V. Ion Mobility-Mass Spectrometry Analysis of Large Protein Complexes. *Nat Protoc* **2008**, *3*, 1139–1152.

(6) Laszlo, K. J.; Munger, E. B.; Bush, M. F. Folding of Protein Ions in the Gas Phase after Cation-to-Anion Proton-Transfer Reactions. *J. Am. Chem. Soc.* **2016**, *138*, 9581–9588.

(7) Allen, S. J.; Schwartz, A. M.; Bush, M. F. Effects of Polarity on the Structures and Charge States of Native-Like Proteins and Protein Complexes in the Gas Phase. *Anal. Chem.* **2013**, *85* (24), 12055–12061.

(8) Bornschein, R.; Hyung, S.-J.; Ruotolo, B. Ion Mobility-Mass Spectrometry Reveals Conformational Changes in Charge Reduced Multiprotein Complexes. *J. Am. Soc. Mass Spectrom.* **2011**, *22* (10), 1690–1698.

(9) Lermyte, F.; Williams, J. P.; Brown, J. M.; Martin, E. M.; Sobott, F. Extensive Charge Reduction and Dissociation of Intact Protein Complexes Following Electron Transfer on a Quadrupole-Ion Mobility-Time-of-Flight MS. *J. Am. Soc. Mass Spectrom.* **2015**, *26*, 1068–1076.

(10) Tureček, F.; Julian, R. R. Peptide Radicals and Cation Radicals in the Gas Phase. *Chem. Rev.* **2013**, *113* (8), 6691–6733.

(11) Campuzano, I. G.; Schnier, P. Coupling Electrospray Corona Discharge, Charge Reduction and Ion Mobility Mass Spectrometry: From Peptides to Large Macromolecular Protein Complexes. *Int. J. Ion Mobil. Spectrom.* **2013**, *16* (1), 51–60.

(12) Laszlo, K. J.; Buckner, J. H.; Munger, E. B.; Bush, M. F. Native-like and Denatured Cytochrome c Ions Yield Cation-to-Anion Proton-Transfer Products with Similar Collision Cross Sections. *J. Am. Soc. Mass Spectrom.* **2017**, DOI: 10.1007/s13361-017-1620-4.

APPENDIX F

Table S1. Ω Values for Protein Structures.

Protein	Method	Native [c]	α-Helix [c]	Linear [c]
Ubiquitin	PA:	9.05 ± 0.01 [a]	14.52 ± 0.02	22.92 ± 0.03
	EHSS:	11.15 ± 0.01 [a]	17.71 ± 0.06	26.11 ± 0.08
Di-ubiquitin	PA:	15.18 ± 0.01 [b]	28.23 ± 0.06	45.54 ± 0.09
	EHSS:	19.08 ± 0.02 [b]	34.6 ± 0.2	51.9 ± 0.2
Tri-ubiquitin	PA:		42.0 ± 0.1	68.2 ± 0.2
	EHSS:		51.5 ± 0.3	77.7 ± 0.4
Tetra-ubiquitin	PA:		55.6 ± 0.2	90.8 ± 0.2
	EHSS:		68.4 ± 0.5	103.8 ± 0.6

[a] Calculated from modified structures based off PDB entry 1UBQ

[b] Calculated from modified structures based off PDB entry 3AXC

[c] Ω values were calculated for models that were constructed as described in the *Methods*. The reported interval was determined using Student's t-test at the 95% confidence level and 512 replicate calculations.

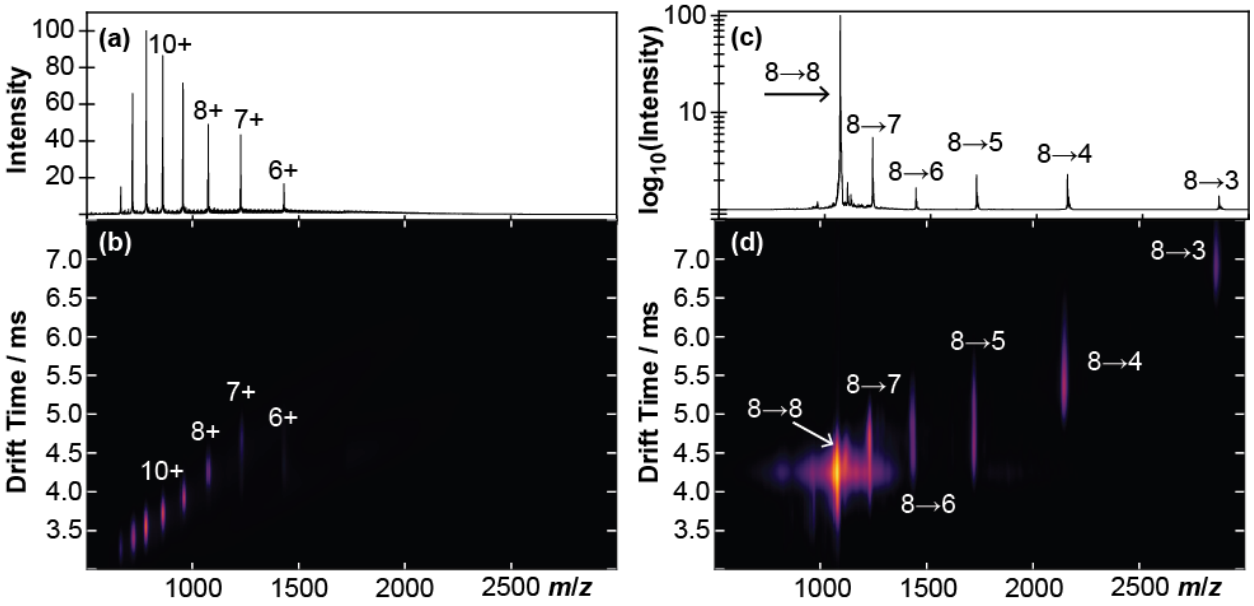

Figure S1: (a) Mass spectrum of denatured Ub_1. (b) IM-MS spectrum of denatured Ub_1. (c) CAPTR mass spectrum of 8+ quadrupole-selected denatured Ub_1. Intensity is plotted on a logarithmic axis to aid in visualizing the product ion peaks. (d) IM-MS spectrum of 8+ quadrupole-selected denatured Ub_1. Intensity is plotted on a $\log_{10}(\log_{10}(\text{intensity}))$ axis.

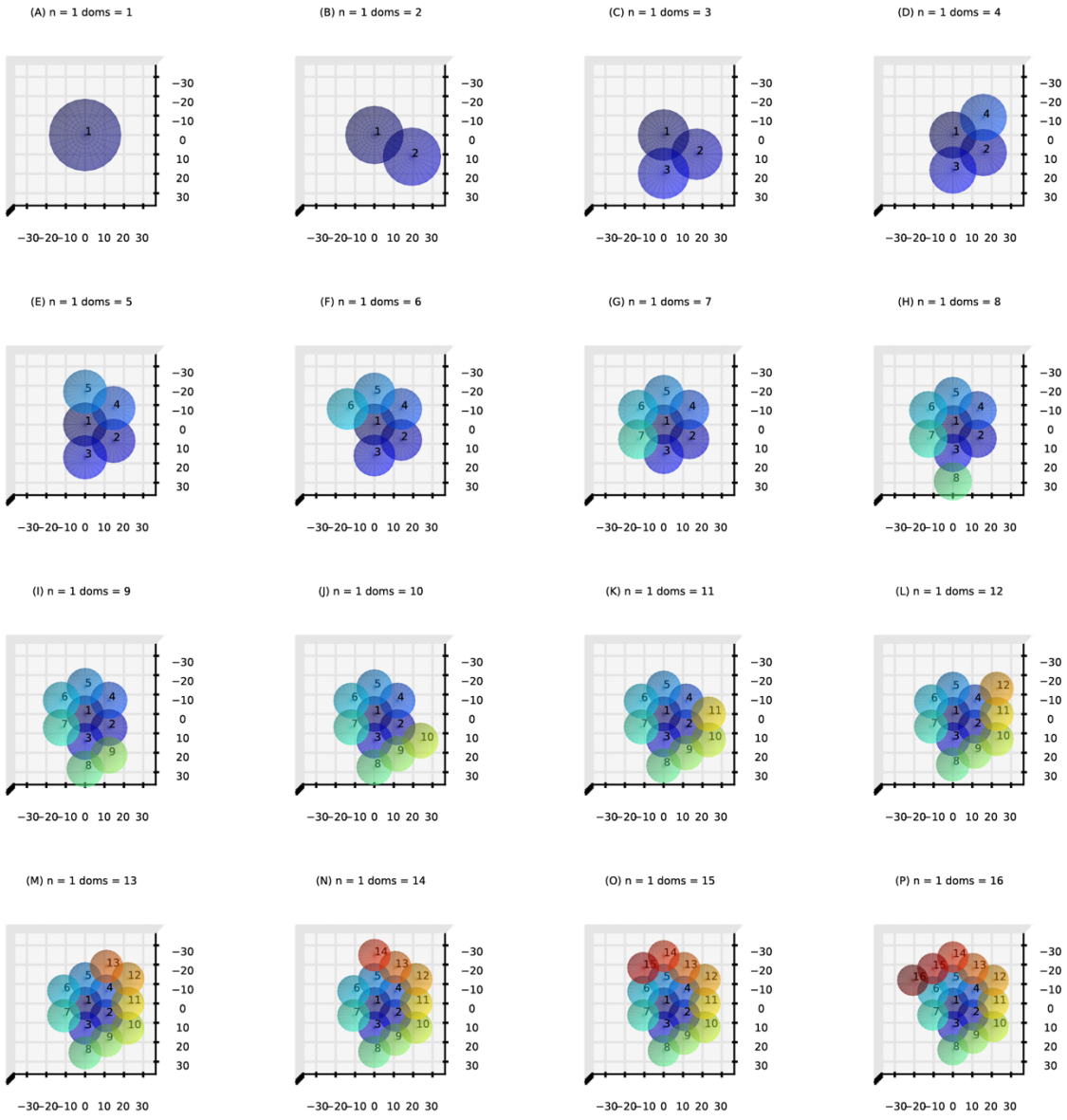

Figure S2. Arrangement of beads (doms) in planar model, using Ub_1 (n=1) as an example, where one domain is added in each subsequent panel. Axis units are in angstroms.

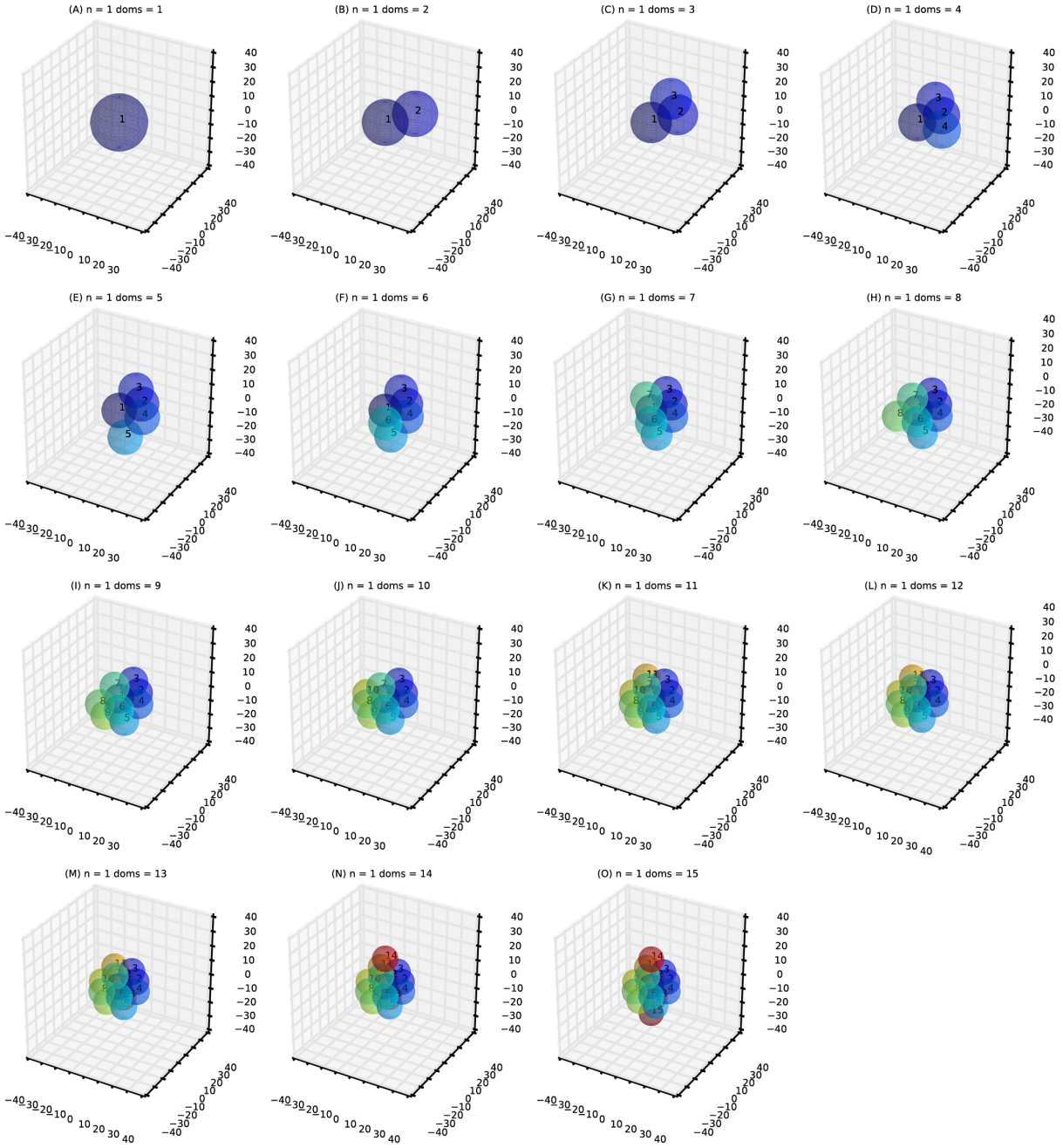

Figure S3. Arrangement of beads in close-packing model, using Ub_1 as an example, where one domain is added in each subsequent panel. Axis units are in angstroms.

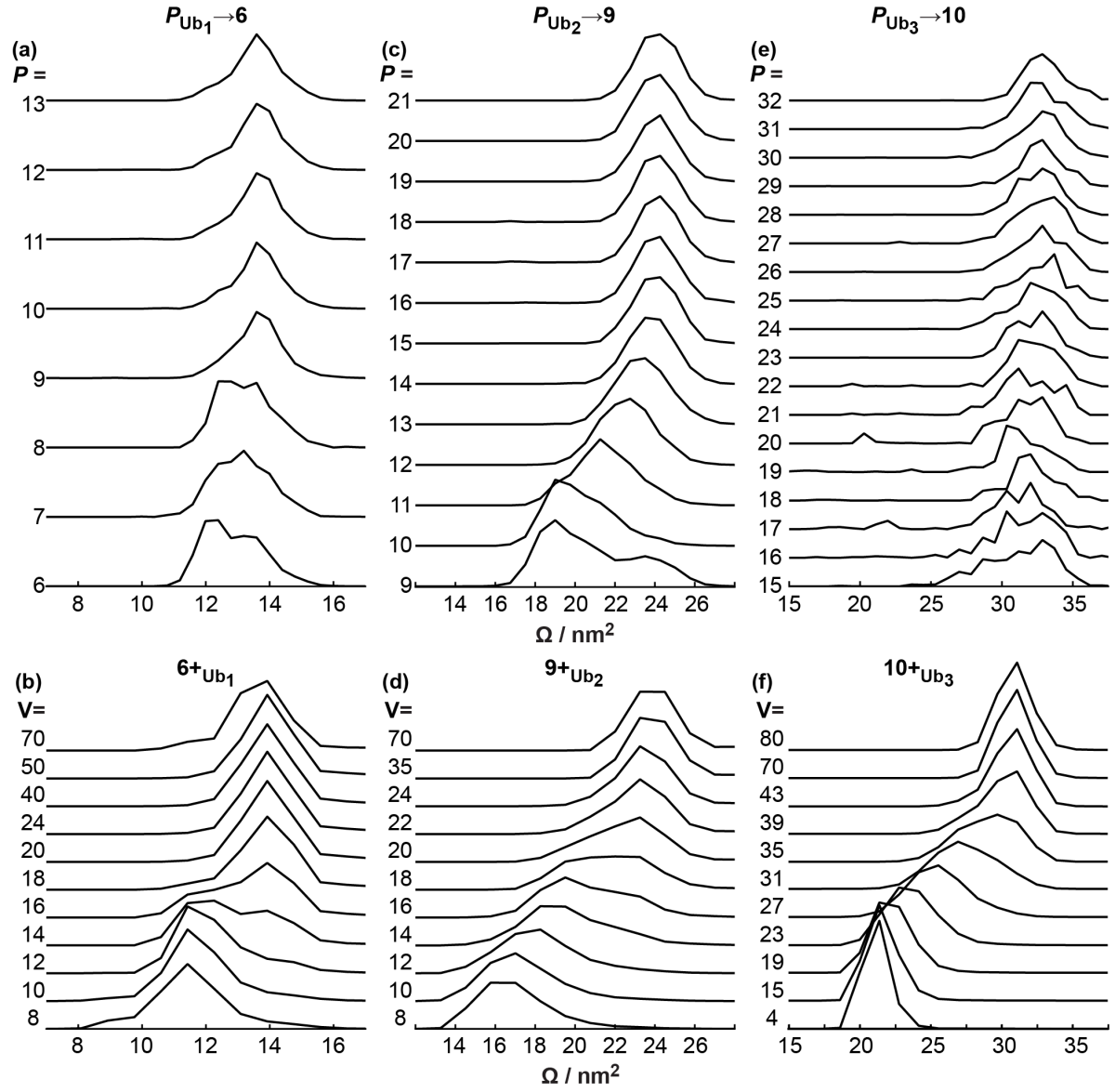

Figure S4. Ω distributions of CAPTR product ions of (a) $\mathrm{Ub}_1^{DP\rightarrow 6}$, (c) $\mathrm{Ub}_2^{DP\rightarrow 9}$, and (e) $\mathrm{Ub}_3^{DP\rightarrow 10}$, and energy dependent collisional activation of (b) $\mathrm{Ub}_1^{\mathrm{N}6}$, (d) $\mathrm{Ub}_2^{\mathrm{N}9}$, and (f) $\mathrm{Ub}_3^{\mathrm{N}10}$. Time was converted to Ω using a single-field strength method with a 212 V drop across the drift cell.

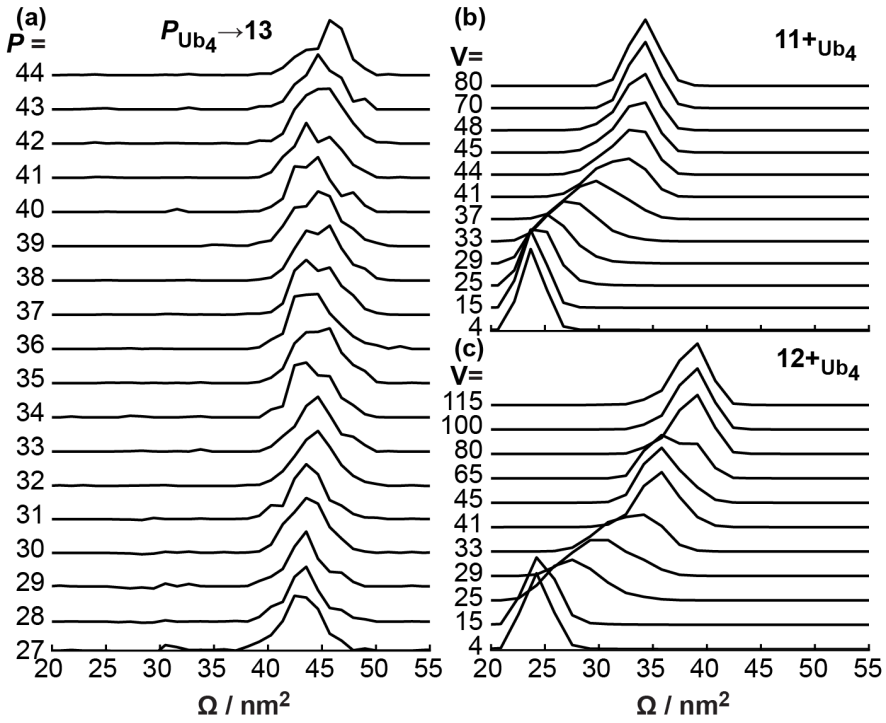

Figure S5. Ω distributions of CAPTR product ions of (a) $Ub_4^{DP \rightarrow 13}$, and energy dependent collisional activation of (b) Ub_4^{N11}, and (c) Ub_4^{N12}. Time was converted to Ω using a single-field strength method with a 212 V drop across the drift cell.

APPENDIX G

This Appendix is reproduced with permission the Supporting Information of Laszlo, K. J.; Bush, M. F. "Effect of Charge State, Partial Charge Distribution, and Structure on Momentum Transfer Collision Cross Sections of Protein Ions" **2017**, manuscript in preparation

TM Calculation Settings in IMoS.

excelfile Savefile Gas
Input/UBQ1_N_amberEven_5.xlsx /OutPut/OUTPUT_UBQ1_N_amberEven_5+_14.txt He

interface 0 0
fromvalue 1
tovalue 1
partialc 0
Charge 1
Mgas 4
radgas 1.4
Polarizability 0.205
Pressure 199.98
Mweight 8555

Temperature 301.15
redCoef 1.0
NrotationsPA 100
NrotationsEHSS 100
NrotationsTM 3
NgastotalEHSS 3000
NgastotalTM 10000
Acommodation 0.0
Timestep 100
Boxdomain 16
Diffuse? 0
reemvel 6
Other 0
Simplify 0

PA 0
EHSS/DHSS 0
TM 1

DTM 0

PATSA 0
Cutoff 0
Mobcal 0
LennardJones 1
TDHSS 0
SimplifiedTM 1

seed 1627
Numthreads 4
chargelines 55 62

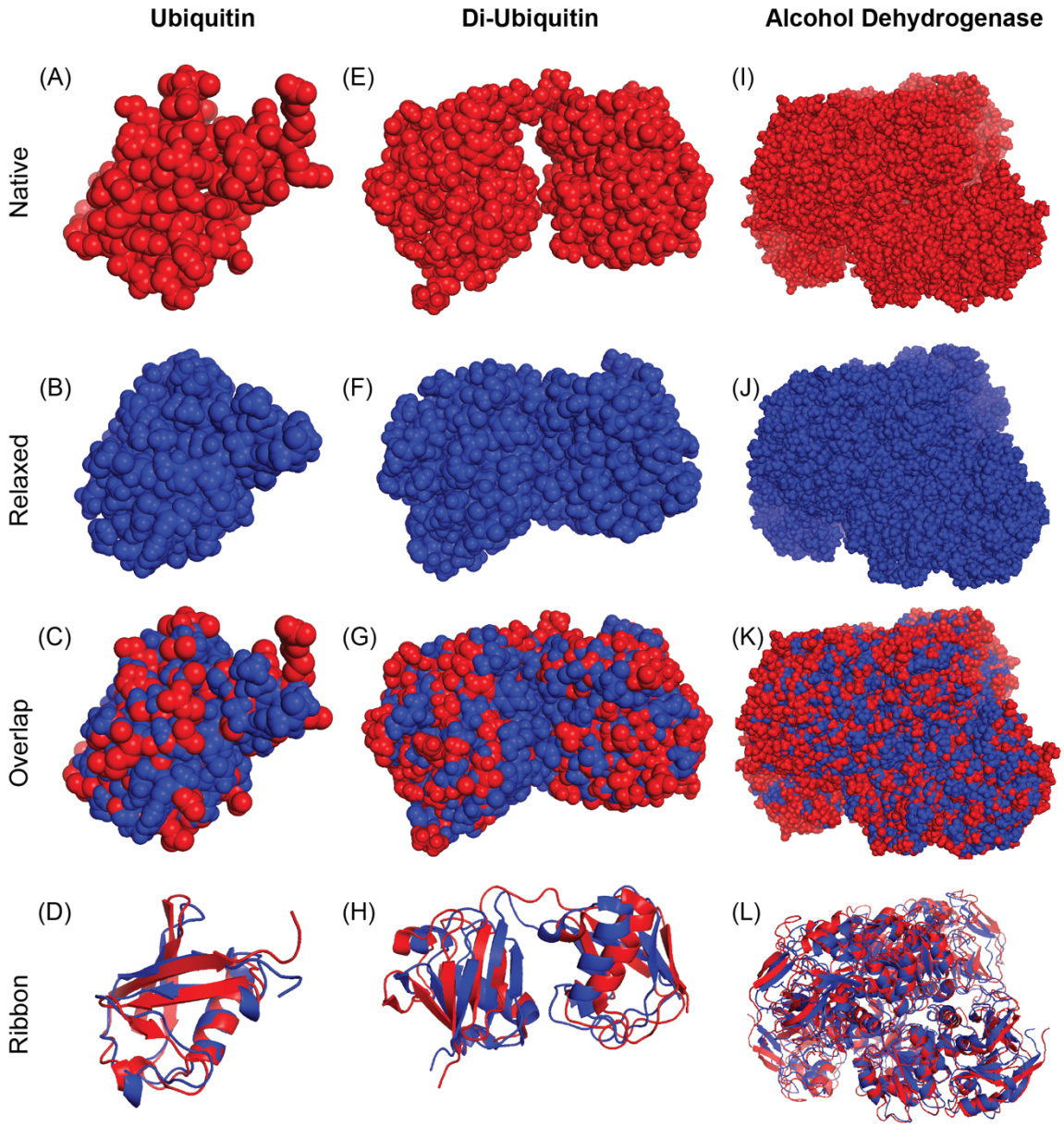

Figure S1. Structural models of native proteins (red) and the relaxed models (*blue*) for Ub_1 (A to D), Ub_2 (E to H) and ADH (I to L).

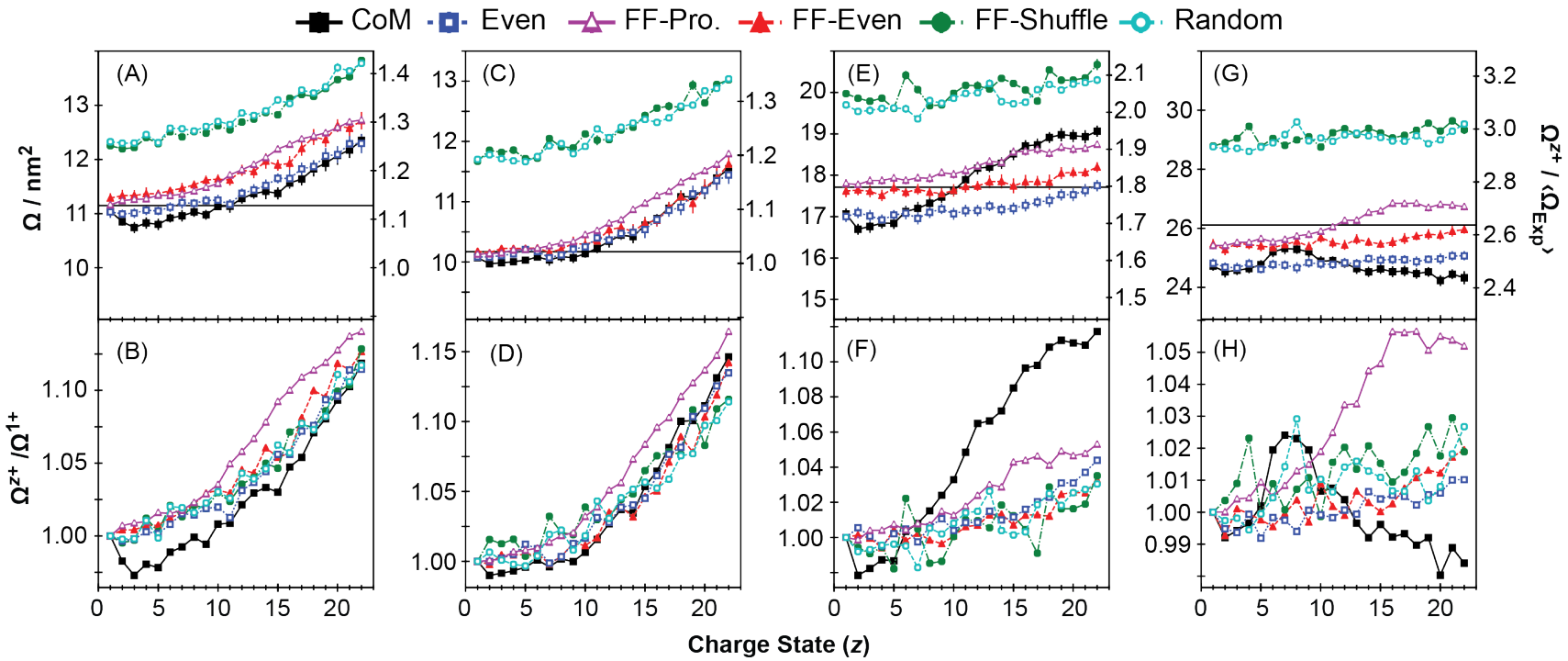

Figure S2. Ω_{TM} of native, energy-relaxed, α-helical, and linear Ub_1 (A, C, E, and G, respectively) with helium as a function of charge state. The lower limit on the y axis corresponds to Ω_{PA} of each structural model, and the solid horizontal black line corresponds to the Ω_{EHSS} of each model (Table 8.1), and the ratio of Ω_{TM} to $\langle\Omega_{Exp}\rangle$ can be found on the right axis. Ω_{TM} values relative to the 1+ ion for each model and PCD method are shown in panels B, D, E, and H.

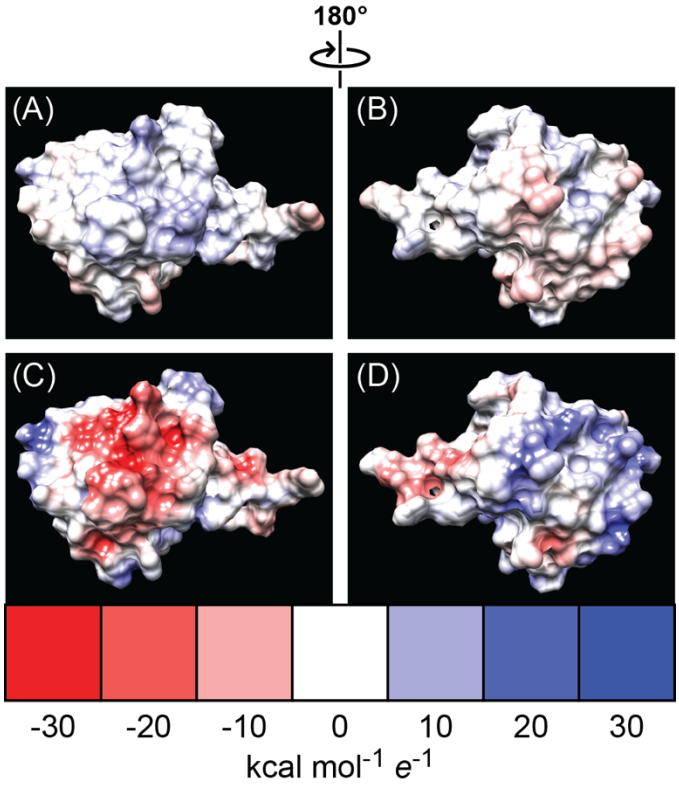

Figure S3. Coulombic surface of 1+ Ub_1using the native model and the FF-Even PCD method (A and B) and FF-Shuffle PCD method (C and D). Colors indicate -30 (red) to 30 (blue) kcal mol^{-1} e^{-1}.

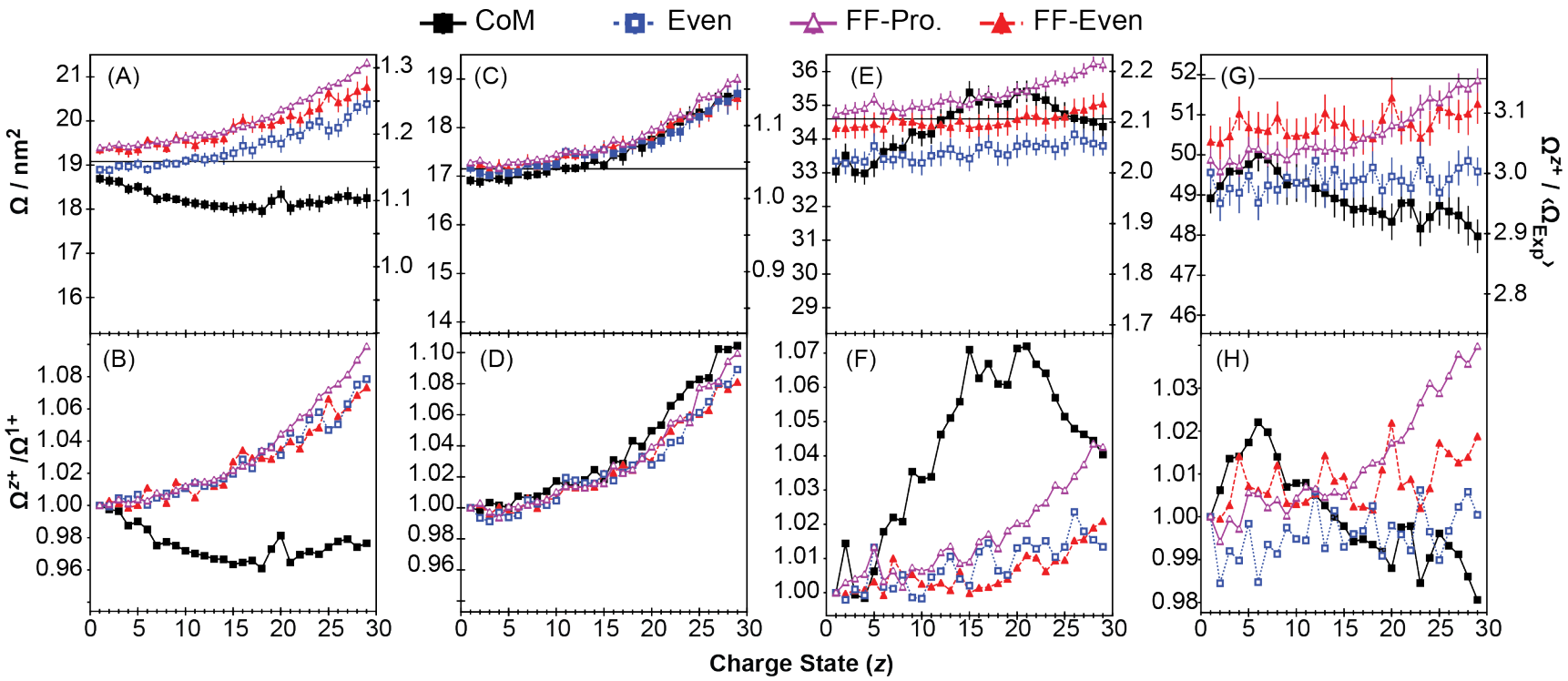

Figure S4. Ω_{TM} of native, energy-relaxed, α-helical, and linear Ub_2 (A, C, E, and G, respectively) with helium as a function of charge state. The lower limit on the y axis corresponds to Ω_{PA} of each structural model, and the solid horizontal black line corresponds to the Ω_{EHSS} of each model (Table 8.1), and the ratio of Ω_{TM} to $\langle\Omega_{Exp}\rangle$ can be found on the right axis. Ω_{TM} values relative to the 1+ ion for each model and PCD method are shown in panels B, D, E, and H.

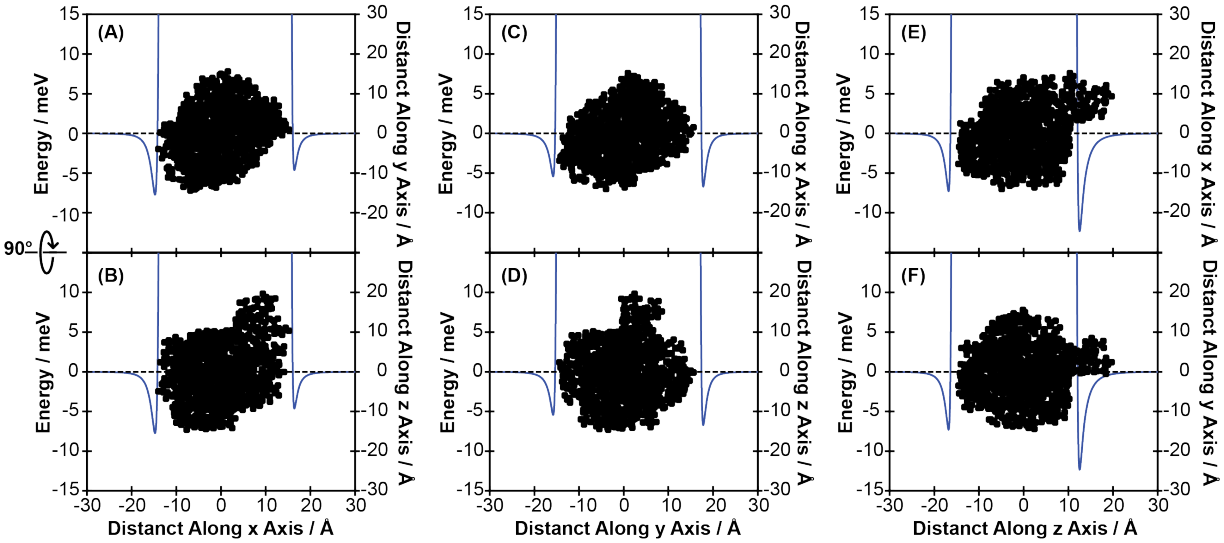

Figure S5: Potential energy (*blue line*) of the interaction of 1+ energy-minimized Ub_1 using the FF-Even method (*black spheres*) along the (A-B) x-axis, (C-D) y-axis, and (E-F) z-axis. The black dashed line indicates a potential energy of 0.0 meV. Upper and lower panels are related to one another through a 90˚ rotation along the axis of interest.

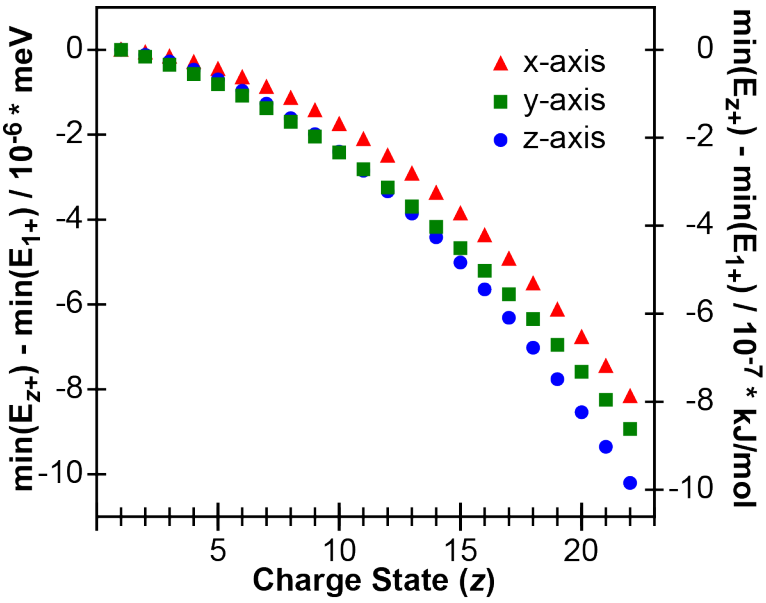

Figure S6: Difference between the minimum of the potential energy of the interaction between a *z*+ and 1+ energy-minimized Ub_1 ion using the FF-Even method and helium as a function of *z*. Differences along the (*red triangles*) x-axis, (*green squares*) y-axis, and (*blue* circles) z-axis are shown in meV and kj/mol.

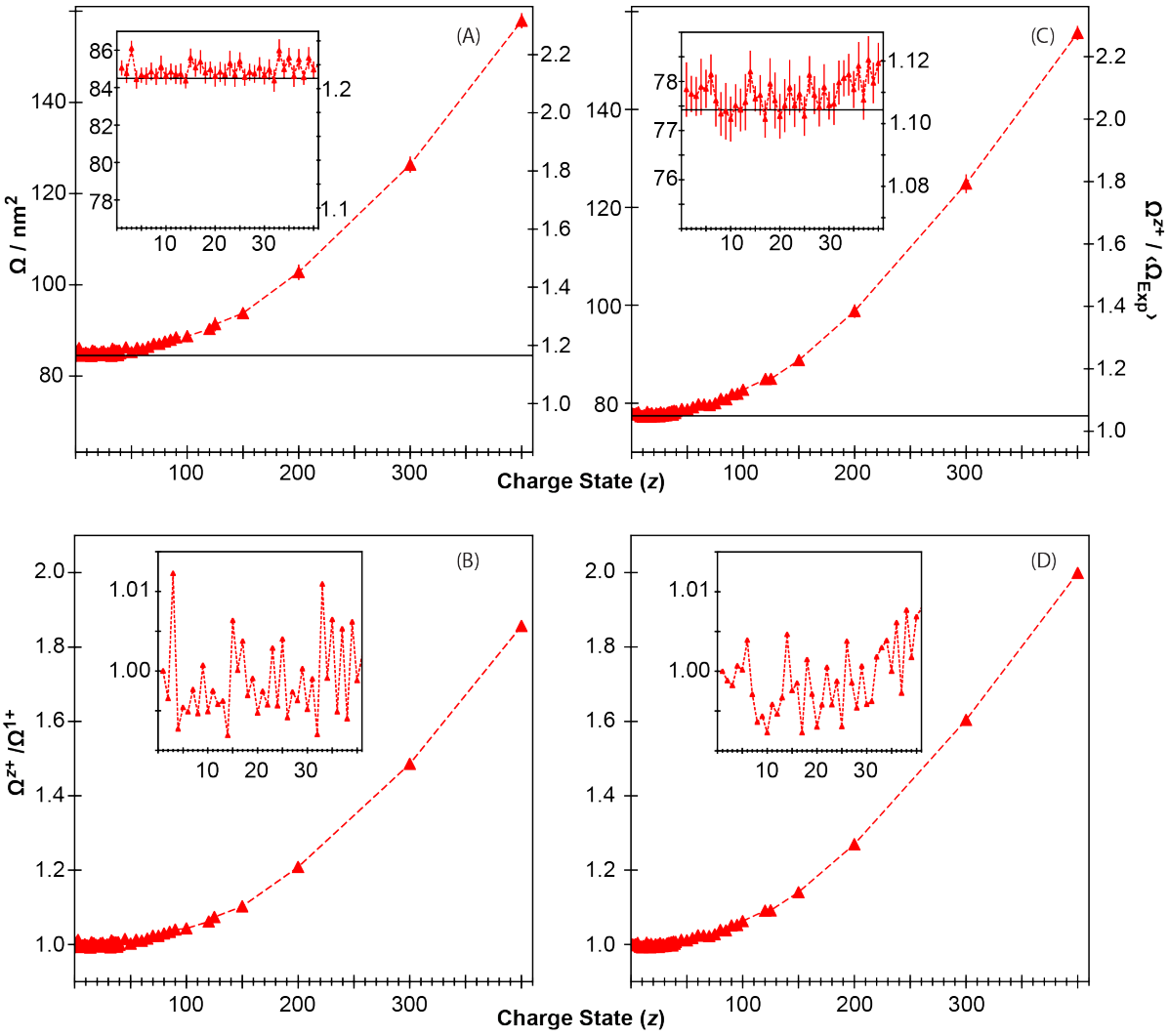

Figure S7. Ω_{TM} of native and energy-relaxed ADH (A and C, respectively) with helium as a function of charge state. The lower limit on the y axis corresponds to Ω_{PA} of each model, and the solid horizontal black line corresponds to the Ω_{EHSS} of each model (Table 8.1), and the ratio of Ω_{TM} to $\langle\Omega_{Exp}\rangle$ can be found on the right axis. Ω_{TM} values relative to the 1+ ion for each model and PCD method are shown in panels B and D.

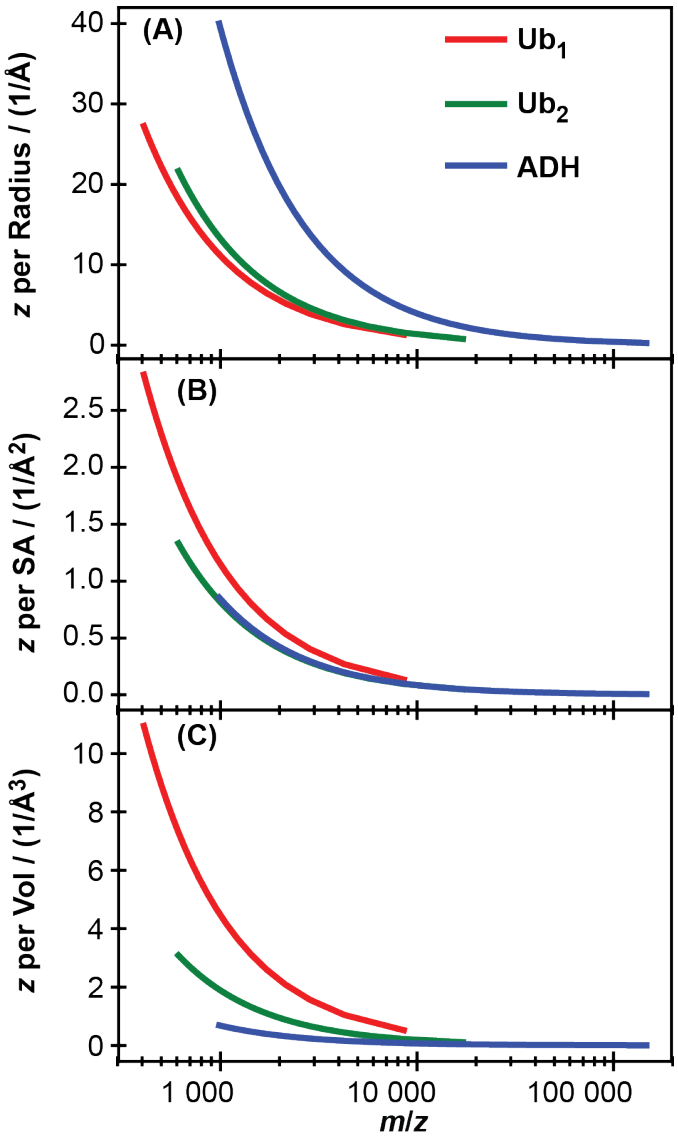

Figure S8: Charge per unit (A) radius, (B) surface area, (C) volume for a sphere with a Ω equal to the average Ω_{Exp} of (*red line*) Ub_1, (*green line*) Ub_2, and (*blue line*) ADH.

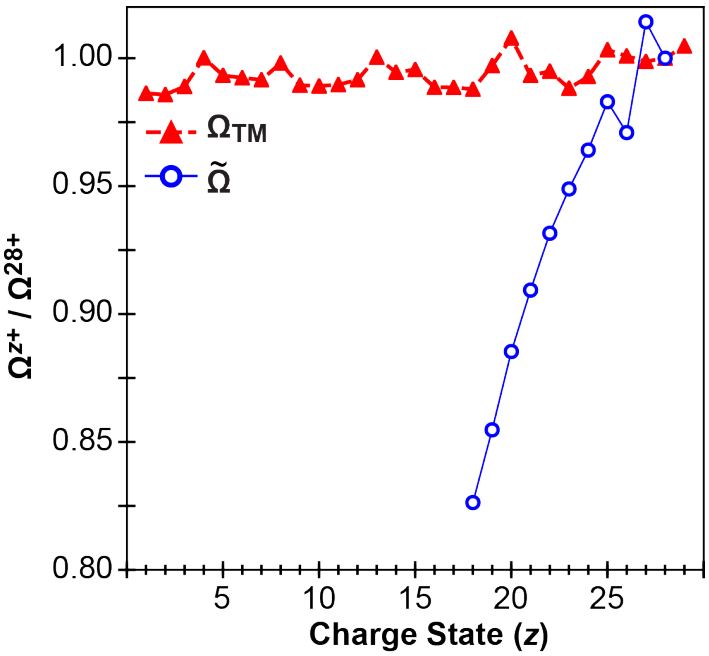

Figure S9. Ω values relative to the Ω of the 27+ ion for linear model of Ub_2 (Figure S2G) using the FF-Even method, and supercharged Ub_2 (Figure 8.1A) as a function of charge state.

VITA

Kenneth Jeffrey Laszlo was born in 1990 to Mary and Jeff Laszlo. Ken attended the Georgia Institute of Technology and received a Bachelor's of Science in chemistry in the Spring of 2012. During his undergraduate studies, Ken was mentored by Prof. Facundo Fernandéz and investigated nanostructure initiator mass spectrometry (NIMS) and the use of cyclodextrins as mobility shift reagents to study lipids. Ken began is graduate studies with Prof. Matthew F. Bush at the University of Washington in the Summer of 2012.